Civil Aircraft Aero-thermo-propulsive Performance Assessment by an Exergy Analysis of High-fidelity CFD-RANS Flow Solutions

Submitted by
Aurélien Arntz

To obtain
Doctorate from Lille 1 University – Sciences and Technologies

Specialty
Mechanics and Energetics

Dissertation defended November 28th, 2014 to the Doctoral Committee composed of:

Mr. Olivier Atinault	Research Engineer	ONERA	*Supervisor*
Pr. Allan Bonnet	Professor	ISAE	*Chairman*
Pr. Philippe Devinant	Professor	Université d'Orléans	*Reviewer*
Pr. Mark Drela	Professor	Massachusetts Institute of Technology	*Reviewer*
Pr. Alain Merlen	Professor	Université de Lille & ONERA	*Director*
Dr. Simon Trapier	Engineer	Airbus	*Examiner*
Dr. Zdenek Johan	Design Engineer	Dassault Aviation	*Invited*
Dr. Christophe Maury	Research Engineer	SAFRAN	*Invited*

Détermination des performances aéro-thermo-propulsives des avions civils par une analyse exergétique de solutions haute-fidélité CFD-RANS

Soutenue par
Aurélien Arntz

Pour l'obtention
Doctorat de Université de Lille – Sciences and Technologies

Spécialité
Mécanique et Energétique

Thèse soutenue le 28 Novembre 2014, devant le jury composé de :

M. Olivier Atinault	Ingénieur de Recherche	ONERA	*Examinateur*
M. Allan Bonnet	Professeur	ISAE	*Président*
M. Philippe Devinant	Professeur	Université d'Orléans	*Rapporteur*
M. Mark Drela	Professeur	Massachusetts Institute of Technology	*Rapporteur*
M. Alain Merlen	Professeur	Université de Lille & ONERA	*Directeur*
M. Simon Trapier	Ingénieur	Airbus	*Examinateur*
M. Zdenek Johan	Ingénieur de Conception	Dassault Aviation	*Invité*
M. Christophe Maury	Ingénieur de Recherche	SAFRAN	*Invité*

Abstract

A new exergy-based formulation is derived for the assessment of the aerothermopropulsive performance of civil aircraft. The choice of exergy is motivated by its ability to provide a well-established and consistent framework for the design of aerospace vehicles. The output of the derivation process is an exergy balance between the exergy supplied by a propulsion system or by heat transfer, the mechanical equilibrium of the aircraft, and the exergy outflow and destruction within the control volume. The theoretical formulation is subsequently numerically implemented in a Fortran code named *ffx* for the post-processing of CFD-RANS flow solutions. Unpowered airframe configurations are examined with grid refinement studies and a turbulence model sensitivity analysis is preformed. A numerical correction is introduced and calibrated to obtain an accuracy similar to the near-field drag method. The code is thereby validated against well-tried methods of drag prediction and wind-tunnel tests, when available.

The investigation of powered configurations demonstrates the ability of the approach for assessing the performance of configurations with aerothermopropulsive interactions. First, the formulation is validated for the simple case of a turbojet engine for which consistent figures of merit are exhibited. The method is also proved robust for assessing the overall performance of a boundary layer ingesting propulsion system placed on the upper surface of a simplified blended wing-body architecture. Moreover, this configuration enables the investigation of thermopropulsive interactions by the transfer of heat upstream of the propulsion system. Subsequently, the integration of a heat exchanger on a commercial aircraft is examined for which the exergy point of view provides guidelines for an efficient design. The ability of the formulation to consistently assess all these types of subsystems is a clear benefit of this method.

Keywords: exergy, energy, performance, CFD, aerodynamics, propulsion, boundary-layer ingestion

Résumé

Une nouvelle formulation basée sur la notion d'exergie est introduite pour la détermination des performances aéro-thermo-propulsives des avions civils. Le choix du concept d'exergie est motivé par sa capacité à fournir un cadre de travail bien établi pour la conception de véhicules aérospatiaux. Les performances avions sont établies à partir d'une équation bilan qui met en relation l'exergie fournie, par un système propulsif ou par transfert de chaleur, l'équilibre mécanique de l'appareil, et sa destruction partielle dans le volume de contrôle. Cette formulation théorique est ensuite implémentée numériquement dans un code Fortran, appelé *ffx*, pour le post-traitement de solutions CFD-RANS. Des configurations non propulsées sont étudiées avec raffinement de maillage et une analyse de la sensibilité du code au modèle de turbulence employé pour obtenir la solution CFD est réalisée. Le code est ainsi validé par rapport à des méthodes éprouvées de détermination de la traînée et à des essais en soufflerie, si disponibles.

L'approche est ensuite appliquée pour la détermination des performances de configurations propulsées présentant de fortes interactions aéro-thermo-propulsives. Dans un premier temps, la cohérence de la formulation est validée pour un turbojet pour lequel des indicateurs de performances cohérents sont obtenus. La méthode est également prouvée robuste pour l'analyse des performances globales de l'ingestion de couches limites par un moteur placé à l'arrière d'une aile volante simplifiée. Cette architecture permet également l'étude des interactions thermopropulsives lors d'un transfert de chaleur imposé en amont du système propulsif. Enfin, l'intégration d'un échangeur de chaleur sur un avion commercial est examinée pour en déduire des recommandations pour une conception efficace d'un point de vue exergétique. La capacité de la formulation à pouvoir traiter de façon cohérente ces différents types de sous-systèmes est le principal avantage de cette méthode.

Keywords: exergie, énergie, performances, CFD, aérodynamique, propulsion, ingestion couches limites

Acknowledgments

Nomenclature

According to BOREL, despite great efforts deployed by many scientists around the world, the exergy analysis has not been completely standardized yet, neither in the terminology nor in the notation [31]. As a consequence, the author has been unable to find a commonly accepted nomenclature regarding the exergy analysis [38, 45, 149, 167, 168]. The one adopted here provides pedagogical advantages in agreement with the terminology proposed by RANT [129].

Formulation

$\dot{\mathcal{A}}_q$	=	rate of heat anergy supplied by conduction (J.s^{-1})
$\dot{\mathcal{A}}_{\nabla T}$	=	rate of anergy generation by thermal mixing (J.s^{-1})
$\dot{\mathcal{A}}_\phi$	=	rate of anergy generation by viscous dissipation (J.s^{-1})
$\dot{\mathcal{A}}_{tot}$	=	rate of total anergy generation (J.s^{-1}), $= \dot{\mathcal{A}}_\phi + \dot{\mathcal{A}}_{\nabla T} + \dot{\mathcal{A}}_w$
$\dot{\mathcal{A}}_w$	=	rate of anergy generation by shock waves (J.s^{-1})
$\dot{\mathcal{A}}^*$	=	sum of exergy outflows and anergy generation (J.s^{-1}), $= \dot{\mathcal{E}}_m + \dot{\mathcal{E}}_{th} + \dot{\mathcal{A}}_{tot}$
D	=	aerodynamic drag (N)
$\dot{E}_u$	=	streamwise kinetic energy deposition rate (J.s^{-1})
$\dot{E}_p$	=	boundary pressure-work rate (J.s^{-1})
$\dot{E}_\phi$	=	rate of thermal energy generation by viscous dissipation (J.s^{-1})
$\dot{E}_q$	=	rate of heat energy supplied by conduction (J.s^{-1})
$\dot{E}_{th}$	=	rate of thermal energy outflow (J.s^{-1})
$\dot{\mathcal{E}}_{th(\rho)}$	=	outflow rate of thermal exergy associated with volume change
$\dot{\mathcal{E}}_{th(T)}$	=	outflow rate of thermal exergy at constant volume
$\dot{E}_v$	=	transverse kinetic energy deposition rate (J.s^{-1})
$\dot{E}_W$	=	surroundings-work rate (J.s^{-1})
$\dot{\mathcal{E}}_m$	=	rate of mechanical exergy outflow (J.s^{-1}), $= \dot{E}_u + \dot{E}_v + \dot{E}_p$
$\dot{\mathcal{E}}_{prop}$	=	rate of exergy supplied by the propulsion system (J.s^{-1})
$\dot{\mathcal{E}}_{prop,m}$	=	rate of mechanical exergy supplied by the propulsion system (J.s^{-1})
$\dot{\mathcal{E}}_{prop,th}$	=	rate of thermal exergy supplied by the propulsion system (J.s^{-1})
$\dot{\mathcal{E}}_\phi$	=	rate of thermal exergy generation by viscous dissipation (J.s^{-1})
$\dot{\mathcal{E}}_q$	=	rate of heat exergy supplied by conduction (J.s^{-1})
$\dot{\mathcal{E}}_{th}$	=	rate of thermal exergy outflow (J.s^{-1})
$\mathbf{F_A}$	=	momentum change across the aircraft surface (N)
$\mathbf{F_{prop}}$	=	momentum change across the propulsive surface (N)
$\mathbf{F_O}$	=	momentum change across the outer boundary (N)
F_x	=	streamwise resultant force acting on the vehicle (N)
γ	=	aircraft climb angle (deg)
Γ	=	weight specific aircraft energy height (m)
$\mathbf{n}$	=	unit normal vector
$\tilde{\mathbf{n}}$	=	unit normal vector for the shock wave
$\hat{\mathbf{n}}$	=	unit normal vector, $= -\mathbf{n}$
Φ_{eff}	=	effective dissipation rate per unit volume (J.s^{-1}.m^{-3}), $= \left(\bar{\bar{\tau}}_{eff} \cdot \nabla\right) \cdot \mathbf{V}$

ψ_ε = overall exergy efficiency

ψ_i = engine intrinsic exergy efficiency

ψ_m = mechanical exergy efficiency

ψ_p = propulsive efficiency

$\mathbf{q}_{eff}$ = effective heat flux by conduction (J.s^{-1}), $-k_{eff}\nabla\mathbf{T}$

W = aircraft weight (N)

$\mathcal{S}_A$ = aircraft surface

$\mathcal{S}_B$ = body surface

$\mathcal{S}_O$ = outer boundary of the control volume

$\mathcal{S}_P$ = surface delimiting the propulsion system

dTP = streamwise distance of the transverse plane

Fluid and Flow Properties

α = flow incidence relative to body (deg)

c_p = mass specific heat capacity at constant pressure (J.kg^{-1}.K^{-1})

c_v = mass specific heat capacity at constant volume (J.kg^{-1}.K^{-1})

e = mass specific internal energy (J.kg^{-1}), $= c_v T$

ε = mass specific flow exergy (J.kg^{-1}), $= \delta h_i - T_\infty \delta\mathsf{s}$

h = mass specific enthalpy (J.kg^{-1}), $= e + p/\rho = c_p T$

h_i = mass specific total/stagnation enthalpy (J.kg^{-1}), $= h + V^2/2$

k_{eff} = effective thermal conductivity (W.m^{-1}.K^{-1}), $= c_p(\mu/Pr + \mu_t/Pr_t)$

M = *Mach*-number

$M_\perp$ = normal shock *Mach*-number

μ = laminar dynamic viscosity (kg.m.s^{-1})

μ_t = turbulent dynamic viscosity (kg.m.s^{-1})

μ_{eff} = effective dynamic viscosity (kg.m.s^{-1}), $= \mu + \mu_t$

p = static pressure (kg.m.s^{-2})

p_i = total/stagnation pressure (kg.m.s^{-2}), $= p\left[1 + (\gamma-1)M^2/2\right]^{\frac{\gamma}{\gamma-1}}$

Pr = *Prandtl*-number

Pr_t = turbulent *Prandtl*-number

ρ = density (kg.m^{-3})

Re = *Reynolds*-number

s = mass specific entropy (J.K^{-1}.kg^{-1})

$\bar{\bar{S}}$ = strain rate (s^{-1})

T = static temperature (K)

T_i = total/stagnation temperature (K), $= T\left[1 + (\gamma-1)M^2/2\right]$

T_w = wall temperature (K)

$\bar{\bar{\tau}}_{eff}$ = effective viscous stress tensor (N), $= (\mu + \mu_t)\bar{\bar{S}}$

$\mathbf{V}$ = fluid velocity vector (m.s^{-1}), $= (V_\infty + u)\mathbf{x}, v\mathbf{y}, w\mathbf{z}$

Subscripts

$adiab$ = adiabatic

∞ = quantity at freestream conditions

TP = transverse plane

Superscripts

$(\ )'$ =   quantity neglected numerically
$(\ )^c$ =   quantity with numerical correction

Operators

$:=$ =   equal by definition
$\equiv$ =   numerically equivalent
$[\![\ ]\!]$ =   discontinuous jump of a quantity
$\dot{(\ )}$ =   time derivative of a quantity, $= \mathrm{d}(\ )/\mathrm{d}t$
$\delta(\ )$ =   quantity relative to freestream, $= (\ ) - (\ )_\infty$
$\nabla(\ )$ =   gradients of a vector quantity, $= [\partial(\ )/\partial x, \ \partial(\ )/\partial y, \ \partial(\ )/\partial z]^T$
$\nabla \cdot (\ )$ =   divergence of a vector quantity, $= \partial(\ )/\partial x + \partial(\ )/\partial y + \partial(\ )/\partial z$
$\otimes$ =   tensor product

Acronyms

BLI =   boundary-layer ingestion
BWB =   blended wing-body
ERC =   exergy-recovery coefficient
ESC =   exergy-saving coefficient
$ESFC$ =   exergy specific fuel consumption
EWC =   exergy-waste coefficient
FPR =   fan pressure ratio
MAC =   mean aerodynamic chord
$MFR_\%$ =   non-dimensionalized massflow rate

Other Notations

Δh_f =   mass specific fuel heating value (J.kg^{-1})
dc =   drag counts (10^{-4})
$\bar{\bar{I}}$ =   identity matrix
λ_w =   shock wave criterion
$\dot{m}_f$ =   fuel mass flow (kg.s^{-1})
pc =   power counts (10^{-4})

We are not to tell nature what she's gotta be.
She's always got better imagination than we have...

RICHARD P. FEYNMAN (1918–1988)
Theoretical Physicist, Nobel Prize (1965)

Contents

Introduction

Context

Market Forecast.   A century after the first commercial flight made in January 1914, the air transportation industry has seen fantastic growth. Global Civil Market development is driven by many factors as diverse as market liberalization, infrastructure, network development, high speed rail, economic growth, environment, fuel price and emerging markets. The world air travel has grown by 5% per annum[1] since 1980 despite four recessions, two financial crises, two Gulf wars, two oil shock and more recently 9/11 which has resulted in many changes in the way people fly since then. Driven by emerging economies of Asia Pacific and Latin America, the same trend is expected for the next 20-year period. In fact, despite a different approach on how would the world travel demand evolve, last year, Airbus and Boeing agree that more than new 29,000 aircraft[2] will be necessary to meet this increasing demand over the 2013–2032 period [90, 160].

Environmental Concern.   Today, around 2% of the CO_2 man-made emissions are attributed to air travel, but this percentage may grow significantly in the future. Such growth has raised environmental concern and driven international institutions and major research agencies to set ambitious objectives of performance. Among these objectives emerged a dramatic reduction in both fuel combustion and noise/pollutant emissions: NO_x by 80% and CO_2 by 50% for the European Commission through *ACARE* [5].

In 2010, ONERA published an overview [86] of key technologies that require to be investigated based on four different scenarios identified a few years earlier in the *Consave 2050* project [27]. Regarding aircraft, the current conventional *tube and wing* configuration has been justified by a function-driven approach: carrying people in the pressurized fuselage, lifting the airplane with wings and a propulsive system. Each separate part has been designed and optimized separately, their final assembly somehow providing an optimum. Because harder and harder improvements of the current architecture could only provide a short term answer to the future challenges, a breakthrough similar to the advent of the wide-bodies in the early 70's is likely to be needed.

---

[1]Keeping in mind that a 5% per year growth is equivalent to doubling the number of passengers every 15 years.

[2]Airbus evaluates the potential to 29,226 aircraft (1,711 very large) while Boeing forecasts 35,280 aircraft (760 very large) worth respectively 4.4 and 4.8 trillion USD.

Advanced Designs. In October 2008, NASA launched a 18-month program by asking industry and academia to develop advanced concepts for aircraft that can satisfy anticipated commercial air transportation needs while meeting specific energy efficiency, environmental and operational goals[3] in 2030 and beyond [17]. The type of advanced designs able to cope with the aforementioned challenges may be illustrated by two of the revolutionary conceptual studies conducted for the NASA N+3 Program depicted in Fig. 0-1.

(a) MIT D8 Concept.

(b) NASA N3-X Concept.

Figure 0-1: Two of the main advanced conceptual designs for a 2030+ time-frame.

The "double-bubble" D8 transport configuration [50] has been designed by a team from MIT, Aerodyne Research, Aurora Flight Sciences, and Pratt&Whitney. This double-tube and wing is intended to serve the B737/A320 mission and includes the benefits of boundary layer ingestion (BLI) on the top surface of the fuselage. The propulsion system-airframe integration was identified as *the critical technology challenge to be resolved* [66].

Another promising configurations in the long-term is the blended-wing body (BWB) featuring BLI propulsion [65]. A key example of advanced configuration is the N3-X concept which is a blended wing-body architecture that decouples the power producing parts of the system from the thrust producing parts of the system thereby allowing each to be optimized for its task [54, 55]. It utilizes superconducting electrically driven, distributed low-pressure-ratio fans with power provided by two remote superconducting electric generators based on a conventional turbofan core engine design [15].

Thermal Management. Another area of interest is thermal management which has been identified as a major area of gain in military aircraft performance [61]. These thermal aspects are also expected to play an increasing role for commercial aircraft [43] as a greater number of electromechanical actuation systems are anticipated to create thermal loads that can be challenging to manage. In fact, the *more-electric* architecture [62, 63] increases the electric energy use in order to replace the mix of hydraulic, pneumatic, and electric energy to fulfill the requirements of systems, augmenting the energy efficiency of non-propulsive systems [51]. These subsystem design requirements are often brought into the design cycle after the airframe and propulsion systems engineers have established an optimal aerodynamic configuration. This traditional design process may not enable the design of aerospace vehicles exhibiting the best overall performance because the increase in thermal loads also requires a greater emphasis on the integrated performance of aircraft propulsion and thermal management. In other words, the thermal energy management could provide significant gains of performance for future (complex) civil aircraft configurations.

Problem Statement

Preliminary Design Phase. The complete design process of an aerospace vehicle is traditionally made up of three distinct phases that are carried out in sequence [9]. The phases are, in chronological order,

---

[3]Compared with an aircraft entering service at that time: a 71-decibel reduction, a greater than 75% reduction in NOx emissions and a greater than 70% reduction in fuel burn performance.

conceptual design, preliminary design, and detail design. The first phase starts with a set of specifications for a new airplane for which overall shape, size, weight and performance are determined. In order to evaluate very different design options, rapid analytical (low-fidelity) models are used. Then, in the preliminary design phase, serious structural and control system analysis and design take place and only minor changes of the configuration layout are made. Along with wind-tunnel testing, extensive use of CFD-RANS[4] numerical solutions is made to analyze the complete flow field over the airplane configuration. The methods are higher-fidelity tools that yield more accurate and precise information. At the end of this phase, the airplane configuration is frozen and precisely defined. The detail design phase typically consists of the precise determination of the size, number, and location of fasteners (rivets, welded joints, etc.). Manufacturing tools and jigs are designed and flight simulators for the airplane are developed.

Drag-Thrust Bookkeepings. The performance prediction methods currently used have been developed for the conventional configuration for which they give relatively accurate solutions. The usual approach is to balance these two forces through a so-called *drag-thrust bookkeeping* [42]. This approach appears satisfactory for most aircraft designers in the conceptual phase. However, when moving to the preliminary design phase, more attention should be drawn on actually putting the powerplant on the aircraft. As early as 1979, it was recognized that *the variety of actual and possible powerplant configurations is such that a totally comprehensive bookkeeping system would be extremely complicated* and thus accepted to adopt specific bookkeeping systems specially appropriate to the powerplant under study [157]. MCLEAN, from the Aerodynamics at *Boeing*, recognizes that *a clean separation between drag and thrust involves some serious theoretical difficulties* [103] and that the close-coupling between these two forces is often eluded. The trend towards more efficient configurations with highly integrated propulsion systems only reinforces this observation [54, 96]. Even if some models based on simplifying assumptions can be adopted [68], the basic issue remains [56].

Some of the issues have been described by KAWAI *et al.* [78] for a blended-wing body architecture with a propulsion system on the upper surface, see Fig. 0-2.

(a) 2D sketch of the main characteristics of the flow.

(b) Inlet streamtube.
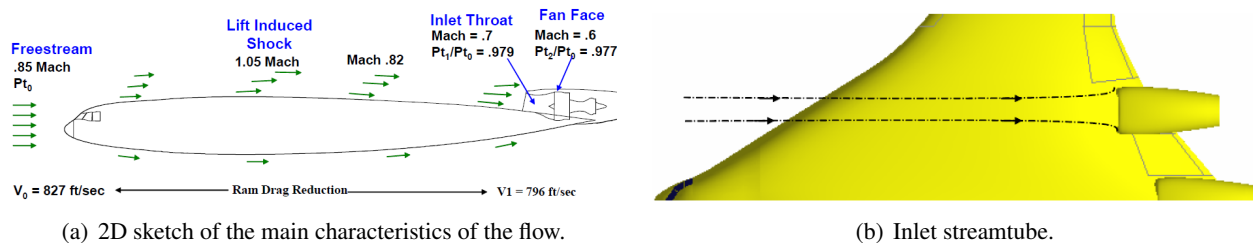
Figure 0-2: Illustration of the drag-thrust bookkeeping issues for boundary layer ingestion performance estimation, from [78].

First, the pre-entry streamtube of air actually entering the engine, on which we would like to calculate ram drag, has in fact washed the surface. This means that integrating on its surface will account for effects (friction) that were formerly attributed to the external flow. Secondly, the pre-entry streamtube has passed through a potential shock structure, as illustrated in Fig. 0-2. How to state whether the momentum changes should be attributed to the shock or to the ram drag? There is a clear *mixing* between what was previously called *external* and *internal* flows.

---

[4]RANS computations provide valuable performance indications at an acceptable computational cost according to *Boeing* engineers [98].

Objectives and Requirements

The lack of a global methodology prevents an accurate estimation of the benefit of a complete advanced configuration and represents the main motivation for the present work whose primary objective is to acquire a validated post-processing tool of RANS flow solutions for the preliminary design of future commercial transport aircraft. Its main identified requirements are:

1. Rely on a formulation that is not based on a drag/thrust bookkeeping in order to be applicable for aircraft with boundary layer-ingesting propulsion systems,

2. The compatibility of the formulation to assess conventional configurations for which such approach is applicable would be a plus,

3. The formulation should allow for the assessment of aerothermopropulsive performance of civil aircraft,

4. The formulation should also provide a phenomenological identification of the main flow phenomena responsible for fuel consumption,

5. The post-processing code should involve a computational cost a few orders of magnitude lower than the one of the CFD computation,

6. The accuracy of the code should be within *standards*, *i.e.* typically within one drag count (10^{-4}) of the reference value[5],

7. The code should be capable of treating any kind of turbulence models with a particular emphasis on the popular *Spalart-Allmaras* turbulence model [156],

8. For validation purpose and flow analysis, the visualization in the flow-field of all terms involved in the theoretical formulation should be possible.

Thesis Outline

The thesis consists of the development of an exergy-based formulation for the aero-thermo-propulsive performance assessment of civil aircraft by post-processing high-fidelity CFD-RANS flow solutions. The document is organized in four main chapters:

1. The first chapter is a literature review of existing studies related to the present thesis. It includes the description of a performance formulation which is only partially-suited for the global analysis of advanced configurations [49]. Then, introduction is made to the concept of exergy and to its recent interest in the aerospace community. The absence of a formulation and numerical tool that satisfy all the aforementioned requirements is highlighted and the key advantages of the exergy analysis for a global aircraft performance assessment are summarized.

2. From the literature review's conclusions, the second chapter (p. 27) focuses on theoretically establishing an exergy balance for the assessment of advanced aircraft in terms of aero-thermo-propulsive performance. The domain of validity of the formulation is described and connections are made to existing formulations, both for powered and unpowered configurations. The original contributions and connections to existing work are discussed. Finally, the numerical implementation of the formulation into a post-processing code named *ffχ* is described.

---

[5]The choice of *reference* value is not straightforward. Validation will be made with respect to experimental wind-tunnel testing when available [69, 136, 137], but even for those, *there is some question as to how well they should agree since the wind-tunnel test and CFD problem setups are inherently different* [92].

3. The third chapter (p. 63) presents the validation of the numerical implementation of the proposed formulation for the aerodynamic performance prediction of unpowered configurations. The validation methodology considers test cases of increasing geometry and flow complexities, ranging from a subsonic flow over an academic 2D-airfoil to transonic flow over an industrial-like 3D-Wing-body aircraft.

   In this restricted set of test cases, comparisons can be made to well-tried drag prediction approaches, namely the near-field and far-field drag methods, to determine the accuracy-dependence of the post-processing tool in terms of grid-refinement, turbulence models and control volume definition.

4. The fourth chapter (p. 119) concentrates on the application of the numerical post-processing code *ffx* to assess the thermo-propulsive performance of powered configurations. The methodology adopted is again of increasing geometry and flow complexities. An isolated nacelle is first investigated to verify the consistency of the propulsion-related terms of the exergy balance.

   Then investigation is made of a wake-ingesting simplified configuration for which the exergy approach provides an efficient point of view. After that, the influence of heat transfer on the overall performance of a simplified blended wing-body configuration is assessed and finally, thermal aspects are covered by a study of the integration of heat exchangers on aircraft.

Chapter 1 is not original while, except mentioned otherwise, chapters 2, 3 and 4 are original. Although a linear reading of the manuscript is advised, references to prior considerations are made to allow each application to be examined in (relative) isolation.

Communication

The work contained in this dissertation has been presented in two international conferences. The newly-introduced formulation has also been accepted for publication in the *AIAA Journal* and two subsequent articles focusing on the numerical applications have been submitted.

Conference Proceedings

[10] ARNTZ, A., ATINAULT, O., AND DESTARAC, D., "Numerical Airframe Aerodynamic Performance Prediction: An Exergy Point of View," 49th International Symposium of Applied Aerodynamics, AAAF, Lille, France, 24–26 March 2014.

[11] ARNTZ, A., ATINAULT, O., DESTARAC, D., AND MERLEN, A., "Exergy-based Aircraft Aero-propulsive Performance Assessment: CFD Application to Boundary Layer Ingestion," 32nd AIAA Applied Aerodynamics Conference, AIAA Aviation 2014, Atlanta, GA, 16–20 June 2014.

Peer-reviewed Journal Articles

[12] ARNTZ, A., ATINAULT, O., AND MERLEN, A., "Exergy-based Formulation for Aircraft Aeropropulsive Performance Assessment: Theoretical Development," *AIAA Journal*, doi: 10.2514/1.J053467

[13] ARNTZ, A., AND ATINAULT, O., "Exergy-based Performance Assessment of a Blended Wing-Body with Boundary-Layer Ingestion," *AIAA Journal*,   **In review**.

[14] ARNTZ, A., AND HUE, D., "Exergy-based Performance Assessment of the NASA Common Research Model," *AIAA Journal*,   **In review**.

Chapter 1

Literature Review and Introduction to the Concept of Exergy

This chapter introduces the only existing formulation devoted to the performance assessment of commercial aircraft with boundary layer ingestion (BLI) proposed by DRELA. *The strengths and limitations of this approach are first examined. Then, the necessary background for understanding the derivation of the performance formulation introduced in the next chapter is provided. The many advantages of this concept are detailed and the choice of the exergy analysis is based on the various successful applications of the approach in aerospace engineering.*

*"Just as a viable country must have a common currency to facilitate commerce and trade,
so must vehicle design have a common currency to facilitate design trades."*

ROTH [140]

7

1.1 The *Power Balance* Method of DRELA

The formulation of DRELA (MIT) [49] is the only one found in the literature that tackles the challenge of evaluating the global performance of an aircraft that has a propulsion system ingesting a boundary layer. It forms an appropriate introduction to the exergy balance derived in chapter 2 (p. 27).

1.1.1 Context

Performance calculation and design of aircraft using BLI was addressed in the MIT-Cambridge Silent Aircraft Initiative [72]. The performance accounting was conducted using a momentum balance where numerous assumptions about the viscous flow details needed to be made to evaluate the benefit of BLI, according to SATO [146]. A few years later, in 2009, DRELA proposed a formulation based on a mechanical energy analysis which does not rely on the expression of forces (thrust/drag).

1.1.2 Mechanical Energy Balance

1.1.2.1 Derivation of the Formulation

DRELA published a formulation valid for periodic-unsteady and steady flows up to the supersonic regime. The control volume in which the analysis is made is delimited by the aircraft surface $\mathcal{S}_A$ and an outer boundary $\mathcal{S}_O$, as depicted in Fig. 1-1. This latter surface is eventually broken down into a side cylinder $\mathcal{SC}$ parallel to $\mathbf{V}_\infty$ and a *Trefftz* plane $\mathcal{TP}$ perpendicular to the freestream. These restrictions have the great advantage of isolating different physical flow process in the case of supersonic flows.

Because the focus of the present study is on transonic commercial aircraft, the following presentation is restricted to steady flows at transonic speed.
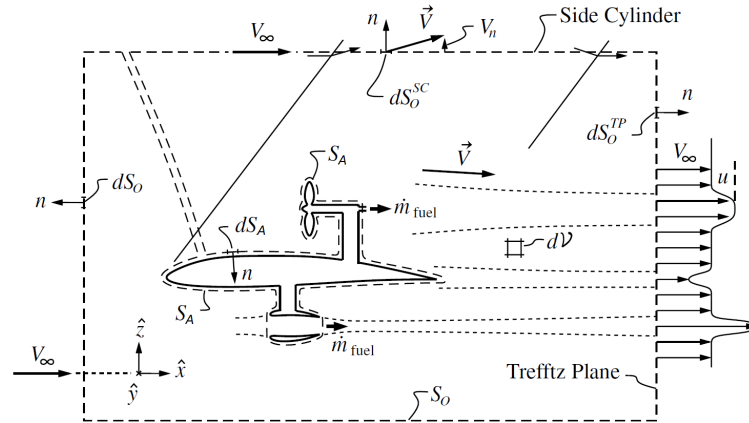
Figure 1-1: Power Balance Method: definition and description of the control volume, adapted from [49].

The *Power Balance* is based on a scalar equation derived from the dot product of the momentum conservation and the fluid velocity, *i.e.* the conservation of kinetic energy:

$$\nabla \cdot \left(\frac{1}{2} \rho V^2 \mathbf{V} \right) = -\nabla p \cdot \mathbf{V} + (\nabla \cdot \bar{\bar{\tau}}) \cdot \mathbf{V} \tag{1.1}$$

Using general vector identities to manipulate the two right-hand side terms, and integrating within the control volume, one gets the following relation between the mechanical energy provided to the flow and its outflow and dissipation:

$$\boxed{P_K + P_V = W\dot{\Gamma} + \dot{E}_u + \dot{E}_v + \dot{E}_p + \dot{E}_w + \dot{E}_\phi} \tag{1.2}$$

The two terms on left hand side represent the total mechanical power production and inflow, ultimately from fuel, batteries or other sources. According to the author, *a major goal* [of the formulation] *is the determination of the total power required for flight, via the prediction and estimation of the right-hand side terms of* Eq. (1.2).

Total mechanical power production and inflow.

P_K : net propulsor mechanical energy flow rate into the control volume

$$P_K := \int_{\mathcal{S}_A} - \left[(p - p_\infty) + \frac{1}{2}\rho(V^2 - V_\infty^2) \right] (\mathbf{V} \cdot \mathbf{n}) \, \mathrm{d}\mathcal{S} \tag{1.3}$$

This is the net pressure-work rate and kinetic energy flow rate across the aircraft surface and into the control volume. This accounts for power sources whose moving blading is not covered by $\mathcal{S}_A$ or whose combustors are outside of the control volume. Note that $\mathbf{n}$ points into the propulsor, so that the nozzle has $\mathbf{V} \cdot \mathbf{n} < 0$, and $P_K > 0$ for a propulsor with net thrust.

P_V : net pressure-volume "$P \, \mathrm{d}V$" power

$$P_V := \int_{\mathcal{V}} (p - p_\infty)\nabla \cdot \mathbf{V} \, \mathrm{d}\mathcal{V} \tag{1.4}$$

According to the author, this is a volumetric mechanical power provided by the fluid expanding against atmospheric pressure. Its integrand will have strong net contributions at locations wherever heat is added at a pressure far from ambient, for example, if a turbomachinery combustor is chosen to be inside the control volume or if external combustion is present, as in some hypersonic vehicles.

Potential Energy Rate.

$W\dot{\Gamma}$: aircraft potential energy rate

$$W\dot{\Gamma} := -F_x V_\infty = W V_\infty \sin\gamma \tag{1.5}$$

where F_x is net streamwise force acting on the aircraft[1], W is the aircraft weight and γ is climb angle. This term is simply the power consumption needed to increase the aircraft's potential [and kinetic[2]] and becomes a power source during descent.

The derivation of this term is provided in appendix A.2 (p. 180).

Energy-Outfow Decomposition Rate.

$\dot{E}_u$: wake streamwise kinetic energy deposition rate[3]

$$\dot{E}_u := \int_{\mathcal{TP}} \frac{1}{2}\rho \, u^2 \, (V_\infty + u) \, \mathrm{d}\mathcal{S} \tag{1.6}$$

This is the rate of streamwise kinetic energy being deposited in the flow out of the control volume, through the *Trefftz* plane $\mathcal{TP}$. Note that this is always positive, both in the case of a propulsive jet where the axial perturbation velocity u is positive and also for a wake where u is negative.

---

[1] In the aerodynamics reference frame in which drag is accounted positively and therefore thrust is accounted negatively.

[2] DRELA only considers the aircraft potential energy therefore the original notation is $W\dot{h}$ where h is the height.

[3] Original notation is $\dot{E}_a$.

$\dot{E}_v$: wake transverse kinetic energy deposition rate

$$\dot{E}_v := \int_{TP} \frac{1}{2}\rho \left(v^2 + w^2\right)\left(V_\infty + u\right) \mathrm{d}\mathcal{S} \tag{1.7}$$

This is the rate of transverse kinetic energy being deposited in the flow out of the control volume, through the *Trefftz* plane. For $u \ll V_\infty, v, w$, this is in fact the same as V_∞ times the induced drag D_i for the case of a relatively nearby *Trefftz* plane where the vortex wake has not yet dissipated significantly.

$\dot{E}_p$: wake pressure-defect work rate

$$\dot{E}_p := \int_{TP} \left(p - p_\infty\right) u \, \mathrm{d}\mathcal{S} \tag{1.8}$$

This is the rate of pressure work done on the fluid crossing the *Trefftz* plane at some pressure p different from the ambient p_∞.

Dissipation of the Mechanical Energy.

$\dot{E}_\phi$: viscous dissipation rate

$$\dot{E}_\phi := \int_{\mathcal{V}} \left(\bar{\bar{\tau}} \cdot \nabla\right) \cdot \mathbf{V} \, \mathrm{d}\mathcal{V} \tag{1.9}$$

This measures the rate at which kinetic energy of the flow is converted into heat inside the control volume. The dissipation mechanism is the viscous stress $\bar{\bar{\tau}}$ working against fluid deformation, the latter related to the velocity gradients $\nabla\mathbf{V}$. In practice, most of the dissipation occurs in the thin layers on the aircraft surface, including the propulsion elements, and also in shock waves. Additional dissipation also occurs in the downstream wakes and jets, as shown in Fig. 1-2.
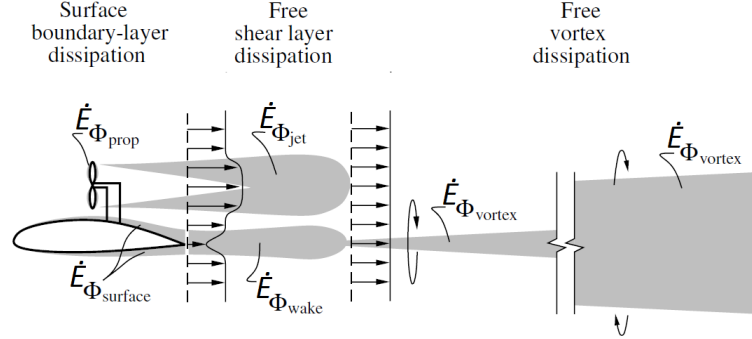
Figure 1-2: Power Balance Method: dissipation within the flow field, adapted from [49].

$\dot{E}_w$: nearby strong-shock losses

$$\dot{E}_w \simeq \int_{\mathcal{S}_w} \left(p_i - p_{i_\infty}\right)\left(\mathbf{V} \cdot \hat{\mathbf{n}}_{shock}\right) \mathrm{d}\mathcal{S} \tag{1.10}$$

where the integration is over the shock surface $\mathcal{S}_w$ with unit normal vector $\hat{\mathbf{n}}_{shock}$, see Fig. 1-3. The total pressure drop depends on the normal *Mach* number $M_\perp$ *via* standard normal-shock relations.

All power sources $\sum P$ in excess of the change in aircraft's energy rate $W\dot{\Gamma}$ are eventually balanced by the dissipation if the *Trefftz* plane is extended sufficiently far downstream, see Fig. 1-4.

The streamwise kinetic energy, initially equal to some fraction of the net axial force power, decays relatively quickly as the axial velocity perturbation u decays by mixing and diffusion, with the lost energy appearing as the $\dot{E}_{\phi,wake} + \dot{E}_{\phi,jet}$ part of the overall dissipation $\dot{E}_\phi$. After a much greater distance
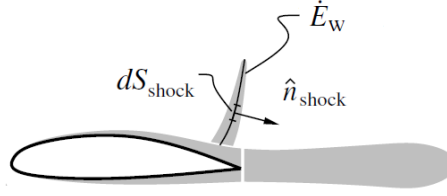
Figure 1-3: Power Balance Method: nearby-strong shock wave treatment, adapted from [49].
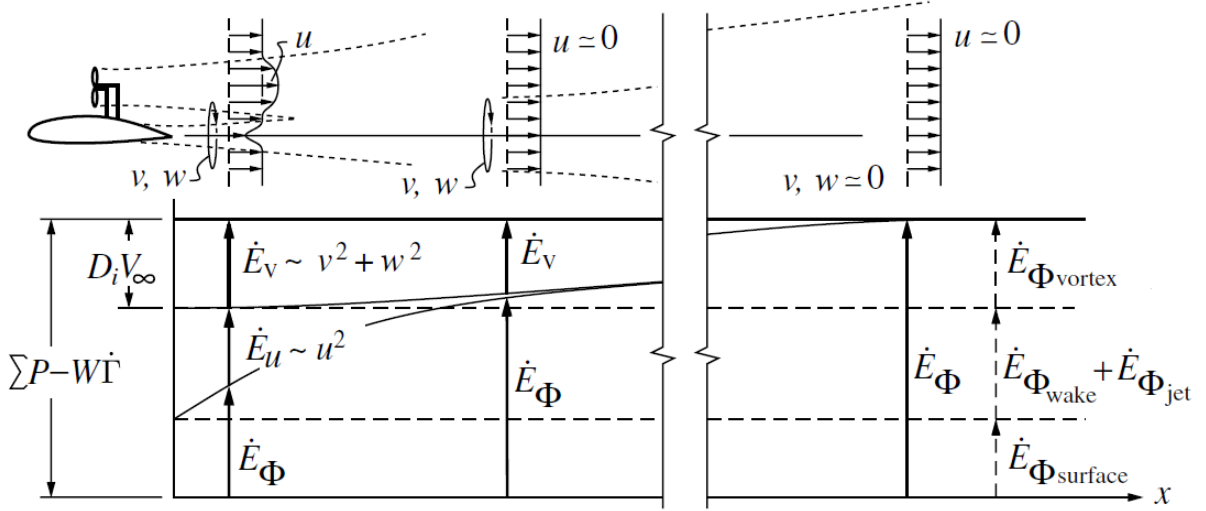
Figure 1-4: Power Balance Method: representation of the dissipation in the wake, adapted from [49].

downstream, the transverse velocities v, w of the trailing vortices also eventually diffuse, and the transverse kinetic energy integral $\dot{E}_v$ initially equal to $D_i V_\infty$, decays accordingly. Again, the dissipation $\dot{E}_\phi$ is correspondingly increased by the $\dot{E}_{\phi,vortex}$ part, so that the total power remains unchanged.

1.1.2.2 Restriction to Aerodynamic Flows over Unpowered Configurations

The restriction of the power balance to unpowered configurations in the most general case of a body immersed in a transonic flow is unfortunately not explicitly given in [49]. However, if one considers the absence of permeable surfaces on the aircraft ($P_K = 0$), there is no thrust meaning that $W\dot{\Gamma} = -DV_\infty$ and therefore Eq. (1.2) strictly reduces to:

$$DV_\infty = \dot{E}_u + \dot{E}_v + \dot{E}_p + \dot{E}_w + \dot{E}_\phi - P_V \tag{1.11}$$

In order to isolate the rate of work of the drag DV_∞, the term P_V has been moved to the right-hand side of Eq. (1.11). This term would be zero only for strictly incompressible flow and is therefore somewhat more difficult to grasp for unpowered configurations where there is no obvious *source/sink* of energy within the flow field that would modify the drag experienced by the body.

The author additionally demonstrated that outside of the viscous wakes and propulsion plumes, the total mechanical energy represents what is generally referred to as the drag power of the lift-induced vortices

$$\dot{E}_u + \dot{E}_v + \dot{E}_p = D_i V_\infty \tag{1.12}$$

This result is also found in agreement with several previous approaches derived from very different initial considerations [100, 154, 155].

Dissipation-Based Drag Buildup. DRELA made further connections to the *dissipation coefficient* $C_\mathcal{D}$ [44], which, for a 2D shear layer[4], yields:

$$\dot{E}_\phi = \int \rho_e u_e^3 \, C_\mathcal{D} \, \mathrm{d}x \, \mathrm{d}z \tag{1.13a}$$

where the subscript e refers to the *edge* of the shear layer. This coefficient is analogous to the more traditional friction drag coefficient

$$D_f = \int \frac{1}{2} \rho_e u_e^2 \, C_f \, \mathrm{d}x \, \mathrm{d}z \tag{1.13b}$$

but has a number of advantages because:

- $C_\mathcal{D}$ and $\dot{E}_\phi$ capture all drag-producing loss mechanisms. In contrast, C_f and D_f still leave out the pressure-drag contribution,
- $C_\mathcal{D}$ and $\dot{E}_\phi$ are scalars, and so the orientation of the $\mathrm{d}x \, \mathrm{d}z$ surface element in Eq. (1.13a) integral is immaterial. In contrast, Eq. (1.13b) represents a force vector integral and, as written, is strictly correct only for flat-plate surfaces aligned with the freestream flow,
- $C_\mathcal{D}$ is strictly positive, and so there are no force-cancellation problems which often occur with near-field force integration,
- Also, $C_\mathcal{D}$ depends much less on the shape factor than the shearing stress at the wall [147].

The u_e^3 factor in Eq. (1.13a) has also significant implications for excrescence and interference drag. To illustrate the difference between force-based and dissipation-based drag buildup, the author considered a configuration consisting of a large and a small body, as shown in Fig. 1-5a. Their relative sizes are such that, when the bodies are far apart, the drags are 100 and 1 for a total drag of $D = 101$.

(a) Two isolated bodies. (b) Two closely interacting bodies.
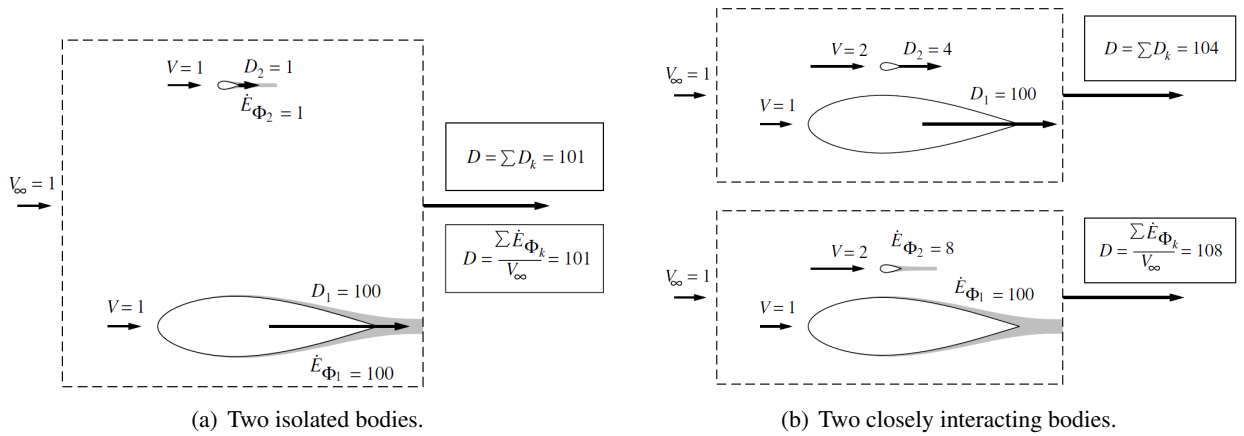
Figure 1-5: Power Balance Method: drag buildup by force summation (top) and dissipation summation (bottom), adapted from [49].

When the small body is placed near the large body where the local velocity is $V = 2$, as shown in Fig. 1-5b, the force-based drag buildup gives

$$D = \sum D_k = 100 + 4 = 104 \tag{1.14a}$$

whereas the dissipation-based buildup gives

$$D = \frac{1}{V_\infty} \sum \dot{E}_{\phi_k} = 100 + 8 = 108 \tag{1.14b}$$

---

[4]Considering that $w = 0$. The term w can always be added if needed to give the 3D form.

which is a rather different result.

According to DRELA, viscous CFD calculations indicate that the dissipation-based buildup Eq. (1.14a) is far more accurate than the force-based buildup Eq. (1.14b). The reason invoked is that the latter approach neglects the additional pressure drag on the large body, due to the potential source flow created by the viscous displacement on the small body. Traditionally, this might be labeled *interference drag* (see HOERNER [74]) of some possibly uncertain origin, but the mechanism and effect is captured quite well by the dissipation-based drag buildup.

1.1.3   Experimental and Numerical Applications

In his PhD Dissertation [146], SATO demonstrated the major benefits of the method with a focus on the conceptual design phase: 1) derivation of analytical expression of profile drag estimates for conceptual design applications, 2) aerodynamic performance estimation for three basic integrated configurations, 3) performance quantification of a hybrid wing body with BLI propulsion system [145]. In order to reduce computational cost by evaluating the terms of Eq. (1.2) directly from CFD computations, lower fidelity correlations were introduced and validated for attached flows over 2D and axisymmetric bodies. Using CFD, this author also highlighted the weaker dependency of the method to potential pressure-field effects in the case of two bodies aerodynamically interfering.

More recently, the method was applied for a computational performance assessment of the boundary layer ingesting propulsion system of the D8 aircraft [119, 120]. The analysis was conducted at low speed ($M_\infty < 0.1$) and the main performance metric for comparison to a baseline configuration with podded engine was the net mechanical power supplied to the flow P_K, which exhibited a 9% reduction with BLI. Note that in these applications, there is no mention of a post-processing code for high-fidelity RANS flow solutions based on the *Power Balance* method.

(a) D8 podded-engine baseline configuration.   (b) D8 BLI configuration.
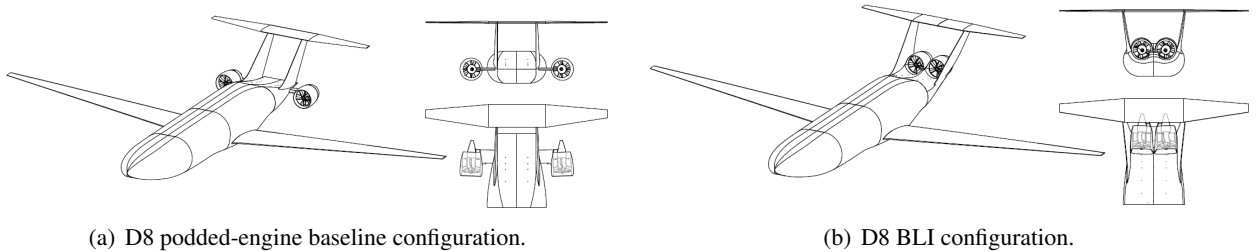
Figure 1-6: Power Balance Method: D8 podded and boundary layer ingesting configurations, adapted from [171].

This numerical performance assessment of the D8 configuration with BLI [50] was then validated against wind-tunnel experiments under the same flow conditions [171]. In this case, the most convenient performance metric was the electrical power supplied to the engine simulator. The measurements with BLI showed a 6% saving with a 95% confidence interval of 2.3% in power[5]. It was recognized that the flow mechanical power P_K would be more appropriate figure of merit. Therefore, further work was conducted to relate the electrical power of the engine simulator and the mechanical power provided to the fluid, with or without boundary layer ingestion [151]. It was found that the propulsor utilized exhibited a fan efficiency degradation of 1-2% due to the ingestion of distortions representative of the ingestion of the boundary layer on the fuselage.

---

[5]For a full-size D8 aircraft, the authors estimated that *the total savings amounts 15% when including secondary drag and weight reductions enabled by having the engines located on the top rear fuselage*.

1.1.4 Advantages and Limitations

To put things in a nutshell, the main identified advantages of the *Power Balance* method are:

- A clear identification of the quantities [and flow phenomena[6]] that directly influence flight power requirements,

- A consistency with previous analyses based on momentum considerations,

- No need to define rather ambiguous thrust and drag in configurations with tightly integrated propulsion systems,

- A higher reliability of the loss definition for interference effects that are not captured by the force approach,

- A validation of the method through numerical and experimental applications [120, 151, 171].

Although, the *Power Balance* method seems to provide a valuable approach for mechanical performance estimation, it does not allow for aircraft thermal management. As this area is believed to become a major source of performance gain for future aircraft, thermal management was considered as a key requirement for the method to be adopted, see OBJECTIVES AND REQUIREMENTS (p. 4). In other words, the present work aims at providing a more global tool for the design of complex configurations by taking into account the thermal energy in addition to the mechanical energy.

The mechanical and thermal energy represent the total energy of the fluid flow and appear equivalent by virtue of the First Law of thermodynamics. However, in the perspective of producing work, it is clear that while the mechanical energy is completely convertible into mechanical work, the thermal energy is not. According to the Second Law of thermodynamics, only a portion of it could be ideally converted into mechanical work *via* a *Carnot* cycle of efficiency lower than unity. The mechanical energy can thus be considered a higher quality form of energy than the thermal energy. Even for thermal energy itself, there can be a ranking because, the hotter the gas, the higher the thermodynamic efficiency[7]. The distinction of the *quality* and *level* of an energy form is only made possible by the introduction of the Second Law of thermodynamics; the combination of both laws enabling an EXERGY ANALYSIS.

↪ In chapter 2 (p. 27), a detailed comparison will be made between this mechanical energy balance and the exergy balance derived in the framework of this thesis.

1.2 Introduction to the Concept of Exergy

This section is devoted to the introduction of the concept of exergy. First, thermodynamics fundamentals are reminded to yield a proper definition of this notion. Then, a broad literature review is conducted to highlight the various domain in which it has proved itself a valuable metric. Finally, recent applications of this concept for the design of aerospace vehicle are reviewed.

1.2.1 Basics of Thermodynamics

Key textbooks include those of BEJAN [18, 19, 20, 21, 24], BOREL [31], CENGEL AND BOLES [38], DE OLIVEIRA [45], DINCER AND ROSEN [47], and OHTA [117].

---

[6]Shock waves, lift-induced vortices and wake dissipation.

[7]In the perspective of producing work, $1kWh$ of thermal energy at $50K$ is not *equivalent* to $1kWh$ of thermal energy at $500K$; their respective work potential are different.

1.2.1.1 First and Second Laws of Thermodynamics

The First Law of thermodynamics states that energy can neither be destroyed nor created, it can only change in forms. It merely serves as a necessary tool for the bookkeeping of energy during a process and offers no challenges to the engineer. The Second Law, however, deals with *quality* of energy. More specifically, it is concerned with the degradation of energy during a process, for which the *entropy* can account for, and the lost opportunities to do work, and it offers plenty of room for improvement [38]. There are however several statements of the Second Law which are usually specifically adapted to a particular situation and not easily grasped.

To the author's understanding, one of the difficulty[8] that makes the concept of entropy somewhat nebulous is that it has no absolute reference, as opposed to most quantities that the engineer deals with like velocity and temperature. For example, the velocity is defined with reference to the reference frame of the study: the velocity of a car is measured relative to the Earth reference frame. The temperature of a fluid is generally measured with reference to the *absolute zero* or to the temperature at which water freezes. One such absolute reference for measuring entropy is somewhat less well defined. It could be measured with reference to the *entropy of the universe* but even this is not a constant because its magnitude is constantly increasing.

More important than its magnitude, is the *variation* of entropy during a process that is crucial. The interpretation of this concept developed by DENTON [44] (when considering turbomachines, but generalizable) is found very appropriate:

> Entropy may be considered to be like "smoke" that is created within the flow whenever something deleterious to machine efficiency is taking place. [...] Once created, the "smoke" cannot be destroyed and it is convected downstream through the machine and diffuses into the surrounding flow. The concentration of "smoke" at the exit from the machine includes contribution from every source within the machine and the loss of the machine efficiency is proportion to the average concentration of "smoke" at its exit.

Entropy, in itself, is an indicator of the inefficiency of a system: the more *smoke*, the greater the losses and therefore the more room for improvement.

1.2.1.2 Exergy/Anergy Framework

The development of this field of research started by recognizing the incapacity of the First Law in determining the degree of perfection of a system and therefore its efficiency [31]. In addition to the mass and momentum conservations, the conservation of energy provide necessary, but *not* sufficient, quantifiable relationships to determine a processes directionality and feasibility [34]: the Second Law is in fact as fundamental as the First Law. Considerable work has been devoted in the past decades to bridge the gap between thermodynamics, heat transfer and fluid mechanics [20] in the form of EXERGY ANALYSIS.

An exergy analysis starts by splitting any form of energy in two parts: a first part (theoretically) fully convertible into mechanical work and a second part that is (theoretically) impossible to be converted into mechanical work. Following the early work of RANT [129] to establish an international terminology, it seems that the words *exergy* and *anergy* are well suited to represent these two parts:

$$\textbf{Energy} = \textbf{Exergy} + \textbf{Anergy} \quad \Longleftrightarrow \quad \textbf{Total} = \textbf{Useful} + \textbf{Useless} \qquad (1.15)$$

which is illustrated in Fig. 1-7. *Useful* and *useless* are here defined in the perspective of producing work.

---

[8]Another difficulty is associated to its unit: J.K^{-1}. As such, the entropy is not directly comparable to energy which is measured in Joules.
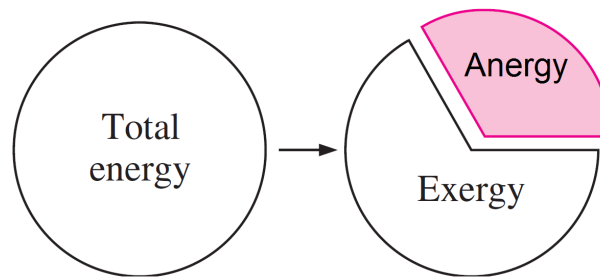
Figure 1-7: Representation of the decomposition of energy into a useful part (exergy) and a useless part (anergy), adapted from [38].

According to DINCER, as exergy is the part of energy that has economic value, it is the only part worth managing carefully. The term exergy comes from the Greek words *ex* and *ergon*, meaning *from* and *work* [47]. Other names can be found in the literature for exergy, especially *availability* and *available energy*.

Unlike energy, exergy is always destroyed during conversions because of the irreversible nature of energy conversion process. The key differences between the two notions are summarized in Table 1.1.

Energy	Exergy
Dependent on properties of only a matter or energy flow, and independent of environment properties	Dependent on properties of both a matter or energy flow and the environment
Has values different from zero when in equilibrium with the environment	Equal to zero when in the dead state by virtue of being in complete equilibrium with the environment
Conserved for all processes, based on the First Law of Thermodynamics	Conserved only for reversible processes and not conserved for real processes, based on the Second Law of Thermodynamics
Can be neither destroyed nor produced	Always destroyed in an irreversible (real) process
A measure of quantity only	A measure of quantity and quality

Table 1.1: Comparison of Energy and Exergy, adapted from [47].

In a nutshell, exergy is a *measure of the work potential of any form of energy* which has a few key characteristics:

– Exergy is a measure of the departure of the state of a system from that of the environment. A system in complete equilibrium with its environment does not have any exergy. The greater the difference, say, between the temperature T at a given state and the temperature T_∞ of the environment, the greater the value of for exergy. This applies equally when $T > T_\infty$ and $T < T_\infty$, [114]. A block of ice carries little exergy in winter while it can have significant exergy in summer [47].

– A system in complete equilibrium with its environment (dead state) does not have any exergy: no differences appears in temperature, pressure, concentration, etc. so there is no driving force for any process [47]. The atmosphere around us contains a tremendous amount of energy. However, because the atmosphere is in the dead state, the energy it contains has no work potential [38].

– When measured relative to the environment, the kinetic and potential energies of the system contribute their full magnitudes to the exergy magnitude, for in principle each is fully convertible to work as the system passes to the dead state [114]. Also, high-valued forms of energy such as electricity and mechanical work consists of pure exergy.

The word *anergy* is seldom reported in the literature[9], yet, because the exergy/anergy terminology pro-

---

[9]RANT only suggested and justified (with grammar considerations) the adoption of the *exergy* [129].

vides a simple and clear framework for the design of energy systems, this convention is adopted in the present work. Note that anergy is expressed in Joules and that its magnitude is therefore directly comparable to energy, as opposed to entropy.

As with energy, there are various forms of exergy. Herein we neglect nuclear, magnetic, and surface tension effects. Therefore, the major forms of exergy of a flow stream to be discussed include *physical* exergy and *chemical* exergy [23, 38, 114]:

$$\varepsilon = \left(h + \frac{1}{2}V^2 + gz + e_{ch}\right) - \left(h_\infty + \frac{1}{2}V_\infty^2 + gz_\infty + e_{ch,\infty}\right) - T_\infty(\mathsf{s} - \mathsf{s}_\infty) \tag{1.16}$$

Potential and kinetic energy are a form of mechanical energy, and thus can be entirely converted to work. On the other hand, the work potential of thermal energy depends on the temperature of the source; only a portion can be converted into work according to a *Carnot* efficiency $\eta_C = (1 - T_{cold}/T_{hot})$. The work potential from the chemical substance comes from its difference in composition relative to the dead state.

↪ The various terms of the specific flow exergy ε will be examined in greater details in the derivation of the formulation in chapter 2 (p. 27).

1.2.2 Literature Review on Exergy

1.2.2.1 A Few Pioneers

A few milestones in the development of the concept of exergy are selected from the extensive literature review conducted by SCIUBBA and WALL [149].

It is widely recognized today that the concept of exergy has its roots in the early work of the Frenchman CARNOT when he stated 190 years ago that *the work that can be extracted of a heat engine is proportional to the temperature difference between the hot and cold reservoir* [37]. However, the rigorous introduced of the notion of *available energy* is generally attributed to GIBBS (American) in 1873. With no direct reference to GIBBS's work, the Frenchman GOUY (1889) and the Slovak STODOLA independently derived an expression for *useful energy* (1898). For their pioneering work, the statement[10] that the *lost available work* [24] is equal to entropy generation $\dot{\mathsf{s}}_{gen}$ times the reference temperature T_∞

$$\dot{W}_{lost} = T_\infty \, \dot{\mathsf{s}}_{gen} \geq 0 \tag{1.17}$$

is referred to as the GOUY-STODOLA theorem [33]. These early reflections were continued in Europe and in the US. BOSNJAKOVIC, a Croatian who taught in Braunschweig, Dresden, Stuttgart, and Zagreb, laid the foundation of the German school of applied and theoretical Thermodynamiscists, that were to further develop the concept of exergy two decades later. At the same time, KEENAN expanded and clarified the concept of exergy in the US and founded the *Keenan School of Thermodynamics* (MIT) with his own notion of *availability* [79]. Considerable progress has been made in the past decades towards development and unification of the once separate fields of thermodynamics, fluid mechanics, and heat transfer [20].

1.2.2.2 Recent Influential Publications

A first insight into the recent literature review on the exergy analysis is given by a historical perspective of publications. As of July 22nd, 2014 the scientific citation indexing service *Web of Science* references 9,108 publications from 1950 to 2012 on the topic *exergy*. This appears to be a relatively growing field of research judging from the increasing number of published and cited documents plotted in Fig. 1-8.

---

[10]The work obtained from a device is always less than the maximum obtainable work due to the irreversibilities in the process.

(a) Published documents over the period 1969 – 2012.

(b) Cited documents over the period 1975 – 2014.
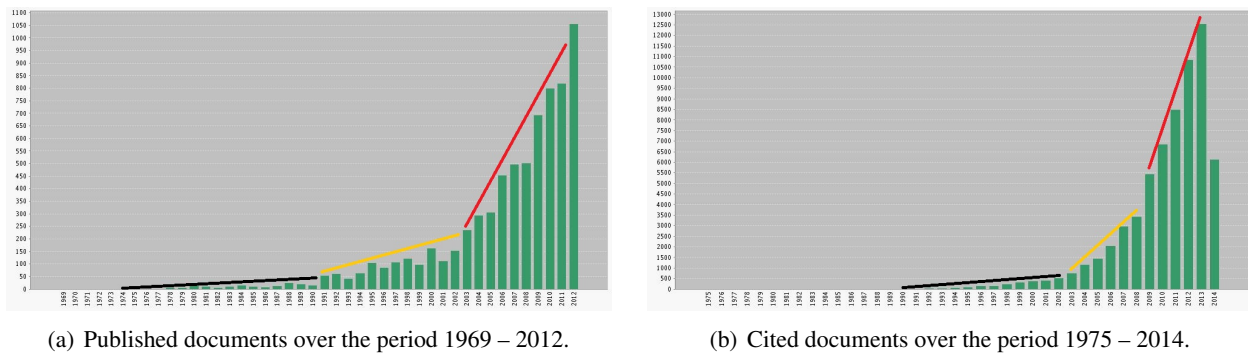
Figure 1-8: Historical perspective of the publications on *exergy*, as of July 22nd, 2014.

From Fig. 1-8a, first publications are referenced right after the oil crisis of 1974 which drew a lot of attention to energy efficiency [23]. The beginning of the 1970's marks the advent of the mature exergy theory for which most publications deal with the optimization of systems [149]. Starting from the early 1990's (yellow line), the number of publications increases non-uniformly during about 10 years: some years are more prolific than others. Then, the number of published documents raises steadily and steeply over the past decade (red line). Regarding citations plotted in Fig. 1-8b, the same trend can be observed: the pioneering work published in the 1970's-80's was further developed during the 1990's and since 2000 with a steep rise in the last five years.

The most cited document has been published in 1996 by BEJAN, A., "Entropy Generation Minimization: The New Thermodynamics of Finite-size Devices and Finite-time Processes," *Journal of Applied Physics*, [20]. This J. A. Jones Distinguished Professor of Mechanical Engineering at Duke University has published 28 books and 580 peer-referred articles and is considered the most influential researcher in the field. He is the founder of the CONSTRUCTAL LAW of design in nature, which, in a nutshell, considers that *for a finite-size flow system to persist in time (to live/to survive), its configuration must evolve in such a way that it provides an easier access to the imposed (global) currents that flow through it*. The approach has even recently been applied to interpret the evolution of aircraft designs [25].

1.2.2.3 Countries Ranking

To get more insight into which countries contribute the most to the spreading of this field of research, a ranking is proposed in Table 1.2. From the database of publications provided by *Web of Knowledge*, the following methodology was applied to asses the quality of the scientific production for each country:

1. The average number of citations of the ten most-cited publications (first column) is the prime criterion,
2. The number of citations of the most-cited publications (second column) is the second criterion,
3. The total number of publications (third column) is the third and last criterion, also given in percentage of the total production in the field (9,108 publications).

Selected countries that contribute the most to the exergy field have been considered; they represent 5,167 publications, *i.e.* roughly 60% of the total production. This ranking, although relatively subjective[11], gives an indication of which country is interested in this field.

The USA appears well ahead in the field, both in quality and quantity with about 8% of the total scientific production. Italy is second, with a relatively low number of articles but with good quality. Down the table, China has a very large number of publications but that are rarely cited while France stands at the 11th rank, just below Germany. The major European countries, if gathered together[12], would only occupy the 7th rank.

---

[11]If one were to consider only the number of publications, he would end up with a very different ranking.

[12]Italy, Netherlands, Switzerland, Spain, Germany, and France. Average = 102, Highest = 359, Number = 1196 (13%).

Rank	Country	Top-ten publications			
		Average citations	Highest citations	Number of publications	
1	USA	205	640	735	8.1%
2	Italy	123	359	353	3.9%
3	Canada	123	153	565	6.2%
⋮	⋮	⋮	⋮	⋮	⋮
9	China	90	157	1,723	18.9%
10	Germany	85	130	216	2.3%
11	France	79	129	152	1.7%

Table 1.2: USA, Italy, Canada, China, Germany, and France contributions to the field of exergy.

1.2.3 Exergy Analysis in Engineering

Far from being an obscure scientific notion or a simple fashion, the exergy analysis yields a fundamental definition of *loss* in an engineering perspective: exergy destruction, or equivalently anergy generation, by irreversible phenomena. As a consequence, only the exergy accounting is capable of determining the degree of perfection of a system [31]. DINCER AND ROSEN [47] identified two main reasons why exergy analyses more than energy analyses provide insights into the *best*[13] direction for Research and Development effort:

– Exergy losses represent true losses of the potential that exists to generate the desired product from the given driving input. This is not true in general for energy losses,

– Exergy efficiencies always provide a measure of how nearly the operation of a system approaches the ideal or theoretical upper limit. This is not in general true for energy efficiencies.

About 3,574 publications are referenced by the citation indexing service *Web of Science* under *engineering* and of application of the exergy analysis is extremely vast. It has been notably applied to the design of ground-based systems such as fuel cells, heat exchangers and heat networking, steam power cycles, gas turbine cycles, renewable energy cycles, refrigeration and cryogenics, chemical processes, solar power, distillation and desalination, but also for studies on environmental impact and human body behavior [20, 24, 45, 47, 149].

1.3 Exergy Analysis in Aerospace Engineering

In the aerospace community, a growing interest in the exergy analysis can be observed since the very early 2000's [45]. In 2003, a special section of an AIAA *Journal of Aircraft* [178] gathered existing studies and spread fundamental ideas along with detailed examples focused on aerospace systems. More recently, a dedicated AIAA Progress in Astronautics and Aeronautics "Exergy Analysis and Design Optimization for Aerospace Vehicles and Systems" was published by MOORHOUSE and CAMBEROS [111]. It introduced the fundamentals of the exergy analysis with examples taken from the aerospace industry. Much of the book content was recently presented at lectures series[14] entitled "Physics-Based Modeling & Simulation for Aerospace Systems" organized in 2012 by the Von Karman Institute for Fluid Dynamics and the US Air Force Research Laboratory. This event, the first fully dedicated to the advancement of the approach in aerospace, gathered about 70 researchers, mostly Americans and Europeans.

---

[13]According to the authors, *best* is loosely taken to mean *most promising for significant efficiency gains*.
[14]Which the present author attended.

1.3.1 System-level Flight Vehicle Design

Current aerospace vehicle design methodologies are primarily based on individual component-level or subsystem-level that are developed and optimized in relative isolation. The resulting overall system performance is then essentially a product of the net effect of this nonsynergistic approach. MOORHOUSE expanded exergy methods to the design of a complete flight vehicle by defining mission requirements as an exergy problem cascading down to each component in the same framework [110]. He also suggested that *the use of exergy-based methods will allow more complete system integration and facilitate the connection of all traditional results into a design framework with a common metric.*

The pioneering PhD Thesis of ROTH [139] and related publications [140, 141, 142, 143, 144] is also seminal to the system-level design of modern flight vehicles. Noticing the lack of a *universal measure of risk* (applicable at the system and sub-systems levels), this author developed methods to assist aerospace systems designers in quantifying risk in a rational and analytical manner. He introduced a theory to unify the weight[15] and thermodynamic performance aspects of vehicle design such that they can be expressed interchangeably and applied from the system-level down to the component-level. The approach considers that *it is the usage and loss of thermodynamic work potential that drives virtually every aspect of a vehicle's environmental and economic performance* [140]. Implementation and demonstration of the proposed methodology was applied for the F-5E[16]. As the ultimate figure of merit for loss in any vehicle regardless of type or construction is cost [144], ROTH suggested that the exergy analysis could be combined with costing considerations to form a thermoeconomic analysis [89, 166] which provides information not available through conventional energy analysis and economic evaluations but crucial to the design of a cost effective system [19].

Also, the ability to perform exergy accounting in smaller and smaller subsystems makes it possible to draw a map of how the destruction of exergy is distributed over the system of interest [33] which is a real advantage in the search for improving efficiency of a system [without *a priori* knowledge], because it tells us from the start how to allocate engineering efforts and resources [23].

An ideal candidate which benefits from such an approach is a vehicle flying at hypersonic regime ($M_\infty > 5$) like the X-51, see Fig. 1-9. For such aircraft, the interactions between the propulsion system and the airframe become predominant. Additionally, thermal aspects are significant in the boundary layers: the temperature at the surface can reach around 1,400K.
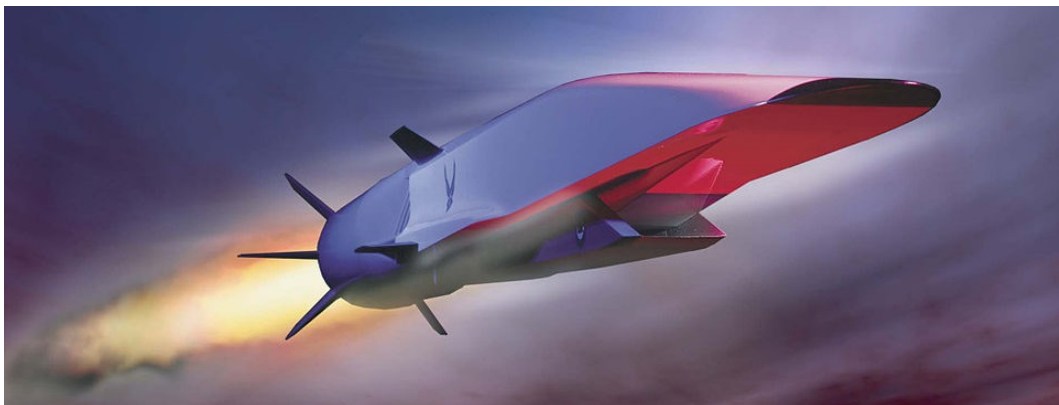
Figure 1-9: Artist representation of the X-51 vehicle flying at hypersonic regime.

An analytical model was developed by RIGGINS *et al*. [133, 134, 135] by bringing together the equa-

---

[15]Current thinking in the aerospace industry is centered on vehicle weight. According to the author, companies have expended considerable resources in creating large organizations dedicated to tracking and controlling vehicle mass properties, and it is always given a high priority.

[16]The F-5E is a light supersonic fighter aircraft, initially designed in the late 1950's by Northrop Corporation.

tions of motion of the vehicle and an exergy balance. Time-integration across the vehicle missions provided the fundamental overall governing balance between total input energy, mission-integrated vehicle performance, and cumulative losses. The authors stressed the importance of the exergy loss in the wake which are *extremely large compared with the vehicle exergy losses*. The formulation is significant because it provides the correct quantitative construct for assessing all mission, vehicle, subsystem, and component losses in terms of a single, fundamental, and universal currency of entropy generation [135].

At ONERA, MOUTON was the first to suggest an exergy approach for the assessment of aircraft aero-propulsive performance in 2011 [113].

1.3.2 Propulsion Systems

The exergy approach has historically begun in the study of turbomachines whose design heavily relies on applied thermodynamics and most applications today of the exergy analysis have focused on propulsion systems. Pioneers CLARKE AND HORLOCK [40] and LEWIS [93] analysed a propulsive device in the light of the combined first and second law in the mid-1970's. The former authors identified a *unique means whereby a steady-flow machine can be divided arbitrarily into regions (e.g. components) and the losses in each region when added together account for the difference between the maximum work possible from the fuel and the actual work (or work equivalent) obtained from the device*. They also found a *consistent framework within which losses can be compared within machines, between machines of different types for the same job and with perfection represented by the concept of the completely reversible machine*.

In 1993, DENTON published a detailed examination of the loss mechanisms in turbomachines [44] with an emphasis *trying to understand the physical origins of loss rather than on reviewing the available prediction methods*. Loss was defined in terms of entropy increase and its relationship to more familiar loss coefficients was derived. The source of entropy discussed included viscous effects in boundary layers, viscous effects in mixing processes, shock waves, and heat transfer across temperature differences. It was suggested that loss coefficients should really be defined in terms of entropy increase rather than the more traditional stagnation pressure or kinetic energy loss. The author concluded that *a good physical understanding of the origins of loss may be more valuable than a quantitative prediction*. A direct application of this methodology is due to NATALINI AND SCIUBBA who were able to provide useful information for the assessment of different blade configurations with minimal thermodynamic loss in a turbine cascade [115].

The basic exergy analysis yields absolute loss relative to the maximum work allowed by the Second Law of thermodynamics whereby any departure from a *Carnot* cycle appears as a loss. It has been found that application of this approach to jet propulsion devices concludes that the largest exergy losses are due to nonequilibrium combustion and exhaust heat and kinetic energy [40]. However, it appears that optimization of a thrust-producing device to produce maximum exergy output may lead to less-than-optimal result if the objective is to produce thrust for propulsion [130].

Two additional figures of merit derived from exergy considerations are therefore worth noticing: Gas Horsepower and Thrust Work Potential [141]. The former only considers mechanical equilibrium and thus concludes that nonequilibrium combustion and heat losses no longer appear as losses; the only inefficiency being associated with exhaust kinetic energy. Thrust work potential is defined as the thrust work that would be obtained in expanding a flow at a given temperature and pressure to ambient such that the thrust work obtained is equal to the thrust produced multiplied by the flight velocity of the aircraft [131]. As a consequence, exhaust residual kinetic energy is not counted as being available for propulsive purposes and therefore not accounted as loss, unlike exergy and GHP. Also, relationships between classic measures of component efficiencies to modern measures of work potential have been proposed, the former having the disadvantage of not being directly comparable to one another [143].

TURAN examined the effect of reference altitudes for a turbofan engine in cruise conditions with the aid of specific-exergy based methods [169]. An exergy efficiency from 50.34% at 4,000m to 48.91% at 9,000m was exhibited. Results of this study show that increase in reference altitude decreases the exergy efficiency and increases the energy efficiency of the engine. As similar analysis was conducted by ETELE AND ROSEN for a turbojet [52]. The percentage of the total exergy loss due to the exhaust emission, which is the single largest source of exergy loss in a turbojet, was found to increase from 65% at sea level to 70% at 15,000m. These results are consistent with the investigation of MARLEY AND RIGGINS who found that the wake contribution to the overall entropy generation in the wake region of a turbojet engine operating at cruise conditions is up to three times the rate of entropy generation inside the engine [99].

TONA *et al.* examined a turbofan engine during a typical commercial flight from an exergy standpoint combined with thermoeconomic considerations [162]. A maximum exergy efficiency of 23.7% was reported during cruise phase even though this phase also corresponds to the highest level of exergy destruction within the engine (36%). The authors also emphasized the use of a reference frame attached to the engine as opposed to one fixed on the ground especially when associating costing considerations.

FERNANDEZ-VILLACÉ *et al.* evaluated a hypersonic propulsion concept at flight *Mach* numbers ranging from 2.5 to 5 and variable throttling [57]. It was found that classical figures of merit was proven incomplete meaning that thermal efficiency was recast into a thermal effectiveness by establishing the exergy as the common metric.

1.3.3 Energy Systems

According to BEJAN, energy systems for modern aircraft are ideal candidates for the application of the exergy analysis for which the approach could significantly improve the energy management [22]. It stands to reason, that, as a greater number of energy forms is expected to be dealt with for future aircraft, the need for a single metric to assess the performance of various sub-systems (and their interactions) may be reinforced. The exergy analysis precisely provides this single currency whereby thermal and chemical energies are directly comparable to mechanical and electrical energies [26].

The idea of using thermodynamic irreversibility in aircraft design decision making has been widely discussed and several exergy analyzes have been conducted to evaluate the benefit of replacing conventional systems of commercial aircraft by *more-electric* ones. More electric systems are thermodynamically more efficient than bleed based systems, mainly because of the better use of electric power in the cabin compressors and the electric de-ice systems. GANDOLFI *et al.* found that the integration over the complete mission (climbing, cruise, and landing), exhibited that the exergy efficiency of the more electric aircraft is 17% higher than for the conventional aircraft [62, 63, 124].

All aircraft subsystems power and cooling requirements are ultimately traced back to the propulsion system and MASER *et al.* showed that increasing cooling requirements may results in levels of exergy destruction that have an impact on propulsion system design tradeoffs. These authors emphasized that the characterization of the integrated system in terms of component irreversibility allows for a consistent and absolute measure of overall performance that can aid in these tradeoffs and lead to the design of an improved engine cycle [101]. Exergy-based and energy-based approaches were compared for the design of an environmental control system of an advanced aircraft by FIGLIOLA *et al.* with simplified analytical models [59]. It was reported that both methods seek answers to different questions, making direct comparisons awkward. Nonetheless, exergy methods provided decision information to aid design by providing a ready estimate for efficiency on a component and system basis and indicating optimal operating conditions.

1.3.4 External Aerodynamics

There has been significantly less interest on external flows even if it is one the most important aspects of aircraft design. The primary reason is that the aerodynamic performance of aerospace configurations have been historically determined by evaluating the mechanical force that opposes an aircraft's motion through the air, *i.e.* the *drag*. The (near-field and far-field) drag prediction methods [46, 173] yield satisfactory results as long as the airframe can be examined as a separate sub-system of the entire flight vehicle. However, as interactions arise, for example with the propulsion system, this figure of merit becomes essential not comparable on an *apples-to-apples* basis with the performance metric of the propulsion system.

As proposed by ROTH, the exergy approach can be extended to define aerodynamic loss as *the reduction in total vehicle work potential due to irreversible fluid-dynamic interactions between the vehicle and the atmosphere* [142]. On that account, aerodynamic loss is directly comparable to thermodynamic loss in the engine and part of the system global cost accounting [71, 144]. For example, PERIANNAN analytically compared the effects of various energy and exergy-based figures of merit on the optimization of a high performance aircraft system comprising a propulsion subsystem, an environmental control subsystem, and an airframe subsystem [125, 126]. He found that the incorporation of the losses associated with the airframe subsystem, which are traditionally not expressed in terms of energy, in the design objective yielded a significantly better optimum vehicle.

Very few studies with high-fidelity CFD were reported in the literature survey for the assessment of the aerodynamic performance of aerospace configurations.

LI *et al.* examined many different low-*Re* turbulence models for flow past NACA 0012 Airfoils [94, 107]. They found several $k-\epsilon$ turbulence models to be among the best for *Mach* numbers below 0.3. By comparing the drag and entropy generation predictions with their corresponding experimental values, they found that the model of ABE *et al.* [1] was the best predicting drag coefficient to within 10% and the entropy generation within 6% in their validation study. As regards the assessment of the flow over a 3D wing, the authors proposed the following drag relation restricted to incompressible flows:

$$D = \frac{1}{V_\infty} \left(T_\infty \int_{CV} \dot{\mathbf{s}}_{gen} \, d\mathcal{V} + \int_{\mathcal{TP}} \rho u \frac{v^2 + w^2 + (V_\infty^2 - u^2)}{2} \, d\mathcal{S} \right) \tag{1.18}$$

which results from a two-steps methodology: 1) determination of the entropy generated within the control volume (first term) and 2) (simple) addition of the entropy that *is to be generated* as a consequence of the dissipation of the lift-induced vortex (second term). They applied this formulation to different wing shapes composed of NACA 0012 airfoil sections with a constant chord length. The flow conditions were $M_\infty = 0.2$ and $Re_c = 4.66 \ 10^6$ with the realizable $k-\epsilon$ model. Eq. (1.18) provided results in agreement to within 2% of a semi-empirical drag value determined by adding wind-tunnel values for the NACA 0012 Airfoil and lift-induced drag from *Prandtl*'s lifting line theory. These results were also in better agreement than the drag predicted by the near-field integration of the stresses on the wing.

ALABI *et al.* [6] were the first to apply the methodology to a realistic configuration by examining the generation of entropy over a Boeing B747-200 in cruise conditions. Both *Euler* and *Navier-Stokes* calculations were carried out using high-order discretization. It was determined that most of the entropy generation in the viscous calculations were due to turbulent eddy viscosity which was about 1000 times the molecular viscosity in the application flow field. Comparison of the entropy generation terms showed that the viscous dissipation contributes approximately 90% of the total entropy production, with the heat transfer-related term contributing the remaining 10%. In the region of the wing-fuselage junction, these ratios moved to 70% and 30% respectively. However, no formulation was given to determine the total drag of the configuration.

1.3.5 Entropy Generation from CFD-RANS

In the perspective of acquiring a post-processing of RANS flow solutions, a brief overview of the challenges faced by accurate numerical prediction of the entropy generation in turbulent flow is given.

The most general form of the entropy transport equation reads:

$$\frac{\partial \rho \mathbf{s}}{\partial t} + \nabla \cdot (\rho \, \delta \mathbf{s} \, \mathbf{V}) = \frac{1}{T} \mathcal{D}_v + \frac{1}{T^2} \mathcal{D}_T - \nabla \cdot \frac{\mathbf{q}}{T} \tag{1.19}$$

where the first and second right-hand side terms refer to the entropy production by respectively viscous dissipation and heat transfer with finite temperature gradients [81]. Application of the RANS (*Reynolds-averaged Navier–Stokes*) approach, whereby instantaneous values are split into time-mean and fluctuating parts, introduces additional turbulent terms that need to be modeled [6]. These terms have mean and fluctuating components and involve correlations between temperature which makes this relation highly complex [3]. A detailed examination of these issues can be found in the PhD Thesis ADEYINKA [4].

The first documented effort to tackle this challenge is attributed to MOORE AND MOORE [108] who proposed in 1983 an eddy viscosity model for mean entropy production:

$$\text{Mean Entropy Generation} = \frac{1}{T} (\bar{\bar{\tau}}_{eff} \cdot \nabla) \cdot \mathbf{V} + \frac{1}{T^2} k_{eff} (\nabla \mathbf{T})^2 \tag{1.20}$$

where T and $\mathbf{V}$ are mean flow quantities and:

$$\bar{\bar{\tau}}_{eff} = (\mu + \mu_t) \bar{\bar{S}} \tag{1.21}$$

$$k_{eff} = c_p \left(\mu/Pr + \mu_t/Pr_t \right) \tag{1.22}$$

where μ and μ_t are respectively the molecular viscosity and the eddy viscosity associated with turbulence. $\bar{\bar{S}}$ is the mean strain rate, Pr and Pr_t are respectively the *Prandtl* and turbulent *Prandtl* numbers.

This simplified model requires the assumption that the rate of production of turbulence kinetic energy equals the rate of its dissipation. Similarly, it is assumed that the rate of production of temperature fluctuations equals their rate of dissipation. Knowing these conceptual limitations, the authors validated their model on a turbulent boundary layer in an increasingly adverse pressure gradient on a flat plate and found results comparable to experimental data. In a subsequent paper, the authors applied the model to reveal the sources of loss production in an accelerating elbow with 90 degrees of turning [109]. In both cases, very acceptable results were obtained. This simplified model was used by LI *et al.* [94, 107] and ALABI *et al.* [6] for their RANS flows solutions analyzes.

KRAMER-BEVAN [84] showed that this model exhibits certain inconsistentices for confined flows with small temperature gradients close to the wall, where the production of turbulent kinetic energy is not equal to the dissipation of turbulent kinetic energy. Furthermore, other assumptions leads to difficulties when generalizing the formulation [3]. Only a few alternative models have been recently developed [81, 82] and they are out of the scope of the current work since they require the dissipation of the turbulent kinetic energy which is unavailable in typical RANS flow solutions using the *Spalart-Allmaras* turbulence model [156], chosen as the *standard* turbulence model in the OBJECTIVES AND REQUIREMENTS (p. 4).

1.4   Summary of the Key Findings

The literature review enabled to introduce a powerful mechanical energy analysis of the flow recently published by DRELA [49]. This formulation has a number of advantages among which the possibility of assessing the global performance of airplanes with highly integrated propulsion system which has been both numerically and experimentally validated. Additionally, a clear identification of the flow phenomena that directly influence flight power requirements is provided. However, this formulation only partially satisfies the requirement established in the Introduction (p. 4). Most importantly, it does not allow for a clear thermal energy management.

As a consequence, considering the thermal energy in addition to the mechanical energy leads to a total energy analysis which can be greatly improved by the introduction of the notion of entropy. The combination of the First and Second Laws of thermodynamics enables an exergy analysis which provides more detailed information about the system. Exergy is the part of energy that has economic value and which is therefore worth managing carefully, as opposed to anergy which is the *useless* counterpart (in terms of work potential). A considerable body of work exist on the application of such concept to the design of modern aerospace vehicles[17] for which the key aspects are summarized:

- A well-established thermodynamic analysis that is well suited for R&D projects and that can be directly linked to costing considerations,
- A common currency whereby all forms of energy (electrical, thermal, chemical, mechanical) can be accounted for and their work potential clearly identified,
- A system-level approach for the design of flight vehicles whereby the performance of each sub-system can be *consistently* investigated separately and summed together to yield the performance of the entire system,
- A multi-disciplinary approach for aero-thermo-propulsive performance assessment of aerospace vehicles for tracking and estimating any potentially recoverable loss,
- A multi-fidelity (analytical or CFD methods) approach for which a simple model for mean entropy generation in turbulent flows [108] is available.

The choice of exergy is therefore motivated by its ability to provide a consistent system-level to component-level framework to design complex aerospace systems.

The literature review has highlighted the absence of a post-processing code for CFD-RANS flow solutions based on a formulation devoted to the aero-thermo-propulsive performance assessment of transonic commercial aircraft satisfying the OBJECTIVES AND REQUIREMENTS listed in the Introduction (p. 4). As a consequence, the thesis consists in the development of an exergy-based formulation valid for complex configurations and its numerical implementation in a post-processing code (next Chap. 2, p. 27) which must be validated for unpowered (Chap. 3, p. 63) and powered (Chap. 4, p. 119) aerospace configurations.

---

[17]Note that only a few publications involving aerospace companies were referenced: Boeing [102, 135], Embraer [62, 63, 124], Lockheed Martin Aeronautics [59].

Chapter 2

Exergy-based Formulation for Civil Aircraft Aero-thermo-propulsive Performance Assessment

The literature review has highlighted the lack of a post-processing tool for CFD-RANS flow solutions based on a formulation for the assessment of the aero-thermo-propulsive performance of transonic commercial aircraft. As a consequence, this chapter introduces the exergy analysis that yields a new performance formulation. The formulation, restricted to steady flows, consists in a balance of the forces acting on the aircraft and a fluid flow analysis based on the First and Second laws of thermodynamics. Further specifications of this formulation are given with an emphasis on the analysis of propulsion systems and on its connection to popular momentum-based methods for the prediction and decomposition of the drag experienced by unpowered configurations. Finally, the adaptation of the theoretical formulation to the numerical constraints is given through its numerical implementation.

2.1 Exergy Balance for Aero-thermo-propulsive Performance Assessment

The exergy analysis starts by defining the control volume in which the analysis is made along with First and Second laws considerations. Then, the general exergy balance is manipulated to highlight the key elements involved in the aerothermopropulsive performance. The final exergy balance relates the exergy supplied by the propulsion system, its (partial) destruction within the control volume along with the aircraft mechanical equilibrium.

2.1.1 Preliminary Considerations

2.1.1.1 System Definition

The fluid flow analysis is carried out in a continuous volume $\mathcal{V}$ delimited by the aircraft surface $\mathcal{S}_A$ and an outer boundary $\mathcal{S}_O$, as illustrated in Fig. 2-1. Both surfaces are closed and may be permeable; a vector pointing outwards of the volume and locally normal to the surface is noted $\mathbf{n}$. We also consider the case of discontinuous shock waves being surrounded by a surface $\widetilde{\mathcal{S}}_w$ of negligible width[1] and with normal vector $\tilde{\mathbf{n}}$.
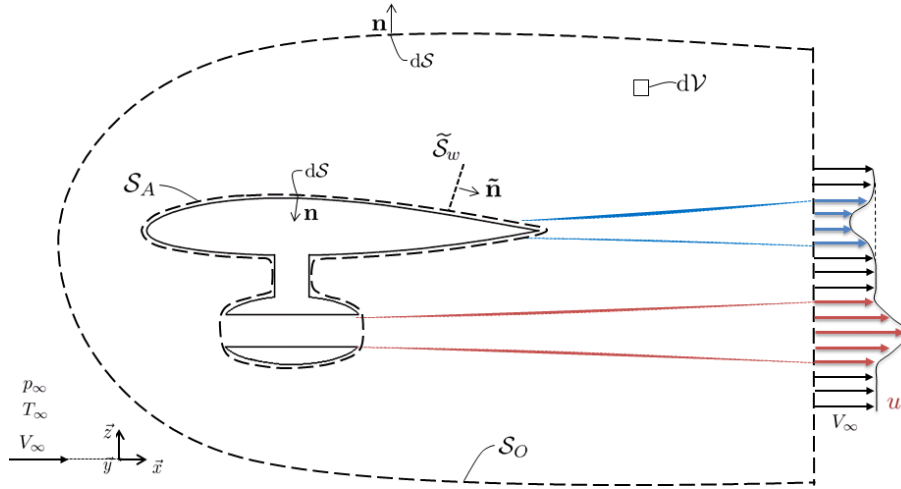
Figure 2-1: 2D cutaway view of 3D control volume surrounding the aircraft.

The control volume delimits the system under study which is said to be thermodynamically open as it can exchange mass, work, and heat with the surrounding fluid across its boundaries. The atmosphere is considered as a thermal and mechanical reservoir, which means that we neglect the influence of the process being studied on the (much larger) environment. The analysis is made in the aircraft reference frame, which is assumed inertial, the control volume is therefore fixed and the air is flowing in and out of it.

Note that, although the form of the outer boundary is arbitrary, it is sometimes found advantageous to choose a downstream plane perpendicular to the freestream velocity and to push the remaining lateral and upstream surfaces as far as possible from the aircraft. This has the practical advantage of assuming freestream conditions on all surfaces but the downstream plane. Although, this assumption is often made for drag prediction formulations and could be used to slightly simplify the mathematical derivation (and the physical interpretation), this approach is not adopted for the following derivation in order to be as general as possible and to make as few assumptions as possible.

---

[1]Normal steady shocks thickness is of the order of magnitude of the mean free path or less [118]. This gives an idea of how narrow the shock region actually is and justifies the description of the shock as a discontinuous process.

Extensive use of the divergence theorem will be made in the derivation:

$$\int_{\mathcal{V}} \nabla \cdot (\ ) \, \mathrm{d}\mathcal{V} = \int_{\mathcal{S}_A} (\ ) \cdot \mathbf{n} \, \mathrm{d}\mathcal{S} + \int_{\mathcal{S}_O} (\ ) \cdot \mathbf{n} \, \mathrm{d}\mathcal{S} - \int_{\widetilde{\mathcal{S}}_w} [\![\ ]\!] \cdot \tilde{\mathbf{n}} \, \mathrm{d}\mathcal{S} \tag{2.1}$$

where $(\ )$ is any continuous tensor quantity and where $[\![\ ]\!]$ is the jump imposed by the discontinuity. The negative sign of the vector $\tilde{\mathbf{n}}$ normal to the shock surface comes simply from its orientation, see Fig. 2-1.

2.1.1.2 Mean Steady Flows and *Boussinesq*'s Hypothesis

Application of the *Reynolds*- and *Favre*-averaging procedures to the *Navier-Stokes* equations introduces two major unknowns: the turbulent shear stress and the turbulent heat flux. As described in [29], these turbulent quantities can be expressed as functions of mean quantities for mean steady flows.

First, the *Boussinesq*'s hypothesis considers that the turbulent shear stress is locally related linearly to the mean rate of strain $\bar{\bar{S}}$; the proportionality factor being an eddy viscosity noted μ_t. As a consequence, neglecting the turbulent kinetic energy contribution, the *effective* (viscous + turbulent) stress tensor can be expressed as $\bar{\bar{\tau}}_{eff} = (\mu + \mu_t)\bar{\bar{S}}$. Similarly, the effective dissipation rate due to viscous dissipation and turbulence is given by

$$\Phi_{eff} = (\bar{\bar{\tau}}_{eff} \cdot \nabla) \cdot \mathbf{V} \tag{2.2a}$$

Secondly, in a direct analogy to the *Boussinesq*'s hypothesis, the effective heat flux by conduction, introducing the *Fourier* law, can be written as

$$\mathbf{q}_{eff} = -k_{eff} \nabla \mathbf{T} \tag{2.2b}$$

The effective thermal conductivity is expressed as $k_{eff} = c_p(\mu/Pr + \mu_t/Pr_t)$, where the turbulent *Prandtl* number is usually chosen as a constant value of $Pr_t = 0.9$ for air. As a consequence, the turbulent heat flux only requires a value for the eddy viscosity.

All flow properties mentioned in the following development depend *only* of the mean flow. The turbulent kinetic energy is neglected from the onset.

2.1.1.3 Mass Conservation

The mass conservation principle is applied to the control volume to provide a relation used to manipulate and simplify other subsequent integral relations. The steady-state *Reynolds*-averaged mass relation reads, integrated within the control volume:

$$\int_{\mathcal{V}} \nabla \cdot (\rho \mathbf{V}) \, \mathrm{d}\mathcal{V} = 0 \tag{2.3}$$

which, using the divergence theorem, yields, because of mass conservation across the shock wave[2]:

$$\dot{m}_A = \dot{m}_O \tag{2.4}$$

where,

$$\dot{m}_A := - \int_{\mathcal{S}_A} \rho \, (\mathbf{V} \cdot \mathbf{n}) \, \mathrm{d}\mathcal{S} = \dot{m}_f \simeq 0 \tag{2.5a}$$

$$\dot{m}_O := \int_{\mathcal{S}_O} \rho \, (\mathbf{V} \cdot \mathbf{n}) \, \mathrm{d}\mathcal{S} = \dot{m}_f \simeq 0 \tag{2.5b}$$

The fuel mass flow $\dot{m}_f$ will be assumed negligible compared to the air mass flow considered within the control volume, so that both integrals are negligible. Thus, we have, for any scalar quantity convected by

---

[2] $\int_{\widetilde{\mathcal{S}}_w} [\![\rho \, \mathbf{V}]\!] \cdot \tilde{\mathbf{n}} \, \mathrm{d}\mathcal{S} = 0.$

the flow like the total enthalpy h_i:

$$\int_{\mathcal{S}} \rho\, h_i\, (\mathbf{V} \cdot \mathbf{n})\, \mathrm{d}\mathcal{S} = \int_{\mathcal{S}} \rho\, (h_i - h_{i_\infty})\, (\mathbf{V} \cdot \mathbf{n})\, \mathrm{d}\mathcal{S} = \int_{\mathcal{S}} \rho\, \delta h_i\, (\mathbf{V} \cdot \mathbf{n})\, \mathrm{d}\mathcal{S} \tag{2.6}$$

where $\mathcal{S}$ is any closed surface of the analysis. This property is used to decompose the total enthalpy outflow in paragraph 2.1.2.4.

2.1.1.4 Momentum Relation

The momentum relation is used to obtain a far-field expression for the power developed by the net force acting on the aircraft. The steady-state *Reynolds*-averaged momentum relation in divergence form reads

$$\nabla \cdot (\rho\, \mathbf{V} \otimes \mathbf{V}) = -\nabla \mathbf{p} + \nabla \cdot \bar{\bar{\tau}}_{eff} \tag{2.7}$$

Again, integrating within the control volume and invoking the divergence theorem yields, because of momentum conservation across the shock wave[3], the two following momentum fluxes:

$$\mathbf{F_A} = \mathbf{F_O} \tag{2.8}$$

where the two terms represent the net force acting on the aircraft, $\mathbf{F_A}$ being a near-field integral while $\mathbf{F_O}$ is a far-field expression:

$$\mathbf{F_A} := \int_{\mathcal{S}_A} \left[\rho\, \mathbf{V}\, (\mathbf{V} \cdot \mathbf{n}) + (p - p_\infty)(\bar{\bar{I}} \cdot \mathbf{n}) - (\bar{\bar{\tau}}_{eff} \cdot \mathbf{n}) \right] \mathrm{d}\mathcal{S} \tag{2.9a}$$

$$\mathbf{F_O} := - \int_{\mathcal{S}_O} \left[\rho\, \mathbf{V}\, (\mathbf{V} \cdot \mathbf{n}) + (p - p_\infty)(\bar{\bar{I}} \cdot \mathbf{n}) - (\bar{\bar{\tau}}_{eff} \cdot \mathbf{n}) \right] \mathrm{d}\mathcal{S} \tag{2.9b}$$

The projection of these two vectors on the flight path yields the net axial force acting on the airplane.

As shown in appendix A.2 (p. 180), the rate of work done by this force, as viewed in the Earth-fixed reference frame, is $W\dot{\Gamma}$:

$$
\begin{aligned}
W\dot{\Gamma} = -\mathbf{F_O} \cdot \mathbf{V}_\infty &= \int_{\mathcal{S}_O} \left[\rho\, (\mathbf{V} \cdot \mathbf{V}_\infty)\, (\mathbf{V} \cdot \mathbf{n}) + (p - p_\infty)(\mathbf{V}_\infty \cdot \mathbf{n}) - (\bar{\bar{\tau}}_{eff} \cdot \mathbf{V}_\infty) \cdot \mathbf{n} \right] \mathrm{d}\mathcal{S} \\
&= V_\infty \int_{\mathcal{S}_O} \left[\rho\, u\, (\mathbf{V} \cdot \mathbf{n}) + (p - p_\infty) n_x - (\tau_{x,eff} \cdot \mathbf{n}) \right] \mathrm{d}\mathcal{S} = -F_x V_\infty
\end{aligned}
\tag{2.10}
$$

where Γ is the weight specific aircraft *energy height*, *i.e.* the sum of the aircraft potential and kinetic energies [85]. This expression represents the power of the resultant force and there is no need (and no possibility) to distinguish thrust from drag. The following subsections aims at building a First and Second laws balance which will identify this far-field expression of $W\dot{\Gamma}$ in paragraph 2.1.2.4.

2.1.2 Exergy and the Combined First and Second Laws of Thermodynamics

2.1.2.1 General Exergy Balance

Exergy is a thermodynamic property describing the maximum theoretical work that can be obtained from a substance in taking it from a given temperature and pressure/velocity to a state of thermal and mechanical equilibrium with the environment[4]. Exergy is a property of both the system and the reference environment, the latter being here taken as the atmosphere at the altitude of flight and whose properties are noted with

---

[3] $\int_{\tilde{\mathcal{S}}_w} [\![\rho\, \mathbf{V}\, \mathbf{V} + (p - p_\infty)\bar{\bar{I}} - \bar{\bar{\tau}}_{eff}]\!] \cdot \tilde{\mathbf{n}}\, \mathrm{d}\mathcal{S} = 0.$
[4] Not considering chemical exergy and chemical equilibrium.

the subscript ∞. As mentioned in the introduction, the specific exergy of a flowing fluid is expressed mathematically for an open system as

$$\varepsilon = (h_i - h_{i_\infty}) - T_\infty (\mathsf{s} - \mathsf{s}_\infty) = \delta h_i - T_\infty \, \delta \mathsf{s} \tag{2.11}$$

where we have neglected the gravitational potential energy in the specific *flow exergy* ε defined in Eq. (1.16) (p. 17). We also assume that the mixture of air and fuel behaves as a perfect gas and therefore neglect the chemical exergy.

We are interested in calculating the change in exergy which can be written in its divergence form as:

$$\int_{\mathcal{V}} \nabla \cdot (\rho \, \varepsilon \, \mathbf{V}) \, \mathrm{d}\mathcal{V} = \int_{\mathcal{S}_A} \rho \, \varepsilon \, (\mathbf{V} \cdot \mathbf{n}) \, \mathrm{d}\mathcal{S} + \int_{\mathcal{S}_O} \rho \, \varepsilon \, (\mathbf{V} \cdot \mathbf{n}) \, \mathrm{d}\mathcal{S} - \int_{\widetilde{\mathcal{S}}_w} [\![\rho \, \varepsilon \, \mathbf{V}]\!] \cdot \tilde{\mathbf{n}} \, \mathrm{d}\mathcal{S} \tag{2.12}$$

which, simply using the definition of exergy $\varepsilon = \delta h_i - T_\infty \delta \mathsf{s}$, can be written after rearrangement:

$$- \int_{\mathcal{S}_A} \rho \, \delta h_i \, (\mathbf{V} \cdot \mathbf{n}) \, \mathrm{d}\mathcal{S} + T_\infty \int_{\mathcal{S}_A} \rho \, \delta \mathsf{s} \, (\mathbf{V} \cdot \mathbf{n}) \, \mathrm{d}\mathcal{S} = - \int_{\mathcal{V}} \nabla \cdot (\rho \, \delta h_i \, \mathbf{V}) \, \mathrm{d}\mathcal{V} + T_\infty \int_{\mathcal{V}} \nabla \cdot (\rho \, \delta \mathsf{s} \, \mathbf{V}) \, \mathrm{d}\mathcal{V}$$
$$+ \int_{\mathcal{S}_O} \rho \, \delta h_i \, (\mathbf{V} \cdot \mathbf{n}) \, \mathrm{d}\mathcal{S} - T_\infty \int_{\mathcal{S}_O} \rho \, \delta \mathsf{s} \, (\mathbf{V} \cdot \mathbf{n}) \, \mathrm{d}\mathcal{S}$$
$$- \cancel{\int_{\widetilde{\mathcal{S}}_w} [\![\rho \, \delta h_i \, \mathbf{V}]\!] \cdot \tilde{\mathbf{n}} \, \mathrm{d}\mathcal{S}} + T_\infty \int_{\widetilde{\mathcal{S}}_w} [\![\rho \, \delta \mathsf{s} \, \mathbf{V}]\!] \cdot \tilde{\mathbf{n}} \, \mathrm{d}\mathcal{S} \tag{2.13}$$

The derivation is consistent with normal shock theory [36, 118] which treats nearby strong shocks as inviscid and adiabatic flow phenomena thereby canceling the fifth right-hand side term. No assumption is made in the derivation process other than this simplification.

The three following paragraphs provide alternative expressions for the first three right-hand side terms that are subsequently introduced back in Eq. (2.13) to form an exergy balance for aero-thermo-propulsive performance assessment.

2.1.2.2 Energy and the First Law of Thermodynamics

In this subsection we derive an alternative expression for the first right-hand side term of Eq. (2.13):

$$\int_{\mathcal{V}} \nabla \cdot (\rho \, \delta h_i \mathbf{V}) \, \mathrm{d}\mathcal{V} \tag{2.14}$$

which is the rate of change of total enthalpy within the control volume. From the First law of thermodynamics it can be directly expressed through the following transport equation:

$$\int_{\mathcal{V}} \nabla \cdot (\rho \, \delta h_i \mathbf{V}) \, \mathrm{d}\mathcal{V} = \int_{\mathcal{V}} \nabla \cdot (\bar{\bar{\tau}}_{eff} \cdot \mathbf{V}) \, \mathrm{d}\mathcal{V} - \int_{\mathcal{V}} \nabla \cdot \mathbf{q}_{eff} \, \mathrm{d}\mathcal{V} \tag{2.15}$$

and invoking the divergence theorem, the two right-hand side terms can be re-written as:

$$\int_{\mathcal{V}} \nabla \cdot (\rho \, \delta h_i \mathbf{V}) \, \mathrm{d}\mathcal{V} = \int_{\mathcal{S}_A} (\bar{\bar{\tau}}_{eff} \cdot \mathbf{V}) \cdot \mathbf{n} \, \mathrm{d}\mathcal{S} - \int_{\mathcal{S}_A} (\mathbf{q}_{eff} \cdot \mathbf{n}) \, \mathrm{d}\mathcal{S}$$
$$+ \int_{\mathcal{S}_O} (\bar{\bar{\tau}}_{eff} \cdot \mathbf{V}) \cdot \mathbf{n} \, \mathrm{d}\mathcal{S} - \int_{\mathcal{S}_O} (\mathbf{q}_{eff} \cdot \mathbf{n}) \, \mathrm{d}\mathcal{S} \tag{2.16}$$
$$- \cancel{\int_{\widetilde{\mathcal{S}}_w} [\![\bar{\bar{\tau}}_{eff} \cdot \mathbf{V}]\!] \cdot \tilde{\mathbf{n}} \, \mathrm{d}\mathcal{S}} + \cancel{\int_{\widetilde{\mathcal{S}}_w} [\![\mathbf{q}_{eff}]\!] \cdot \tilde{\mathbf{n}} \, \mathrm{d}\mathcal{S}}$$

Considering the shock waves as adiabatic and inviscid flow phenomena cancels the two last terms of this relation which is exact; no further manipulations are required.

2.1.2.3 Anergy and the Second Law of Thermodynamics

In this subsection we derive an alternative expression for the second right-hand side term of Eq. (2.13):

$$T_\infty \int_\mathcal{V} \nabla \cdot (\rho\, \delta \mathsf{s}\, \mathbf{V})\, \mathrm{d}\mathcal{V} \tag{2.17}$$

which represents the rate of change of anergy within the control volume.

The *Gibbs* equation provides a relation between entropy and internal energy ($e = c_v\, T$) which, in time-averaged form, reads

$$T\, \nabla \mathsf{s} = \nabla e + p \nabla \frac{1}{\rho} \qquad \Longleftrightarrow \qquad T\, \nabla \cdot (\rho\, \delta \mathsf{s}\, \mathbf{V}) = \nabla \cdot (\rho\, \delta e\, \mathbf{V}) + p\, \nabla \cdot \mathbf{V} \tag{2.18}$$

Inserting the steady-state expression of the internal energy variation

$$\nabla \cdot (\rho\, \delta e\, \mathbf{V}) = -p\, \nabla \cdot \mathbf{V} + (\bar{\bar{\tau}}_{eff} \cdot \nabla) \cdot \mathbf{V} - \nabla \cdot \mathbf{q}_{eff} \tag{2.19}$$

into the *Gibbs* equation (2.18) yields the following entropy relation:

$$\nabla \cdot (\rho\, \delta \mathsf{s}\, \mathbf{V}) = \frac{1}{T} (\bar{\bar{\tau}}_{eff} \cdot \nabla) \cdot \mathbf{V} - \frac{1}{T} \nabla \cdot \mathbf{q}_{eff} \tag{2.20}$$

Introducing the *Fourier* law $\mathbf{q}_{eff} = -k_{eff} \nabla T$ and the effective dissipation rate $\Phi_{eff} = (\bar{\bar{\tau}}_{eff} \cdot \nabla) \cdot \mathbf{V}$, one gets

$$\nabla \cdot (\rho\, \delta \mathsf{s}\, \mathbf{V}) = \frac{1}{T} \Phi_{eff} + \frac{1}{T^2} k_{eff} (\nabla \mathbf{T})^2 - \nabla \cdot \frac{1}{T} \mathbf{q}_{eff} \tag{2.21}$$

where one can identify the *Moore* and *Moore* eddy viscosity model for mean entropy production [108] in the first two right-hand side terms (responsible for entropy generation), see paragraph 1.3.5 (p. 24). The last right-hand side term accounts for the *reversible* anergy change associated with heat transfer.

Now, multiplying Eq. (2.21) by T_∞ and integrating within the control volume, one gets a decomposition for the rate of change of anergy as:

$$T_\infty \int_\mathcal{V} \nabla \cdot (\rho\, \delta \mathsf{s}\, \mathbf{V})\, \mathrm{d}\mathcal{V} = \int_\mathcal{V} \frac{T_\infty}{T} \Phi_{eff}\, \mathrm{d}\mathcal{V} + \int_\mathcal{V} \frac{T_\infty}{T^2} k_{eff} (\nabla \mathbf{T})^2\, \mathrm{d}\mathcal{V} - \int_\mathcal{V} \nabla \cdot \frac{T_\infty}{T} \mathbf{q}_{eff}\, \mathrm{d}\mathcal{V} \tag{2.22}$$

and, invoking the divergence theorem we obtain:

$$\begin{aligned} T_\infty \int_\mathcal{V} \nabla \cdot (\rho\, \delta \mathsf{s}\, \mathbf{V})\, \mathrm{d}\mathcal{V} = &\int_\mathcal{V} \frac{T_\infty}{T} \Phi_{eff}\, \mathrm{d}\mathcal{V} + \int_\mathcal{V} \frac{T_\infty}{T^2} k_{eff} (\nabla \mathbf{T})^2\, \mathrm{d}\mathcal{V} - \int_{\mathcal{S}_A} \frac{T_\infty}{T} (\mathbf{q}_{eff} \cdot \mathbf{n})\, \mathrm{d}\mathcal{S} \\ &- \int_{\mathcal{S}_O} \frac{T_\infty}{T} (\mathbf{q}_{eff} \cdot \mathbf{n})\, \mathrm{d}\mathcal{S} + \int_{\widetilde{\mathcal{S}}_w} [\![\frac{T_\infty}{T} \mathbf{q}_{eff}]\!] \cdot \tilde{\mathbf{n}}\, \mathrm{d}\mathcal{S} \end{aligned} \tag{2.23}$$

The heat transfer at the wave surface is assumed to be zero which cancels out the last term. This equation describes the rate of change of anergy within the control volume and will be inserted later in Eq. (2.13) and described in greater details in paragraph 2.1.3 (p. 35).

2.1.2.4 Total Enthalpy Outflow Decomposition

The manipulation here consists in the decomposition of the total enthalpy outflow

$$\int_{\mathcal{S}_O} \rho \, \delta h_i \, (\mathbf{V} \cdot \mathbf{n}) \, \mathrm{d}\mathcal{S} \tag{2.24}$$

to identify the far-field expression of $W\dot{\Gamma}$. To do so, we shall recall the definition of the total enthalpy and then add and subtract terms to introduce the expression $W\dot{\Gamma}$ in Eq. (2.10).

The total enthalpy is the sum of the enthalpy h and of the kinetic energy $1/2V^2$. Its potential relative to the freestream reference is:

$$\delta h_i = \delta h + \delta \frac{V^2}{2} = \delta e + \delta \left(\frac{p}{\rho} \right) + \delta \frac{V^2}{2} = \delta e + \left(\frac{p}{\rho} - \frac{p_\infty}{\rho_\infty} \right) + \delta \frac{V^2}{2} \tag{2.25}$$

Multiplying Eq. (2.25) by $\rho(\mathbf{V} \cdot \mathbf{n})$ and integrating over the outer boundary $\mathcal{S}_O$ yields

$$\int_{\mathcal{S}_O} \rho \, \delta h_i \, (\mathbf{V} \cdot \mathbf{n}) \, \mathrm{d}\mathcal{S} = \int_{\mathcal{S}_O} \rho \, \delta e \, (\mathbf{V} \cdot \mathbf{n}) \, \mathrm{d}\mathcal{S} + \int_{\mathcal{S}_O} p(\mathbf{V} \cdot \mathbf{n}) \, \mathrm{d}\mathcal{S} - \int_{\mathcal{S}_O} \rho \, \frac{\cancel{p_\infty}}{\cancel{\rho_\infty}} \cancel{(\mathbf{V} \cdot \mathbf{n})} \, \mathrm{d}\mathcal{S}$$
$$+ \int_{\mathcal{S}_O} \frac{1}{2} \rho (\mathbf{V}^2 - \mathbf{V}_\infty^2)(\mathbf{V} \cdot \mathbf{n}) \, \mathrm{d}\mathcal{S} \tag{2.26}$$

From the mass conservation relation Eq. (2.5b), the third right-hand side integral is zero.
Now, to identify the far-field expression of $W\dot{\Gamma}$, we have to add and subtract $\int_{\mathcal{S}_O} p_\infty (\mathbf{V} \cdot \mathbf{n}) \, \mathrm{d}\mathcal{S}$:

$$\int_{\mathcal{S}_O} \rho \, \delta h_i \, (\mathbf{V} \cdot \mathbf{n}) \, \mathrm{d}\mathcal{S} = \int_{\mathcal{S}_O} \rho \, \delta e \, (\mathbf{V} \cdot \mathbf{n}) \, \mathrm{d}\mathcal{S} + \int_{\mathcal{S}_O} (p - p_\infty)(\mathbf{V} \cdot \mathbf{n}) \, \mathrm{d}\mathcal{S} + \int_{\mathcal{S}_O} p_\infty (\mathbf{V} \cdot \mathbf{n}) \, \mathrm{d}\mathcal{S}$$
$$+ \int_{\mathcal{S}_O} \frac{1}{2} \rho (\mathbf{V}^2 - \mathbf{V}_\infty^2)(\mathbf{V} \cdot \mathbf{n}) \, \mathrm{d}\mathcal{S} \tag{2.27}$$

we shall further add and subtract $\int_{\mathcal{S}_O} (p - p_\infty)(\mathbf{V}_\infty \cdot \mathbf{n}) \, \mathrm{d}\mathcal{S}$ to get

$$\int_{\mathcal{S}_O} \rho \, \delta h_i \, (\mathbf{V} \cdot \mathbf{n}) \, \mathrm{d}\mathcal{S} = \int_{\mathcal{S}_O} \rho \, \delta e \, (\mathbf{V} \cdot \mathbf{n}) \, \mathrm{d}\mathcal{S} + \int_{\mathcal{S}_O} (p - p_\infty)[(\mathbf{V} - \mathbf{V}_\infty) \cdot \mathbf{n}] \, \mathrm{d}\mathcal{S} + \int_{\mathcal{S}_O} p_\infty (\mathbf{V} \cdot \mathbf{n}) \, \mathrm{d}\mathcal{S}$$
$$+ \int_{\mathcal{S}_O} (p - p_\infty)(\mathbf{V}_\infty \cdot \mathbf{n}) \, \mathrm{d}\mathcal{S} + \int_{\mathcal{S}_O} \frac{1}{2} \rho (\mathbf{V}^2 - \mathbf{V}_\infty^2)(\mathbf{V} \cdot \mathbf{n}) \, \mathrm{d}\mathcal{S} \tag{2.28}$$

Then, the last term, *i.e.* the relative kinetic energy outflow, can be decomposed as:

$$\int_{\mathcal{S}_O} \rho \, \delta h_i \, (\mathbf{V} \cdot \mathbf{n}) \, \mathrm{d}\mathcal{S} = \int_{\mathcal{S}_O} \rho \, \delta e \, (\mathbf{V} \cdot \mathbf{n}) \, \mathrm{d}\mathcal{S} + \int_{\mathcal{S}_O} (p - p_\infty)[(\mathbf{V} - \mathbf{V}_\infty) \cdot \mathbf{n}] \, \mathrm{d}\mathcal{S} + \int_{\mathcal{S}_O} p_\infty (\mathbf{V} \cdot \mathbf{n}) \, \mathrm{d}\mathcal{S}$$
$$+ \int_{\mathcal{S}_O} (p - p_\infty)(\mathbf{V}_\infty \cdot \mathbf{n}) \, \mathrm{d}\mathcal{S} + \int_{\mathcal{S}_O} \frac{1}{2} \rho [2uV_\infty + u^2 + v^2 + w^2](\mathbf{V} \cdot \mathbf{n}) \, \mathrm{d}\mathcal{S} \tag{2.29}$$

and re-arranged into:

$$\int_{\mathcal{S}_O} \rho \, \delta h_i \, (\mathbf{V} \cdot \mathbf{n}) \, \mathrm{d}\mathcal{S} = \int_{\mathcal{S}_O} \rho \, \delta e \, (\mathbf{V} \cdot \mathbf{n}) \, \mathrm{d}\mathcal{S} + \int_{\mathcal{S}_O} (p - p_\infty) [(\mathbf{V} - \mathbf{V}_\infty) \cdot \mathbf{n}] \, \mathrm{d}\mathcal{S} + \int_{\mathcal{S}_O} p_\infty (\mathbf{V} \cdot \mathbf{n}) \, \mathrm{d}\mathcal{S}$$
$$+ \int_{\mathcal{S}_O} [(p - p_\infty)(\mathbf{V}_\infty \cdot \mathbf{n}) + \rho \, uV_\infty (\mathbf{V} \cdot \mathbf{n})] \, \mathrm{d}\mathcal{S}$$
$$+ \int_{\mathcal{S}_O} \frac{1}{2} \rho (u^2 + v^2 + w^2)(\mathbf{V} \cdot \mathbf{n}) \, \mathrm{d}\mathcal{S} \tag{2.30}$$

Lastly, adding and subtracting $\int_{\mathcal{S}_O} (\bar{\bar{\tau}}_{eff} \cdot \mathbf{V}_\infty) \cdot \mathbf{n} \, d\mathcal{S}$, we can identify the exact expression for $W\dot{\Gamma}$ in Eq. (2.10) and finally obtain

$$
\int_{\mathcal{S}_O} \rho \, \delta h_i \, (\mathbf{V} \cdot \mathbf{n}) \, d\mathcal{S} = \int_{\mathcal{S}_O} \rho \, \delta e \, (\mathbf{V} \cdot \mathbf{n}) \, d\mathcal{S} + \int_{\mathcal{S}_O} p_\infty (\mathbf{V} \cdot \mathbf{n}) \, d\mathcal{S} + \int_{\mathcal{S}_O} (p - p_\infty) \left[(\mathbf{V} - \mathbf{V}_\infty) \cdot \mathbf{n} \right] \, d\mathcal{S}
$$
$$
+ W\dot{\Gamma} + \int_{\mathcal{S}_O} (\bar{\bar{\tau}}_{eff} \cdot \mathbf{V}_\infty) \cdot \mathbf{n} \, d\mathcal{S} + \int_{\mathcal{S}_O} \frac{1}{2} \rho (u^2 + v^2 + w^2)(\mathbf{V} \cdot \mathbf{n}) \, d\mathcal{S}
$$
$$(2.31)$$

This final total enthalpy relation is exact.

2.1.2.5   Mathematically-exact Exergy Balance

Inserting Eqs. (2.16, 2.31 & 2.23), into Eq. (2.13) yields the following mathematically-exact exergy balance:

$$
- \int_{\mathcal{S}_A} \rho \, \delta h_i \, (\mathbf{V} \cdot \mathbf{n}) \, d\mathcal{S} + T_\infty \int_{\mathcal{S}_A} \rho \, \delta s \, (\mathbf{V} \cdot \mathbf{n}) \, d\mathcal{S} + \int_{\mathcal{S}_A} (\bar{\bar{\tau}}_{eff} \cdot \mathbf{V}) \cdot \mathbf{n} \, d\mathcal{S} - \int_{\mathcal{S}_A} \left(1 - \frac{T_\infty}{T} \right) (\mathbf{q}_{eff} \cdot \mathbf{n}) \, d\mathcal{S}
$$
$$
= W\dot{\Gamma} - \int_{\mathcal{S}_O} (\bar{\bar{\tau}}_{eff} \cdot \mathbf{V}) \cdot \mathbf{n} \, d\mathcal{S} + \int_{\mathcal{S}_O} (\mathbf{q}_{eff} \cdot \mathbf{n}) \, d\mathcal{S}
$$
$$
- \int_{\mathcal{S}_O} \frac{T_\infty}{T} (\mathbf{q}_{eff} \cdot \mathbf{n}) \, d\mathcal{S} + \int_{\mathcal{V}} \frac{T_\infty}{T} \Phi_{eff} \, d\mathcal{V} + \int_{\mathcal{V}} \frac{T_\infty}{T^2} k_{eff} \, (\nabla \mathbf{T})^2 \, d\mathcal{V}
$$
$$
+ \int_{\mathcal{S}_O} \rho \, \delta e \, (\mathbf{V} \cdot \mathbf{n}) \, d\mathcal{S} + \int_{\mathcal{S}_O} p_\infty (\mathbf{V} \cdot \mathbf{n}) \, d\mathcal{S} - T_\infty \int_{\mathcal{S}_O} \rho \, \delta s \, (\mathbf{V} \cdot \mathbf{n}) \, d\mathcal{S}
$$
$$
+ \int_{\mathcal{S}_O} (p - p_\infty) \left[(\mathbf{V} - \mathbf{V}_\infty) \cdot \mathbf{n} \right] \, d\mathcal{S} + \int_{\mathcal{S}_O} (\bar{\bar{\tau}}_{eff} \cdot \mathbf{V}_\infty) \cdot \mathbf{n} \, d\mathcal{S}
$$
$$
+ \int_{\mathcal{S}_O} \frac{1}{2} \rho (u^2 + v^2 + w^2)(\mathbf{V} \cdot \mathbf{n}) \, d\mathcal{S}
$$
$$
+ T_\infty \int_{\widetilde{\mathcal{S}}_w} [\![\rho \, \delta s \, \mathbf{V}]\!] \cdot \tilde{\mathbf{n}} \, d\mathcal{S} - \int_{\widetilde{\mathcal{S}}_w} [\![\rho \, \delta h_i \, \mathbf{V}]\!] \cdot \tilde{\mathbf{n}} \, d\mathcal{S}
$$
$$
+ \int_{\widetilde{\mathcal{S}}_w} [\![\bar{\bar{\tau}}_{eff} \cdot \mathbf{V}]\!] \cdot \tilde{\mathbf{n}} \, d\mathcal{S} - \int_{\widetilde{\mathcal{S}}_w} [\![\mathbf{q}_{eff}]\!] \cdot \tilde{\mathbf{n}} \, d\mathcal{S}
$$
$$
+ \int_{\widetilde{\mathcal{S}}_w} [\![\frac{T_\infty}{T} \mathbf{q}_{eff}]\!] \cdot \tilde{\mathbf{n}} \, d\mathcal{S}
$$
$$(2.32)$$

This equation is considered exact because no terms have been neglected in its derivation. It relies on the First and Second laws of thermodynamics as well as on the conservation of mass and momentum. Shock waves have been treated as inviscid and adiabatic phenomena in agreement with normal shock theory [36, 118]. The *Moore* and *Moore* model for mean entropy production [108] described in paragraph 1.3.5 (p. 24) requires the assumption that the rate of production of turbulence kinetic energy equals the rate of its dissipation. Similarly, it is assumed that the rate of production of temperature fluctuations equals their rate of dissipation.

2.1.3 Physically-approximated Exergy Balance for Transonic Flows

Based on physical considerations, four terms of the exact relationship are neglected. These terms are discussed in paragraph 2.5.1.3 (p. 56) and the domain of validity of this more relevant exergy balance is defined accordingly:

$$\int_{\mathcal{S}_A} \rho\, \delta h_i\, (\mathbf{V}\cdot\hat{\mathbf{n}})\, \mathrm{d}\mathcal{S} - T_\infty \int_{\mathcal{S}_A} \rho\, \delta\mathsf{s}\, (\mathbf{V}\cdot\hat{\mathbf{n}})\, \mathrm{d}\mathcal{S} + \int_{\mathcal{S}_A} \left(1 - \frac{T_\infty}{T}\right)(\mathbf{q}_{eff}\cdot\hat{\mathbf{n}})\, \mathrm{d}\mathcal{S} = W\dot{\Gamma}$$

$$+ \int_{\mathcal{V}} \frac{T_\infty}{T}\Phi_{eff}\, \mathrm{d}\mathcal{V} + \int_{\mathcal{V}} \frac{T_\infty}{T^2} k_{eff}\, (\nabla\mathbf{T})^2\, \mathrm{d}\mathcal{V} + \int_{\mathcal{S}_O} \rho\, \delta e\, (\mathbf{V}\cdot\mathbf{n})\, \mathrm{d}\mathcal{S}$$

$$+ \int_{\mathcal{S}_O} p_\infty (\mathbf{V}\cdot\mathbf{n})\, \mathrm{d}\mathcal{S} + \int_{\mathcal{S}_O} (p - p_\infty)\left[(\mathbf{V} - \mathbf{V}_\infty)\cdot\mathbf{n}\right]\, \mathrm{d}\mathcal{S} \qquad (2.33)$$

$$+ \int_{\mathcal{S}_O} \frac{1}{2}\rho(u^2 + v^2 + w^2)(\mathbf{V}\cdot\mathbf{n})\, \mathrm{d}\mathcal{S} - T_\infty \int_{\mathcal{S}_O} \rho\, \delta\mathsf{s}\, (\mathbf{V}\cdot\mathbf{n})\, \mathrm{d}\mathcal{S}$$

$$+ T_\infty \int_{\widetilde{\mathcal{S}_w}} [\![\rho\, \delta\mathsf{s}\, \mathbf{V}]\!]\cdot\tilde{\mathbf{n}}\, \mathrm{d}\mathcal{S}$$

where we introduced $\hat{\mathbf{n}} = -\mathbf{n}$ for writing convenience. Eq. (2.33) forms the general exergy-based formulation for the assessment of aero-thermo-propulsive performance of powered configurations:

$$\boxed{\dot{\mathcal{E}}_{prop} + \dot{\mathcal{E}}_q = W\dot{\Gamma} + \dot{\mathcal{E}}_m + \dot{\mathcal{E}}_{th} + \dot{\mathcal{A}}_\phi + \dot{\mathcal{A}}_{\nabla T} + \dot{\mathcal{A}}_w} \qquad (2.34)$$

where the rate of exergy outflow is decomposed into $W\dot{\Gamma} + \dot{\mathcal{E}}_m + \dot{\mathcal{E}}_{th}$.

Left-hand side terms represent exergy sources supplied (either by convection or conduction) while right-hand side terms represent exergy outflows and sinks, except for $W\dot{\Gamma}$ which is a (reversible) accumulation/restitution of exergy. All terms are defined hereafter and sketched in Fig. 2-2.
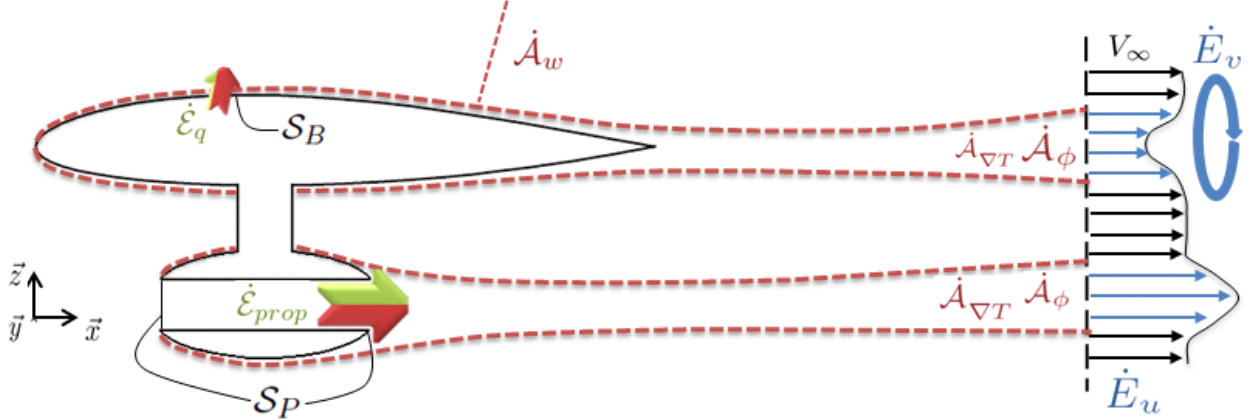
Figure 2-2: Main terms of the exergy balance in the flow field. Green is associated with exergy, red with anergy and blue with energy. $\dot{\mathcal{E}}_{th}$ and $\dot{E}_p$ are not shown.

The aircraft surface has been split in two surfaces: one solid *body* surface $\mathcal{S}_B$ which may be non-adiabatic and one permeable surface on which $\mathbf{V}\cdot\mathbf{n} \neq 0$. In the latter case, we only consider a *propulsive* surface $\mathcal{S}_P$ but we could further add another permeable surface to consider air systems that ingest and release air. Note that $\mathcal{S}_A = \mathcal{S}_B \bigcup \mathcal{S}_P$.

Exergy Supply.

$\dot{\mathcal{E}}_{prop}$: the rate of exergy supplied by the propulsion system

$$\dot{\mathcal{E}}_{prop} := \underbrace{\int_{\mathcal{S}_P} \rho\, \delta h_i\, (\mathbf{V} \cdot \hat{\mathbf{n}})\, \mathrm{d}\mathcal{S}}_{\dot{\mathcal{H}}_{prop}} - \underbrace{T_\infty \int_{\mathcal{S}_P} \rho\, \delta s\, (\mathbf{V} \cdot \hat{\mathbf{n}})\, \mathrm{d}\mathcal{S}}_{\dot{\mathcal{A}}_{prop}} \tag{2.35}$$

Both terms are non-zero only on permeable surfaces of the aircraft $\mathcal{S}_A$ considered to be only the one associated with the propulsion system $\mathcal{S}_P$. The first term is the total power supplied to the flow while the second term represents all unavoidable thermodynamic cycle inefficiencies and aerodynamic losses that have occurred within the propulsion system delimited by the surface $\mathcal{S}_P$ [64]. The combination of both forms the exergy delivered by the propulsion system to the fluid.

For convenience, $\dot{\mathcal{E}}_{prop}$ will be referred to as ***propulsive exergy***.

↪ A decomposition of this term is provided in subsection 2.2.1 and investigated in the case of an isolated turbojet engine in section 4.2 (p. 122).

$\dot{\mathcal{E}}_q$: the rate of heat exergy supplied by conduction

$$\dot{\mathcal{E}}_q := \underbrace{\int_{\mathcal{S}_B} (\mathbf{q}_{eff} \cdot \hat{\mathbf{n}})\, \mathrm{d}\mathcal{S}}_{\dot{E}_q} - \underbrace{\int_{\mathcal{S}_B} \frac{T_\infty}{T_w} (\mathbf{q}_{eff} \cdot \hat{\mathbf{n}})\, \mathrm{d}\mathcal{S}}_{\dot{\mathcal{A}}_q} \tag{2.36}$$

where T_w is the temperature the wall of the body, *i.e.* the one at which the heat transfer occurs. The terms are non-zero only on non-adiabatic surfaces of the body that are noted $\mathcal{S}_B$. The first term is the amount of energy of the heat transferred by conduction while the second term is the associated anergy. The combination of both terms yields the exergy supplied to the fluid by conduction. In other words, heat is being supplied to the flow and a potential for being converted to work exists: the higher the temperature (with reference to atmospheric conditions), the greater the work potential. A heat transfer at temperature $T_w = T_\infty$ has no practical value: its thermal exergy is zero [31]. Note that if $T_w < T_\infty$, the term $\dot{\mathcal{E}}_q$ is still positive meaning that there is a potential to improve a CARNOT cycle efficiency by using the cold surface as a heat sink. These terms could notably be used to evaluate systems like heat exchangers. If adiabatic surfaces are considered, which is generally assumed for most civil aircraft, these terms are simply zero.

↪ Heat transfer is introduced in the aero-thermo-propulsive assessment of a simplified 2D BWB in section 4.4.3 (p. 154) and investigated through the integration of a heat exchanger on an aircraft in section 4.5 (p. 160).

Exergy Loss.

$\dot{\mathcal{E}}_m$: the rate of mechanical exergy outflow

$$\dot{\mathcal{E}}_m := \underbrace{\int_{\mathcal{S}_O} \frac{1}{2}\rho\, u^2\, (\mathbf{V} \cdot \mathbf{n})\, \mathrm{d}\mathcal{S}}_{\dot{E}_u} + \underbrace{\int_{\mathcal{S}_O} \frac{1}{2}\rho\, (v^2 + w^2)\, (\mathbf{V} \cdot \mathbf{n})\, \mathrm{d}\mathcal{S}}_{\dot{E}_v} + \underbrace{\int_{\mathcal{S}_O} (p - p_\infty)\, [(\mathbf{V} - \mathbf{V}_\infty) \cdot \mathbf{n}]\, \mathrm{d}\mathcal{S}}_{\dot{E}_p} \tag{2.37}$$

$\dot{E}_u$ is the streamwise kinetic energy deposition rate and is associated with jet/wake while $\dot{E}_v$ is the transverse kinetic energy deposition rates and is mainly associated with lift-induced vortices. $\dot{E}_p$ is a

boundary pressure-work rate associated with these flow phenomena. All three terms being linked by velocity/pressure exchanges, they are gathered to form the rate of mechanical exergy outflow.

These terms are of mechanical nature and are therefore also part of the mechanical energy balance of DRELA [49]. This author demonstrated that outside of the viscous wakes and propulsion plumes, the total mechanical energy represents what is generally referred to as the drag power of the lift-induced vortices, see paragraph 1.1.2.1 (p. 8) and appendix A.3 (p. 180) for the derivation. The potential for improvement with these flow features is not recovered for most aerospace applications and, for that reason, represent an exergy *loss*.

↪ Further specifications of these terms are provided in section 2.2.2 (p. 41) and are particularly investigated for wake ingestion in section 4.3 (p. 133).

$\dot{\mathcal{E}}_{th}$: the rate of thermal exergy outflow

$$\dot{\mathcal{E}}_{th} := \underbrace{\int_{\mathcal{S}_O} \rho\, \delta e\, (\mathbf{V} \cdot \mathbf{n})\, \mathrm{d}\mathcal{S}}_{\dot{E}_{th}} + \underbrace{\int_{\mathcal{S}_O} p_\infty\, (\mathbf{V} \cdot \mathbf{n})\, \mathrm{d}\mathcal{S}}_{\dot{E}_W} - \underbrace{T_\infty \int_{\mathcal{S}_O} \rho\, \delta \mathsf{s}\, (\mathbf{V} \cdot \mathbf{n})\, \mathrm{d}\mathcal{S}}_{\dot{\mathcal{A}}} \qquad (2.38)$$

Assuming a perfect gas, internal energy is solely proportional to temperature ($e = c_v\, T$), so that the first term is the rate of *thermal energy* outflow. The second term is usually referred to as the rate of *(isobaric) surroundings work* [34, 38] and is a non available work that the system performs, or receives, due to its interaction with the reference atmospheric pressure field at p_∞ [45]. The last term is the outflow rate of anergy. The combination of the three terms yields the maximum amount of work that is theoretically extractable from the thermal energy.

For most aerospace applications, this term is not recovered and therefore represents an exergy *loss*.

↪ Note that the terminology of *thermal exergy* is not in agreement with traditional definitions given in the literature; a more appropriate adjective would be *thermocompressible* as discussed in paragraph 2.2.2.3 (p. 43). This term is also characterized for an isolated turbojet engine in section 4.2 (p. 122).

Exergy Destruction/Anergy Generation.

$\dot{\mathcal{A}}_\phi$: the rate of anergy generation by viscous dissipation

$$\dot{\mathcal{A}}_\phi := \int_{\mathcal{V}} \frac{T_\infty}{T} \Phi_{eff}\, \mathrm{d}\mathcal{V} \qquad (2.39)$$

$\dot{\mathcal{A}}_\phi$ is linked to viscous dissipation and turbulence which transform any difference in kinetic energy into thermal energy. For that reason, these phenomena act towards reducing the mechanical exergy to zero by building a new homogeneous field of velocity (and pressure), in which the system and its surroundings are back in mechanical equilibrium.

This term is positive[5] and hence will always increase anergy; it indicates an irreversible process that *destroys* mechanical exergy. Even if at high *Reynolds* numbers the dissipation is mainly associated with turbulence rather than viscous stresses[6], for convenience, $\dot{\mathcal{A}}_\phi$ is referred to as ***viscous anergy***.

↪ Further specifications of this term are provided in paragraph 2.2.3.2 (p. 45).

---

[5] An alternative expression for the viscous dissipation Φ_{eff} is provided in appendix A.7 (p. 184).
[6] Paragraphs 3.2.4 (p. 76) and 3.3.1 (p. 79) will precisely quantify the influence of turbulence on the *viscous* dissipation.

$\dot{\mathcal{A}}_{\nabla T}$: the rate of anergy generation by thermal conduction

$$\dot{\mathcal{A}}_{\nabla T} := \int_{\mathcal{V}} \frac{T_\infty}{T^2} k_{eff} \left(\nabla \mathbf{T}\right)^2 \mathrm{d}\mathcal{V} \qquad (2.40)$$

$\dot{\mathcal{A}}_{\nabla T}$ is linked to thermal mixing which reduces the difference in temperature and therefore reduces the thermal exergy to zero. It acts towards building a new homogeneous field of temperature in which the system and its surroundings are back in thermal equilibrium. The thermal mixing is a function of the square of the temperature gradients so that avoiding strong temperature variations would reduce this term.

This term is positive and hence will always increase anergy; it indicates an irreversible process that *destroys* thermal exergy. For convenience, $\dot{\mathcal{A}}_{\nabla T}$ is referred to as ***thermal anergy***.

↪ This term is precisely characterized for the isolated turbojet engine in section 4.2 (p. 122).

$\dot{\mathcal{A}}_w$: the rate of anergy generation by discontinuous shock waves

$$\dot{\mathcal{A}}_w := T_\infty \int_{\widetilde{\mathcal{S}}_w} [\![\rho \, \delta \mathsf{s} \, \mathbf{V}]\!] \cdot \tilde{\mathbf{n}} \, \mathrm{d}\mathcal{S} \qquad (2.41)$$

This phenomenon converts mechanical energy into thermal energy; this process being irreversible, it is an exergy *destruction*. For convenience, $\dot{\mathcal{A}}_w$ is referred to as ***wave anergy***.

↪ Further details on the numerical treatment of this term are given in paragraph 2.5.1.1 (p. 54), as well as in the transonic flows investigated for the NACA 0012 in paragraph 3.3.3.3 (p. 86).

Physical Description. For adiabatic surfaces, the exergy relation (2.34) can be described as follows: the exergy supplied by the propulsive system has been used to effectively apply a net force that drives the vehicle through the air. Exergy has been supplied in excess to that requirement in the form of streamwise and transverse kinetic energy and a boundary pressure work. This loss of mechanical exergy is associated with wakes/jets and lift-induced vortices and will be dissipated by viscous dissipation. Additionally, work could be extracted from the thermal energy flowing out of the control volume. If not valued, this work potential will be destroyed by thermal mixing. To conclude, in a vehicle performance perspective, the design that wastes and destroys the less exergy is the most efficient one because a correspondingly lower propulsive exergy will be required to compensate.

2.2 Further Specifications of the Formulation

A few further specifications of the formulation are given in the following section. First, the propulsive exergy $\dot{\mathcal{E}}_{prop}$ is decomposed to provide performance efficiencies applicable to any type of propulsion system. Then, a physical interpretation of the outflows of mechanical $\dot{\mathcal{E}}_m$ and thermal $\dot{\mathcal{E}}_{th}$ exergy is provided. Precision on the dissipative phenomena allow to quantify the influence of turbulence. Finally, far-field asymptotic considerations are given to emphasize the vanishing work potential associated with the exergy wasted in the jet/wake of an aerospace vehicle.

2.2.1 Near-field Propulsion Analysis

2.2.1.1 Exergy Efficiencies

Intrinsic Efficiency. The scope of this analysis is voluntarily large so as being able to deal with any kind of propulsive device. As $\dot{\mathcal{E}}_{prop}$ represents the potential to produce propulsive power, one can first introduce an engine intrinsic exergy efficiency ψ_i:

$$\psi_i := \frac{\dot{\mathcal{E}}_{prop}}{\dot{\mathcal{H}}_{prop}} = 1 - \frac{\dot{\mathcal{A}}_{prop}}{\dot{\mathcal{H}}_{prop}} \tag{2.42}$$

where $\dot{\mathcal{H}}_{prop}$ is the rate of total energy supplied to the flow while $\dot{\mathcal{A}}_{prop}$ represents all anergy generation that has occured within the propulsive device delimited by the surface boundary $\mathcal{S}_P$, including losses associated with combustion (if any). The primary source of energy for $\dot{\mathcal{H}}_i$ could be of any form (electrical or chemical). For example, for fuel-based propulsion, the total power supplied to the flow is equal to the rate of energy released by combustion [64] $\dot{\mathcal{H}}_{prop} = \dot{m}_f \, \Delta h_f$ where Δh_f is the fuel higher heating value, roughly[7] equal to the (standard) chemical exergy stored in the fuel [47]. We can therefore define a combustion efficiency as the ratio of the exergy stored in the fuel $\dot{\mathcal{E}}_{fuel}$ and the exergy released by the exergy ideally available for the propulsion system $\dot{\mathcal{E}}_{prop,i}$:

$$\psi_c := \frac{\dot{\mathcal{E}}_{prop,i}}{\dot{\mathcal{E}}_{fuel}} = \frac{\dot{\mathcal{E}}_{prop,i}}{\dot{\mathcal{H}}_{prop}} \tag{2.43}$$

where $\dot{\mathcal{E}}_{prop,i} = (1 - T_\infty/T_c)\dot{\mathcal{E}}_{fuel}$ with T_c being the temperature at which the fuel is burn (around 1,700K for current propulsion turbofans [41]).

It is also crucial to note that, if the propulsion system is modeled in the computation, use of the divergence theorem could be made to decompose $\dot{\mathcal{A}}_{prop}$ into viscous anergy, thermal anergy, wave anergy and heat transfer (by conduction) anergy, according to the approach of DENTON [44]. Moreover, this decomposition could be obtained for each component of the complete propulsive device, as proposed by CLARKE and HORLOCK [40] and LEWIS [93].

Mechanical Efficiency. The exergy delivered by the propulsion can be decomposed into a mechanical exergy and a thermal exergy (if any):

$$\dot{\mathcal{E}}_{prop} = \dot{\mathcal{E}}_{prop,m} + \dot{\mathcal{E}}_{prop,th} \tag{2.44}$$

where

$$\dot{\mathcal{E}}_{prop,m} = \int_{\mathcal{S}_P} \left[(p - p_\infty) + \frac{1}{2}\rho \left(V^2 - V_\infty^2 \right) \right] (\mathbf{V} \cdot \hat{\mathbf{n}}) \, \mathrm{d}\mathcal{S} \tag{2.45a}$$

$$\dot{\mathcal{E}}_{prop,th} = \int_{\mathcal{S}_P} \left[\rho(\delta e - T_\infty \delta \mathsf{s}) + p_\infty \right] (\mathbf{V} \cdot \hat{\mathbf{n}}) \, \mathrm{d}\mathcal{S} \tag{2.45b}$$

In terms of propulsion, only the mechanical part of the total exergy is in a usable form. One can therefore introduce a mechanical efficiency as:

$$\psi_m := \frac{\dot{\mathcal{E}}_{prop,m}}{\dot{\mathcal{E}}_{prop}} \tag{2.46}$$

---

[7]Strictly speaking, the chemical exergy is function of the reference conditions [114], *i.e.* those at the altitude of flight.

For a given exergy supplied to the flow, as the thermal exergy is reduced, the mechanical efficiency is increased. The mechanical exergy can then be expanded into:

$$\dot{\mathcal{E}}_{prop,m} = \underbrace{\int_{\mathcal{S}_P} [\rho \mathbf{V} (\mathbf{V} \cdot \hat{\mathbf{n}}) + (p - p_\infty)\hat{\mathbf{n}}] \; \mathrm{d}\mathcal{S} \cdot \mathbf{V}_\infty}_{\mathbf{F_{prop}}} + \underbrace{\int_{\mathcal{S}_P} \frac{1}{2}\rho \, u^2 \, (\mathbf{V} \cdot \hat{\mathbf{n}}) \; \mathrm{d}\mathcal{S}}_{Axial \; Kinetic \; Power}$$

$$+ \underbrace{\int_{\mathcal{S}_P} \frac{1}{2}\rho \, (v^2 + w^2) \, (\mathbf{V} \cdot \hat{\mathbf{n}}) \; \mathrm{d}\mathcal{S}}_{Transverse \; Kinetic \; Power} + \underbrace{\int_{\mathcal{S}_P} (p - p_\infty) \, [(\mathbf{V} - \mathbf{V}_\infty) \cdot \hat{\mathbf{n}}] \; \mathrm{d}\mathcal{S}}_{Pressure-Work \; Rate}$$

(2.47)

where the first term is the dot product of the momentum change across the surface $\mathcal{S}_P$ and of the flight velocity $\mathbf{V}_\infty$. Whether or not the force $\mathbf{F_{prop}}$ should be considered an *(integrated) thrust* is left at the discretion of airframe and propulsion designers, with the understanding that the surface $\mathcal{S}_P$ *has to be defined*. The difficulty lies in the fact that the definition of $\mathcal{S}_P$ is not unique, especially for highly integrated propulsion devices, as illustrated in Fig. 2-3, where it could be any combination of inlet/outlet surfaces.
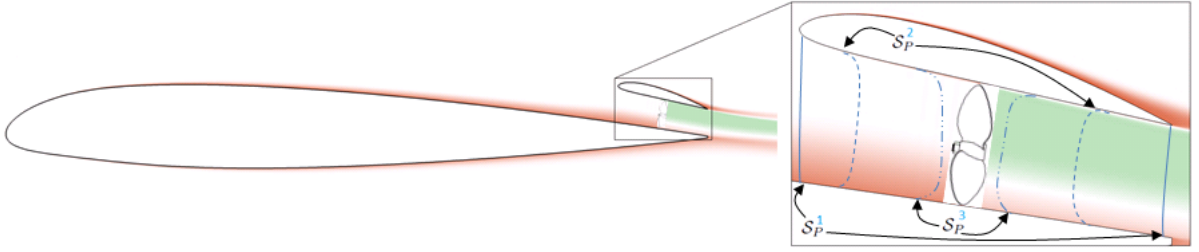

Figure 2-3: Possible choices for the propulsive surface definition for a highly integrated propulsion system.

Propulsive Efficiency.   In fact, the force $\mathbf{F_{prop}}$ is only identical to thrust under the conditions that the surface is carefully chosen so at to satisfy a given drag/thrust bookkeeping, which always involves some kind of arbitrariness [53] and must be adapted to any particular situation [42].

The propulsive efficiency ψ_p indicates the portion of mechanical energy that has been effectively converted into gross propulsive power:

$$\psi_p := \frac{\mathbf{F_{prop}} \cdot \mathbf{V}_\infty}{\dot{\mathcal{E}}_{prop,m}}$$

(2.48)

Another expression of ψ_p can be obtained by dividing Eq. (2.47) by $\dot{\mathcal{E}}_{prop,m}$ to get:

$$\psi_p = 1 - \frac{Axial \; Kinetic \; Power}{\dot{\mathcal{E}}_{prop,m}} - \frac{Transverse \; Kinetic \; Power}{\dot{\mathcal{E}}_{prop,m}} - \frac{Pressure-Work \; Rate}{\dot{\mathcal{E}}_{prop,m}}$$

(2.49)

and one can briefly describe two cases:

1. Considering a traditional propulsive system which consists of a nacelle enclosing a turbofan engine, one of the legitimate choice for the surface $\mathcal{S}_P$ is the inlet/outlet of the nacelle. In this case, it is reasonable to consider a perfectly-expanded jet ($p = p_\infty$) as well as to neglect the transverse kinetic energy. As a consequence, the only term remaining in Eq. (2.49) is the axial kinetic power and therefore ψ_p reduces to its standard expression as ratio of thrust power to kinetic power [53].

2. Considering a highly integrated propulsion system as sketched in Fig. 2-3, the surface $\mathcal{S}_P$ is not unique. It might be possible to neglect the transverse kinetic power but the pressure is likely to be different than freestream. As the surface is moved closer to the fan, the axial kinetic power reduces to

zero and the only term remaining becomes the pressure-work rate. If the axial velocity in the vicinity of the fan is lower than freestream, as in the case of a ducted fan, it is eventually possible to obtain values of ψ_p that are greater than one. Note that the force $\mathbf{F_{prop}}$ that would be calculated for this choice of surface ($\mathcal{S}_P^3$ on Fig. 2-3) could be compared to the force acting on the fan which could be experimentally measured in wind-tunnel tests for such complex configurations.

Overall Efficiency. One can finally introduce an overall exergy efficiency ψ_ε:

$$\psi_\varepsilon := \frac{\mathbf{F_{prop}} \cdot \mathbf{V_\infty}}{\dot{\mathcal{E}}_{fuel}} = \frac{\dot{\mathcal{E}}_{prop,i}}{\dot{\mathcal{H}}_{prop}} \times \frac{\dot{\mathcal{E}}_{prop}}{\dot{\mathcal{E}}_{prop,i}} \times \frac{\dot{\mathcal{E}}_{prop,m}}{\dot{\mathcal{E}}_{prop}} \times \frac{\mathbf{F}_{prop} V_\infty}{\dot{\mathcal{E}}_{prop,m}} = \psi_c \times \psi_i \times \psi_m \times \psi_p \qquad (2.50)$$

which corresponds to the rational efficiency introduced by CLARKE and HORLOCK [40].

Figure 2-4: Fuel exergy decomposition

These efficiencies are applicable to any type of propulsion system and should therefore be well-suited for technology comparison. Also, since the approach does not require $p = p_\infty$ on the surface S_P, it is possible to evaluate under/over-expanded nozzles.

↪ An isolated turbojet engine is investigated in section 4.2 (p. 122) where all the aforementioned terms are characterized.

2.2.2 Mid-field Outflows Characterization and Recovery

Although it does not necessarily take an exergy analysis to recognize that the flow downstream a configuration could offer improvements, by redefining the loss as entropy generation, the exergy/anergy framework provides a consistent approach to evaluate any recoverable potential. As soon as the local state is not in equilibrium with the reference conditions, exergy is available, and the more it deviates from equilibrium, the greater the work potential [140]. For unconventional configurations for which we have little knowledge, this approach would make any (mechanical or thermal) waste clearly visible.

In the following, some considerations are given in the mid-field of typical aerospace configurations, *i.e.* within a few body lengths.

2.2.2.1 Streamwise Kinetic Energy

$\dot{E}_u$ is positive regardless the sign of the perturbation axial velocity u which is positive in a jet and negative in a wake. From streamwise momentum considerations, the wake of an aircraft is seen as a deficit, and as a consequence, is considered a loss. The exergy analysis tells us that it actually represents a potential for improvement.

One of the concepts that take advantage from the drawback of having generated a wake is called *wake ingestion*, or, by extension, boundary layer ingestion [152]. The idea is to place the propulsive system downstream of the configuration so as to ingest its wake, and to ideally re-energize it by just the right amount to match freestream conditions, leaving no wake/jet: $\dot{E}_u = 0$. From Eq. (2.34), one can see that it would result in a correspondingly lower exergy to be supplied by the propulsion system.

In an exergy point of view, the following interpretation can be suggested: from Second law considerations, the flow has to return to equilibrium with its environment in the far-field of the body. This is usually

(a) Conventional podded-engine configuration.
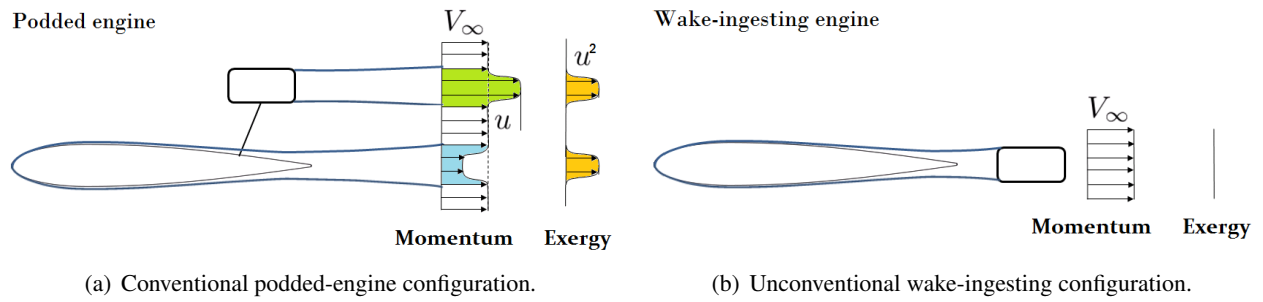(b) Unconventional wake-ingesting configuration.

Figure 2-5: Streamwise kinetic energy associated with wake and exhaust jets.

achieved by viscous dissipation which tends to provide a uniform field of velocity. Placing the propulsive system downstream of the fuselage enables to balance the deficit in axial velocity and thereby to bring the fluid closer to equilibrium with its environment in a (more) reversible manner than if viscous dissipation was the mechanism involved.

↪ It will be shown in section 4.3 (p. 133) that such arrangement enables the recovery of a portion of the exergy present in the fuselage wake.

2.2.2.2 Transverse Kinetic Energy

$\dot{E}_v$ represents (mainly) the kinetic energy associated with lift-induced vortices. Traditional far-field analysis based on momentum conclude that these vortices generate drag and are thus generally viewed as losses. In the exergy/anergy framework, the formation of the vortex is not considered as a direct loss; the loss is the subsequent viscous anergy generated to dissipate the transverse kinetic energy. One way to prevent this exergy destruction is formation flight where interactions between the leading and the trailing aircraft reduces the induced drag of the trailing aircraft[8], and therefore its fuel burn up to 18% [172]. In an exergy point of view, the trailing aircraft has generated a vortex that is rotating the other way around, thereby reducing the transverse velocities. By doing so, equilibrium with the environment is reached in a (more) reversible manner than if viscous dissipation was involved.

(a) *Lanchester*'s representation of the velocity field associated with lift production [87].

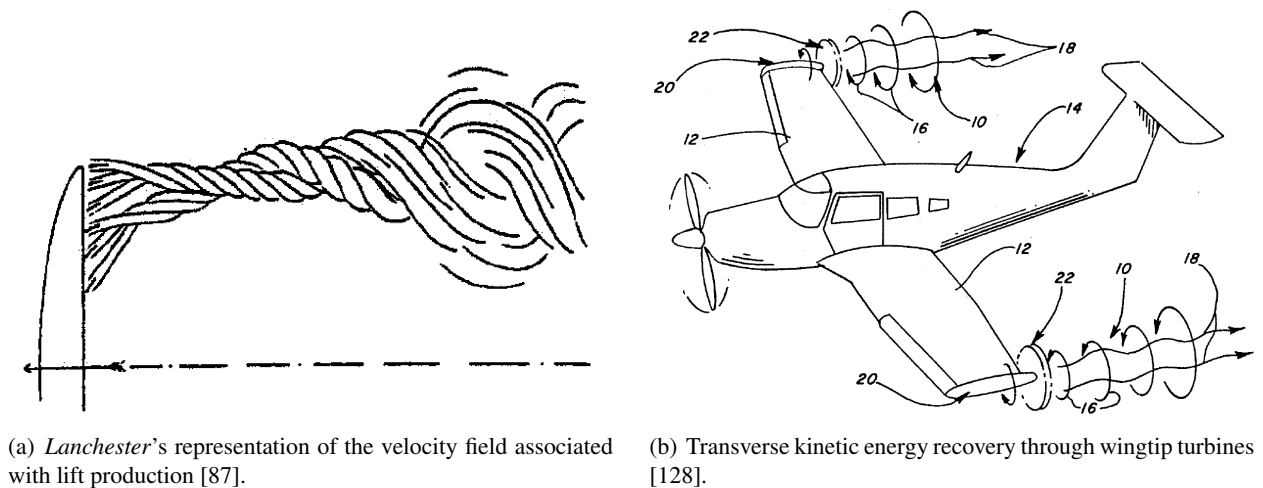(b) Transverse kinetic energy recovery through wingtip turbines [128].

Figure 2-6: Lift-induced transverse kinetic energy representation and possible recovery.

The exergy approach also offers a different flow perspective in considering the vortex formation as a

---

[8]No notable influence was observed for the lead aircraft, for which we could have expected a reduction in induced drag.

potential for work extraction. This potential could also be valued through the use of wingtip turbines which can convert the transverse kinetic energy of the vortex into power generation [122, 123, 128]. Here the benefit seems to be twofold: reduction in induced drag and generation of electrical power for aircraft systems [2, 158]. In a practical point of view, this benefit should balance the additional weight and complexity involved by the power generation systems.

↪ The work potential associated with lift-induced vortex will be evaluated for the body-wing configuration examined in section 3.5 (p. 101).

2.2.2.3 Thermal Exergy

$\dot{\mathcal{E}}_{th}$ could actually be termed *thermocompressible* exergy as it can be decomposed into a (*pure*) thermal exergy at constant volume and a thermal exergy associated with volume change. From *Gibbs* equation, Eq. (2.18), for a perfect gas ($p/\rho = RT$), one can show that entropy, and therefore anergy, is a function of two independent variables such as temperature and density:

$$\nabla \mathsf{s} = c_v \frac{\nabla T}{T} + R\rho\,\nabla \frac{1}{\rho} \tag{2.51}$$

The integration of this relation between the local state (T, ρ) and the reference conditions (T_∞, ρ_∞) yields:

$$\delta \mathsf{s}\{T, \rho\} = \delta \mathsf{s}\{T, \rho_\infty\} + \delta \mathsf{s}\{T_\infty, \rho\} := c_v\,\ln\left(\frac{T}{T_\infty}\right) + R\,\ln\left(\frac{\rho_\infty}{\rho}\right) \tag{2.52}$$

It is thus possible to isolate the anergy variation due to pure thermal processes (first term) and due to compressibility effects (second term). This decomposition can be introduced into the thermal exergy definition:

$$\dot{\mathcal{E}}_{th} = \int_{\mathcal{S}_O} \left[\rho\,\delta e + p_\infty\right] (\mathbf{V}\cdot\mathbf{n})\,\mathrm{d}\mathcal{S} - T_\infty \int_{\mathcal{S}_O} \rho\,\delta \mathsf{s}\,(\mathbf{V}\cdot\mathbf{n})\,\mathrm{d}\mathcal{S} \tag{2.53}$$

to get

$$\dot{\mathcal{E}}_{th} = \underbrace{\int_{\mathcal{S}_O} \rho\,\left[\delta e - T_\infty\,\delta \mathsf{s}\{T, \rho_\infty\}\right] (\mathbf{V}\cdot\mathbf{n})\,\mathrm{d}\mathcal{S}}_{\dot{\mathcal{E}}_{th(T)}} + \underbrace{\int_{\mathcal{S}_O} \left[p_\infty - T_\infty\,\rho\,\delta \mathsf{s}\{T_\infty, \rho\}\right] (\mathbf{V}\cdot\mathbf{n})\,\mathrm{d}\mathcal{S}}_{\dot{\mathcal{E}}_{th(\rho)}} \tag{2.54}$$

where the two terms are defined hereafter:

$\dot{\mathcal{E}}_{th(T)}$: the outflow rate of thermal exergy at constant volume

$$\dot{\mathcal{E}}_{th(T)} = \dot{\mathcal{E}}_{th}\{T, \rho_\infty\} := \int_{\mathcal{S}_O} \rho\,c_v T \left[1 - \frac{T_\infty}{T}\,\ln\left(\frac{T}{T_\infty}\right)\right] (\mathbf{V}\cdot\mathbf{n})\,\mathrm{d}\mathcal{S} \tag{2.55}$$

This is the part of thermal exergy that is proportional to c_v and thus named *thermal exergy at constant volume*. When the magnitude of δT is small compared to T_∞, we can use a second order Taylor series of $\ln(T/T_\infty) = \ln(1 + \delta T/T_\infty)$ to prove that the integrand is equal to $\rho\,c_v(T - T_\infty)^2/(2T_\infty)(\mathbf{V}\cdot\mathbf{n})$ and that the convected quantity is positive no matter if T is higher than T_∞ or not [117]. This is because a temperature lower than reference conditions can be used as a temperature sink to improve the efficiency of an ideal Carnot cycle while a temperature higher than T_∞ could be used as a source.

$\dot{\mathcal{E}}_{th(\rho)}$: the outflow rate of thermal exergy associated with volume change

$$\dot{\mathcal{E}}_{th(\rho)} = \dot{\mathcal{E}}_{th}\{T_\infty, \rho\} := \int_{\mathcal{S}_O} p_\infty \left[1 - \frac{\rho}{\rho_\infty}\,\ln\left(\frac{\rho_\infty}{\rho}\right)\right] (\mathbf{V}\cdot\mathbf{n})\,\mathrm{d}\mathcal{S} \tag{2.56}$$

The integrand can be re-written as $\rho R T_\infty [1/x + \ln(x)](\mathbf{V} \cdot \mathbf{n})$ where $x = \rho/\rho_\infty > 0$ to prove that the convected quantity is strictly positive.

The dominance of one aspect over the other one will depend on the application under study. For example, for a realistic powered aircraft flying at low speed, it is likely that the thermal exergy at constant volume part would be the largest contributor to the overall thermocompressible exergy due to high-temperature jet exhaust. For an unpowered configuration at transonic regime, the thermal exergy associated with volume change may be the largest contributor. For convenience, ***thermal*** **exergy** is kept to designate $\dot{\mathcal{E}}_{th}$.

2.2.3 Precisions on Dissipative Mechanisms

2.2.3.1 Flow Characterization from an Anergy Generation Standpoint

Predominant Anergy Generation Mechanisms.   In order to characterize the flows, it is worth introducing the three following indicators:

$$\zeta_\phi := \frac{\dot{\mathcal{A}}_\Phi}{\dot{\mathcal{A}}_{tot}} \qquad ; \qquad \zeta_{\nabla T} := \frac{\dot{\mathcal{A}}_{\nabla T}}{\dot{\mathcal{A}}_{tot}} \qquad ; \qquad \zeta_w := \frac{\dot{\mathcal{A}}_w}{\dot{\mathcal{A}}_{tot}} \tag{2.57}$$

where, $\dot{\mathcal{A}}_{tot} = \dot{\mathcal{A}}_\Phi + \dot{\mathcal{A}}_{\nabla T} + \dot{\mathcal{A}}_w$. These coefficients simply indicate the predominant dissipative mechanism in the flow under study. It is expected that the viscous anergy would be predominant at low speed, that the second coefficient grows with increasing *Mach*-numbers, and that the latter only becomes significant at transonic regimes.

Ratios of Turbulent to Total Anergy Generation.   Similarly, it is interesting to identify the influence of turbulence on the dissipative phenomena. From the *Boussinesq*'s Hypothesis, we have that:

$$\Phi_{eff} = (\bar{\bar{\tau}}_{eff} \cdot \nabla) \cdot \mathbf{V} = (\mu + \mu_t)\phi \tag{2.58}$$

where, as shown in appendix A.7 (p. 184):

$$\phi := \left[2\left(\frac{\partial u}{\partial x}\right)^2 + 2\left(\frac{\partial v}{\partial y}\right)^2 + 2\left(\frac{\partial w}{\partial z}\right)^2 + \left(\frac{\partial u}{\partial y} + \frac{\partial v}{\partial x}\right)^2 + \left(\frac{\partial u}{\partial z} + \frac{\partial w}{\partial x}\right)^2 + \left(\frac{\partial v}{\partial z} + \frac{\partial w}{\partial y}\right)^2 \right]$$
$$- \frac{2}{3}\left[\frac{\partial u}{\partial x} + \frac{\partial v}{\partial y} + \frac{\partial w}{\partial z}\right]^2 \tag{2.59}$$

and we can therefore define a laminar $\dot{\mathcal{A}}_\Phi^{lam}$ and a turbulent $\dot{\mathcal{A}}_\Phi^{turb}$ *viscous* dissipation as:

$$\dot{\mathcal{A}}_\Phi^{lam} := \int_\mathcal{V} \frac{T_\infty}{T} \mu \, \phi \, d\mathcal{V} \tag{2.60a}$$

$$\dot{\mathcal{A}}_\Phi^{turb} := \int_\mathcal{V} \frac{T_\infty}{T} \mu_t \, \phi \, d\mathcal{V} \tag{2.60b}$$

Similarly, we can introduce a laminar $\dot{\mathcal{A}}_{\nabla T}^{lam}$ and a turbulent $\dot{\mathcal{A}}_{\nabla T}^{turb}$ thermal dissipation as:

$$\dot{\mathcal{A}}_{\nabla T}^{lam} := \int_\mathcal{V} \frac{T_\infty}{T^2} \, c_p \frac{\mu}{Pr} \, (\nabla \mathbf{T})^2 \, d\mathcal{V} \tag{2.61a}$$

$$\dot{\mathcal{A}}_{\nabla T}^{turb} := \int_\mathcal{V} \frac{T_\infty}{T^2} \, c_p \frac{\mu_t}{Pr_t} \, (\nabla \mathbf{T})^2 \, d\mathcal{V} \tag{2.61b}$$

Now, to determine the influence of turbulence on these dissipative mechanisms, we introduce the two following coefficients:

$$\xi_\phi := \frac{\dot{\mathcal{A}}_\Phi^{turb}}{\dot{\mathcal{A}}_\Phi^{lam} + \dot{\mathcal{A}}_\Phi^{turb}} \qquad ; \qquad \xi_{\nabla T} := \frac{\dot{\mathcal{A}}_{\nabla T}^{turb}}{\dot{\mathcal{A}}_{\nabla T}^{lam} + \dot{\mathcal{A}}_{\nabla T}^{turb}} \tag{2.62}$$

which quantify the portion of anergy generation associated with turbulence. In laminar flows, these coefficients are simply zero.

↪ Sections 3.2.4 (p. 76) and 3.3.1 (p. 79) will provide more information about how these coefficients vary with *Reynolds* and *Mach* numbers, respectively.

2.2.3.2 Energy, Exergy and Anergy Associated with Viscous Dissipation

Relation (2.34) somehow hides the fact that the viscous dissipation is a process that represents a loss in mechanical exergy $\dot{E}_\phi$, but a gain in thermal exergy $\dot{\mathcal{E}}_\phi$ at temperature T, the net destruction of exergy being $\dot{\mathcal{A}}_\phi$:

$$\dot{\mathcal{A}}_\phi = \int_\mathcal{V} \frac{T_\infty}{T} \Phi_{eff} \, \mathrm{d}\mathcal{V} = \underbrace{\int_\mathcal{V} \Phi_{eff} \, \mathrm{d}\mathcal{V}}_{\dot{E}_\phi} - \underbrace{\int_\mathcal{V} \left(1 - \frac{T_\infty}{T}\right) \Phi_{eff} \, \mathrm{d}\mathcal{V}}_{\dot{\mathcal{E}}_\phi} \tag{2.63}$$

As expected, exergy is the portion that could be converted into mechanical work *via* an ideal *Carnot* cycle of efficiency $1 - T_\infty/T$. The thermal exergy associated with viscous dissipation is highest when the temperature at which the process takes place is highest, with reference to the ambient conditions. Equivalently, the loss (anergy generation) associated with viscous dissipation is lowest when the temperature at which it occurs is highest [31]. This statement is true for any irreversibility meaning that entropy generation at high temperature is less crucial than at lower temperature [40].

2.2.3.3 Alternative Expression of the Exergy Balance

From Eq. (2.63), it is possible to re-write the main exergy balance Eq. (2.34) as:

$$\dot{\mathcal{E}}_{prop} + \dot{\mathcal{E}}_q + \dot{\mathcal{E}}_\phi = W\dot{\Gamma} + \dot{\mathcal{E}}_m + \dot{\mathcal{E}}_{th} + \dot{E}_\phi + \dot{\mathcal{A}}_{\nabla T} + \dot{\mathcal{A}}_w \tag{2.64}$$

where $\dot{E}_\phi$ appears as a sink of mechanical exergy while $\dot{\mathcal{E}}_\phi$ represents a source of thermal exergy (thus placed left-hand side). In the light of these developments, Eq. (2.34) can be graphically represented as in Fig. 2-7 for an aircraft in equilibrium.

The transverse kinetic energy is dissipated much later than the streamwise component. Both kinetic energies dissipation provides the thermal exergy $\dot{\mathcal{E}}_\phi$ which is itself dissipated by thermal mixing. Thermal anergy $\dot{\mathcal{A}}_{\nabla T}$ is mostly associated with jet exhaust thermal exergy dissipation while viscous anergy $\dot{\mathcal{A}}_\phi$ is linked to both wake and jet exhaust dissipation. $\dot{\mathcal{A}}^* = \dot{\mathcal{E}}_m + \dot{\mathcal{E}}_{th} + \dot{\mathcal{A}}_{tot}$ is the sum of the anergy that has been generated within the control volume ($\dot{\mathcal{A}}_{tot}$) and of the outflows that are going to be dissipated, which is constant when the downstream plane is moved away from the body. For practical applications, $\dot{\mathcal{E}}_{prop}$ is expected to have several times the magnitude of $\dot{\mathcal{E}}_q$.
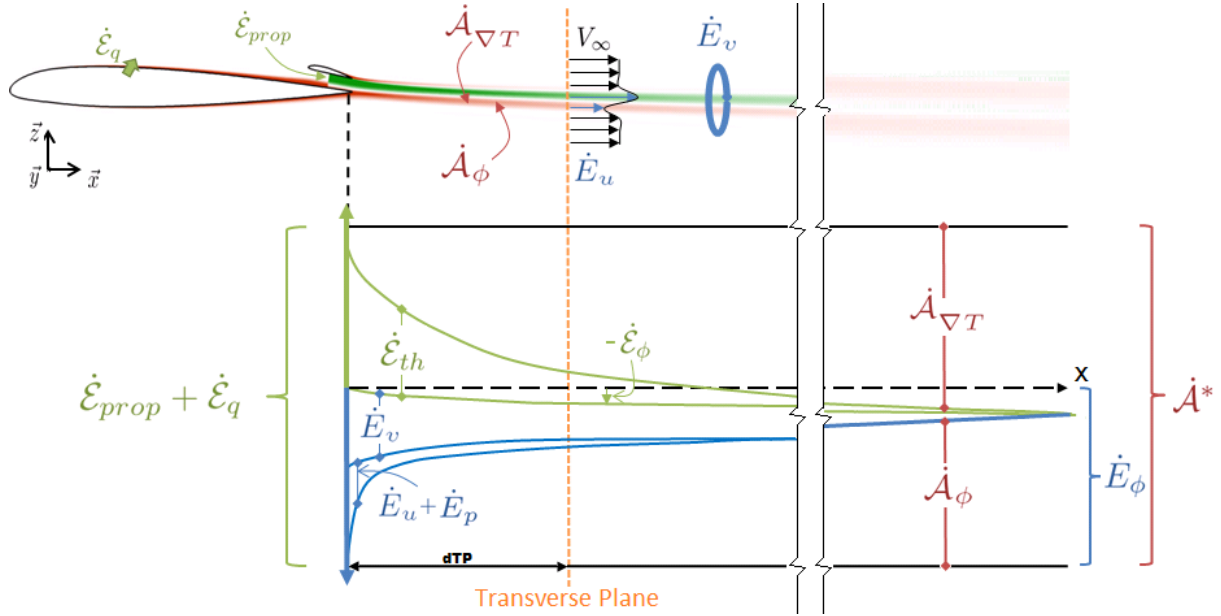
Figure 2-7: Variation in the exergy balance terms of Eq. (2.34) versus position of the downstream plane for an aircraft in mechanical equilibrium. $\dot{\mathcal{A}}_w$ is not shown.

2.2.3.4 Thermal Exergy and Mechanical Exergy Relations

For low-subsonic flow regimes, typically for $M_\infty < 0.3$, we can consider the flow incompressible. As a consequence, the mechanical and thermal aspects of the flow can be considered, to the leading order, only weakly coupled. Hence, we can isolate all terms of mechanical (resp. thermal) nature from Eq. (2.34) to form a mechanical (resp. thermal) exergy relation:

$$\dot{\mathcal{E}}_{prop,m} = W\dot{\Gamma} + \dot{\mathcal{E}}_m + \dot{E}_\phi \tag{2.65a}$$

$$\dot{\mathcal{E}}_{prop,th} + \dot{\mathcal{E}}_q + \dot{\mathcal{E}}_\phi = \dot{\mathcal{E}}_{th} + \dot{\mathcal{A}}_{\nabla T} \tag{2.65b}$$

The important point is that Eq. (2.65a) is actually equal to Eq. (37) of DRELA's formulation [49] if we consider incompressible flows, ignore unsteadiness and assume the outer boundary to reduce to a *Trefftz* plane. As expected, the exergy approach provides the capability of thermal energy management on top of mechanical energy considerations *via* Eq. (2.65b).

2.2.4 Far-field Asymptotic Considerations

It is relevant to study asymptotic developments of the various terms involved in the present formulation when the downstream surface is extended at *infinity* downstream. We use the superscript $^\infty$ to indicate the value of an integral over such a surface:

$$\dot{\mathcal{A}}^\infty := \lim_{\mathcal{S}_O \to \mathcal{S}_\infty} T_\infty \int_{\mathcal{S}_O} \rho\, \delta\mathbf{s}\, (\mathbf{V} \cdot \mathbf{n})\, \mathrm{d}\mathcal{S} \tag{2.66}$$

The terms we are interested in are those of Eq. (2.34) for the case of an adiabatic surface:

$$\dot{\mathcal{E}}_{prop} = W\dot{\Gamma} + \dot{\mathcal{E}}_m + \dot{\mathcal{E}}_{th} + \dot{\mathcal{A}}_{tot} \tag{2.67}$$

The behavior of the right-hand side terms of Eq. (2.67) will be examined keeping in mind that, as the outer boundary is moved downstream of the airplane, $W\dot{\Gamma}$ remains constant.

2.2.4.1 Thermal Exergy

In the far-field of the body, assuming the fluid locally weakly perturbed in terms of temperature and pressure, we can linearize Eq. (2.18) around ($T \simeq T_\infty$, $p \simeq p_\infty$) and neglect second order terms to get:

$$T_\infty \, \delta\mathbf{s} = \delta e + p_\infty \delta(\frac{1}{\rho}) \tag{2.68}$$

which, multiplying by the local mass flow $\rho(\mathbf{V} \cdot \mathbf{n})$ and summing over the outer boundary far downstream yields, using the mass conservation Eq. (2.5b):

$$\lim_{\mathcal{S}_O \to \mathcal{S}_\infty} T_\infty \int_{\mathcal{S}_O} \rho \, \delta\mathbf{s} \, (\mathbf{V} \cdot \mathbf{n}) \, \mathrm{d}\mathcal{S} = \lim_{\mathcal{S}_O \to \mathcal{S}_\infty} \int_{\mathcal{S}_O} \rho \, \delta e \, (\mathbf{V} \cdot \mathbf{n}) \, \mathrm{d}\mathcal{S} + \lim_{\mathcal{S}_O \to \mathcal{S}_\infty} \int_{\mathcal{S}_O} p_\infty \, (\mathbf{V} \cdot \mathbf{n}) \, \mathrm{d}\mathcal{S} \tag{2.69}$$

which can be combined with the definition of thermal exergy Eq. (2.38) to prove that the thermal exergy far downstream of the airplane is zero, $\dot{E}_{th}^\infty + \dot{E}_W^\infty - \dot{A}^\infty = \dot{\mathcal{E}}_{th}^\infty = 0$. On the contrary, the linearization of GIBBS relation is not possible when the surface of integration S_O is close to the engine exhaust jet in which case the temperature may be far from the reference conditions which precisely indicates that the thermal exergy $\dot{\mathcal{E}}_{th}$ is substantial.

An analysis based only on the First law only would conclude that there is a large amount of thermal energy available, suggesting room for improvement. However, due to thermal mixing, the temperature is getting locally closer and closer to the reference temperature T_∞ while the surface of integration is getting bigger and bigger. So that the integrated *quantity* can become large even if the local contribution is vanishingly small. As shown by a zero thermal exergy, the total thermal energy, also large, has not practical *value* as its conversion into work would involve an extremely low *Carnot* efficiency.

2.2.4.2 Aircraft Energy Height

To satisfy the Second law of thermodynamics, the outflows of mechanical exergy have to decrease towards zero, being dissipated by viscous dissipation: $\dot{\mathcal{E}}_m^\infty = 0$. Inserting these considerations into Eq. (2.67) yields:

$$\boxed{\dot{\mathcal{E}}_{prop} - \dot{A}_{tot}^\infty = W\dot{\Gamma}} \tag{2.70}$$

As a result, one can briefly consider three different cases:

a. $\dot{\mathcal{E}}_{prop} = \dot{A}_{tot}^\infty$, which means that all work potential (initially stored in the fuel) has been destroyed. $W\dot{\Gamma} = 0$: the aircraft is in mechanical equilibrium.

b. $\dot{\mathcal{E}}_{prop} > \dot{A}_{tot}^\infty$, which means that the propulsion system has provided more exergy than required for equilibrium flight. $W\dot{\Gamma} > 0$: the aircraft would gain energy height and store the exergy supplied in excess as mechanical energy.

c. $\dot{\mathcal{E}}_{prop} < \dot{A}_{tot}^\infty$, which means that the exergy supplied by the propulsion system is not able to balance the total exergy destruction involved. $W\dot{\Gamma} < 0$: the aircraft would lose energy height[9] and become a power source in descent [49].

In agreement with [133, 144], the aircraft acts as an accumulator of mechanical energy that is released during descent. The exergy of the system tends to zero and therefore the entire system tends to thermodynamic equilibrium, *i.e.* thermal and mechanical equilibriums. Locally, the temperature, pressure and velocity tend towards their reference values, the system gets in equilibrium with its surroundings.

---

[9]For example, a glider, without propulsion, will have to take advantage from the wind to increase its energy height [113].

2.3   Restriction to Aerodynamic Performance of Unpowered Airframe Configurations

Although the formulation is primarily developed for powered configurations, its restriction to unpowered airframe cases is presented along with the description of the flow from an exergy standpoint. Then, connections are made to some well-known far-field drag expressions to demonstrate that their underlying theory can be related to exergy considerations.

2.3.1   Restricted Exergy Balance for Aerodynamic Performance Assessment

In the absence of propulsion systems, $\dot{\mathcal{E}}_{prop}$ = 0, and, considering adiabatic surfaces, we have $\dot{\mathcal{E}}_q$ = 0. As no thrust is being generated, from Eq. (A.5) in appendix A.2, we get $W\dot{\Gamma} = -DV_\infty$, which means that Eq. (2.34) simply reads:

$$\boxed{DV_\infty = \dot{\mathcal{E}}_m + \dot{\mathcal{E}}_{th} + \dot{\mathcal{A}}_\phi + \dot{\mathcal{A}}_{\nabla T} + \dot{\mathcal{A}}_w} \tag{2.71}$$

which can be considered as an extension to transonic flows of the exergy-based approach to incompressible flows of Li *et al.* [94, 107], see Eq. (1.18) (p. 23).

2.3.1.1   Flow Description from an Exergy Standpoint

Physically speaking, if we consider a fixed body with an incoming flow as in wind tunnel testing, the following exergy-based interpretation can be suggested. The incoming flow has a certain exergy due to its velocity with reference to the fixed body reference frame. As the flow passes in the vicinity of the obstacle, boundary layers develop and slow the fluid down. This reduction in kinetic energy means that a portion of the exergy of the flow is destroyed. The total enthalpy massflow across the outer boundary is zero [64], meaning that the total energy is effectively conserved. However, there has been a change in forms: viscous dissipation has converted kinetic energy into thermal energy at temperature T whose field is then made uniform by thermal mixing.

2.3.1.2   Connection to the *Power Balance*

In order to connect the present exergy formulation to the *Power Balance* [49], one must first derive an alternative expression for the thermal exergy. This is achieved by simply inserting the internal energy relation (2.19) into the thermal exergy outflow definition Eq. (2.38) and by invoking the divergence theorem to get:

$$\dot{\mathcal{E}}_{th} = \dot{\mathcal{E}}_\phi - \dot{\mathcal{A}}_{\nabla T} + \underbrace{\int_{\mathcal{V}} (p_\infty - p) \, \nabla \cdot \mathbf{V} \, d\mathcal{V}}_{\dot{E}_{PV}} \tag{2.72}$$

The viscous dissipation is a source of thermal exergy resulting from the conversion of kinetic energy into thermal energy while the thermal anergy destroys this work potential. The last term $\dot{E}_{PV}$ being associated with compressibility, the duality of what is named thermal exergy is highlighted once again.

Inserting Eq. (2.72) into Eq. (2.71), one gets that, except for the shock wave which is slightly different, Eq. (2.71) is equal to the restriction to unpowered configurations of the mechanical energy balance proposed by DRELA if we consider subsonic and steady mean flows:

$$DV_\infty = \dot{E}_u + \dot{E}_v + \dot{E}_p + \dot{E}_\phi + \dot{E}_{PV} + \dot{\mathcal{A}}_w \tag{2.73}$$

which is precisely equal to Eq. (1.11) when noting that $\dot{E}_{PV} = -P_V$.

As regards nearby-strong shock waves, the precise relation between the two coefficients is derived in appendix A.6 (p. 183).

↪ The *indirect* method of calculating the thermal exergy of Eq. (2.72) is compared to the *direct* method of Eq. (2.38) in section 3.2 (p. 67). It will be shown that the direct method exhibits a behavior in better agreement with Second Law considerations.

2.3.2 Connection to Momentum-based Far-field Drag Approaches

In 1925, BETZ proposed to evaluate the impact on the flow of the body *via* Eq. (2.9b) with a focus on experimental wake survey [28] which led to a great variety of *far-field* drag expressions since then. As a consequence, the present section does not pretend to be an extensive review of all available expressions but rather aims at making connections between the proposed exergy-based relation (2.71) and some of the most popular/recent formulations.

2.3.2.1 Wake-integral Formulations

In 1999, VAN DAM gave a review of existing methodologies with a focus on computational fluid dynamics experiences [173]. Building on the original work of many contributors, it was first assumed that the viscous stresses can be dropped from Eq. (2.9b) and variations of total enthalpy neglected. Then, introducing the Gibbs equation and neglecting small interaction drag as well as density fluctuations, the following popular drag expression was proposed:

$$D = \int_{TP} p_\infty \frac{\delta \mathsf{s}}{R}\, \mathrm{d}\mathcal{S} + \int_{TP} \frac{1}{2} \rho_\infty (\psi \xi)\, \mathrm{d}\mathcal{S} \tag{2.74}$$

where ψ and ξ are respectively the crossflow stream function and the streamwise or trailing vorticity. This expression was proposed by VAN DER VOOREN and SLOOFF [175] who also suggested the use of Eq. (2.23) to distinguish between boundary layer drag and wave drag. According to GILES and CUMMINGS [64], this equation can equivalently be written as follows:

$$D = \int_{TP} p_\infty \frac{\delta \mathsf{s}}{R}\, \mathrm{d}\mathcal{S} + \int_{TP} \frac{1}{2} \rho_\infty (v^2 + w^2)\, \mathrm{d}\mathcal{S} \tag{2.75}$$

As the vortex drag term decreases, there is a corresponding increase in the entropy term, because the total drag must remain constant. Note however that application of this expression is actually tricky for numerical flows because, due to numerical dissipation, the accurate computation of the kinetic energy term can only be achieved close to the body [46, 64] so that the downstream plane should be located nearby the solid. This may violate the assumptions made for the derivation, mainly that density and axial velocity fluctuations may not be negligible. As a consequence, whatever the location of the downstream plane, there is an inherent imprecision in applying Eq. (2.75) for numerical far-field drag prediction.

This approach, which still forms the underlying theory of many current formulations for the far-field drag prediction and decomposition [39, 64, 121, 170, 173, 175], can actually be considered as a simplification of the exergy-based relation (2.71). This statement is proved by multiplying Eq. (2.75) by the freestream velocity V_∞ and by replacing p_∞ by $\rho_\infty R T_\infty$ to get:

$$DV_\infty = T_\infty \int_{TP} \rho_\infty\, \delta \mathsf{s}\, V_\infty\, \mathrm{d}\mathcal{S} + \int_{TP} \frac{1}{2} \rho_\infty (v^2 + w^2) V_\infty\, \mathrm{d}\mathcal{S} \tag{2.76}$$

If we consider the outer boundary $\mathcal{S}_O$ to reduce to a *Trefftz* plane, on which $(\mathbf{V} \cdot \mathbf{n})\, \mathrm{d}\mathcal{S} = (V_\infty + u)\, \mathrm{d}\mathcal{S} \simeq$

$V_\infty \, \mathrm{d}\mathcal{S}$, Eq. (2.71) reduces to relation (2.76) if $\rho \simeq \rho_\infty$ and if $\dot{E}_u$, $\dot{E}_p$, and $\dot{\mathcal{E}}_{th}$ are neglected. In comparison, the derivation of relation (2.71) has not required any assumption[10] about the flow, and, as a consequence, is expected to have a greater level of accuracy.

2.3.2.2   Oswatitsch

In 1956, OSWATITSCH came to a result generally referred to as *entropy drag* [118]. Choosing the control surface in the far field of the body, he neglected second order terms in the drag expression Eq. (2.9b) and showed that:

$$DV_\infty = \lim_{\mathcal{S}_O \to \mathcal{S}_\infty} \int_{\mathcal{S}_O} \rho \left(T_\infty \, \delta \mathbf{s} - \delta h_i \right) \left(\mathbf{V} \cdot \mathbf{n} \right) \mathrm{d}\mathcal{S} \tag{2.77}$$

which he further simplified by neglecting the change in total enthalpy:

$$DV_\infty = \lim_{\mathcal{S}_O \to \mathcal{S}_\infty} T_\infty \int_{\mathcal{S}_O} \rho \, \delta \mathbf{s} \left(\mathbf{V} \cdot \mathbf{n} \right) \mathrm{d}\mathcal{S} \tag{2.78}$$

This last equation is well-known by drag prediction specialists as being capable of determining the rate of work of *total drag* experienced by a body that does not exchange energy (neither mechanical nor thermal) with the flowing fluid. The outer boundary of the control volume must *enclose all entropy changes caused by the body in the flow field* that *in some cases extend far away from the body, for example, those caused by the decay of the vortex sheet behind a wing*. As the integral converges towards its final value, the overall impact of the body on the flow is considered and from an energy standpoint, this illustrates the fact that the system tends towards a thermodynamic equilibrium, which is characterized by a maximum entropy.

The aerodynamic conditions of OSWATITSCH development[11] are similar to those assumed for the asymptotic considerations introduced in paragraph 2.2.4 so that the same result is to be found: Eq. (2.70) precisely reduces to Eq. (2.78). OSWATITSCH's formulation is an asymptotic development which makes it rather difficult to apply to realistic CFD applications due to constraints on mesh extent. In comparison, Eq. (2.71) has the advantage of being valid close to the body under study.

Noteworthy, OSWATITSCH additionally made the connection to a *theorem of thermodynamics according to which the decrease of the useful work of a heat engine (as compared with the theoretical efficiency) is equal to the entropy increase of the total system multiplied by the ambient temperature*: the GOUY-STODOLA Theorem [24]. As a consequence, and by virtue of Eq. (2.77), OSWATITSCH can be considered as having provided the first exergy-based formulation for the prediction of airframe aerodynamic performance [133, 134, 135].

2.4   Discussion on the Formulation

A discussion on the relevance of the formulation is given by first introducing some figures of merit to assess the performance of an aircraft. Then, connections to existing work are provided to emphasize the originality of the proposed exergy balance.

---

[10]Besides neglecting the viscous stresses and the heat flux on the outer boundary.

[11]It is shown in appendix A.8 (p. 185) that if we do not assume small perturbations in terms of velocity, then the three mechanical outflows $\dot{E}_u$, $\dot{E}_v$ and $\dot{E}_p$ are present in OSWATITSCH formulation.

2.4.1 Aerospace Vehicle Design Considerations

2.4.1.1 Figures of Merit

In considering that any perturbation of the flow represents a potential for improvement, the exergy/anergy framework suggests the introduction of a few Figures of Merit (FoM) to quantity the performance of a given architecture.

Exergy-Waste Coefficient.   The most general exergy balance reads, in compact form:

$$\dot{\mathcal{E}}_{prop} + \dot{\mathcal{E}}_q = W\dot{\Gamma} + \dot{\mathcal{E}}_m + \dot{\mathcal{E}}_{th} + \dot{\mathcal{A}}_{tot} \tag{2.79}$$

In the *ideal* steady cruise phase, the propulsion system supplies as much exergy as destroyed by all dissipative phenomena over its surface, *i.e.* within the boundary layers[12]:

$$\dot{\mathcal{E}}_{prop}^{\,ideal\ cruise} = \dot{\mathcal{A}}_{tot}^{BL} \tag{2.80}$$

However, this is not observed in practice because the body has generated (mechanical and thermal) perturbations that have not yet been dissipated. These additional perturbations are gradually dissipated over time in the wake of the body. This process is asymptotic and can converge slowly as in the case of lift-induced vortex dissipation. These deviations from the reference state represents a potential for work extraction and it has been shown in the previous paragraphs that the exergy analysis enables to track and estimate their work potential. In any flow field, the *recoverable exergy* is made up of mechanical and thermal exergy:

$$\text{Recoverable Exergy} = \dot{\mathcal{E}}_{rec} := \dot{\mathcal{E}}_m + \dot{\mathcal{E}}_{th} \tag{2.81}$$

It is of much interest to express this quantity relative to the total anergy that is going to be produced. This can be achieved by the following Exergy-Waste Coefficient:

$$\boxed{\text{Exergy-Waste Coefficient}_{distance} = EWC_d := \frac{\dot{\mathcal{E}}_{rec}}{\dot{\mathcal{A}}_{tot} + \dot{\mathcal{E}}_{rec}}} \tag{2.82}$$

This figure of merit quantifies how much exergy is flowing out of the control volume relative to the total anergy that is to be generated[13]. The difficulty lies in the definition of the *recoverable exergy* because the exergy potential is destroyed downstream of the configuration, see Fig. 2-7 (p. 46). As a consequence, EWC depends on *where* that potential is evaluated and this information should be clearly stated to avoid any misunderstanding. For a powered configuration at equilibrium, from Eq. (2.79), EWC is equivalent to:

$$EWC_{powered}^{\ eq} = \frac{\dot{\mathcal{E}}_{rec}}{\dot{\mathcal{E}}_{prop}}\bigg|_{F_x=0} = \frac{Recoverable\ Exergy}{Propulsive\ Exergy} \tag{2.83}$$

while for an airframe configuration without exergy supply, from Eq. (2.71), EWC is equivalent to:

$$EWC_{airframe} = \frac{\dot{\mathcal{E}}_{rec}}{DV_\infty} = \frac{Recoverable\ Exergy}{Total\ Anergy} \tag{2.84}$$

It yields an absolute figure of merit for quantifying the degree of perfection of any aircraft and gives an indication of how inefficient is the configuration: high values indicate high potential for improvement.

---

[12]If this goal is achieved, the next design step would be to reduce the viscous and thermal dissipation within the boundary layers.
[13]We do not account for the possible change in aircraft mechanical energy $W\dot{\Gamma}$ which is not considered as a loss.

Now let us consider a concept that can recover the exergy wasted in the jet/wake of a given configuration. One such concepts is the wake-ingestion examined in section 4.3 (p. 133). In this case, two additional figures of merit are worth introducing to asses the efficiency of the recovery.

Exergy-Recovery Coefficient.   Having specified the recoverable exergy and the effective exergy saving, it is possible to quantify how efficient was the recovery of the initial potential $\dot{\mathcal{E}}_{rec}^{REF}$ through an exergy-recovery coefficient:

$$ERC := \frac{\dot{\mathcal{E}}_{prop}^{REF} - \dot{\mathcal{E}}_{prop}^{BLI}}{\dot{\mathcal{E}}_{rec}^{REF}} = \frac{Exergy\ Saving}{Recoverable\ Exergy} \tag{2.85}$$

High values indicate an efficient BLI arrangement to recover the available exergy. It will be shown in paragraph 4.3.2.4 (p. 140) that the difference can be attributed to two distinct mechanisms: destruction by interactions between the two bodies and simple loss due to a modification of the initial flow field.

Exergy-Saving Coefficient.   Finally, to quantify the benefit of ingesting the wake, it is worth comparing the exergy saving from the initial supply. The adapted figure is therefore the exergy-saving coefficient:

$$ESC := \frac{\dot{\mathcal{E}}_{prop}^{REF} - \dot{\mathcal{E}}_{prop}^{BLI}}{\dot{\mathcal{E}}_{prop}^{REF}} = \frac{Exergy\ Saving}{Reference\ Propulsive\ Exergy} \tag{2.86}$$

This is the most important FoM as it directly indicates how much exergy can be saved. First, by virtue of Eq. (2.79), it is independent on where it is calculated as opposed to the more traditional Power Saving Coefficient[14] (PSC). Secondly, it takes into account the pressure field interactions. This FoM tells us how much the reference configuration was improved but it does not provide information as to how much the reference configuration *could have been* improved.

To conclude, the ESC can be expressed with the two other figures of merit as:

$$ESC = ERC \times EWC \tag{2.87}$$

suggesting that a large fuel saving requires a good recovery of a high initial improvement potential.

↪ Section 4.3 (p. 133) will provide more information about how the wake ingestion can recover some of the recoverable exergy present in the wake of a simplified fuselage.

2.4.1.2   Exergy-based Range Equation

Although the absence of thrust and drag could appear somewhat puzzling in a design perspective, the knowledge of these two forces is not mandatory for estimating basic performance of the configuration under study. For example, as for the *Power Balance* method [67], an exergy-based range equation can be introduced, see appendix A.4 (p. 181):

$$\mathcal{R}_\varepsilon = \frac{1}{ESFC} \left(\frac{CL}{C\dot{\mathcal{A}}_{tot} + C\dot{\mathcal{E}}_m + C\dot{\mathcal{E}}_{th}} \right) \ln\left(\frac{W_0}{W_1} \right) \tag{2.88}$$

where, for propulsion, $ESFC := \dot{W}_f / \dot{\mathcal{E}}_{prop}$ is the exergy specific fuel consumption ($\dot{W}_f$ is the time rate of weight of fuel burnt). For aerodynamics, CL is the (traditional) lift coefficient and for structures, it is the (usual) ratio of the initial W_0 to final weight W_1. As expected, reducing the specific exergy consumption as well as all exergy outflow and destruction would improve the performance of the vehicle.

---

[14]The so-called Power-Saving Coefficient [152] (PSC) is the most commonly accepted FoM to investigate boundary layer ingestion [58] $PSC := (P_{REF} - P_{BLI})/P_{REF}$ with $P := \dot{m}\left(V_{jet}^2 - V_\infty^2\right)$ where P represents the (mechanical) propulsive power. The PSC only takes into account the kinetic energy supplied to the flow to generate thrust and assumes the pressure potential field to be negligible. Another drawback of the PSC is that it is likely to be dependent on *where* the kinetic energy is evaluated.

2.4.1.3 Relation between Drag Coefficient and Power Coefficient

To obtain non-dimensionalized parameters to compare different configurations, in a direct analogy to traditional drag coefficient, all power terms of relation (2.34) can be non-dimensionalized by the power of the freestream dynamic pressure-force in order to express *power coefficients*. For example, for the viscous anergy:

$$CD = \frac{D}{\frac{1}{2}\rho_\infty V_\infty^2 A_{ref}} \qquad ; \qquad C\dot{\mathcal{A}}_\Phi = \frac{\dot{\mathcal{A}}_\Phi}{\frac{1}{2}\rho_\infty V_\infty^3 A_{ref}} \tag{2.89}$$

The magnitude of these power coefficients is directly comparable to the traditional drag coefficients.

2.4.2 Original Contributions and Connections to Existing Work

The present formulation is a continuation of the various recent efforts mentioned in the introduction, especially those of RIGGINS *et al.* [133, 134, 135] focusing on hypersonic vehicles with simplified model examples. On the contrary, the focal point of the present formulation is commercial aircraft flying at subsonic to transonic regimes with an emphasis on high-fidelity CFD applications. Also, the present formulation provides a richer phenomenological decomposition of the outflows which is analogous, for the mechanical part, to the one proposed by DRELA [49]. The exergy balance shares the main features of this mechanical analysis described in paragraph 1.1.4 (p. 14): a clear identification of the flow phenomena that directly influence flight power requirements and a high reliability of the loss definition for interference effects.

Compared to the mechanical energy balance, the formulation proposed here has the advantage of being a component of a larger and well-founded vehicle design philosophy based on exergy management [110, 140, 142] for tracking and estimating any potentially recoverable waste and linked to thermoeconomic considerations [19, 144]. Additional benefit comes from the thermal management capability which could be applied, for example, to efficiently integrate heat exchangers on aircraft, as investigated in section 4.5 (p. 160).

Using the present formulation, a wide variety of highly integrated propulsion devices can be evaluated and efficiency characterization can be achieved with thermal energy considerations and for under-/over-expanded nozzles. In the case of more traditional propulsion systems integration, the propulsive exergy term can be decomposed to express the propulsive thrust power and therefore the approach proposed here could fit conventional drag/thrust bookkeepings [42, 53]. Also, greater insight into jet engine performance could be achieved through the use of dedicated figures of merit such as gas horsepower or thrust work potential [131, 141].

For unpowered configurations, although not the main focus of the present work, the restricted formulation is well-founded and can be considered as an extension to transonic flows of existing drag formulation based on exergy considerations [94, 107]. Additionally, its derivation requires less assumptions about the flow than for many drag prediction formulations based on momentum analysis [39, 64, 121, 170, 173].

Finally, having a single formulation for both engine/airframe integration and aircraft thermal management to provides a rational and consistent framework for the design of advanced architectures. To the author's knowledge, no formulation that combines all these various aspects for high-fidelity RANS computations post-processing is currently available to the aerospace community. It represents a first-of-a-kind exergy-based formulation for aero-thermo-propulsive performance assessment of transonic commercial aircraft.

2.5 Numerical Implementation of the Formulation

The theoretical formulation has been numerically implemented in an existing Fortran code. First, adaptation of the theoretical exergy balance to the numerical constrains is given. Then, the general characteristics of the post-processing code are given.

2.5.1 Numerical Adaptation of the Theoretical Formulation

2.5.1.1 Shock Wave Treatment

On the Shock Surface. In the theoretical formulation, nearby strong shocks have been treated in agreement with normal shock theory, *i.e.* as an adiabatic and inviscid *discontinuity* with the corresponding surface $\widetilde{\mathcal{S}}_w$ considered being of negligible width. Numerically speaking however, with finite-volume computations, the whole computational domain is continuous and discontinuities do no exist. This would involve two different values of, say, pressure at a given node. As a consequence, the surface $\mathcal{S}_w$ enclosing any transonic shock wave is delimiting a finite-size volume $\mathcal{V}_w$, see Fig. 2-8.

(a) Numerical shock surface with normal **n**.

(b) Numerical shock surface with normal $\hat{\mathbf{n}}$.
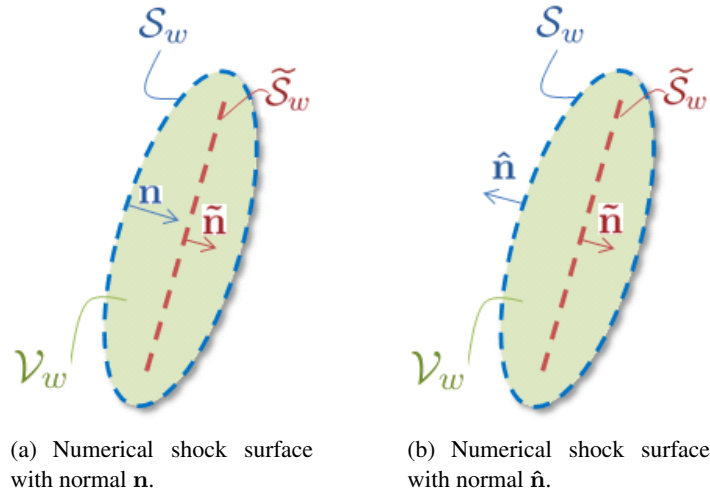
Figure 2-8: Numerical treatment of the theoretically discontinuous shock waves.

The following equivalence is therefore obtained:

$$T_\infty \int_{\mathcal{V}_w} \nabla \cdot (\rho\, \delta\mathsf{s}\, \mathbf{V})\, \mathrm{d}\mathcal{V} \equiv T_\infty \int_{\mathcal{S}_w} \rho\, \delta\mathsf{s}\, (\mathbf{V} \cdot \hat{\mathbf{n}})\, \mathrm{d}\mathcal{S} - T_\infty \int_{\widetilde{\mathcal{S}}_w} [\![\rho\, \delta\mathsf{s}\, \mathbf{V}]\!] \cdot \tilde{\mathbf{n}}\, \mathrm{d}\mathcal{S} \tag{2.90}$$

which we can rearrange to isolate the wave anergy

$$\dot{\mathcal{A}}_w := T_\infty \int_{\widetilde{\mathcal{S}}_w} [\![\rho\, \delta\mathsf{s}\, \mathbf{V}]\!] \cdot \tilde{\mathbf{n}}\, \mathrm{d}\mathcal{S} \equiv T_\infty \int_{\mathcal{S}_w} \rho\, \delta\mathsf{s}\, (\mathbf{V} \cdot \hat{\mathbf{n}})\, \mathrm{d}\mathcal{S} - T_\infty \int_{\mathcal{V}_w} \nabla \cdot (\rho\, \delta\mathsf{s}\, \mathbf{V})\, \mathrm{d}\mathcal{V} \tag{2.91}$$

and decompose the second right-hand side term as in Eq. (2.22) to get:

$$\begin{aligned}
\dot{\mathcal{A}}_w \equiv T_\infty \int_{\mathcal{S}_w} \rho\, \delta\mathsf{s}\, (\mathbf{V} \cdot \hat{\mathbf{n}})\, \mathrm{d}\mathcal{S} &- \int_{\mathcal{V}_w} \frac{T_\infty}{T} \Phi_{eff}\, \mathrm{d}\mathcal{V} - \int_{\mathcal{V}_w} \frac{T_\infty}{T^2} k_{eff}\, (\nabla \mathbf{T})^2\, \mathrm{d}\mathcal{V} \\
&+ \int_{\mathcal{S}_w} \frac{T_\infty}{T}\, (\mathbf{q}_{eff} \cdot \hat{\mathbf{n}})\, \mathrm{d}\mathcal{S}
\end{aligned} \tag{2.92}$$

Ideally, all three last terms are zero. But it is possible that this surface encloses some entropy that is not associated with the shock wave phenomenon. Eq. (2.92) ensures that no phenomenon is numerically accounted twice. In the case of overlap, priority is given to the viscous and thermal anergy generation: their

contribution in the wave volume is removed from $\dot{\mathcal{A}}_w$ and added to the viscous and thermal anergy:

$$\dot{\mathcal{A}}_\phi = \int_{\mathcal{V}} \frac{T_\infty}{T} \Phi_{eff} \, \mathrm{d}\mathcal{V} + \int_{\mathcal{V}_w} \frac{T_\infty}{T} \Phi_{eff} \, \mathrm{d}\mathcal{V} \tag{2.93}$$

$$\dot{\mathcal{A}}_{\nabla T} = \int_{\mathcal{V}} \frac{T_\infty}{T^2} k_{eff} \left(\nabla \mathbf{T}\right)^2 \mathrm{d}\mathcal{V} + \int_{\mathcal{V}_w} \frac{T_\infty}{T^2} k_{eff} \left(\nabla \mathbf{T}\right)^2 \mathrm{d}\mathcal{V} \tag{2.94}$$

As shown in the following applications, the shock surface is usually determined with sufficient care that such overlaps do not happen: the contribution of the viscous and thermal anergy integrated within the wave volume generally accounts for less than 0.01 pc.

Neglected Terms.   Similarly, for the total enthalpy, we have:

$$\int_{\mathcal{S}_w} \rho \, \delta h_i \left(\mathbf{V} \cdot \hat{\mathbf{n}}\right) \mathrm{d}\mathcal{S} = \int_{\mathcal{V}_w} \nabla \cdot \left(\rho \, \delta h_i \, \mathbf{V}\right) \mathrm{d}\mathcal{V} - \cancel{\int_{\widetilde{\mathcal{S}}_w} [\![\rho \, \delta h_i \, \mathbf{V}]\!] \cdot \hat{\mathbf{n}} \, \mathrm{d}\mathcal{S}} \tag{2.95}$$

Application of the First law of thermodynamics to the fluid contained within the finite-size wave volume $\mathcal{V}_w$ provides an alternative expression for the right-hand side term

$$\int_{\mathcal{V}_w} \nabla \cdot \left(\rho \, \delta h_i \, \mathbf{V}\right) \mathrm{d}\mathcal{V} = - \int_{\mathcal{S}_w} \left(\bar{\bar{\tau}}_{eff} \cdot \mathbf{V}\right) \cdot \hat{\mathbf{n}} \, \mathrm{d}\mathcal{S} + \int_{\mathcal{S}_w} \left(\mathbf{q}_{eff} \cdot \hat{\mathbf{n}}\right) \mathrm{d}\mathcal{S} \tag{2.96}$$

which, introduced in Eq. (2.95), yields

$$\underbrace{\int_{\mathcal{S}_w} \rho \, \delta h_i \left(\mathbf{V} \cdot \hat{\mathbf{n}}\right) \mathrm{d}\mathcal{S}}_{\dot{\mathcal{H}}'_w} + \underbrace{\int_{\mathcal{S}_w} \left(\bar{\bar{\tau}}_{eff} \cdot \mathbf{V}\right) \cdot \hat{\mathbf{n}} \, \mathrm{d}\mathcal{S}}_{\tau'_w} + \underbrace{\int_{\mathcal{S}_w} -\left(\mathbf{q}_{eff} \cdot \hat{\mathbf{n}}\right) \mathrm{d}\mathcal{S}}_{\dot{E}'_{qw}} = 0 \tag{2.97}$$

The satisfaction of this equation $\dot{\mathcal{H}}'_w + \tau'_w + \dot{E}'_{qw} = 0$ will be used as a criterion for the correct definition of the shock surface $\mathcal{S}_w$.

↪ The numerical treatment of shock waves is introduced in for a 2D Airfoil in section 3.3 (p. 79) and consolidated for transonic flows over a 3D wing for various turbulence models in section 3.4 (p. 91).

2.5.1.2   Correction for Numerical Accuracy

As highlighted in the following chapter, Eq. (2.23) may not be numerically satisfied leading to a discrepancy in the anergy:

$$\Delta \dot{\mathcal{A}} := \dot{\mathcal{A}} - \left(\dot{\mathcal{A}}_\phi + \dot{\mathcal{A}}_{\nabla T} + \dot{\mathcal{A}}_w + \dot{\mathcal{A}}_{qO}\right) \tag{2.98}$$

The main identified reason is that the grid may be too coarse to enable an accurate computation of the velocity and temperature gradients. As the viscous ($\dot{\mathcal{A}}_\phi$) and thermal anergy ($\dot{\mathcal{A}}_{\nabla T}$) are functions of the square of these quantities, these two terms may be underestimated. They can be *corrected* by evaluating $\Delta \dot{\mathcal{A}}$ in the wake of the body in order to compensate the viscous and thermal anergy by that amount. The split of this quantity between the viscous anergy and the thermal anergy is made as follows:

$$\dot{\mathcal{A}}_\Phi^c := \dot{\mathcal{A}}_\Phi + \zeta_\phi^{wake} \times \Delta \dot{\mathcal{A}} \tag{2.99a}$$

$$\dot{\mathcal{A}}_{\nabla T}^c := \dot{\mathcal{A}}_{\nabla T} + \left[1 - \zeta_\phi^{wake}\right] \times \Delta \dot{\mathcal{A}} \tag{2.99b}$$

where ζ_ϕ^{wake} represents the proportion of viscous anergy generated in the wake. The determination of this coefficient is made by evaluating the ratio of viscous anergy to the total anergy generated within the

boundary layers ζ_ϕ^{BL}. This ratio is higher in the boundary layers than in the wake since the thermal gradients are higher in the boundary layers than in the wake. As a consequence, the following rule of thumb is used for the correction:

$$\zeta_\phi^{wake} := \kappa \; \zeta_\phi^{BL} \qquad\qquad \text{with } \kappa \geq 1 \qquad\qquad (2.100)$$

In the following test cases, κ is taken as a constant, but should actually range from 1 at the trailing edge of a wing and rapidly asymptote to provide $\zeta_\phi^{wake} \approx 1$ within a few body lengths.

This correction ensures the consistency of the exergy analysis with the flow solution. But because the total anergy outflow $\dot{\mathcal{A}}$ is also subjected to spurious variations, this method does not discriminate between the spurious (numerical) anergy and the physical anergy. As a consequence, an accuracy *only* equivalent to the near-field approach for drag prediction is expected.
Note that the correction heavily relies on the accurate definition and calculation of the wave anergy $\dot{\mathcal{A}}_w$.

$\hookrightarrow$ The correction is calibrated for transonic flows over a 2D Airfoil in section 3.3 (p. 79) and over a 3D wing for various turbulence models in section 3.4 (p. 91).

2.5.1.3 Domain of Validity of the Numerically-adapted Exergy Balance

The exergy balance (2.34) is a theoretical formulation applicable to transonic viscous and mean steady flows with energy supply from a propulsion system and *via* heat transfer at the surface of the aircraft. However, to make it more pertinent, a few assumptions have been made. Also, this equation does not take into account the adaptation required for the adequate treatment of the shock waves and for the correction necessary for accurate viscous and thermal anergy calculation. The numerically-adapted formulation used for the performance assessment of all following aerospace applications is:

$$\int_{\mathcal{S}_A} \rho \, \delta h_i \, (\mathbf{V} \cdot \hat{\mathbf{n}}) \, \mathrm{d}\mathcal{S} - T_\infty \int_{\mathcal{S}_A} \rho \, \delta \mathsf{s} \, (\mathbf{V} \cdot \hat{\mathbf{n}}) \, \mathrm{d}\mathcal{S} - \int_{\mathcal{S}_A} (\bar{\bar{\tau}}_{eff} \cdot \mathbf{V}) \cdot \hat{\mathbf{n}} \, \mathrm{d}\mathcal{S} + \int_{\mathcal{S}_A} \left(1 - \frac{T_\infty}{T}\right) (\mathbf{q}_{eff} \cdot \hat{\mathbf{n}}) \, \mathrm{d}\mathcal{S}$$

$$= W\dot{\Gamma} - \int_{\mathcal{S}_O} (\bar{\bar{\tau}}_{eff} \cdot \mathbf{V}) \cdot \mathbf{n} \, \mathrm{d}\mathcal{S} + \int_{\mathcal{S}_O} (\mathbf{q}_{eff} \cdot \mathbf{n}) \, \mathrm{d}\mathcal{S}$$

$$- \int_{\mathcal{S}_O} \frac{T_\infty}{T} (\mathbf{q}_{eff} \cdot \mathbf{n}) \, \mathrm{d}\mathcal{S} + T_\infty \int_{\mathcal{V}} \frac{T_\infty}{T} \Phi_{eff} \, \mathrm{d}\mathcal{V} + T_\infty \int_{\mathcal{V}} \frac{T_\infty}{T^2} k_{eff} \, (\nabla \mathbf{T})^2 \, \mathrm{d}\mathcal{V}$$

$$+ \int_{\mathcal{S}_O} \rho \, \delta e \, (\mathbf{V} \cdot \mathbf{n}) \, \mathrm{d}\mathcal{S} + \int_{\mathcal{S}_O} p_\infty (\mathbf{V} \cdot \mathbf{n}) \, \mathrm{d}\mathcal{S} - T_\infty \int_{\mathcal{S}_O} \rho \, \delta \mathsf{s} \, (\mathbf{V} \cdot \mathbf{n}) \, \mathrm{d}\mathcal{S}$$

$$+ \int_{\mathcal{S}_O} (p - p_\infty) \left[(\mathbf{V} - \mathbf{V}_\infty) \cdot \mathbf{n}\right] \mathrm{d}\mathcal{S} + \int_{\mathcal{S}_O} (\bar{\bar{\tau}}_{eff} \cdot \mathbf{V}_\infty) \cdot \mathbf{n} \, \mathrm{d}\mathcal{S}$$

$$+ \int_{\mathcal{S}_O} \frac{1}{2}\rho(u^2 + v^2 + w^2)(\mathbf{V} \cdot \mathbf{n}) \, \mathrm{d}\mathcal{S}$$

$$- \int_{\mathcal{S}_w} \rho \, \delta h_i \, (\mathbf{V} \cdot \hat{\mathbf{n}}) \, \mathrm{d}\mathcal{S} + T_\infty \int_{\mathcal{S}_w} \rho \, \delta \mathsf{s} \, (\mathbf{V} \cdot \hat{\mathbf{n}}) \, \mathrm{d}\mathcal{S}$$

$$+ T_\infty \int_{\mathcal{V}_w} \frac{T_\infty}{T} \Phi_{eff} \, \mathrm{d}\mathcal{V} + T_\infty \int_{\mathcal{V}_w} \frac{T_\infty}{T^2} k_{eff} \, (\nabla \mathbf{T})^2 \, \mathrm{d}\mathcal{V}$$

$$+ \int_{\mathcal{S}_w} (\bar{\bar{\tau}}_{eff} \cdot \mathbf{V}) \cdot \hat{\mathbf{n}} \, \mathrm{d}\mathcal{S} - \int_{\mathcal{S}_w} (\mathbf{q}_{eff} \cdot \hat{\mathbf{n}}) \, \mathrm{d}\mathcal{S}$$

$$+ \int_{\mathcal{S}_w} \frac{T_\infty}{T} (\mathbf{q}_{eff} \cdot \hat{\mathbf{n}}) \, \mathrm{d}\mathcal{S}$$

$$(2.101)$$

which, from the notations introduced in paragraph 2.1.3 (p. 35), can be written as:

$$\dot{\mathcal{E}}_{prop} \quad - \int_{\mathcal{S}_A} (\bar{\bar{\tau}}_{eff} \cdot \mathbf{V}) \cdot \hat{\mathbf{n}} \, d\mathcal{S} + \dot{\mathcal{E}}_q = W\dot{\Gamma} + \dot{\mathcal{E}}_m + \dot{\mathcal{E}}_{th} + \dot{\mathcal{A}}_\phi^c + \dot{\mathcal{A}}_{\nabla T}^c + \dot{\mathcal{A}}_w$$

$$- \int_{\mathcal{S}_O} (\bar{\bar{\tau}}_{eff} \cdot \mathbf{V}) \cdot \mathbf{n} \, d\mathcal{S} + \int_{\mathcal{S}_O} (\bar{\bar{\tau}}_{eff} \cdot \mathbf{V}_\infty) \cdot \mathbf{n} \, d\mathcal{S} + \int_{\mathcal{S}_O} (\mathbf{q}_{eff} \cdot \mathbf{n}) \, d\mathcal{S} \quad (2.102)$$

$$+ \dot{\mathcal{H}}_w' + \tau_w' + \dot{E}_{qw}'$$

or equivalently,

$$\boxed{\dot{\mathcal{E}}_{prop} + \dot{\mathcal{E}}_q - \tau_A' = W\dot{\Gamma} + \dot{\mathcal{E}}_m + \dot{\mathcal{E}}_{th} + \dot{\mathcal{A}}_\phi^c + \dot{\mathcal{A}}_{\nabla T}^c + \dot{\mathcal{A}}_w + \tau_O' + \tau_{x,O}' - \dot{E}_{qO}' + \dot{\mathcal{H}}_w' + \tau_w' + \dot{E}_{qw}'} \quad (2.103)$$

where the prime ( )$'$ denotes the terms neglected in Eq. (2.34) and given hereafter:

- The aircraft surface $\mathcal{S}_A$:

  $\tau_A' := \int_{\mathcal{S}_A} (\bar{\bar{\tau}}_{eff} \cdot \mathbf{V}) \cdot \hat{\mathbf{n}} \, d\mathcal{S} = \int_{\mathcal{S}_P} (\bar{\bar{\tau}}_{eff} \cdot \mathbf{V}) \cdot \mathbf{n} \, d\mathcal{S} \simeq 0$. This term is only non-zero on the permeable surfaces of the aircraft, being here associated with the propulsion system for which the shear forces are usually negligible. In the absence of propulsion this term is strictly zero.

- The outer boundary $\mathcal{S}_O$:

  $\tau_O' := - \int_{\mathcal{S}_O} (\bar{\bar{\tau}}_{eff} \cdot \mathbf{V}) \cdot \mathbf{n} \, d\mathcal{S} \simeq 0$. This term is the rate of work of the viscous force acting on the outer boundary and is usually negligible.

  $\tau_{xO}' := \int_{\mathcal{S}_O} (\bar{\bar{\tau}}_{eff} \cdot \mathbf{V}_\infty) \cdot \mathbf{n} \, d\mathcal{S} = V_\infty \int_{\mathcal{S}_O} (\bar{\tau}_{x,eff} \cdot \mathbf{n}) \, d\mathcal{S} \simeq 0$. The second integral term is usually neglected in the momentum equation Eq. (2.9b) at distances greater than one body length downstream of the configuration [118, 173]. It is therefore expected that this term will be negligible compared to the other terms involved in the formulation.

  $\dot{E}_{qO}' := \int_{\mathcal{S}_O} -(\mathbf{q}_{eff} \cdot \mathbf{n}) \, d\mathcal{S} \simeq 0$. This term represents the thermal energy associated with heat conduction across the outer boundary which is negligible except for configurations which exchange a significant amount of heat.

- The wave surface $\mathcal{S}_w$: $\dot{\mathcal{H}}_w' + \tau_w' + \dot{E}_{qw}'$

  Even if each of these three terms may not be completely negligible, their sum should be close to zero by virtue of the First law, see Eq. (2.97). These terms are used to assess the determination of the surface $\mathcal{S}_w$, as shown in section 3.3 (p. 79).

As a consequence, the global performance balance introduced in the theoretical derivation of the formulation, Eq. (2.34), is only valid upon a careful definition of the boundaries of the control volume: the aircraft surface $\mathcal{S}_A$, the outer boundary $\mathcal{S}_O$, and the shock surface $\mathcal{S}_w$. Its domain of validity will be assessed in each of the applications in Chapter 3 (p. 63).

2.5.2 Post-processing Code Description

The formulation has been implemented in an existing Fortran 77/90 code called $ffd72$ which is dedicated to the post-processing of RANS (and *Euler*) flow solutions.

2.5.2.1 $ffd72$ Code for Drag Prediction and Decomposition

ONERA has pioneered the prediction and decomposition of the drag from numerical flow solutions *via* a far-field drag method [46, 174] developed by VAN DER VOOREN (NLR, retired) and DESTARAC (ONERA).

The main advantages of this formulation are an identification of the spurious (numerical) drag and a physical decomposition into viscous drag, lift-induced (or vortex) drag and wave drag.

As early as 1993, the approach has been numerically implemented in a post-processing code named *ffd* for *far-field drag*. A cell-by-cell approach with physical sensors was developed and a correction for spurious vortex diffusion was implemented one year later. Face-based management was adopted in 2003 for the drag extraction to allow the post-processing of flow solutions computed on structured and unstructured grids. Multiblock structured data are converted into unstructured face-based data by interfaces, so as to ensure uniform treatment of structured and unstructured solutions. This feature is particularly useful for treating numerical solutions from various flow solvers especially for cell-centered solvers (Onera-*elsA* [35]) and cell-vertex solvers (DLR-TAU [148]).

Among its recent internal (ONERA) use could be cited the investigation of the CRM configuration in cruise conditions [75] and the aerodynamic optimization of a blended wing-body [104]. The success of this code is also shared by industrial teams of major aerospace companies like Airbus [7] and Dassault Aviation.

2.5.2.2 *ffx* Module for Exergy Assessment

A module named *ffx* (for *far-field exergy*) has been implemented in the *ffd*72 code for the assessment of the aerothermopropulsive performance of complex configurations[15]. It contains 75 subroutines for about 15,500 lines[16]. As illustrated in Fig. 2-9, it is a post-processing code meaning that its input data comes from a CFD-RANS solver. In the course of this thesis, only cell-centered finite-volume discretization flow solutions computed with the ONERA-*elsA* software [35] have been treated.
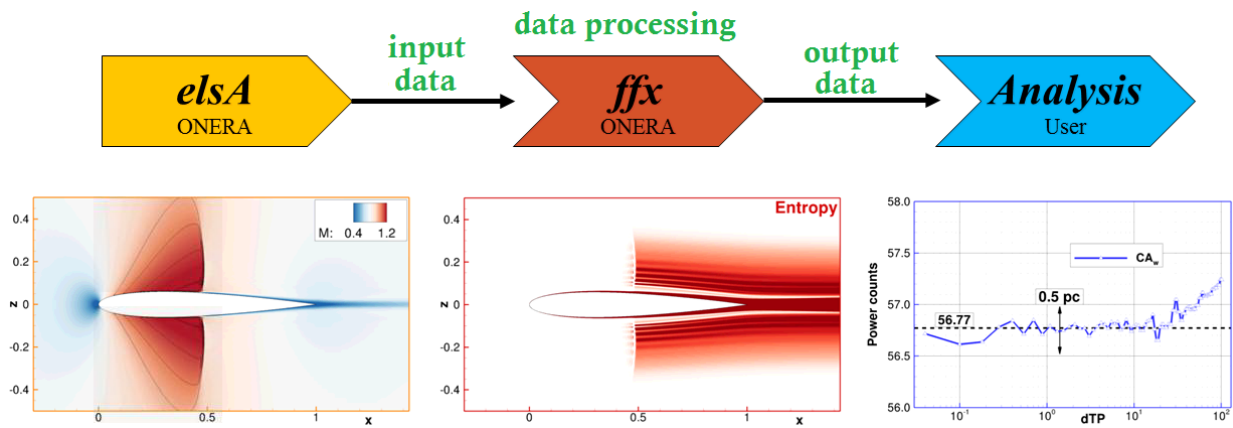
Figure 2-9: Simplified schematic of the post-processing code *ffx* execution chain.

In a nutshell, the flow solution computed from the CFD solver (left —) is extracted and represents the input data for the post-processing code which recalculates any quantity of interest (like entropy, middle —) and subsequently gives the user the required information for the assessment of the performance of the configuration from an exergy point of view (right —).

Input Data. The input data for the post-processing code contain the flow conservative variables (ρ, ρu, ρv, ρw, ρE) as well as the turbulent to laminar viscosity ratio (μ_t/μ) for each cell that are extracted from the flow solution. In the case of non-adiabatic surfaces, the heat transferred at the body surface(s) must also be extracted.

↪ All these data are commonly extracted from typical RANS flow solutions.

---

[15]Another ongoing extension of the code relates to unsteady drag prediction and decomposition [164, 165].

[16]The code *ffd*72 contained about 300 subroutines for 75,000 lines before the present development.

Data Processing. The processing of typical flow solutions ranges from a few seconds to a few minutes depending on the grid density. Only the main steps of the processing are described here.

– From the input data, all flow properties necessary for the exergy analysis are calculated. The subscript *CFD* refers to quantities extracted from the flow CFD solution. The density $\rho = \rho_{CFD}$ comes directly from the CFD solutions. The streamwise and transverse velocities are calculated as

$$V_\infty + u = \frac{(\rho[V_\infty + u])_{CFD}}{\rho_{CFD}} \qquad ; \qquad v = \frac{(\rho v)_{CFD}}{\rho_{CFD}} \qquad ; \qquad w = \frac{(\rho w)_{CFD}}{\rho_{CFD}} \qquad (2.104a)$$

From which we can compute the static pressure

$$p = (\gamma - 1)\left[(\rho E)_{CFD} - \frac{1}{2}\rho_{CFD}([V_\infty + u]^2 + v^2 + w^2)\right] \qquad (2.104b)$$

as well as the static temperature:

$$T = \frac{1}{c_v}\left[\frac{(\rho E)_{CFD}}{\rho_{CFD}} - \frac{1}{2}([V_\infty + u]^2 + v^2 + w^2)\right] \qquad (2.104c)$$

Likewise, the total enthalpy is computed as $h_i = h + \frac{1}{2}V^2$:

$$h_i = c_p T + \frac{1}{2}([V_\infty + u]^2 + v^2 + w^2) \qquad (2.104d)$$

and the entropy relative to reference conditions:

$$\delta\mathsf{s} = \frac{r_{gas}}{\gamma - 1}\log\left[\left(\frac{p}{p_\infty}\right)\cdot\left(\frac{\rho_\infty}{\rho_{CFD}}\right)^\gamma\right] \qquad (2.104e)$$

All main flow properties are therefore known are calculated or based on this set of relations.

– As discussed in paragraph 2.2.3.1 (p. 44), the thermal and viscous anergy coefficients rely on a laminar and a turbulent dissipation:

$$\dot{\mathcal{A}}_\Phi^{lam} = \int_\mathcal{V} \frac{T_\infty}{T}\mu\,\phi\,\mathrm{d}\mathcal{V} \qquad\qquad \dot{\mathcal{A}}_{\nabla T}^{lam} = \int_\mathcal{V} \frac{T_\infty}{T^2}\,c_p\frac{\mu}{Pr}\,(\nabla\mathbf{T})^2\,\mathrm{d}\mathcal{V} \qquad (2.105a)$$

$$\dot{\mathcal{A}}_\Phi^{turb} = \int_\mathcal{V} \frac{T_\infty}{T}\mu_t\,\phi\,\mathrm{d}\mathcal{V} \qquad\qquad \dot{\mathcal{A}}_{\nabla T}^{turb} = \int_\mathcal{V} \frac{T_\infty}{T^2}\,c_p\frac{\mu_t}{Pr_t}\,(\nabla\mathbf{T})^2\,\mathrm{d}\mathcal{V} \qquad (2.105b)$$

where the viscosity μ is given by the *Sutherland* Law:

$$\mu = \mu_0 \frac{T_0 + S}{T + S}\left(\frac{T}{T_0}\right)^{\frac{3}{2}} \qquad (2.106)$$

where μ_0 and T_0 can be any reference values. Here we take $\mu_0 = 1.716\ 10^{-5}$ kg.s^{-1}.m^{-1}, $T_0 = 273.15$K and $S = 110.56$K. The eddy viscosity μ_t is provided by the turbulence model.
We consider constant *Prandtl* numbers: $Pr = 0.72$ and $Pr_t = 0.90$. Also the specific heats at constant volume and constant pressure are given: $c_v = 717.5$ and $c_p = 1004.5$ J.kg^{-1}.K^{-1}.

– The definition of the control volume is made by iteratively considering each element of the grid. Average coordinates for the element $(x_{elmt}, y_{elmt}, z_{elmt})$ are determined from the known coordinates of each node belonging to the cell under consideration. If $x_{elmt} < x_{TP}$, then the element is tagged as being within the control volume. x_{TP} refers to the streamwise position of the transverse plane. Once

59

its distance d_{TP} from the body is specified by the user, the code *ffχ* determines the corresponding x_{TP} value knowing the maximum x_{max}^{body} of the body: $x_{TP} = x_{max}^{body} + d_{TP}$.

– The wave volume $\mathcal{V}_w$ is determined using a subroutine already implemented in the *ffd72* code. It is based on a physical shock criterion introduced by LOVELY and HAIMES [97] to determine whether a given cell should be considered as being enclosed by the surface

$$\lambda_w := \frac{\mathbf{V} \cdot \nabla \mathbf{p}}{a \|\nabla \mathbf{p}\|} \tag{2.107}$$

where a is the local speed of sound. If $\lambda_w > 0.95$ the cell under consideration is tagged as being enclosed by the wave volume.

As will be highlighted in paragraph 3.3.3.3 (p. 86), the addition of a number of supplementary cells to this initial guess is known to enhance numerical accuracy.

– The propulsive surface $\mathcal{S}_P$ is initially determined by the identification of the boundary condition from the input data of the CFD solution. Yet, here again, the addition of a number of cells can improve the numerical treatment of some boundary conditions, see paragraph 4.4.2.1 (p. 148).

– Once the (wave, propulsive and control) volumes are properly defined, the computation of all terms of the exergy balance can be tackled:

$$\dot{\mathcal{E}}_{prop} + \dot{\mathcal{E}}_q - \tau_A^{'} = W\dot{\Gamma} + \dot{\mathcal{E}}_m + \dot{\mathcal{E}}_{th} + \dot{\mathcal{A}}_\phi^c + \dot{\mathcal{A}}_{\nabla T}^c + \dot{\mathcal{A}}_w + \tau_O^{'} + \tau_{x,O}^{'} - \dot{E}_{qO}^{'} + \ddot{\mathcal{H}}_w^{'} + \tau_w^{'} + \dot{E}_{qw}^{'} \tag{2.108}$$

The frontier of each volume is determined by doing an iterative loop on each *face* (of the element) contained in the grid: if the element on the left of this face is tagged within the volume and the element on the right is not tagged, then the face under consideration delimits the frontier of the volume.

– Finally, temperature (and velocity) gradients

$$\nabla \mathbf{T} = \left[\frac{\partial T}{\partial x}; \frac{\partial T}{\partial y}; \frac{\partial T}{\partial z} \right]^T \tag{2.109}$$

by relying on the *Green-Gauss* theorem which states that the surface integral of a scalar function is equal to the volume integral (over the volume bound by the surface) of the gradient of the scalar function.

$$\nabla \mathbf{T} \equiv \frac{1}{\Omega} \sum T_{face} \, \mathbf{n} \, \mathrm{d}\mathcal{S}_{face} \tag{2.110}$$

where $T_{face} = 1/2(T_1 + T_2)$ is calculated by simple averaging of the values of the two elements adjacents to the cell interface.

The effective viscous dissipation is calculated from its expression derived in appendix A.7 (p. 184).

Output Data. Each term of Eq. (2.108) is evaluated and the concise exergy balance is highlighted:

$$\dot{\mathcal{E}}_{prop} + \dot{\mathcal{E}}_q = W\dot{\Gamma} + \dot{\mathcal{E}}_m + \dot{\mathcal{E}}_{th} + \dot{\mathcal{A}}_\phi^c + \dot{\mathcal{A}}_{\nabla T}^c + \dot{\mathcal{A}}_w \tag{2.111}$$

All neglected terms $(\ )^{'}$ are displayed along with warnings if their magnitude is above 0.05 pc. The magnitude of the missing anergy $\Delta\dot{\mathcal{A}}$ is also given as an indication of the consistency of the flow solution analyzed within the control volume.

Options. One data file is read before any execution. A few *keys* can be specified to activate specific options that allow a more detailed analysis of the flow solution.

– A DEBUG mode can give more indications during the execution of the program. Typical information include the entering/exiting of a subroutine and the time that the corresponding task required. Additional routines are involved to assess the consistency of the flow solutions within the control volume: the satisfaction of the fundamental relations of mass, momentum and energy conservation as well as entropy relation are checked.

– Data files for flow visualization can be written in binary. Layouts and macros compatible with the visualization software Tecplot360$^{\text{TM}}$ are then automatically copied in the current directory to allow fast and efficient assessment of the flow.

– A first tuning is the automatic variation of the wave surface $\mathcal{S}_w$ (already implemented in $ffd72$): the definition of the wave surface relies on a shock criterion which gives a first clue to which cells should be considered within the wave volume. Experience shows that the addition of a low number (< 10) of supplementary cells can greatly improve the numerical treatment of this phenomenon.

– Likewise, a second tuning is the automatic variation of the propulsive surface $\mathcal{S}_P$. As we have seen in paragraph 2.2.1 (p. 39), the definition of the propulsion surface is generally not unique. A number a additional cell layers can be required for the efficient numerical treatment of a boundary condition modeling a propulsive system.

– A final useful tuning is the automatic variation of the control volume: the distance between the transverse plane and the body is gradually increased to *scan* the wake. In addition to containing all the terms involved in the formulation, these files can also give the terms of all fundamental relations to ensure the consistency of the flow solution far from the body, if the DEBUG mode is activated. The same option can be used to evaluate the variation of all the terms over the configuration under study.

These options are extensively used in all applications analyzed in Chapters 3 (p. 63) and 4 (p. 119). If these time-consuming tasks are not activated, the post-processing time is generally in the order of a few seconds to a few minutes depending on the grid density.

Further developments of this module could notably consists in the calculation of the gradients of all terms involved in the formulation to allow for gradient-based optimization processes.

2.6   Chapter Summary

An exergy-based formulation has been derived combining a momentum balance along with a First and Second laws analysis. The output of the derivation is a balance between the exergy supplied by the propulsion system and its (partial) destruction within the control volume. Relation is made between the aircraft mechanical equilibrium and the flow phenomena that directly influence flight power requirements. As the formulation relies on a global exergy balance, and not on the separate definitions of thrust and drag, it is suitable for the performance evaluation of aircraft concepts with boundary layer ingestion. Connections to the mechanical energy analysis of DRELA [49] were made and it was shown that the proposed exergy balance provides thermal energy management in addition to mechanical energy considerations.

Characterization of the various outflows that could be valued was made, *i.e.* the wakes and jets as well as lift-induced vortices. It was pointed out that, through the exergy point of view, any flow perturbation is seen as a potential for improvement. This represents a radically different perception of the flow as compared to a traditional momentum analysis. Asymptotic considerations made clear that the thermal and mechanical exergy outflows vanish far downstream of the configuration; their work potential being destroyed by viscous dissipation and thermal mixing. When the aircraft is in mechanical equilibrium, all the fuel work potential is destroyed by the three irreversible flow phenomena (viscous dissipation, thermal mixing, and shock waves [44]), while it stores any exergy supplied in excess when more thrust is generated than drag.

Restriction of the formulation to unpowered airframe cases was made and connections to recent/popular drag prediction formulations were provided. It was demonstrated that many (past and current) momentum-based far-field drag expressions required some thermodynamic considerations and that their underlying theory can be consistently related to the proposed exergy-based formulation.

Finally, the adaptation of the theoretical formulation to the numerical constraints was examined. The theoretically-discontinuous shock waves are treated with a wave surface $\mathcal{S}_w$ enclosing a volume of finite-size. The same procedure as the one existing in the well-tried $ffd72$ code is used. Also, a numerical correction for the accurate calculation of the viscous and thermal anergy production was introduced. It is based on the evaluation of the anergy (entropy) not captured due to coarse meshes that prevent the accurate calculation of the velocity and temperature gradients.

The next chapter tackles the validation of the post-processing code $ff\chi$ for various airframe configurations. The following step in chapter 4 focuses on the application of the code to investigate different powered configurations.

Chapter 3

Validation of the Numerical Implementation for the Aerodynamic Performance Assessment of Unpowered Configurations

The primary objective of this chapter is the validation of the post-processing code ffx for the aerodynamic performance assessment of unpowered configurations. To do so, a step-by-step validation procedure is followed by considering geometries and flow regimes of increasing complexity, ranging from subsonic flows around a 2D airfoil to transonic flows over a 3D wing-body configuration. Also, all the various terms involved in the formulation are physically characterized. Grid convergence studies and turbulence model sensitivity are examined when appropriate. The numerical correction for an accurate calculation of the viscous and thermal anergy generation is introduced and calibrated.

3.1   Methodology for Validation

The analyses is in this chapter are restricted to unpowered configurations that do not exchange either mechanical or thermal energy with the flowing fluid: with adiabatic surfaces and no propulsive devices. The exergy balance Eq. (2.34) reduces to:

$$DV_\infty = \dot{\mathcal{E}}_m + \dot{\mathcal{E}}_{th} + \dot{\mathcal{A}}_\phi + \dot{\mathcal{A}}_{\nabla T} + \dot{\mathcal{A}}_w \tag{3.1}$$

The rate of work of drag can be decomposed into the outflow of mechanical and thermal exergy that have not been dissipated by the viscous and thermal anergy within the control volume, and to any shock wave.

3.1.1   Methodology and Introduction to Test Cases

The methodology considers geometries and flow regimes of increasing complexities on a step-by-step basis: from a 2D airfoil in a subsonic flow to a 3D wing-body configuration in a transonic flow, see Fig. 3-1 and Table 3.1.
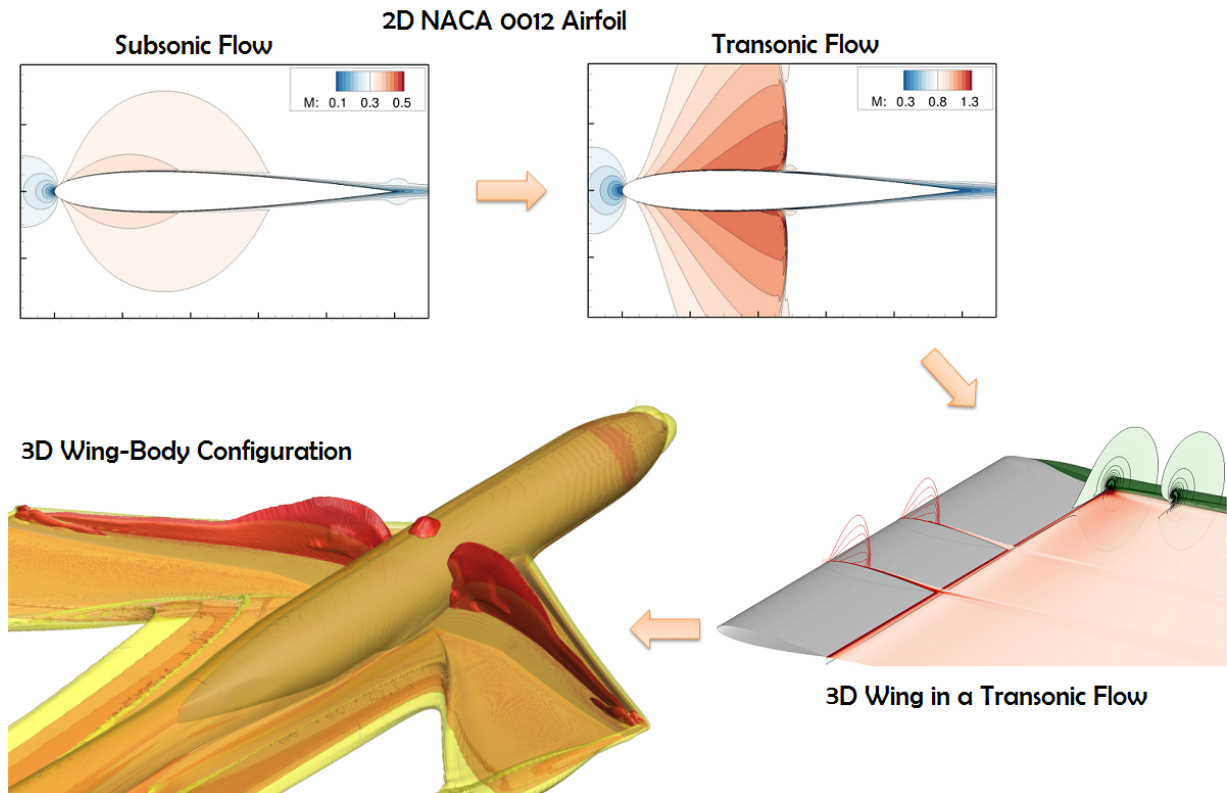
Figure 3-1: Chapter 3: representation of the four test cases of unpowered configurations.

Section	2D/3D	Geometry	Sub/Transonic	Turbulence Model	Grid Convergence
3.2	2D	NACA 0012 Airfoil	Subsonic	*Spalart–Allmaras*	5 Levels
3.3	2D	NACA 0012 Airfoil	Transonic	*Spalart–Allmaras*	4 Levels
3.4	3D	Rectangular Wing	Transonic	4 different	–
3.5	3D	Wing-Body Configuration	Transonic	*Spalart–Allmaras*	6 Levels
B.2	3D	Elliptical Wing	Subsonic	✗ (*Euler*)	3 Levels

Table 3.1: Chapter 3: main characteristics of the four test cases of unpowered configurations.

– The first application in section 3.2 (p. 67) considers the most simple case of a symmetrical airfoil (NACA 0012) immersed in a subsonic flow at M_∞ = 0.30 and zero incidence. This test case will serve to introduce the behavior of the various newly-derived terms of the exergy balance. Then, a 5-levels grid convergence study will allow to evaluate the accuracy of the drag prediction from the code *ffx*. A *Reynolds* number sensitivity analysis will be performed to determine the influence of turbulence on the viscous and thermal anergy dissipation.

– In the second application in section 3.3 (p. 79), we focus on the same simple geometry but immersed in a transonic flow at M_∞ = 0.80. First, a *Mach* number sensitivity analysis is made to highlight the impact of compressibility on the various terms of the exergy balance Eq. (3.1). A special section is dedicated to the numerical treatment of shock waves and to the introduction of the numerical correction for accurate viscous and thermal anergy production. Finally, a 4-levels grid convergence study is conducted to determine the sensitivity of the code *ffx* to grid refinement.

– Based on these two analyses, section 3.4 (p. 91) focuses on a viscous and transonic flow over a 3D rectangular wing. A set of four turbulence models is considered to evaluate the capability of the code to post-process numerical flow solutions from different turbulence models. The correction for accurate anergy production is applied to balance the underestimated vortex diffusion due to numerical dissipation. Finally, an assessment of the drag prediction is made.

– The last section 3.5 (p. 101) builds on the key findings of all three previous test cases and focuses on a 3D wing-body configuration in cruise conditions which represents an industrially-representative configuration. A flow field analysis is made to emphasize the location of the anergy generation in the vicinity of the body and the evolution of the mechanical and thermal exergy is depicted. A 6-levels grid convergence study is finally conducted and the numerical correction is shown to provide an accuracy similar to the near-field method.

An additional test case focusing on the lift-induced vortices in an *Euler* flow is examined with grid convergence study in appendix B.2 (p. 189). Except where mentioned otherwise, the *Spalart–Allmaras* turbulence model [156] is used to simulate fully turbulent flows with the ONERA-*elsA* code [35] (v3.4.04). One of the goals of this chapter is to get confidence in the code by determining its strengths and weaknesses before examining powered configurations in the next chapter.

3.1.2 Numerical Verification and Validation

3.1.2.1 Verification: Flow Solutions Quality Assessment

The verification procedure deals with mathematics and provides evidence that the computational model is solved correctly and accurately [116]. For the code *ffx*, it consists of determining that *the model implementation accurately represents the developer's conceptual description of the model and the solution of the model*. There are two types of verification:

Solution Verification. The activities are directed toward assuring the accuracy of input data for the problem of interest, estimating the numerical solution error and assuring the accuracy of the output data for the problem of interest. These items are checked for each test case through the assessment of the convergence history of the flow solutions and by verifying the outputs from the code *ffx*.

Code Verification. The activities are directed toward finding and removing mistakes in the source code and errors in numerical algorithms. This part will not be presented in the following applications but the code is considered reliable to the knowledge of the developer.

3.1.2.2   Validation: Formulations Comparison

The validation procedure deals with physics and provides evidence that the mathematical model accurately relates to experimental measurements [116]. The validation of the post-processing code *ffx* consists in determining *the degree to which the exergy balance is an accurate representation of the real world from the perspective of the intended uses of the model.*

When available, validation is made with experimental data. In the absence of such data, validation is made with reference to two validated methods already implemented in the post-processing code $ffd72$: the near-field or far-field drag methods.

Near-Field Drag Method. The most straightforward method for evaluation the drag experienced by a body is by a direct integration of the stresses at its surface. The direct integration of the momentum relation (2.9a) in the streamwise direction yields a breakdown into *pressure* drag D_p and *friction* drag D_f:

$$D_p := \int_{\mathcal{S}_A} (p - p_\infty) n_x \, \mathrm{d}\mathcal{S} \tag{3.2a}$$

$$D_f := \int_{\mathcal{S}_A} -(\bar{\tau}_x \cdot \mathbf{n}) \, \mathrm{d}\mathcal{S} \tag{3.2b}$$

forming the *near-field* drag

$$D_{nf} := D_p + D_f \tag{3.3}$$

Numerically speaking, this approach is unambiguous and straightforward but highly dependent on mesh discretization and therefore it suffers from inaccuracy on coarse meshes.

Far-Field Drag Method. The far-field drag formulation of VAN DER VOOREN and DESTARAC [46, 174] will be used as a second reference. This method introduces thermodynamics relation in the momentum relation (2.9b) to obtain a decomposition into viscous drag D_v, lift-induced (or vortex) drag D_i and wave drag D_w:

$$D_{ff} := D_v + D_i + D_w \tag{3.4}$$

This approach has the advantage of providing a physical breakdown of drag which is of interest to the aircraft designer. On top of that, this method is capable of identifying spurious/numerical drag, thereby being more accurate:

$$D_{sp} := D_{nf} - D_{ff} \tag{3.5}$$

If the code *ffx* provides an accuracy similar to one of those two methods methods, it will be considered validated. A key underlying assumption made is to consider that the flow solutions computed by the code ONERA-*elsA* are representative of the real (physical) flows.

3.2 Validation for Viscous Phenomena in 2D Subsonic Flows

The main objective of this section is to provide a first appreciation of the various terms involved in the formulation in a simple case. Evaluation of the accuracy of the numerical code will be made *via* a grid convergence study before investigating the effects of *Reynolds* number on the various terms of the formulation.

Part of this study has been presented at the 49th International Symposium of Applied Aerodynamics in Lille (FR) in March 2014, see [10].

3.2.1 Test Case Presentation

The NACA 0012 Airfoil has been chosen for its popularity and simple symmetrical design. An original geometry was modified to get a sharp trailing edge and an initial grid was generated using an analytic meshing tool provided and adapted by DESTARAC (ONERA). The high-quality C-mesh extends 150 chords in all directions, see Fig. 3-2 and provides an averaged $\bar{y}^+ \simeq 1$ at $Re = 3 \times 10^6$. The (medium) grid that is used here contains $1024 \times 256 = 262,144$ elements.

(a) Global overview.

(b) Zoom on the airfoil.
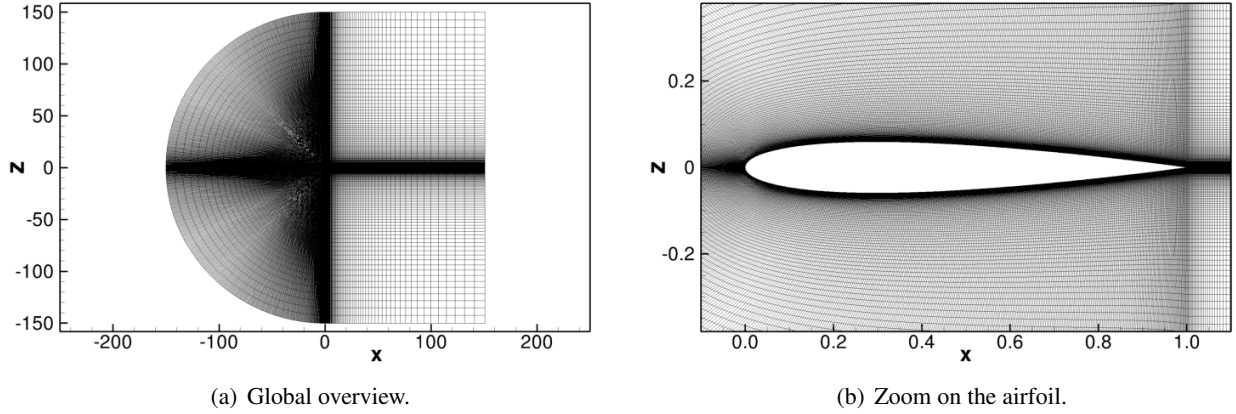
Figure 3-2: 2D NACA 0012 Airfoil in a subsonic flow: medium grid description.

A fully turbulent ($Re = 3 \times 10^6$) and subsonic flow at $M_\infty = 0.30$ and zero incidence was computed with the *Spalart–Allmaras* turbulence model [156]. Extreme care was taken regarding the computation of the numerical flow solution. Artificial viscosity was introduced in the *Jameson* scheme: $\chi_2 = 0.000$ and $\chi_4 = 0.032$. A linear ramp of CFL values from 1 to 100 over the first 1000 iterations was imposed. No low-speed pre-conditioning techniques were used and iterations were continued until the near-field drag coefficient (CD_{nf}) had variations well below 0.0001 drag count[1], see Fig. 3-3a, which corresponds to a global residuals reduction of the energy equation greater than 8 orders, see Fig. 3-3b.

These numerical settings and convergence allow for low numerical errors and therefore trustworthy flow solutions. The corresponding flow field in terms of *Mach* number is given in Fig. 3-4a.

Fig. 3-4b provides a qualitative insight into the main dissipation involved: the fields of viscous and thermal anergy. One can see that these two phenomena are effectively located within the boundary-layers. The magnitude of the viscous anergy is greater than the one of the thermal anergy (same scale).

---

[1] A drag coefficient expressed in drag counts (10^{-4}) that is below a magnitude of 10^{-5} represents data below 10^{-9} which exceeds the precision of the data extracted from the flow solution. This explains the vanishing curves for iterations greater than 37,500 in Fig. 3-3a.
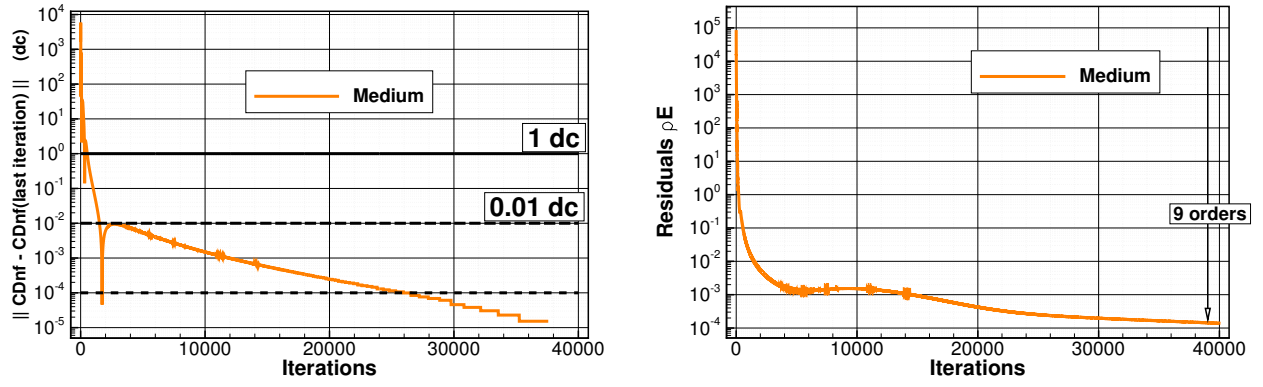
(a) Absolute variation of the near-field drag coefficient with reference to the last iteration.

(b) Equation of Energy residuals reduction.

Figure 3-3: 2D NACA 0012 Airfoil in a subsonic flow: convergence history. Medium grid.
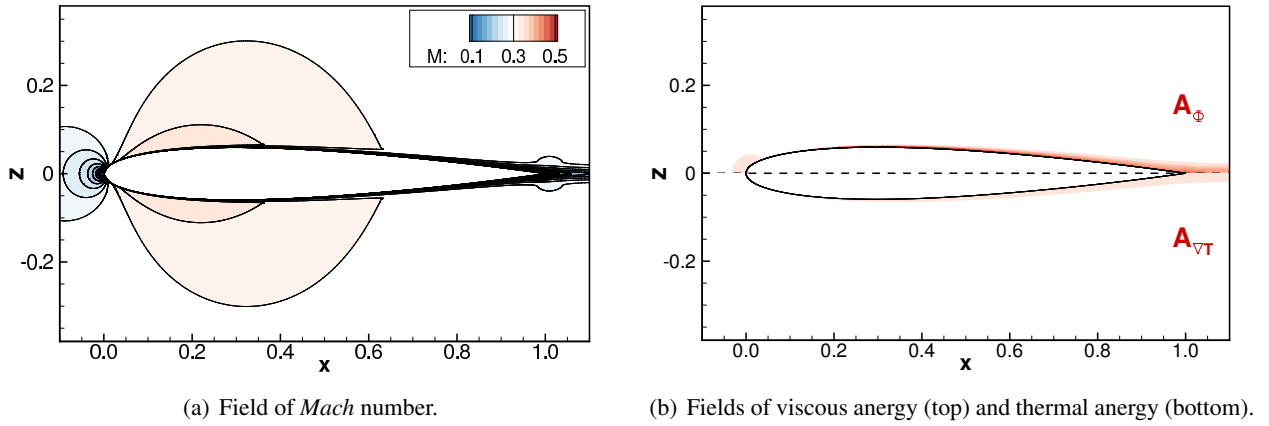
(a) Field of *Mach* number.

(b) Fields of viscous anergy (top) and thermal anergy (bottom).

Figure 3-4: 2D NACA 0012 Airfoil in a subsonic flow: *Mach* number, viscous and thermal anergy fields. Medium grid.

3.2.2 Profile and Wake Analyses at $M_\infty = 0.30$

This subsection provides a quantitative flow analysis of the various terms involved in the exergy-based formulation Eq. (2.71), which for this subsonic flow reads:

$$DV_\infty = \dot{\mathcal{E}}_m + \dot{\mathcal{E}}_{th} + \dot{\mathcal{A}}_\phi + \dot{\mathcal{A}}_{\nabla T} + \dot{\mathcal{A}}_w \tag{3.6}$$

where $\dot{\mathcal{E}}_m = \dot{E}_u + \dot{E}_v + \dot{E}_p$. All these terms are characterized next when expressed in power counts. For example, for the total rate of drag work and viscous anergy:

$$CD_\varepsilon = \frac{DV_\infty}{\frac{1}{2}\rho_\infty V_\infty^3 A_{ref}} \qquad\qquad C\dot{\mathcal{A}}_\phi = \frac{\dot{\mathcal{A}}_\phi}{\frac{1}{2}\rho_\infty V_\infty^3 A_{ref}} \tag{3.7}$$

The magnitude of these coefficients is then directly comparable to the more traditional drag coefficients, see paragraph 2.4.1.3 (p. 53).

3.2.2.1 Profile Analysis in Terms of Anergy Generation

Fig. 3-5 gives the evolution of the anergy generation over the body with reference to the friction drag and to the (total) near-field drag coefficients. These data are directly extracted by the tuning options of the post-

(a) Evolution of the dissipation terms around the airfoil.

(b) Change in laminar (dashed lines) and turbulent (solid lines) viscous and thermal anergy generation rates.
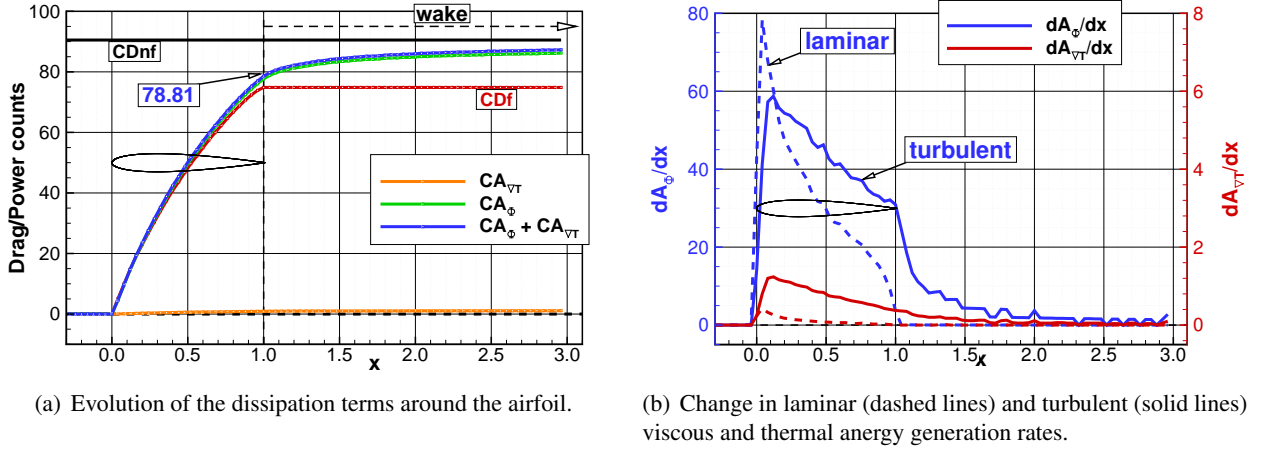
Figure 3-5: 2D NACA 0012 Airfoil in a subsonic flow: profile analysis. Medium grid.

processing code *ffx* developed in the course of this thesis. Also, an illustration of the flow field of entropy is provided in appendix B.1 (p. 188).

Fig. 3-5a quantifies the generation of anergy around the airfoil. As expected from the visualization of the anergy fields in Fig. 3-4b, the thermal anergy ($\dot{\mathcal{A}}_{\nabla T}$ –) is much lower than the viscous anergy ($\dot{\mathcal{A}}_{\phi}$ –). This latter term can be compared with the friction drag (D_f –) which has the very same behavior. The total anergy generated (–) equals to 78.81 pc (power counts) at the airfoil trailing edge and seems to converge towards the (total) near-field drag coefficient (D_{nf} –) of 90.5 dc^2.

Fig. 3-5b gives the change in laminar and turbulent viscous and thermal anergy generation rates[3] over the airfoil. These quantities have been introduced in paragraph 2.2.3.1 (p. 44):

$$\dot{\mathcal{A}}_{\Phi}^{lam} = \int_{\mathcal{V}} \frac{T_{\infty}}{T} \mu \, \phi \, \mathrm{d}\mathcal{V} \qquad\qquad \dot{\mathcal{A}}_{\Phi}^{turb} = \int_{\mathcal{V}} \frac{T_{\infty}}{T} \mu_t \, \phi \, \mathrm{d}\mathcal{V} \qquad (3.8a)$$

$$\dot{\mathcal{A}}_{\nabla T}^{lam} = \int_{\mathcal{V}} \frac{T_{\infty}}{T^2} \, k \, (\nabla \mathbf{T})^2 \, \mathrm{d}\mathcal{V} \qquad\qquad \dot{\mathcal{A}}_{\nabla T}^{turb} = \int_{\mathcal{V}} \frac{T_{\infty}}{T^2} \, k_t \, (\nabla \mathbf{T})^2 \, \mathrm{d}\mathcal{V} \qquad (3.8b)$$

First, note that the thermal anergy rate is about one order of magnitude lower than the viscous component (different y-axes). Both laminar and turbulent dissipations exhibit a peak at the leading edge, where the velocity and temperature gradients are highest. The laminar dissipation then rapidly vanishes towards the trailing edge while the turbulent component continues in the wake of the body.

Although no data have been found for comparison, the evolution and decomposition of the viscous and thermal anergy generation over the body appears physically valid, suggesting that the *Moore* and *Moore* model for mean entropy generation [108] is adapted for this simple flow.

3.2.2.2 Wake Analysis in Terms of Outflows Decomposition and Anergy Generation

A complete overview of the exergy outflows and anergy generation in the wake of the body is given by Fig. 3-6. Each term is evaluated for a downstream plane of the control volume located at a given distance of the body[4]. The log x-axis emphasizes the region near the airfoil and all terms are expressed in power counts.

---

[2]These figures yields an exergy-waste coefficient of about $EWC_0 = (90.50 - 78.81)/90.50 \simeq 13\%$, which rapidly decreases as we get $EWC_2 = 3.1\%$ at a two chord-distance.

[3]These data are calculated by finite difference by the post-processing tool Tecplot360$^{\mathrm{TM}}$.

[4]These data are directly extracted by the tuning options of the post-processing code *ffx* developed in the course of this thesis.

(a) Mechanical outflows.

(b) Thermocompressible aspects.

(c) Anergy generation.
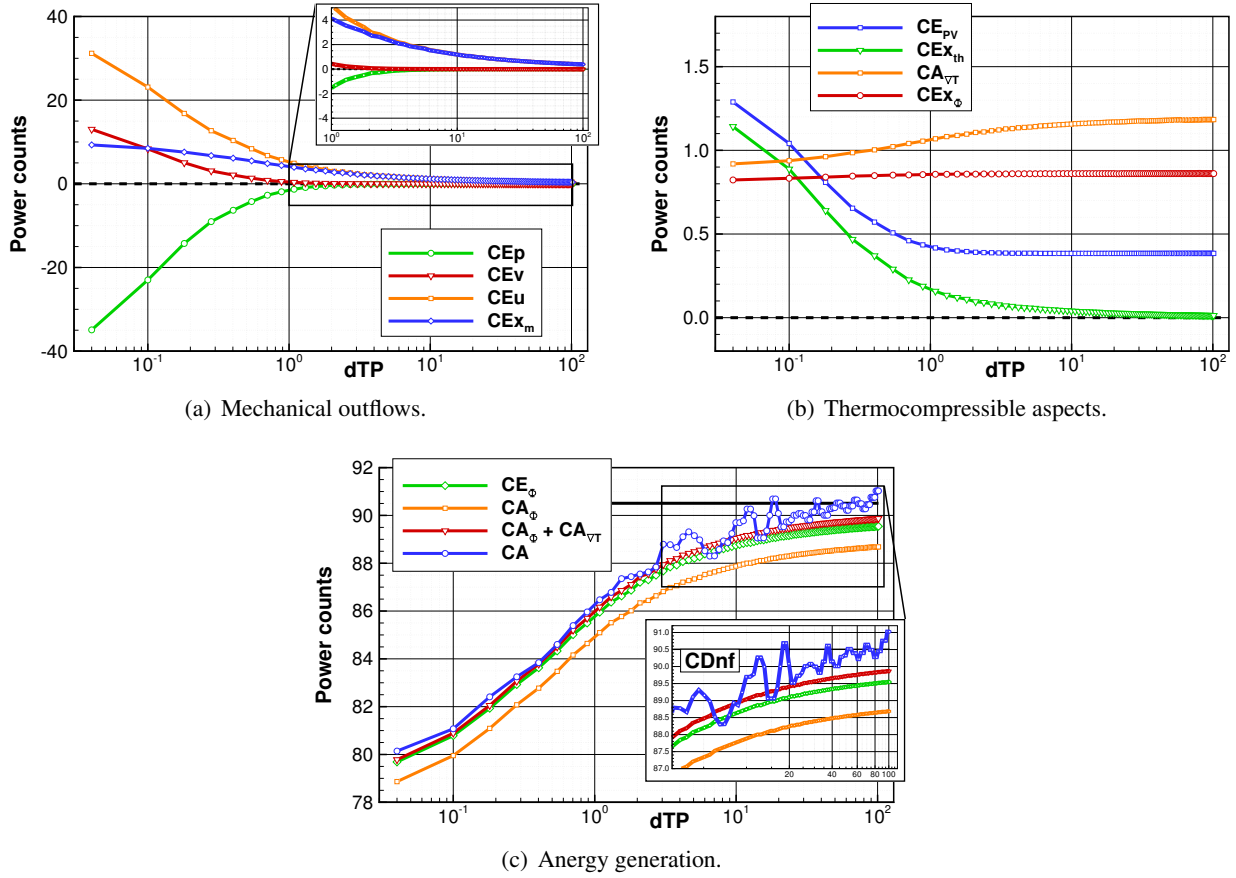
Figure 3-6: 2D NACA 0012 Airfoil in a subsonic flow: wake analysis. Medium grid.

Fig. 3-6a focuses on the mechanical outflows that decrease towards zero as we move downstream of the body. Note that the pressure boundary-work rate ($\dot{E}_p$ –) is negative while the streamwise ($\dot{E}_u$ –) and transverse ($\dot{E}_v$ –) kinetic energy deposition rates are positive, as described by Drela (section 1.1, p. 8). After less than two chords, the total mechanical energy ($\dot{\mathcal{E}}_m$ –) reduces to the streamwise kinetic power associated with the wake of the airfoil, see top zoom. Also, in agreement with Second Law considerations developed in paragraph 2.2.4 (p. 46), the mechanical exergy vanishes in the far wake of the body.

Fig. 3-6b deals with the thermocompressible terms related by: $\dot{\mathcal{E}}_{th}^i = \dot{\mathcal{E}}_\phi - \dot{\mathcal{A}}_{\nabla T} + \dot{E}_{PV}$. First, note that the thermal exergy ($\dot{\mathcal{E}}_{th}$ –) decreases towards zero, as expected from paragraph 2.2.4.1 (p. 47). The viscous exergy ($\dot{\mathcal{E}}_\Phi$ –) stays relatively constant while the thermal anergy ($\dot{\mathcal{A}}_{\nabla T}$ –) slightly increases and converges towards a final value of 1.2 pc. The term ($\dot{E}_{PV}$ –) converges towards 0.4 pc.

Fig. 3-6c focuses on the dissipation occurring in the wake. Regarding viscous dissipation, there is about one power count difference between the energy ($\dot{E}_\phi$ –) and the anergy ($\dot{\mathcal{A}}_\phi$ –) associated with this phenomenon; this corresponds to the viscous exergy ($\dot{\mathcal{E}}_\Phi$ – in Fig. 3-6b). Although in good agreement close to the body, discrepancies appear between the total anergy outflow ($\dot{\mathcal{A}}$ –) and its decomposition into viscous and thermal anergy ($\dot{\mathcal{A}}_\phi + \dot{\mathcal{A}}_{\nabla T}$ –) as the plane is moved downstream. Also, from the bottom zoom, note the much smoother and steady increase[5] of the viscous terms as compared to the total anergy outflow exhibiting non-monotone behavior at distances greater than a few chords due to numerical inaccuracy[6].

---

[5]In agreement with the Second Law of Thermodynamics.

[6]This test case additionally highlights that *Oswatitsch*'s formulation suffers from the requirement of large grid extent where the

Regarding the wake, from Fig. 3-6a-b, one can see a transient region of about three chord length downstream of the airfoil where the flow *re-equilibrates* itself following the disturbance caused by the body. In this region, there are exchanges between the three components of the mechanical exergy outflow as well as a convergence of the thermal exergy and of the $\dot{E}_{PV}$ term.

Then, from Fig. 3-6a-c, one can identify a second region where the streamwise kinetic energy associated with the wake is gradually dissipated by viscous anergy generation. Also, from Fig. 3-6b, we note a vanishing thermal exergy and a corresponding increase in thermal anergy. This corresponds to the process described in paragraph 2.3.1.1 (p. 48) which brings the system back to thermodynamic equilibrium with its environment, thereby destroying any work potential (exergy). This asymptotic process reaches about 99% and 99.3% completion at a distance of respectively 25% and 65% of the grid extent (38 and 98 chord length).

The various terms qualitatively behave in agreement with the theoretical considerations given in the derivation of the formulation in section 2.2 (p. 38). A quantitative assessment of the flow solution can therefore be established next. This will be achieved through a grid convergence study of drag prediction.

3.2.3 Grid Convergence Study on Drag Prediction

In order to determine the dependency of the code to grid density, a grid convergence study is investigated next with reference to classic momentum-based methods that are used for validation purpose. The flow under investigation is viscous flow at zero incidence, $M_\infty = 0.30$ and $Re = 3 \times 10^6$.

3.2.3.1 Numerical Considerations

In the perspective of investigating the influence of the grid refinement on the drag prediction, four additional meshes were generated dividing and multiplying the number of nodes by two and four in all directions, as described in Table 3.2 and illustrated in Fig. 3-7. There is a ratio of 256 between the coarsest grid (16,384 elements) and the finest grid which contains more than 4 millions elements, which is extremely high for a simple 2D Airfoil. Note that an average value of $\bar{y}^+ \simeq 1$ was maintained.

Name	n_i	n_k	Elements	$\bar{y}^+$	Grid Extent
Tiny	256	64	16,384	$\simeq 1$	150 c
Coarse	512	128	65,536	$\simeq 1$	150 c
Medium	1024	256	262,144	$\simeq 1$	150 c
Fine	2048	512	1,048,576	$\simeq 1$	150 c
Extra fine	4096	1024	4,194,304	$\simeq 1$	150 c

Table 3.2: Main characteristics of the five NACA 0012-family grids.

Flows at zero incidence were computed with the *Spalart–Allmaras* turbulence model [156]. Extreme care was taken regarding the computation of the numerical flow solutions. V-cycle multigrid techniques were used and the exact same numerical settings were applied to investigate only the influence of mesh refinement. Again, iterations were continued for all grids until the near-field drag coefficient (CD_{nf}) had variations well below 0.0001 drag count, see Fig. 3-8a, which corresponds to a global residuals reduction of the energy equation greater than 8 orders, see Fig. 3-8b.

All these grids and convergence characteristics are generally out of the scope of practical industrial applications but allows for low numerical errors and therefore trustworthy flow solutions in terms of numerics.

---

flow solution is not trustworthy anymore for accurate drag prediction.

(a) Coarse (top) and Medium (bottom) grids.

(b) Fine (top) and extra fine (bottom) grids.
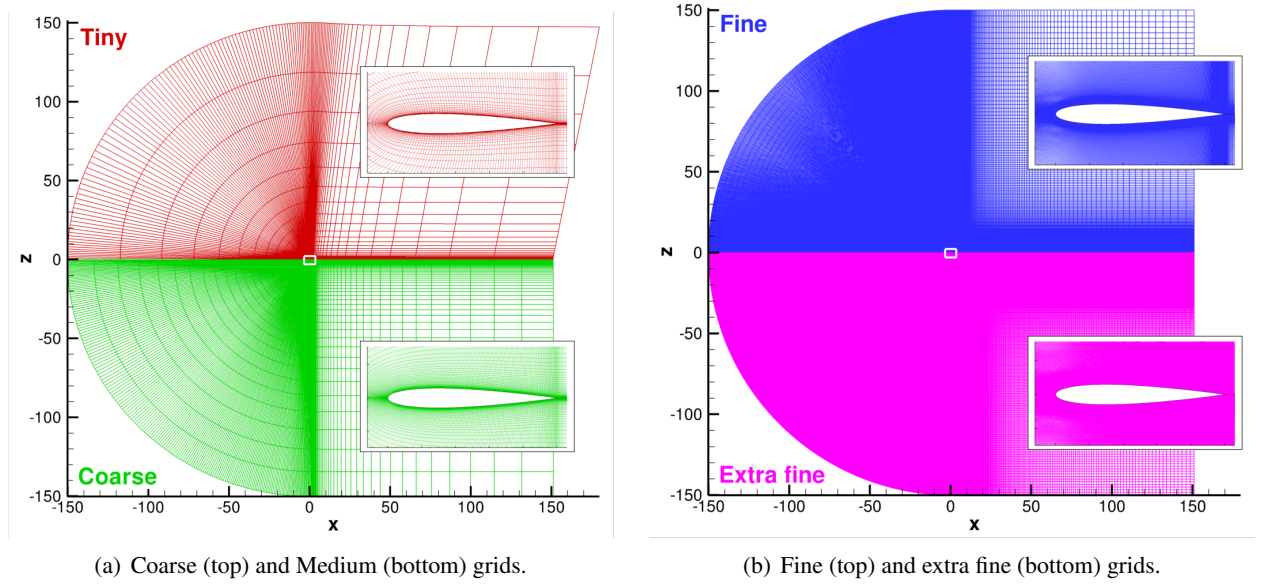
Figure 3-7: 2D NACA 0012 Airfoil grid family: from tiny to extra fine.

(a) Absolute variation of the near-field drag coefficient with reference to the last iteration.

(b) Equation of Energy residuals reduction.
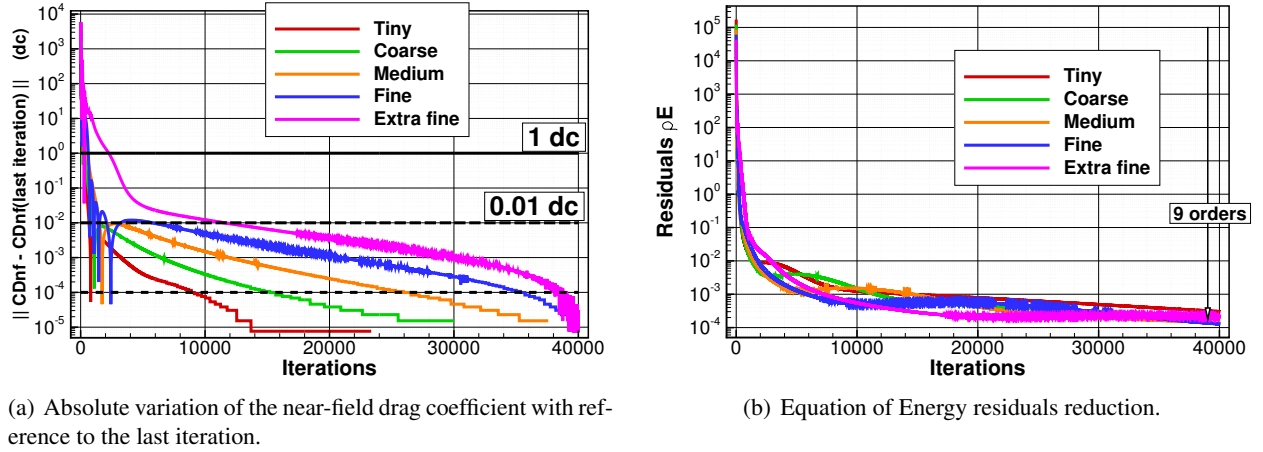
Figure 3-8: 2D NACA 0012 Airfoil in a subsonic flow: convergence history.

3.2.3.2 Momentum-based Drag Methods

Two methods for drag prediction based on a momentum analysis introduced in paragraph 3.1.2.2 (p. 66) are considered next. The most straightforward method integrates the stresses at the surface of the body and leads to a pressure drag D_p and friction drag D_f.

$$D_{nf} = D_p + D_f \qquad ; \qquad D_{ff} = D_v \qquad ; \qquad D_{sp} = D_{nf} - D_{ff}$$

For this subsonic flow, the far-field drag D_{ff} of VAN DER VOOREN and DESTARAC [46] reduces to the viscous drag D_v. The far-field method is capable of discriminating the numerical/spurious drag associated with non-physical phenomena; a *spurious* drag coefficient can therefore be evaluated D_{sp}. Table 3.3 provides the coefficients for the two methods, expressed in drag counts (10^{-4}).

While the pressure drag is monotonically decreasing, the friction drag exhibits a non-monotone behavior. The total near-field drag coefficient varies by 0.38 dc, which is surprisingly low given the factor of 256 between the tiny and the extra fine grid. The total far-field drag coefficient varies by 0.23 dc. Overall, a relatively good agreement between the total near-field and far-field drag coefficients is observed, with very

Mesh	Near-field and far-field drag *via* $ffd72$				
	CD_p	CD_f	CD_{nf}	CD_{ff}	CD_{sp}
Tiny	16.33	74.39	**90.72**	**90.38**	0.34
Coarse	15.81	74.78	**90.59**	**90.55**	0.04
Medium	15.66	74.85	**90.51**	**90.51**	0.00
Fine	15.60	74.80	**90.40**	**90.40**	0.00
Extra fine	15.58	74.76	**90.34**	**90.32**	0.01

Table 3.3: 2D NACA 0012 Airfoil in a subsonic flow: grid convergence study. Near-field and far-field drag coefficients expressed in drag counts (10^{-4}).

little spurious drag even on the coarsest grids.

In terms of grid density, the convergence seems not to be reached for these two total drag coefficients. Nevertheless, all these results are in agreement with experimental data $CD_{expe} = 90.40 \pm 0.10$ dc [69].

3.2.3.3   Exergy-based Drag Method

For the simple case of a subsonic flow over a two-dimensional geometry, the drag relation (2.71) reduces to:

$$DV_\infty = \dot{\mathcal{E}}_m + \dot{\mathcal{E}}_{th} + \dot{\mathcal{A}}_\phi + \dot{\mathcal{A}}_{\nabla T} + \cancel{\mathcal{A}}_w \tag{3.9}$$

where, as described in the previous chapter, from Eq. (2.38) and Eq. (2.72), there are two theoretically equivalent methods to calculate the thermal exergy outflow:

$$\dot{\mathcal{E}}_{th}^d := \dot{E}_{th} + \dot{E}_W - \dot{A} \tag{3.10a}$$

$$\dot{\mathcal{E}}_{th}^i := \dot{\mathcal{E}}_\phi - \dot{\mathcal{A}}_{\nabla T} + \dot{E}_{PV} \tag{3.10b}$$

As established in paragraph 2.3.1.2 (p. 48), if the indirect method is used, then Eq. (3.9) is equal to the mechanical power balance proposed by DRELA [49]. The two methods will be numerically compared.

Application of the exergy-based formulation for drag prediction requires the definition of the control volume. To do so, we first determine the domain of validity of the formulation in terms of the neglected quantities. Then, the direct and indirect methods for thermal exergy calculation are investigated. These two steps give guidelines for the definition of the control volume which is subsequently presented. Finally, the drag decomposition from the exergy-based formulation is given.

1) Domain of Validity of the Formulation.   Fig. 3-9 gives the evolution of the terms neglected in Eq. (3.9) when the transverse plane is moved aft from the body, *i.e.* with increasing d_{TP}.

Fig. 3-9a provides the coefficients of the terms that have been neglected in the theoretical formulation for the medium grid. One viscous term is positive ($\tau'_{x,O}$ –) while the second one is negative (τ'_O –). The exergy associated with heat transfer ($\dot{E}'_{qO}$ –) is very negligible right downstream of the body. The magnitude of their sum (–) is rapidly lower than 0.01 pc.

Fig. 3-9b gives the sum of the neglected terms with grid refinement. There is no observable effect from the grid refinement on the sum of the neglected terms: for all grid densities, this coefficient is lower than 0.01 pc at a distance smaller than one chord.

As a consequence, the approximated relation (3.9) is applicable for a chordwise distance of $d_{TP} \geq 0.5$ chords for all grids.

(a) All four terms for the medium grid.

(b) Sum of the terms with grid refinement.
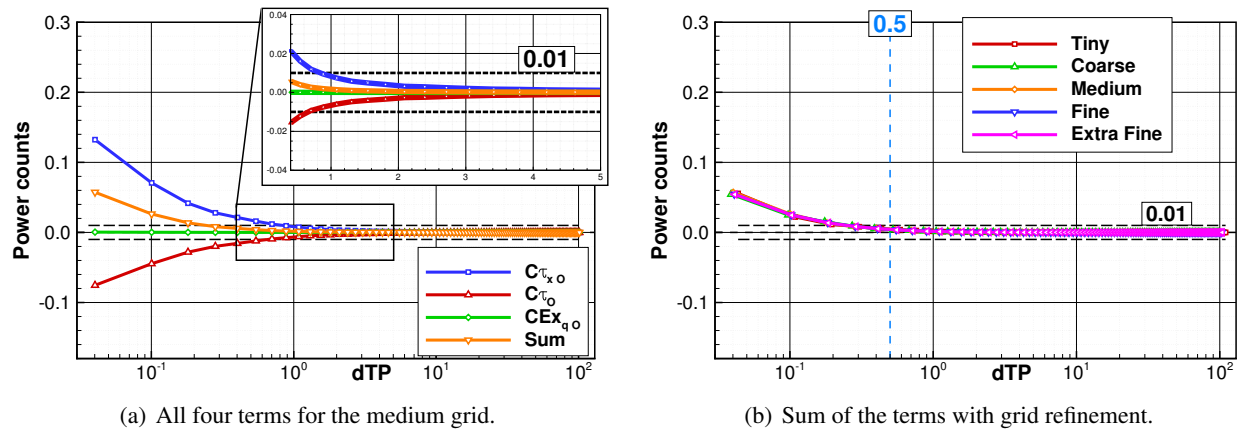
Figure 3-9: 2D NACA 0012 Airfoil in a subsonic flow: terms neglected in the formulation versus transverse plane position.

2) Direct and Indirect Thermal Exergy Methods. The two methods for calculating the thermal exergy are now evaluated from the data given in Fig. 3-10.

(a) Direct and indirect methods for thermal exergy calculation.

(b) Total drag-power with the direct or indirect method for thermal exergy calculation.
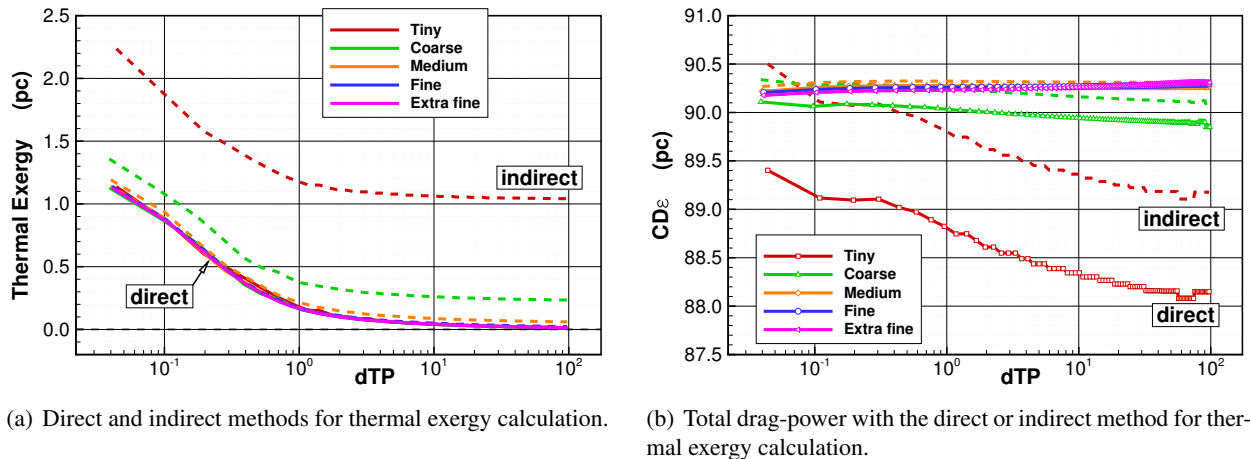
Figure 3-10: 2D NACA 0012 Airfoil in a subsonic flow: total drag-power coefficient with the direct and indirect methods for thermal exergy calculation and with grid refinement.

Fig. 3-10a provides the evolution of the thermal exergy in the wake of the airfoil, with the direct (solid lines) and with the indirect (dashed lines) methods of calculation. One can see that the direct method yields a coefficient quasi-independent on the grid density. For the indirect method, as the grid is refined, the thermal exergy converges towards the same value as the one from the direct method. One can also see that on the two coarsest grids, the coefficient from the indirect method does not seem to converge towards zero, which is not representative of physics in terms of Second Law considerations.

Fig. 3-10b gives the total drag-power coefficient corresponding to the direct method (solid lines with symbols) and to the indirect method (dashed lines). As expected, as the grid is refined, the total drag-power seems to converge towards the same value.

The two methods appear valid for this subsonic flow despite unphysical behavior from the indirect method on the coarse grids.

3) Control Volume Definition.   In agreement with the wake analysis, the transverse plane that delimits the control volume is located one chord downstream of the airfoil, see Fig. 3-11.

(a) Control volume for the medium grid.   (b) Airfoil zoom for the tiny, coarse and medium grids.
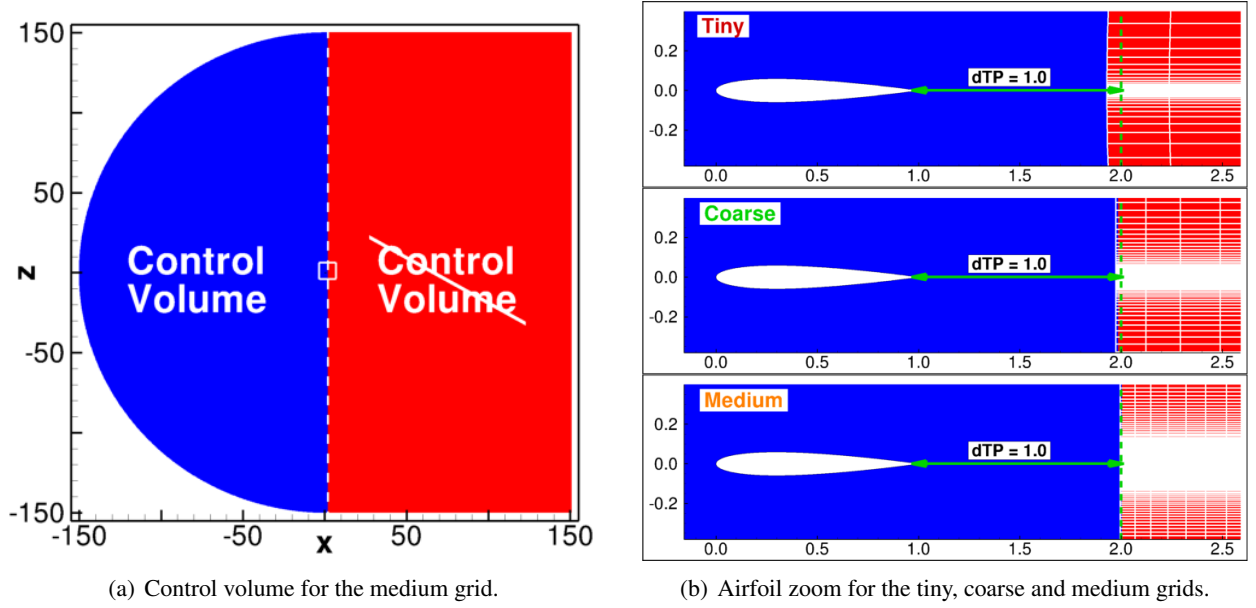
Figure 3-11: 2D NACA 0012 Airfoil in a subsonic flow: control volume definition for drag prediction.

In Fig. 3-11b, the transverse plane is highlighted by the green dashed line for the three coarsest grids. The criterion used by the code is to evaluate the x_{elmt} coordinate of the element and then to compare it with the user input data: if $x_{elmt} \leq x_{TP} = 2.0$, the cell is tagged as being part of the control volume.

One can see that for a given value chosen by the user, the exact location of the transverse plane actually depends on the grid spatial discretization.

4) Drag Assessment and Decomposition.   Table 3.4 gives all terms of the formulation expressed in power counts for a transverse plane located at one chord downstream of the airfoil.

Mesh	far-field exergy *via ffx*						
	$C\dot{\mathcal{E}}_m$	$C\dot{\mathcal{A}}_\phi$	$C\dot{\mathcal{A}}_{\nabla T}$	$C\dot{\mathcal{E}}_{th}^d$	CD_ε^d	$C\dot{\mathcal{E}}_{th}^i$	CD_ε^i
Tiny	4.64	83.00	1.00	0.19	**88.82**	1.18	**89.82**
Coarse	4.26	84.58	1.05	0.17	**90.04**	0.39	**90.25**
Medium	4.10	84.95	1.06	0.17	**90.28**	0.21	**90.32**
Fine	4.05	84.98	1.07	0.17	**90.26**	0.18	**90.27**
Extra fine	4.08	84.92	1.06	0.17	**90.23**	0.17	**90.23**

Table 3.4: 2D NACA 0012 Airfoil in a subsonic flow: grid convergence study. Exergy-based drag-power coefficients expressed in power counts (10^{-4}) for a plane one chord downstream of the body.

In terms of drag prediction, there is a minor underestimation of the total drag experienced by the body with reference to the near-field and far-field drag coefficients of Table 3.3 (p. 73); acceptable results, *i.e.* within one drag count, are found from the coarse grid density.

The direct method for thermal exergy calculation yields a coefficient accurate since the coarsest grid. On the contrary, the indirect method yields a coefficient that varies more but which converges towards the exact same value as the one from the direct method. As a consequence, the direct method is considered more robust.

3.2.4 *Reynolds*-number Sensitivity Analysis

Six additional medium grids (1024×256) have been generated to provide y^+ close to unity for the following *Reynolds* numbers: 6, 9, 15, 25, 35 and 50 millions based on a chord of unit length. For all cases, the incidence and freestream *Mach* number are set respectively to zero degree and to $M_\infty = 0.30$. In terms of computations, the very same settings[7] have been used and a similar convergence was observed for this range of *Reynolds* numbers.

3.2.4.1 Influence on the Flow Characteristics

In order to characterize the influence of *Reynolds* number on the anergy generation, we use the non-dimensionalized coefficients introduced in paragraph 2.2.3.1 (p. 44):

$$\zeta_{\nabla T} = \frac{\dot{\mathcal{A}}_{\nabla T}}{\dot{\mathcal{A}}_{tot}} \qquad ; \qquad \zeta_\phi = \frac{\dot{\mathcal{A}}_\Phi}{\dot{\mathcal{A}}_{tot}} \tag{3.11}$$

$$\xi_{\nabla T} = \frac{\dot{\mathcal{A}}_{\nabla T}^{turb}}{\dot{\mathcal{A}}_{\nabla T}} \qquad ; \qquad \xi_\phi = \frac{\dot{\mathcal{A}}_\Phi^{turb}}{\dot{\mathcal{A}}_\Phi} \tag{3.12}$$

Fig. 3-12 presents the evolution of these coefficients with *Reynolds* number increase. The anergy generation has been calculated in the whole mesh volume, but because the entire mechanical energy has not yet been dissipated within the CFD domain, a residual portion is leaving it. As it represents less than a power count, it is neglected in the anergy generation analysis: it would only involve a second order[8] change in the ratios ζ and ξ.

(a) Ratios of viscous and thermal anergy to total anergy generation.

(b) Ratios of turbulent to total viscous and thermal anergy generation.
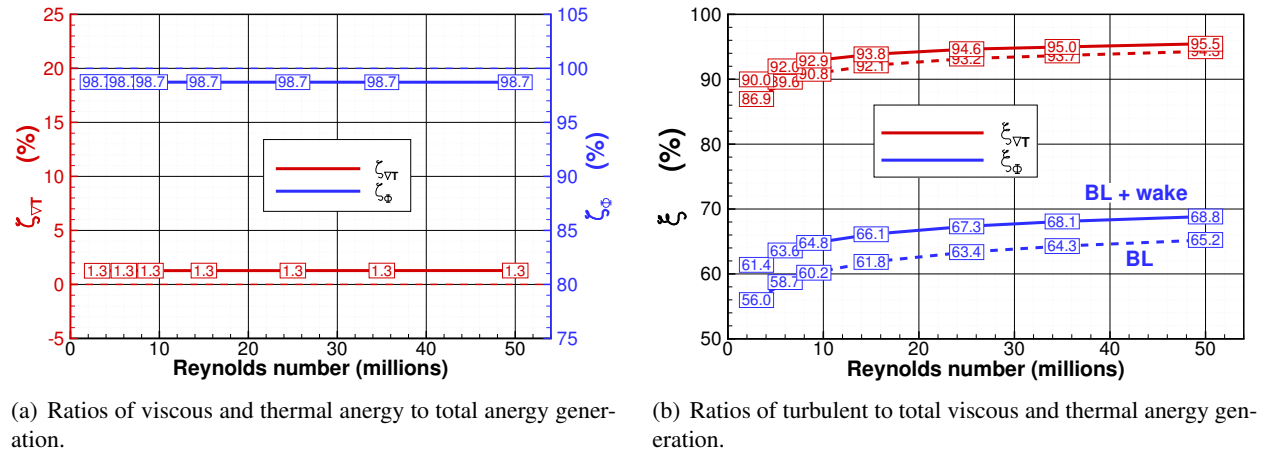
Figure 3-12: 2D NACA 0012 Airfoil in a subsonic flow: *Reynolds* number influence on anergy generation. Medium mesh.

Fig. 3-12a gives the proportion of anergy generated by viscous and thermal dissipations with reference to the total anergy generated within the computational domain. One can see that the flow is largely dominated by viscous anergy (98.7%) as compared to thermal anergy. As expected, there is no influence of the *Reynolds* number on that balance (in the range of 3 to 50 millions).

---

[7]Fully turbulent flows with the *Spalart-Allmaras* turbulence model.

[8]The mechanical (and thermal) exergy not yet dissipated accounts for less than 1% according to the wake analysis in paragraph 3.2.2.2 (p. 69).

Fig. 3-12b shows the ratio of turbulent to total anergy generation within the boundary layers (dotted lines) and in the whole computational domain (solid lines). The viscous dissipation appears mostly associated with turbulence: ξ_Φ (–) ranges from 56 to 65% in the boundary layers and from 61.4 to 68.8% if the wake is accounted for. One can see that the thermal anergy generation is even more associated with turbulence: $\xi_{\nabla T}$ (–) ranges from 86.9 to 94.3% within the boundary layers and from 90 to 95.5% when the dissipation in the wake is accounted for.

These turbulent to total dissipation ratios are higher in the wake than in the boundary layers because, as seen in Fig. 3-5b, the dissipation in the wake is dominated by turbulent phenomena.

As the *Reynolds* number increases, the dominance of the turbulent dissipation over the laminar one is reinforced.

3.2.4.2 Influence on the Accuracy of Drag Prediction

In terms of drag prediction, Table 3.5 gives the drag decomposition for four *Reynolds* numbers: 3, 9, 25 and 50 millions.

	ffd72			far-field exergy *via ffx*						
Re (M)	CD_f	CD_p	CD_{nf}	$C\dot{\mathcal{E}}_m$	$C\dot{\mathcal{A}}_\phi$	$C\dot{\mathcal{E}}_{th}$	$C\dot{\mathcal{A}}_{\nabla T}$	CD_ε	$CD_\varepsilon - CD_{nf}$	
3	76.00	14.51	90.51	2.83	86.24	0.10	1.10	**90.27**	-0.24	(-0.27%)
9	64.00	12.75	76.75	2.23	73.29	0.08	0.95	**76.55**	-0.20	(-0.26%)
25	55.00	11.21	66.21	1.83	63.31	0.07	0.82	**66.04**	-0.17	(-0.26%)
50	50.00	10.12	60.12	1.63	57.53	0.06	0.75	**59.97**	-0.15	(-0.25%)

Table 3.5: 2D NACA 0012 Airfoil in a subsonic flow: *Reynolds* number influence on drag prediction. Coefficients expressed in drag or power counts (10^{-4}) for a plane one chord downstream of the body. Medium mesh.

Between *Reynolds* numbers of 3 and 9 millions, the (viscous and thermal) anergy drops in an equivalent manner as the friction drag (-33%). Likewise, the (mechanical and thermal[9]) exergy reduces similarly to the pressure drag (-30%). The difference between the exergy-based total drag-power and the near-field drag coefficients represents about $-0.26\% \pm 0.01$ and is quasi-independent of the *Reynolds* number.

No noticeable influence of the *Reynolds* number on the accuracy of the drag prediction is observed in the range of 3 to 50 millions for fully turbulent flows. The *Moore* and *Moore* model for mean entropy production [108] is validated for mean steady subsonic flows in a range of *Reynolds* number between 3 and 50 millions.

3.2.5 Summary of the Key Findings

Low-speed ($M_\infty = 0.30$) and fully turbulent ($Re = 3 \times 10^6$) flows at zero incidence have been investigated over a 2D NACA 0012 Airfoil for which it has been shown that thermal aspects (anergy and exergy) are third order contributor to drag generation. The viscous anergy generation over the body is similar to the friction drag. The laminar component is highest at the leading edge and vanishes at the trailing edge while the turbulent dissipation is present in the wake.

A wake analysis showed that all terms behave in agreement with theoretical considerations: the mechanical and thermal exergy vanish in the far-field of the body while the total (viscous + thermal) anergy converges towards the total drag-power experienced by the body.

A family of high-quality grids provided well-converged flow solutions to assess the sensitivity of the code to grid density. The drag predicted by the exergy-based formulation is well in agreement with classical

---

[9]The direct method for thermal exergy calculation is used.

momentum-based drag prediction methods, even without correction. It underestimates slightly the total drag (99.75% ± 0.01 on a medium-density grid) and is quasi-independent on the *Reynolds* number (in the range of 3 to 50 10^6). As a consequence, the exergy-based formulation and the *Moore* and *Moore* model for mean entropy production [108] are validated for subsonic and fully turbulent flows over 2D bodies.

Now that the formulation and its numerical implementation have been validated for this simple flow, the numerical treatment of the shock discontinuities is investigated next.

3.3 Validation for Viscous and Shock Wave Phenomena in 2D Transonic Flows

The objective of this test case is to tackle the numerical treatment of the mathematically-discontinuous shock wave. To do so, we shall first investigate the influence on the flow of an increasing freestream *Mach* number to get confidence in the assessment of a transonic flow which is performed subsequently. A transonic flow at $M_\infty = 0.80$ and zero incidence is then fully characterized in terms of anergy generation over the profile and in the wake. Finally, a grid convergence study is made to assess the accuracy and robustness of the post-processing code.

Part of this study has been presented at the 49th International Symposium of Applied Aerodynamics in Lille (FR) in March 2014, see [10].

3.3.1 *Mach*-number Sensitivity Analysis

A *Mach* number range of $0.20 \leq M_\infty \leq 0.81$ at fixed *Reynolds* number ($Re = 3 \times 10^6$) is investigated for the medium mesh for which a convergence comparable to the baseline case ($M_\infty = 0.30$) was achieved.

3.3.1.1 Influence on the Flow Characteristics

Fig. 3-13 gives an insight on the dependency on the flow characteristics to compressibility. Except where mentioned otherwise, the terms are integrated within the whole computational domain[10].

(a) Predominant dissipative phenomena.   (b) Turbulent to total viscous and thermal dissipations.
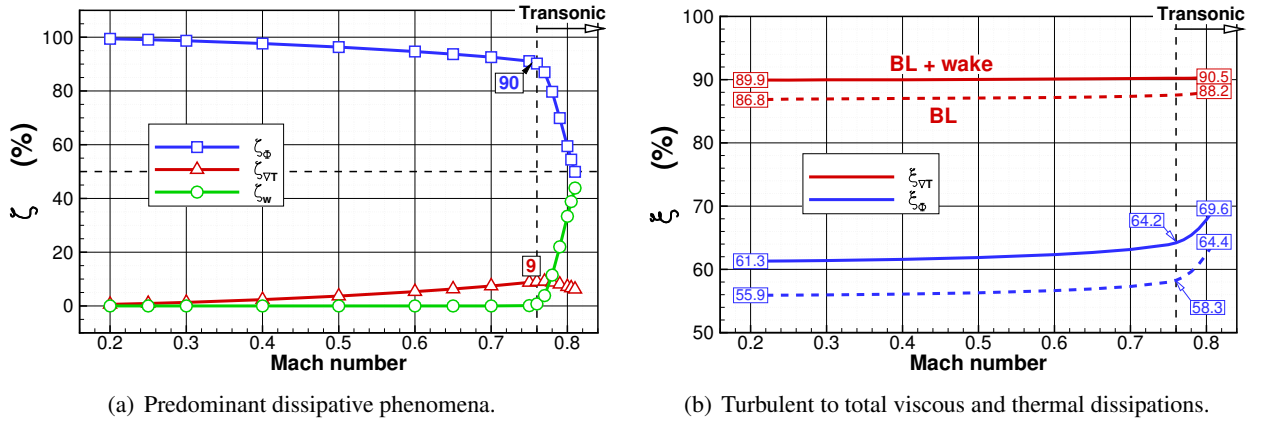
Figure 3-13: 2D NACA 0012 Airfoil at zero incidence: *Mach* number influence on anergy generation. Medium mesh.

Fig. 3-13a exhibits the predominant flow mechanisms responsible for dissipation. At low *Mach* numbers, the viscous anergy (ζ_Φ –) is almost the only mechanism. As the *Mach*-number is increased, the thermal anergy ($\zeta_{\nabla T}$ –) becomes non-negligible with a maximum of 9% reached just after the beginning of the transonic regime. At this point, the wave anergy (ζ_w –) increases steeply to represent more than 40% at $M_\infty = 0.81$ which corresponds to a normal shock *Mach* number of $M_\perp \simeq 1.35$. Conversely, the viscous anergy drops from 90% to about 50% in the transonic range under study.

Fig. 3-13b gives the ratio of turbulent to total anergy for the viscous and thermal anergy production within the boundary layers (dashed lines) and within the whole computational domain (solid lines). The

---

[10]Here again, the entire mechanical energy has not yet been dissipated within the CFD domain and a residual portion is therefore leaving it. As it represents less than a power count, it is neglected in the anergy generation analysis: it would only involve a second order change in the ratios ζ and ξ.

thermal anergy (–) appears weakly dependent on the *Mach* number and on the dissipation in the wake. As regards the viscous dissipation (–), the influence of the turbulence is reinforced with *Mach* number increase and is clearly emphasized in the transonic regime.

Even at high transonic regimes, the predominant dissipative mechanism is the viscous dissipation associated with turbulence. The thermal mixing never exceeds 10% of the total anergy generation and is therefore considered a second order effect.

3.3.1.2 Influence on the Terms of the Formulation

In order to get confidence in the performance assessment of a transonic flow solution, we first investigate the influence of freestream *Mach* number increase on the terms of the exergy-based formulation. All terms given in Fig. 3-14 have been integrated within the entire 150-chord CFD domain. As demonstrated in the previous section, the absolute value of the terms depends on the transverse plane location so that we are more interested in the trends than in the absolute values.

(a) Viscous energy and viscous anergy coefficients.

(b) Thermocompressible aspects.
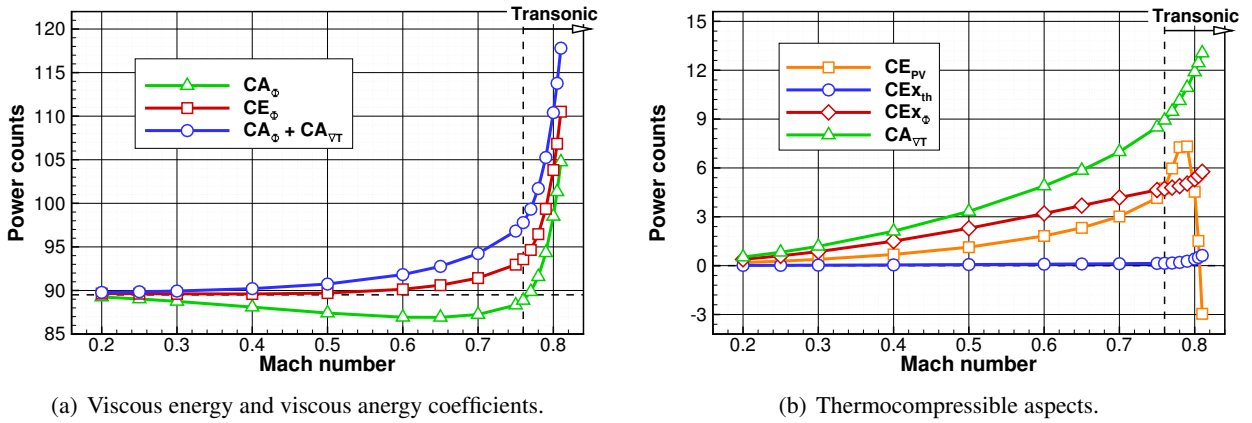
Figure 3-14: 2D NACA 0012 Airfoil at zero incidence: *Mach* number influence. Medium mesh.

Fig. 3-14a gives the terms related to viscous dissipation. The energy associated with viscous dissipation ($\dot{E}_\phi$ –) remains relatively constant for *Mach* numbers up to $M_\infty \geq 0.76$ which corresponds to the onset of the transonic regime. The anergy associated with viscous dissipation ($\dot{\mathcal{A}}_\phi$ –) has a slightly different variation with *Mach* number: due to an increasing (static) temperature within the boundary layer, the entropy generation is lower than the energy dissipated[11]. The total anergy generated (–) is monotonically increasing.

Fig. 3-14b provides the terms related to thermocompressible aspects. In parallel with the viscous dissipation rise observed in Fig. 3-14a, the thermal anergy ($\dot{\mathcal{A}}_{\nabla T}$ –) drastically increases with *Mach* numbers: the viscous exergy ($\dot{\mathcal{E}}_\phi$ –) is destroyed by thermal mixing, leaving very little thermal exergy ($\dot{\mathcal{E}}_{th}$ –). None of these terms is significantly affected by the presence of a shock wave. The term $\dot{E}_{PV}$ (–) stops being negligible, reaches a peak and then rapidly decreases towards negative values[12].

The thermal aspects become more significant at higher *Mach* numbers than for the incompressible flows.

---

[11]In other words, viscous dissipation converts kinetic energy into thermal energy, the latter potentially recoverable and convertible into mechanical work.

[12]The awkward behavior of the term $\dot{E}_{PV}$ has found to be highly-dependent on numerical settings and therefore requires further analysis.

3.3.2 Profile and Wake Analyses at M_∞ = 0.80

This subsection provides a qualitative and quantitative flow analysis of the various terms involved in the exergy-based formulation:

$$DV_\infty = \dot{\mathcal{E}}_m + \dot{\mathcal{E}}_{th} + \dot{\mathcal{A}}_\phi + \dot{\mathcal{A}}_{\nabla T} + \dot{\mathcal{A}}_w \tag{3.13}$$

The investigation is made on the medium grid density which provides a trustworthy flow solution in terms of numerics[13]. Fig. 3-15 illustrates the corresponding flow field on the medium mesh in terms of *Mach* number and anergy generation. Also, an illustration of the flow field of entropy is provided in appendix B.1 (p. 188).

(a) Field of *Mach* number.   (b) Fields of viscous anergy (top) and thermal anergy (bottom).
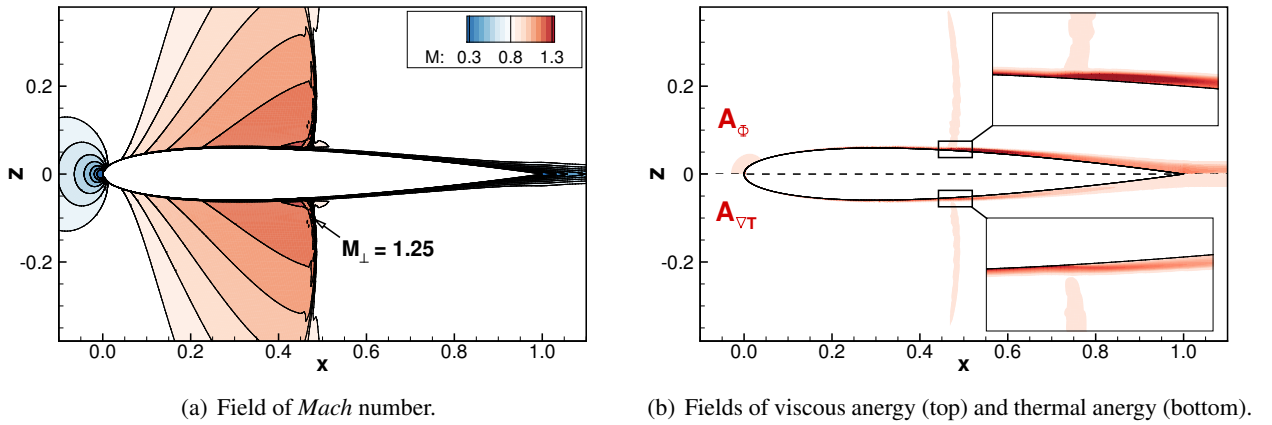
Figure 3-15: 2D NACA 0012 Airfoil in a transonic flow: transonic flow fields. Medium mesh.

The *Mach* number field is well symmetrical, with a normal shock *Mach* number of about $M_\perp \approx 1.25$ located at about $x \approx 0.5$. From Fig. 3-15b we can see that the viscous and thermal anergy generation is mostly located within the boundary layers and wake, as expected. The thickening of the boundary layer right downstream of the shock foot is clearly visible in the upper and lower zooms. Note that the boundary layer stays attached. Qualitatively speaking, the flow solutions appear physically valid.

3.3.2.1 Profile Analysis in Terms of Anergy Generation

Fig. 3-16 gives the qualitative evolution of the anergy generation over the body with reference to the (total) near-field drag coefficient.

Fig. 3-16a gives the physical decomposition of anergy generation around the profile. One can see, as for the subsonic regime in Fig. 3-6 (p. 70), a steady increase in both viscous anergy ($\dot{\mathcal{A}}_\phi$ −) and thermal anergy ($\dot{\mathcal{A}}_{\nabla T}$ −), the latter accounting for about 10 pc. A steep increase at $x = 0.5$ is observed for the total anergy outflow ($\dot{\mathcal{A}}$ −) and is associated with the shock wave. The total near-field drag is given by the solid black line to which the total anergy generated seems to converge, in agreement with Second Law considerations.

Fig. 3-16b provides the change in laminar and turbulent rates of viscous and thermal anergy generation. The laminar viscous dissipation peaks right at the leading edge and drops at half the airfoil length, which coincides with the shock position. It then presents a bump prior to vanishing in the wake. On the

---

[13]A convergence greater than 0.0001 drag count was reached for the near-field drag coefficient corresponding to a 9 orders residuals reduction of the energy equation.

(a) Evolution of the dissipation terms around the airfoil.

(b) Change in laminar (dashed lines) and turbulent (solid lines) viscous and thermal anergy generation rates.
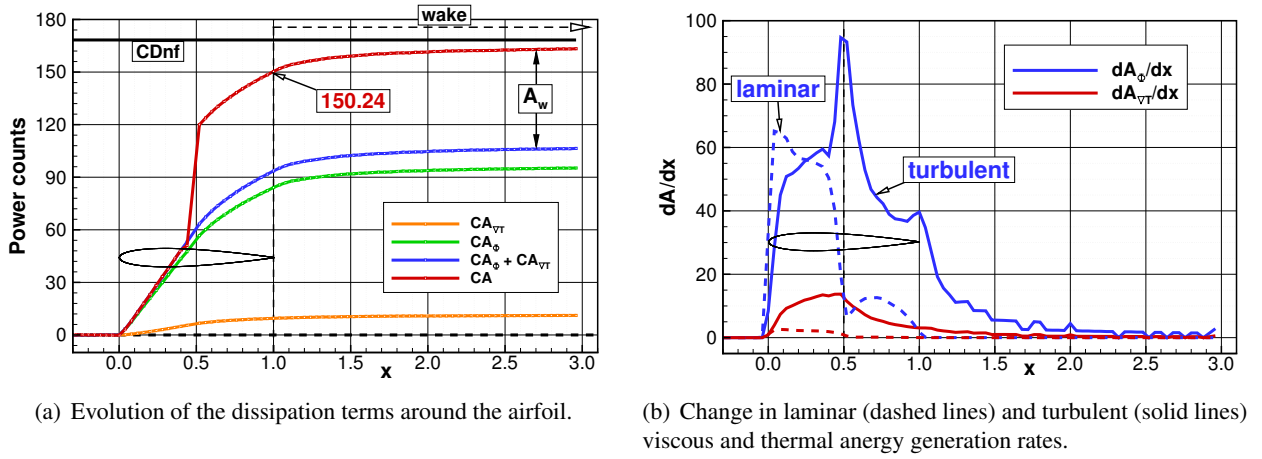
Figure 3-16: 2D NACA 0012 Airfoil in a transonic flow: profile analysis. Medium mesh.

contrary, the turbulent viscous dissipation steadily increases up to the shock position where it exhibits a peak before decreasing towards the wake.

The anergy associated with the presence of the shock is clearly identified by the total anergy outflow. The shock wave emphasizes the turbulent viscous dissipation and reduces the laminar component; their sum appearing unaffected, see ($\dot{\mathcal{A}}_\phi$ −) in Fig. 3-16a.

Quantitatively speaking, the dissipation within the boundary layers is due at ζ_ϕ^{BL} = 90% to viscous anergy; the remaining 10% being associated with thermal anergy[14]. The viscous and thermal anergy are mainly generated by turbulence within the boundary layers ξ_ϕ^{BL} = 63% and $\xi_{\nabla T}^{BL}$ = 88%.

These preliminary results suggest that the *Moore* and *Moore* model [108] is adapted for transonic flows.

3.3.2.2 Outflows Decomposition and Anergy Generation Rates in the Wake

As for the subsonic flow, a complete overview of the exergy outflows and anergy generation in the wake of the body is given by Fig. 3-17. Each term is evaluated for a downstream plane of the control volume located at a given distance of the body. The $\log$ x-axis emphasizes the region near the airfoil and all terms are expressed in power counts.

Fig. 3-17a-b show that the overall behavior of the various terms is comparable to the subsonic case exhibited in Fig. 3-6, their magnitude being however more than twice as high. After about five chords, the total mechanical energy ($\dot{\mathcal{E}}_m$ −) reduces to the streamwise kinetic power ($\dot{E}_u$ −) associated with the wake of the airfoil. The thermal exergy ($\dot{\mathcal{E}}_{th}$ −) decreases towards zero while $\dot{E}_{PV}$ (−) converges towards 4.9 pc. The viscous exergy ($\dot{\mathcal{E}}_\phi$ −) and the thermal anergy ($\dot{\mathcal{A}}_{\nabla T}$ −) slightly increase and converge towards 5.3 pc and 11.9 pc respectively.

Fig. 3-17c focuses on the dissipation occurring in the wake. Regarding viscous dissipation, there is a difference of about 5 pc between the energy ($\dot{E}_\phi$ −) and the anergy ($\dot{\mathcal{A}}_\phi$ −) associated with this phenomenon, which corresponds to the viscous exergy ($\dot{\mathcal{E}}_\phi$ − in Fig. 3-17b). The difference between the total anergy outflow ($\dot{\mathcal{A}}$ −) and the viscous + thermal anergy ($\dot{\mathcal{A}}_\phi + \dot{\mathcal{A}}_{\nabla T}$ −) is associated with the presence of the shock wave. Note that the total anergy outflow converges towards the total near-field drag (D_{nf} −).

Again, the various terms appear to qualitatively behave in agreement with the theoretical considerations given in the derivation of the formulation in paragraph 2.1.3 (p. 35).

---

[14]In agreement with the study of the influence of the *Mach* number in paragraph 3.3.1 (p. 79).

(a) Mechanical outflows.

(b) Thermocompressible aspects.

(c) Anergy generation.
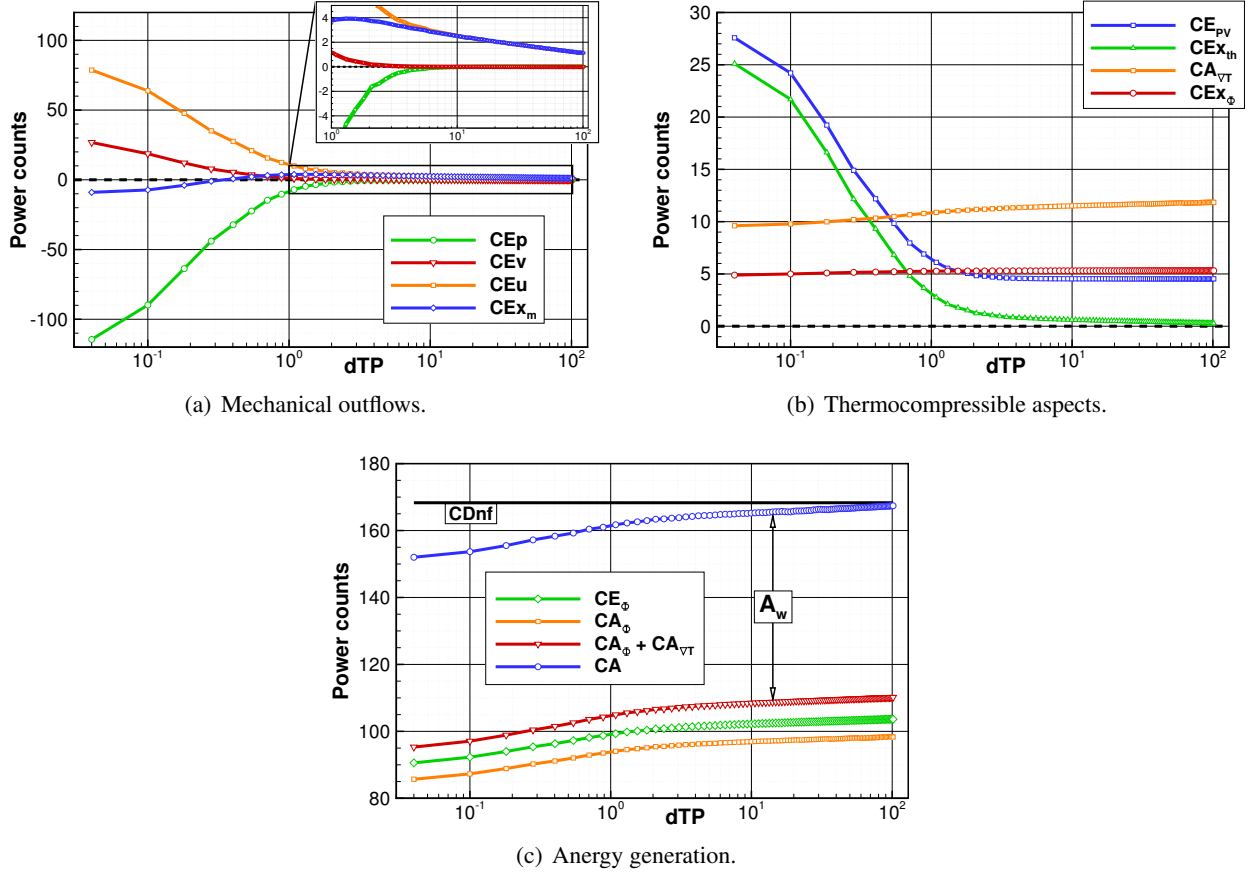
Figure 3-17: 2D NACA 0012 Airfoil in a transonic flow: wake analysis. Medium mesh.

3.3.3 Grid Convergence Study on Drag Prediction

In order to determine the dependency of the code to grid density, a grid convergence study is made. Classic momentum-based methods are used for validation purpose. The flow under investigation is viscous flow at zero incidence, $M_\infty = 0.80$ and $Re = 3 \times 10^6$.

3.3.3.1 Numerical Considerations

As far as CFD is concerned, the exact same grids and numerical settings are used to investigate this transonic flow as for the previous study of subsonic flows. A high level of convergence comparable to the subsonic case was achieved, see Fig. 3-18, both in terms of near-field drag coefficient (a) and in residuals reduction (b). The low numerical dissipation that was added did not allow convergence on the finest grid, as a consequence only four grid densities are available for this transonic case.

3.3.3.2 Momentum-based Drag Prediction

The near-field and far-field drag methods implemented in $ffd72$ are used for comparison purpose:

$$D_{nf} = D_p + D_f \qquad ; \qquad D_{ff} = D_v + D_w \qquad ; \qquad D_{sp} = D_{nf} - D_{ff}$$

where D_w is the wave drag. While the near-field approach is straightforward and unique, any far-field formulation involves some kind of arbitrariness [46]. We shall use here the default settings of the code, determined through decades of experience, except for a case-adapted choice of the shock surface.

(a) Absolute variation of the near-field drag coefficient with reference to the last iteration.

(b) Equation of Energy residuals reduction.
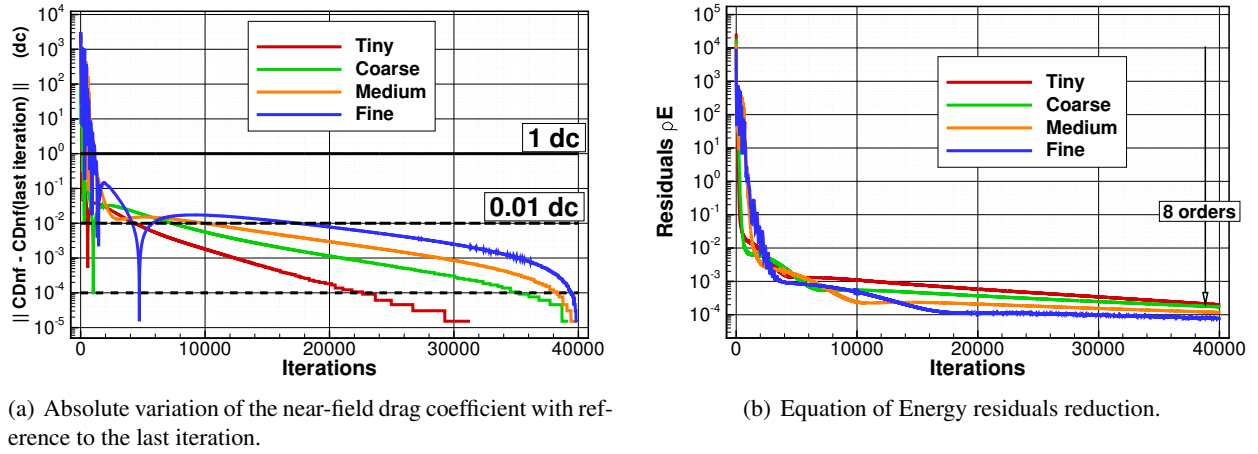
Figure 3-18: 2D NACA 0012 Airfoil in a transonic flow: convergence history with grid refinement.

Shock Wave Treatment. As detailed in paragraph 2.5.1.1 (p. 54), the shock surface determination is based on a physical shock criterion: if $\lambda_w = (\mathbf{V} \cdot \nabla \mathbf{p}) / (a \| \nabla \mathbf{p} \|) > 0.95$, the cell under consideration is tagged as being enclosed by the wave surface. However, it has been found that the addition of a number of cell layers enables the selection of the most adapted value for the wave drag coefficient[15]. The precise number of cell layers is case- and user-dependent; there is no *ultimate* value. According to existing experience, for a given flow solution (grid), the number of cell layers should be the smallest value to provide an independence of the wave drag coefficients to the number of layers. An additional criterion is to provide a monotone variation of the term with grid refinement which is usually increasing as shock waves are underestimated on coarse meshes.

As the grid is refined, the shock is better represented: the wave drag coefficient increases and becomes less sensitive to the number of cell layers, see Fig. 3-19a. Simultaneously, the spurious drag coefficient ($CD_{sp} := CD_{nf} - CD_{ff}$) reduces towards zero for the fine grid.

(a) Wave drag coefficient.

(b) Spurious drag coefficient.
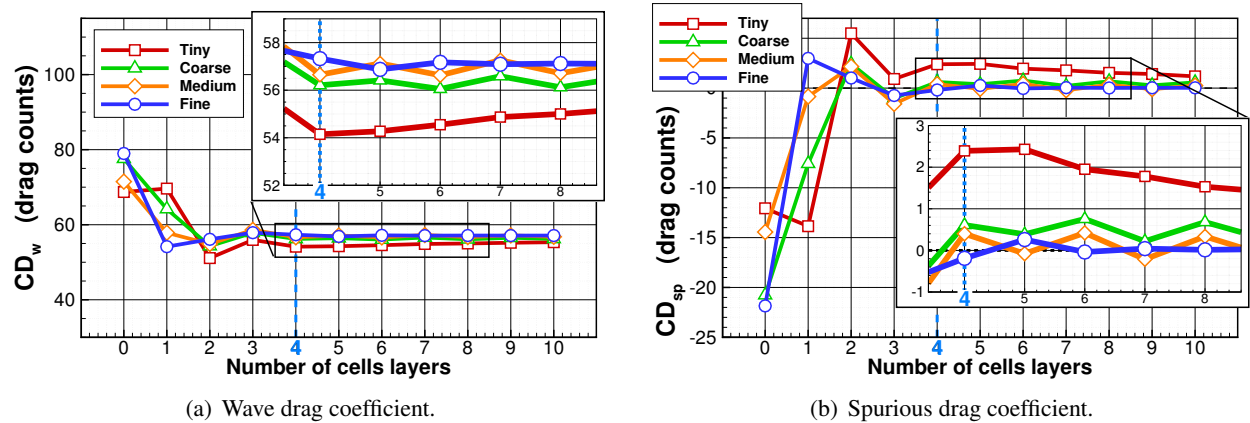
Figure 3-19: 2D NACA 0012 Airfoil in a transonic flow: shock surface determination.

As an even number of layer yields a monotonic behavior the two coefficients, in agreement with existing experience, a number of 4 additional layers was selected.

---

[15]Note that in order to preserve the boundary layers, if the cell under consideration has a positive criterion for viscous volume, the priority is given to the viscous volume.

Drag Assessment and Decomposition. Table 3.6 summarizes the drag components of the near-field and far-field approaches.

Mesh	near-field and far field drag $ffd72$						
	CD_p	CD_f	CD_{nf}	CD_v	CD_w	CD_{ff}	CD_{sp}
Tiny	110.17	62.00	**172.17**	115.67	54.55	**170.22**	1.95
Coarse	106.23	62.77	**169.00**	112.19	56.05	**168.24**	0.75
Medium	105.37	62.94	**168.31**	111.26	56.63	**167.89**	0.42
Fine	105.16	62.94	**168.10**	110.97	57.17	**168.14**	-0.04

Table 3.6: 2D NACA 0012 Airfoil in a transonic flow: near-field and far-field drag coefficients expressed in drag counts (10^{-4}) with grid refinement.

Pressure drag, partially associated with shock waves, is the predominant source for the total near-field drag. This latter coefficient reduces with grid refinement. As for the far-field method, a physical decomposition into viscous drag and wave drag is provided. Note the capability of discriminating the spurious drag which is more significant for this transonic regime[16]. The two methods converge towards a drag coefficient of 168.12 dc ±0.02.

This study confirms the consistency of the flow solutions that was suggested by the numerical analysis of the computations.

3.3.3.3 Exergy-based Drag Prediction

As for the subsonic case, application of the exergy-based formulation requires a few steps: 1) evaluation of the thermal exergy by the direct and indirect methods, 2) calculation of the wave anergy, 3) numerical correction of the viscous and thermal anergy generation in the wake and 4) determination of the domain of validity of the formulation and 5) drag assessment.

1) Direct and Indirect Thermal Exergy Methods. From the subsonic flow study we found that the direct and indirect methods for thermal exergy calculation converged towards the same value as the grid was refined. Fig. 3-20 enables to determine which method is the most suited for a transonic flow.
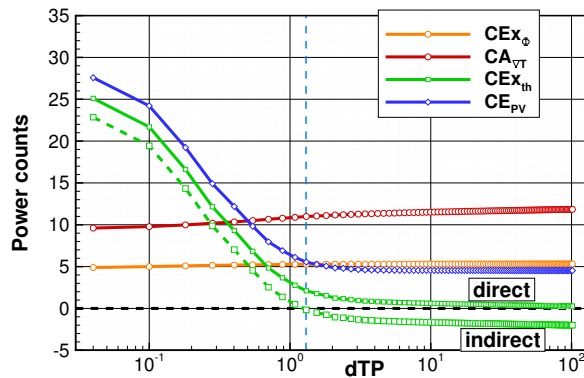
(a) Direct (dashed line) and indirect (solid line) method for thermal exergy calculation. Medium mesh.
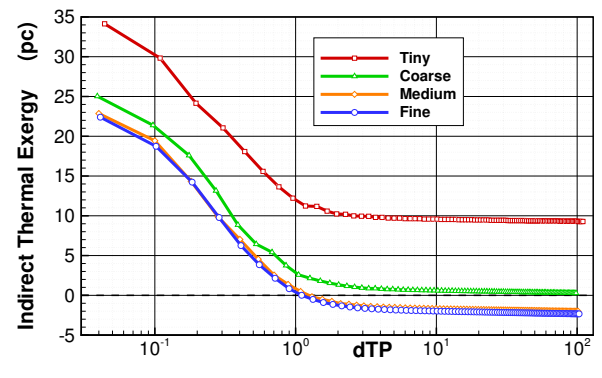
(b) Indirect method for thermal exergy calculation with grid refinement.

Figure 3-20: 2D NACA 0012 Airfoil in a transonic flow: direct and indirect methods for thermal exergy with grid refinement.

---

[16]The slightly negative value for the fine mesh is considered acceptable.

Fig. 3-20a provides the thermal exergy given by the two methods with the decomposition of the indirect method for the medium mesh. At a distance of about 1.5 chord, we notice that the thermal exergy from the indirect method (– –) becomes negative and actually converges towards a negative value, as opposed to the direct method (–) which converges towards zero, in agreement with Second Law considerations given in section 2.2.4 (p. 46).

The behavior of the viscous exergy ($\dot{\mathcal{E}}_\phi$ –) and of the thermal anergy ($\dot{\mathcal{A}}_{\nabla T}$ –) appears qualitatively correct. Also, the correction of the thermal anergy and exergy did not improve the situation, as a consequence, the last term E_{PV} (–) is suspected to be the source of the discrepancy. This idea is reinforced by the unexpected drop observed in *Mach* number study in paragraph 3.3.1 (p. 79).

Fig. 3-20b shows that there is a major effect from the grid density on the indirect method for thermal exergy calculation. As the grid is refined, starting at positive values, the thermal exergy converges towards negative ones.

In fact, the term $\dot{E}_{PV}$ is found to be highly dependent on the numerical parameters: the same flow was modeled with slightly different numerical settings (mainly dissipation) and a very different behavior was reported. As a consequence, the direct method for thermal exergy is more representative of the physics and is preferred for drag prediction.

2) Local Shock Wave Treatment. As described in paragraph 2.5.1.1 (p. 54), the local treatment of the shock wave requires the determination of the surface $\mathcal{S}_w$. This is achieved through the procedure existing in the $ffd72$ code. All terms related to the definition of the wave anergy are given in Fig. 3-21.

(a) Wave anergy coefficient.

(b) Sum of the neglected terms.
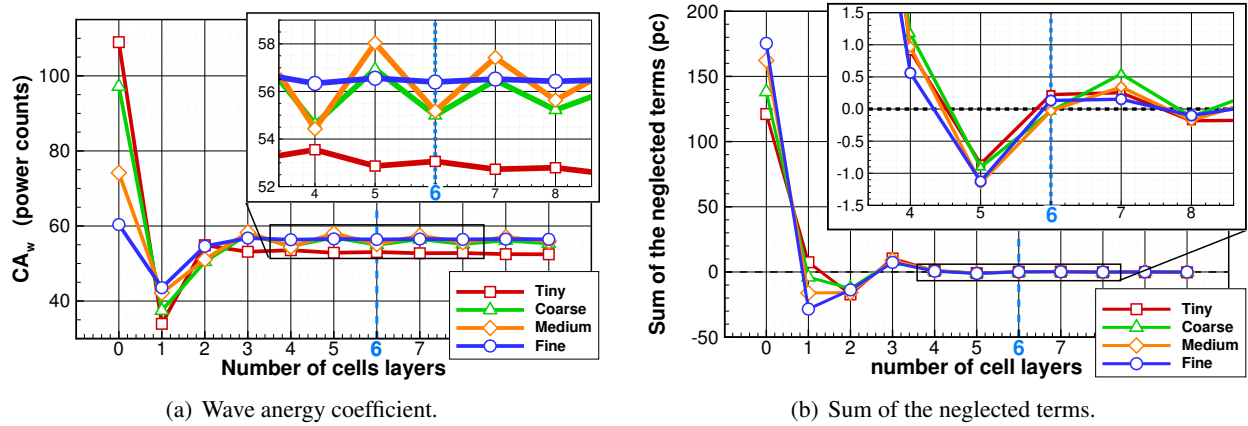
Figure 3-21: 2D NACA 0012 Airfoil in a transonic flow: local shock wave treatment with grid refinement.

Fig. 3-21a provides the anergy massflow across the wave surface which is the main criterion for the selection of the number of cells layers. As the grid is refined, the sensitivity of the coefficient to the number of cell layers decreases and eventually becomes *quasi*-independent for the finest mesh[17]. As an even number of layers provides a monotone variation of the wave anergy, the value of 6 is suitable.

Fig. 3-21b yields the sum of the neglected terms for the shock surface. One can see that values below 0.5 are obtained for all grids for cell layers greater than 6. The best result would be obtained for 8 layers but 6 is considered a good compromise in order to build a shock surface as thin as possible[18].

---

[17]Nevertheless, the sensitivity of this term to grid density appears greater than that of the wave drag coefficient in the $ffd72$ code, see Fig. 3-19 (p. 84).

[18]Normal steady shocks thickness is of the order of magnitude of the mean free path or less [118].

The order of magnitude of the wave anergy is very close to the wave drag determined by the well-tried $ffd72$ software, which tends to validate the approach. One has to recognize that the choice of the number of cell layers is flow- and user-dependent and therefore entails some kind of arbitrariness.

Fig. 3-22 illustrates the wave volume corresponding to the addition of 6 cell layers with fields of entropy change.
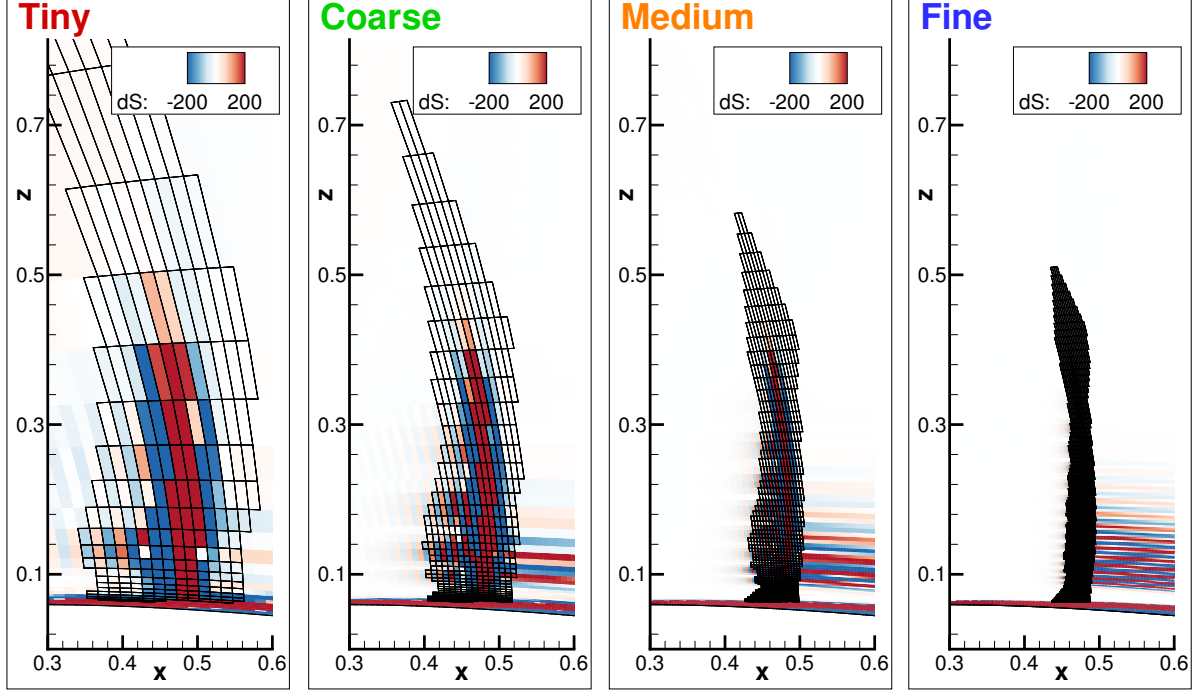
Figure 3-22: 2D NACA 0012 Airfoil in a transonic flow: contours of entropy variation and cells contained within the shock surface with grid refinement.

The theoretically-discontinuous phenomenon is numerically spread over a finite number of cells: regions of increase in entropy (red) are followed by regions of reduction (blue). This explains the oscillatory behavior observed for the wave anergy coefficient in Fig. 3-21a.

As the grid is refined the volume within the shock surface clearly diminishes and the flow phenomenon is better defined: both in terms of prediction (CFD) and numerical treatment ($ff\chi$).

One can also see that the boundary layer is relatively well preserved except for the coarsest grid where some cells can be considered to belong more appropriately to the boundary layers. This observation is verified numerically: the viscous and thermal anergy computed within the wave volume

$$\int_{\mathcal{V}_w} \frac{T_\infty}{T} \Phi_{eff} \, \mathrm{d}\mathcal{V} \qquad \text{and} \qquad \int_{\mathcal{V}_w} \frac{T_\infty}{T^2} k_{eff} (\nabla \mathbf{T})^2 \, \mathrm{d}\mathcal{V}$$

accounts each for less then 0.20 pc.

3) Accuracy Correction. Because accuracy is of utmost importance for an efficient drag prediction method, a numerical correction of the anergy generation was introduced in paragraph 2.5.1.2 (p. 55). Its basic idea is to balance the underestimation of the viscous and thermal terms caused by grids too coarse to allow an accurate calculation of the velocity and temperature gradients. To ensure the consistency of the exergy analysis with the flow solution, the missing anergy that is not captured by $\dot{\mathcal{A}}_\phi$ and $\dot{\mathcal{A}}_{\nabla T}$ must therefore be evaluated:

$$\Delta \dot{\mathcal{A}} := T_\infty \int_{\mathcal{S}_O} \rho \, \delta\mathsf{s} \, (\mathbf{V} \cdot \mathbf{n}) \, \mathrm{d}\mathcal{S} \; - \; (\dot{\mathcal{A}}_\phi + \dot{\mathcal{A}}_{\nabla T} + \dot{\mathcal{A}}_w + \dot{\mathcal{A}}_{qO}) \qquad (3.14)$$

Fig. 3-23a gives the evolution of $\Delta\dot{\mathcal{A}}$ in the wake of the airfoil for the three available grids. The second step is to add this component to the total drag-power initially determined, see Fig. 3-23b.

(a) Missing (not captured) anergy $\Delta\dot{\mathcal{A}}$.

(b) Total drag-power coefficient.
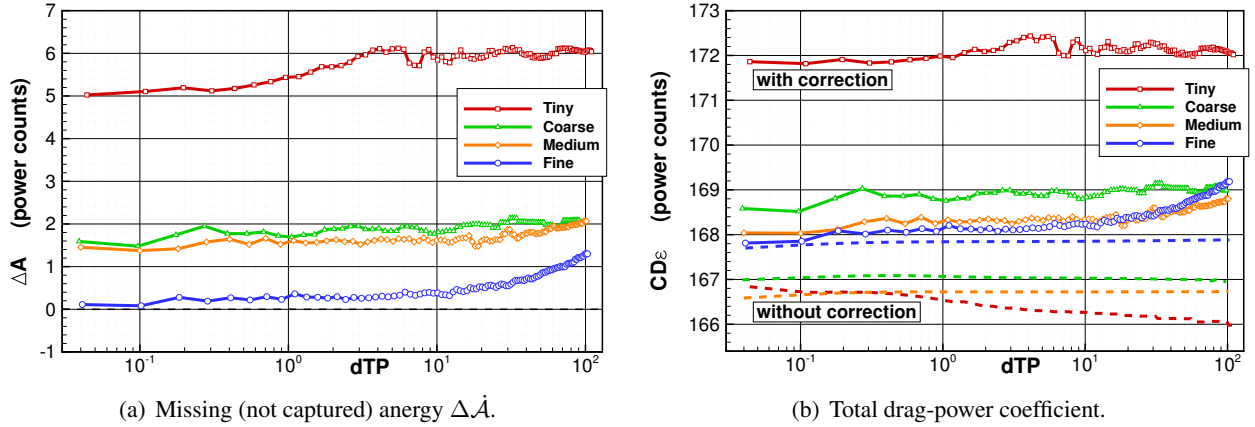
Figure 3-23: 2D NACA 0012 Airfoil in a transonic flow: influence of the numerical correction versus transverse plane position.

Fig. 3-23a gives the evolution of the $\Delta\dot{\mathcal{A}}$ coefficient in the wake. One can see that it accounts for 5-6 pc for the coarsest mesh and that it decreases towards zero as the grid is refined. From the raise observable on the two finest meshes at a distance greater than 10 chords, we consider that the correction is valid in the mid-field of the airfoil, *i.e.* within a few body length (≤ 10).

Fig. 3-23b enables a comparison between the total drag-power coefficient with or without correction. As expected, the difference decreases as the grid is refined. The correction seems very effective within a few body lengths.

Now that the total missing anergy has been identified, the last step consists of its attribution to the viscous anergy and to the thermal anergy. One must therefore determine in what proportion the dissipation in the wake would contribute to each term. From the profile analysis in paragraph 3.3.2.1 (p. 81), we found that the ratio of viscous to total anergy within the boundary layers was about $\zeta_\phi^{BL} = 90\%$. We assume that the dominance of the viscous dissipation over the thermal dissipation is reinforced in the wake of the body $\zeta_\phi^{wake} \geq \zeta_\phi^{BL}$ and therefore a fixed value was chosen:

$$\zeta_\phi^{wake} = 0.95 \qquad ; \qquad \zeta_{\nabla T}^{wake} = 0.05 \qquad (3.15)$$

In other words, 95% of the missing anergy is added to the viscous anergy and the remaining 5% is added to the thermal anergy; the corresponding coefficients are depicted in Fig. 3-24.

4) Domain of Validity of the Formulation.   The three terms neglected in the approximated formulation are given in Fig. 3-25a for the medium mesh. We note a very similar behavior in this transonic flow as in the subsonic flow investigated in section 3.2 (p. 67). Also, very little influence of the grid density is observed, see Fig. 3-25b.

We can therefore consider that the transverse plane should be located at a distance greater or equal to one chord. The transverse plane that delimits the control volume is located 1.5 chords downstream of the airfoil, see Fig. 3-26 for the tiny (a) and medium (b) grids.

Again, the distance given in the post-processing code is highlighted by the green dashed line. One can see that for a given value chosen by the user, the exact location of the transverse plane actually slightly depends on the grid spatial discretization.

(a) Viscous anergy.
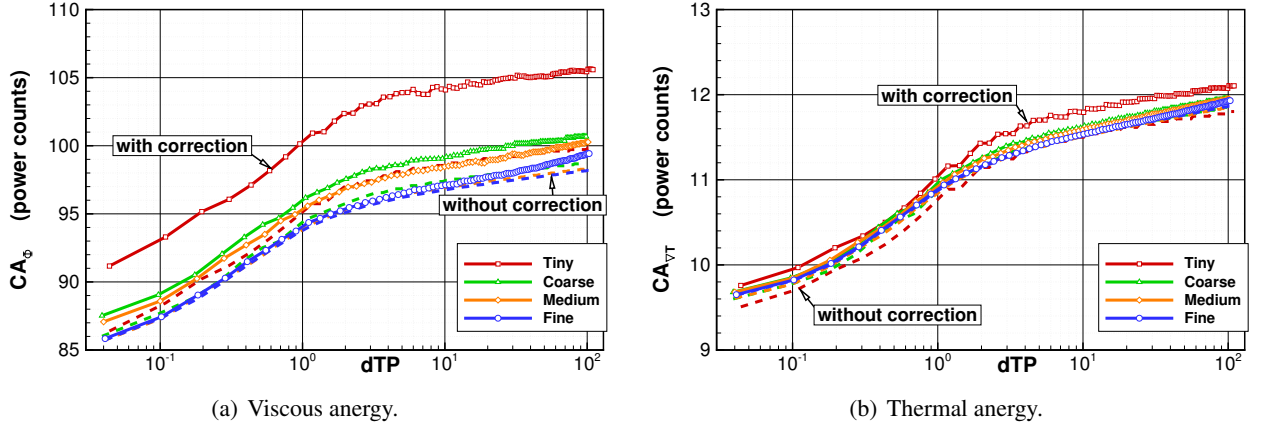
(b) Thermal anergy.

Figure 3-24: 2D NACA 0012 Airfoil in a transonic flow: viscous and thermal anergy generation in the wake with or without correction.

(a) All three neglected terms. Medium mesh.

(b) Sum of the neglected terms with grid refinement.
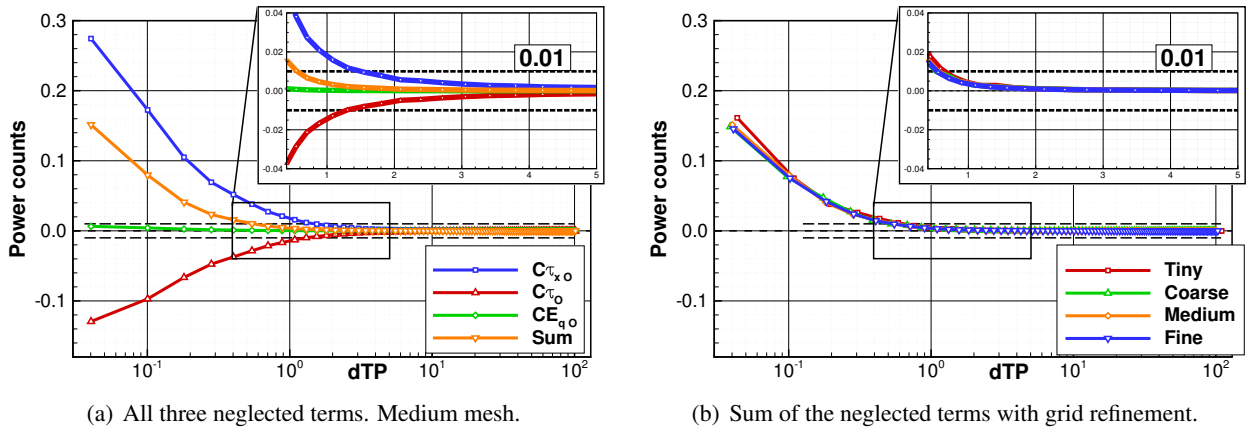
Figure 3-25: 2D NACA 0012 Airfoil in a transonic flow: neglected terms versus transverse plane position and grid refinement.

(a) Tiny grid.

(b) Medium grid.
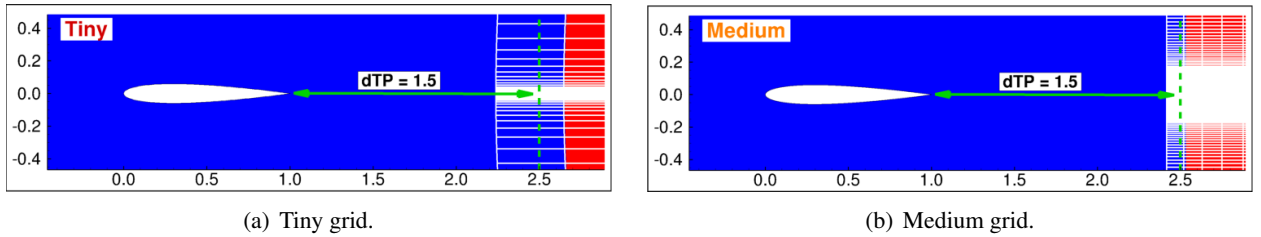
Figure 3-26: 2D NACA 0012 Airfoil in a transonic flow: control volume definition for drag prediction.

5) Drag Assessment. Finally, Table 3.7 gives the magnitude of the exergy terms, with or without correction, evaluated for a plane located 1.5 chords downstream of the body. A monotonic increase with mesh refinement is observed for the three dissipative phenomena. Such trend is however not obtained for the mechanical $\dot{\mathcal{E}}_m$ and thermal $\dot{\mathcal{E}}_{th}$ exergy outflows, which is somewhat undesirable. This may be explained by the difference in transverse plane location, as illustrated in Fig. 3-26.

The influence of the numerical correction for an accurate estimation of the viscous and thermal anergy generation is obvious. Most importantly, one can see a high agreement between the total drag-power coefficient $CD_{\dot{\varepsilon}}^c$ and the total near-field drag coefficient CD_{nf}: the correction effectively provides a drag prediction in agreement with the flow solution. Both methods account for the spurious (numerical) entropy

89

Mesh	far-field exergy *via ffx*							CD_ε	CD_ε^c	CD_{nf}
	$C\dot{\mathcal{E}}_m$	$C\dot{\mathcal{E}}_{th}$	$C\dot{\mathcal{A}}_w$	$C\dot{\mathcal{A}}_\phi$	$C\dot{\mathcal{A}}_\phi^c$	$C\dot{\mathcal{A}}_{\nabla T}$	$C\dot{\mathcal{A}}_{\nabla T}^c$			
Tiny	4.25	1.71	53.06	96.41	101.79	11.03	11.31	**166.45**	**172.12**	172.17
Coarse	3.96	1.83	54.99	95.23	96.91	11.05	11.14	**167.06**	**168.83**	169.00
Medium	3.91	1.78	55.17	94.82	96.32	11.04	11.12	**166.72**	**168.30**	168.31
Fine	3.96	1.84	56.40	94.60	94.89	11.04	11.05	**167.84**	**168.14**	168.10

Table 3.7: 2D NACA 0012 Airfoil in a transonic flow: exergy-based drag-power coefficients expressed in power counts (10^{-4}) for a plane 1.5 chords downstream the body.

contained in the flow solution (and discriminated by the far-field drag method).

3.3.4 Summary of the Key Findings

The extension of the exergy-based formulation to transonic flows over a 2D NACA 0012 Airfoil was made by first investigating the effect on *Mach* number increase on the flow characteristics and on the terms of the formulation in the range of $0.20 \leq M_\infty \leq 0.81$. For high subsonic flows, the viscous dissipation remains the dominant physical mechanism responsible for anergy generation. At the onset of the transonic regime the wave anergy becomes an important source which eventually could become predominant. The thermal anergy never exceeds 10% of the total anergy generation. The presence of the shock wave emphasizes the turbulent dissipation over the laminar one.

As for the subsonic flows, a wake analysis showed that all terms behave in agreement with theoretical considerations given in paragraph 2.3.1.1 (p. 48): the mechanical and thermal exergy vanish in the far-field of the body while the total (viscous + thermal + wave) anergy converges towards the total drag-power experienced by the body, as expected. It was however highlighted that the indirect numerical method for thermal exergy calculation did not yield a coefficient that converges to zero, which is expected as a Second Law-satisfying requirement. As a consequence, it is suggested that the direct method should be preferred.

The numerical treatment of the theoretically-discontinuous shock wave by a method relying on the definition of a shock surface has been introduced. Results in close agreement to the well-tried far-field drag approach of VAN DER VOOREN and DESTARAC [46] have been obtained, thereby validating the method for wave anergy calculation.

Additionally, the numerical correction for an accurate total drag prediction introduced in paragraph 2.5.1.2 (p. 55) was calibrated. It relies on the evaluation of the *missing* anergy not captured by the viscous and thermal anergy terms. This missing anergy is attributed to each component in agreement with its proportion within the boundary layers. The corresponding drag predicted by the exergy-based formulation is well in agreement with classical momentum-based drag prediction methods, especially with the near-field approach. As a consequence, the post-processing tool *ffx* is validated for transonic and fully turbulent flows over 2D bodies.

Now that the formulation and its numerical implementation have been validated for viscous subsonic and transonic flows over 2D bodies, transonic flows over 3D lifting bodies are investigated next.

3.4 Validation for Viscous, Shock Wave and Lift-induced Vortices Phenomena in 3D Transonic Flows

The objective of this section is to add the lift-induced vortices to the viscous and shock wave phenomena investigated previously. This test case represents a complex flow that features all phenomena of interest when dealing with external flows. It is therefore an important step towards the treatment of a more complex geometry in a transonic flow, like the wing-body configuration investigated in section 3.5 (p. 101). A sensitivity analysis of the numerical correction for accuracy to turbulence models is also performed to validate the correction for lift-induced vortices.

3.4.1 Test Case Presentation

3.4.1.1 Computations of the Flow Solutions

Geometry and Grid.   The geometry consists in a rectangular wing based on a NACA 0012 airfoil of unit length and of span length 4. The tip of the wing is rounded. The grid is made up of two symmetrical blocks as illustrated in Fig. 3-27a and contains a total of 1.2 millions elements. The C-type grid extends 30 chords in all directions and provides a y^+ lower than unity. Note that only one mesh density has been generated[19].

(a) Overview of the two-blocks grid with wing surface discretization.

(b) Typical transonic flow solution.
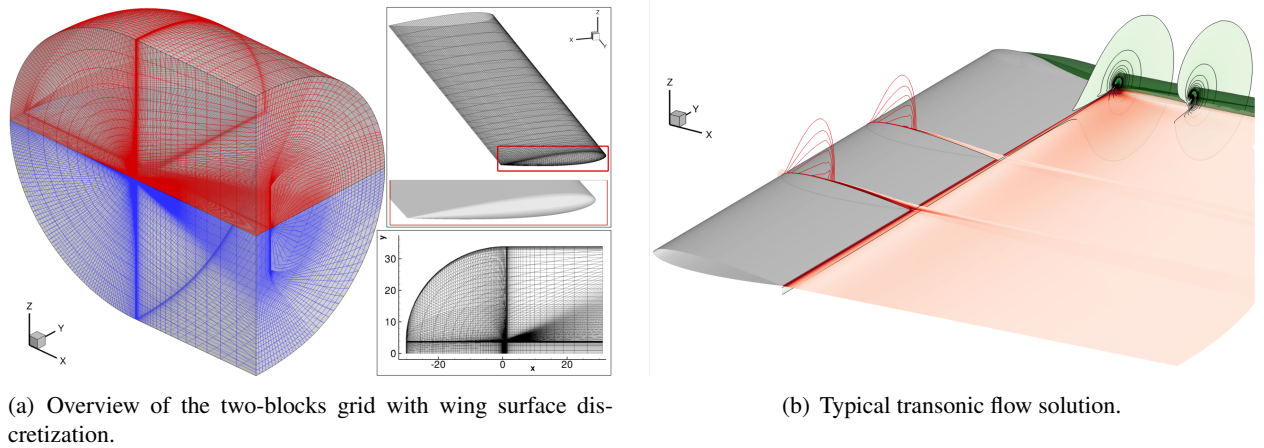
Figure 3-27: 3D rectangular Wing in a transonic flow: two-blocks grid and transonic flow field.

A fully turbulent ($Re_c = 1.3 \times 10^6$) and transonic ($M_\infty = 0.75$) flow at $3 \deg$ incidence was computed and is illustrated in Fig. 3-27b. We can distinguish the presence of a shock wave *via* the two *Mach* number isolines (red) as well the dissipation occurring in the boundary layers and in the wake: the first slice gives the field of viscous anergy while the second slice the one of thermal anergy. Also, the presence of the lift-induced vortices is highlighted by the isosurfaces of transverse kinetic energy (green).

Turbulence Models.   The influence on the drag prediction of the post-processing code has been studied with four different turbulence models implemented in the Onera-*elsA* flow solver [35, 70]. A brief description of their main characteristics is given:

k–ω - *Kok* [83]: this type of model includes two extra transport equations to represent the turbulent properties of the flow. The first transported variable is turbulent kinetic energy, k. The second transported variable in this case is the specific dissipation, ω. It is the variable that determines the scale of the turbulence, whereas the first variable, k, determines the energy in the turbulence. KOK proposed an

---

[19] By ESQUIEU (former ONERA) and made available by MÉHEUT (ONERA).

extension of the *Wilcox* model in order to reduce the dependency of the solution to the imposed value of ω at infinity.

k–ω - *Menter* [106]: the SST correction proposed by MENTER relies on the observation that for models with two transport equations using the eddy viscosity concept, the ratio of the shear stress τ to the value of ρk is proportional to the ratio of production over dissipation of turbulent kinetic energy, whereas in experiments this ratio is found to be relatively constant in a large part of the boundary layer. In the case of flows in the presence of positive pressure gradients, the ratio can be definitely higher than one which leads to overestimation of the shear stress. This inconsistency is cured by a limitation of the eddy viscosity coefficient by introducing an additional function.

k–l - *Smith* [153]: the model of SMITH is a k–l turbulence model with two transport equations; l is a characteristic length of the scale of turbulent structures. Among the strong points of this model, the author quotes its low sensitivity to the distribution of the grid points close to the wall and its aptitude for better taking into account the compressibility effects than the k–ϵ type models.

Spalart-Allmaras [156]: this model uses one transport equation for the kinematic viscosity $\tilde{\nu}$ which, far from the walls, merges with $\nu_t = \mu_t/\rho$. On the basis of a *convection = production + diffusion* form for free flows, this model adds the terms necessary to obtain a logarithmic zone in the velocity profiles, then those for wall effects. This is one of the most popular turbulence models for external steady flows and serves as a reference in the following analysis

We are not particularly interested in the differences in the predicted flow fields, but rather on any discrepancy the turbulence model may produce in the performance prediction made by the post-processing code *ffx*.

Convergence. The convergence of the computations is depicted in Fig. 3-28 for each turbulence model.
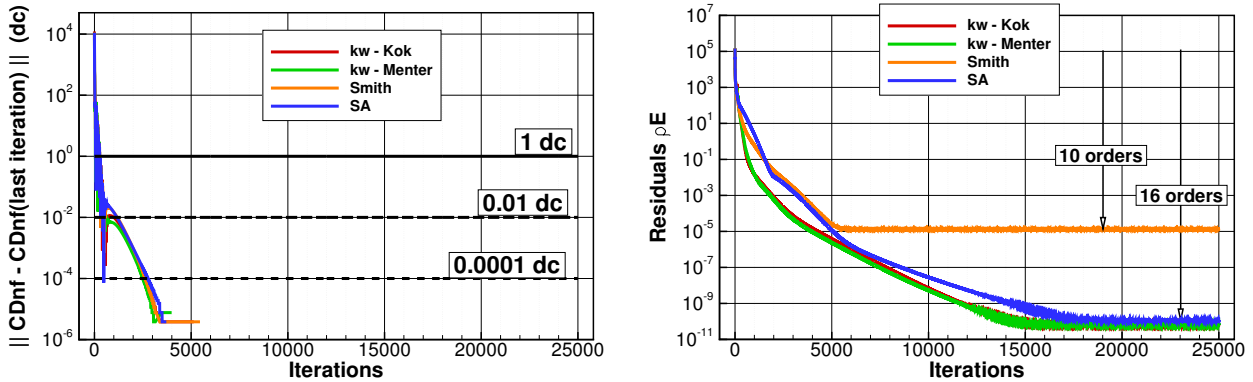
(a) Absolute variation of the near-field drag coefficient with reference to the last iteration.

(b) Equation of Energy residuals reduction.

Figure 3-28: 3D rectangular Wing in a transonic flow: convergence history with different turbulence models.

From Fig. 3-28a, one can see that the total near-field drag coefficient rapidly reaches variations well below 10^{-5} dc which corresponds to *machine zero*. As regards global residuals reduction, the equation of energy reaches a plateau after a 10 orders reduction for the model of *Smith*, and a 16 orders reduction for the three other models, see Fig. 3-28b.

3.4.1.2 Momentum-based Drag Methods

Traditional near-field and far-field drag approaches are first given to have a quantitative appreciation of the flow solutions. For this transonic flow, we simply have to choose the number of cell layers that define the wave surface before applying the post-processing code $ffd72$.

Shock Surface Determination. Fig. 3-29 gives the two basic criteria to choose the number of cell layers to be added for the definition of the shock surface.

(a) Wave drag coefficient.

(b) Spurious drag coefficient.
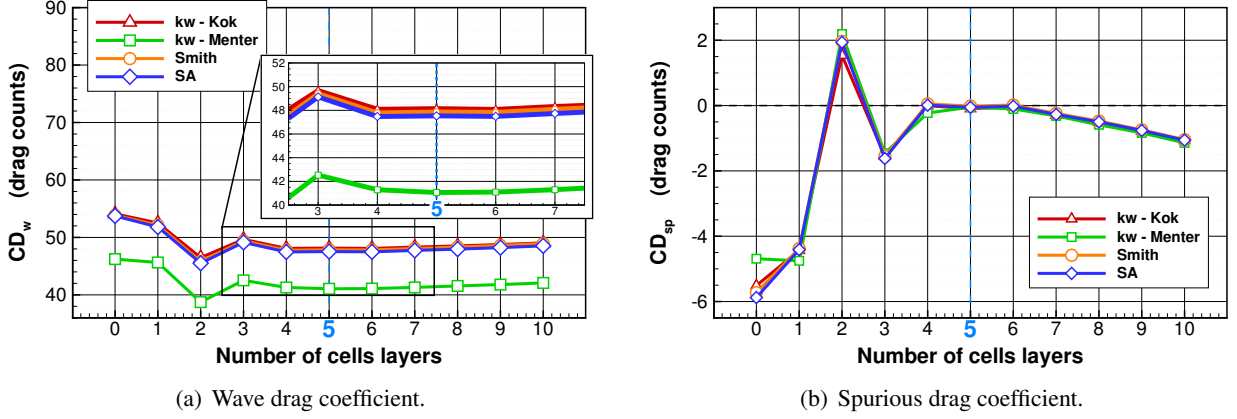
Figure 3-29: 3D rectangular Wing in a transonic flow: wave drag determination from $ffd72$.

From Fig. 3-29a, we observe a low dependency of the wave drag coefficient to the number of cell layers. The k–ω model of *Menter* yields a slightly lower wave drag around 41 dc while all three other turbulence models predict a wave drag around 48 dc. Fig. 3-29b gives the variation of the spurious drag coefficient $CD_{sp} = CD_{nf} - CD_{ff}$. One can see that for values between 4 and 6, there is very little spurious drag. In terms of drag prediction, 5 cell layers are chosen for the definition of the shock surface.

Drag Decomposition. Table 3.8 gives the near- and far-field drag decomposition from the $ffd72$ code:

$$D_{nf} = D_p + D_f \qquad ; \qquad D_{ff} = D_v + D_i + D_w \qquad ; \qquad D_{sp} = D_{nf} - D_{ff}$$

where D_i is the lift-induced (or vortex) drag.

Turbulence Model	near-field drag *via* $ffd72$			far-field drag *via* $ffd72$				
	CD_f	CD_p	CD_{nf}	CD_v	CD_i	CD_w	CD_{ff}	CD_{sp}
k-ω *Kok*	66.25	143.20	**209.46**	116.00	45.41	48.14	**209.55**	-0.09
k-ω *Menter*	67.74	142.83	**210.57**	125.97	43.59	41.06	**210.62**	-0.05
Smith	66.06	143.89	**209.95**	116.55	45.56	47.86	**209.97**	-0.02
SA	64.95	144.17	**209.12**	116.07	45.58	47.53	**209.18**	-0.05

Table 3.8: 3D rectangular Wing in a transonic flow: near-field and far-field drag coefficients .

The near-field drag coefficients are in excellent agreement with a mean value of 209.78 and a very little deviation of ± 0.8 dc. However, the decomposition into pressure drag and friction drag exhibits a slightly different balance according to each turbulence model. The *SA* model gives the lowest friction drag while the k–ω model of *Menter* yields the highest value (+2.79 dc). Less difference is observed for the pressure drag.

The far-field drag coefficients are also in excellent agreement with a mean value of 209.83 and the same deviation of ± 0.8 dc. The choice of flow regime yields lift-induced vortices and shock wave phenomena of

appropriate intensity (45-48 dc). The k–ω model of *Menter* yields lower induced drag and wave drag but a higher viscous drag, which is consistent with the observations made on the near-field drag.

Finally, the low levels of spurious drag, even if slightly negative for all turbulence models, suggest trustworthy flow solutions.

3.4.2 Wing and Wake Analysis in Terms of Anergy Generation

Before predicting the drag experienced by the body, an assessment of the flow in terms of anergy generation is made. First the production of laminar and turbulent viscous and thermal anergy over the wing is investigated. Then, the wake is analyzed regarding the theoretical balance between the rates of anergy generation and exergy destruction.

3.4.2.1 Laminar and Turbulent Viscous and Thermal Anergy Generation

Qualitatively speaking, Fig. 3-30 gives the change in the rates of laminar and turbulent generation of viscous and thermal anergy over the wing, for all four turbulence models.

(a) Viscous anergy generation.

(b) Thermal anergy generation.
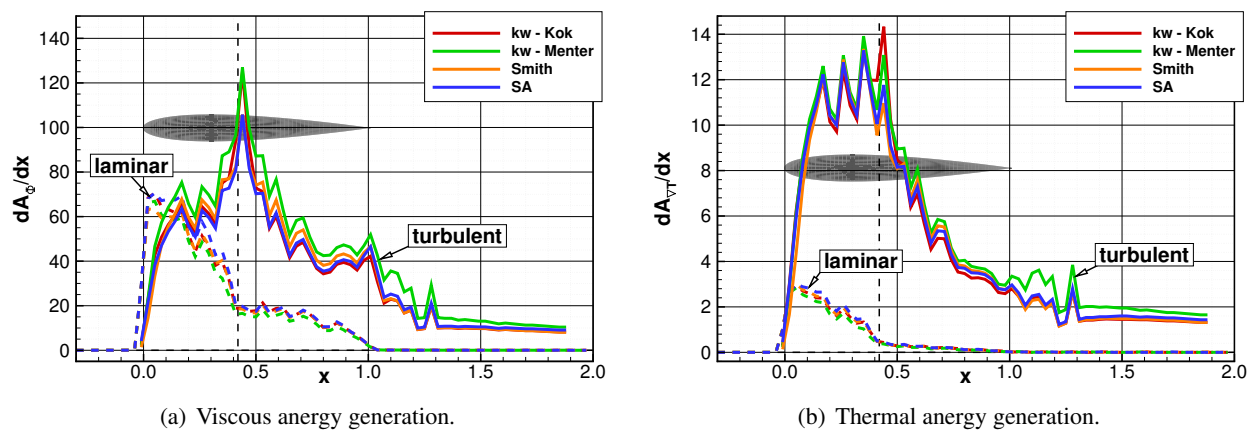
Figure 3-30: 3D rectangular Wing in a transonic flow: laminar (dashed lines) and turbulent (solid lines) anergy generation around the wing, for all four turbulence models.

In Fig. 3-30a, the laminar dissipation (dashed lines) is high right at the leading edge and then reduces towards the shock and vanishes completely at the trailing edge while the turbulent viscous dissipation (solid lines) exhibits a peak right at the shock position ($x \approx 0.42$) and slowly decreases towards the wake. The thermal anergy illustrated in Fig. 3-30b is one order of magnitude lower than the viscous anergy. Except for the shock-related peak that is absent, the distribution over the wing is very similar to one of the viscous anergy, both for the laminar and for the turbulent component.

As regards turbulence modeling, there seems to be little impact on the overall distribution of these dissipative phenomena[20]. With reference to the *SA* model (**–**), the k–ω model of *Menter* (**–**) slightly emphasizes the turbulent dissipation and reduces the laminar one. More quantitative information is given in Table 3.9 which summarizes the turbulent and laminar viscous and thermal anergy generated within the boundary layers as well as the corresponding dissipative ratio ξ.

On average, the viscous dissipation is associated with $\bar{\xi}_\phi^{BL} = 65.6\% \pm 4.2$ with turbulence, at 70% for the k–ω model of *Menter* and with 63% for the *SA* model. Similarly, thermal anergy is associated with

---

[20]For the *SA* model, all these observations are consistent with those made for the NACA 0012 Airfoil in the transonic flow studied in section 3.3 (p. 79).

Turbulence Model	$C\dot{\mathcal{A}}_\Phi^{turb}$	$C\dot{\mathcal{A}}_\Phi^{BL}$	ξ_ϕ^{BL}	$C\dot{\mathcal{A}}_{\nabla T}^{turb}$	$C\dot{\mathcal{A}}_{\nabla T}^{BL}$	$\xi_{\nabla T}^{BL}$	ζ_ϕ^{BL}
k-ω *Kok*	55.61	86.07	64.6 %	7.37	8.31	88.7 %	91.2 %
k-ω *Menter*	64.27	92.02	69.8 %	7.75	8.60	90.1 %	91.5 %
Smith	56.42	86.07	65.6 %	7.20	8.16	88.2 %	91.3 %
SA	53.77	86.03	62.5 %	7.33	8.34	87.9 %	91.6 %

Table 3.9: 3D rectangular Wing in a transonic flow: turbulent and laminar viscous and thermal anergy generation within the boundary layers.

$\bar{\xi}_{\nabla T}^{BL}$ = 88.7% ± 1.4 with turbulence, at 90% for the k–ω model of *Menter* and with 88% for the *SA* model. All turbulence model predict in excellent agreement that dissipation is associated with $\bar{\zeta}_\phi^{BL}$ = 91.4% ± 0.2 to viscous dissipation; the thermal anergy generation being a second order contributor to the total anergy generated, and therefore to the drag experienced by the body. From the study made in paragraph 3.3.1 (p. 79) on the *Mach* number influence on the flow characteristics, we know that these ratios would grow if the wake was accounted for, especially for the thermal anergy.

3.4.2.2 Wake Analysis in Terms of Exergy Destruction and Anergy Generation

To highlight the need for accuracy correction for this lifting case, Fig. 3-31 gives the rates of production of anergy ($\mathrm{d}\dot{\mathcal{A}}/\mathrm{d}x$) and of destruction of exergy ($\mathrm{d}\dot{\mathcal{E}}/\mathrm{d}x$) in the wake of the wing for each turbulence model.
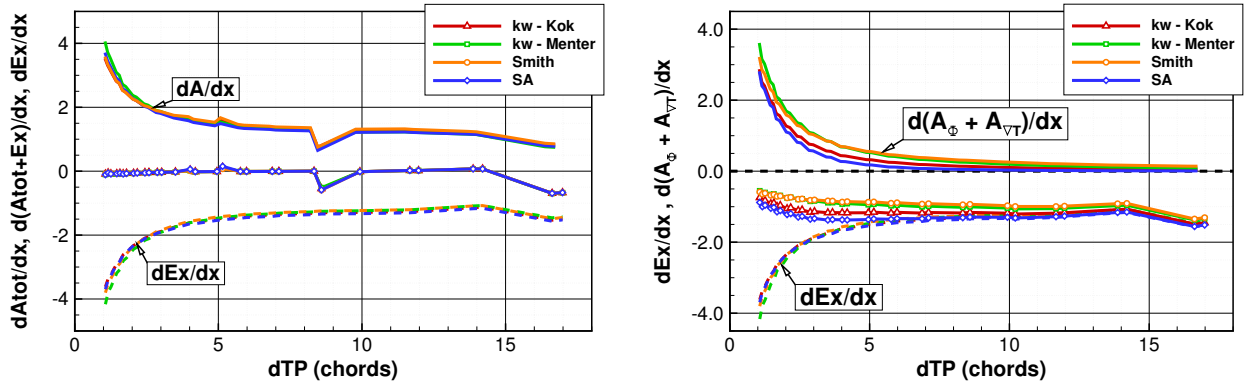
(a) Rate of change of total anergy generation and exergy destruction.

(b) Rate of change of viscous + thermal anergy generation and exergy destruction.

Figure 3-31: 3D rectangular Wing in a transonic flow: rate of change of anergy generation and exergy destruction in the wake.

Fig. 3-31a gives the rate of change of the total anergy generation (solid lines), of the exergy destruction (dashed lines) and of their sum (solid lines with symbols). The magnitude of the rate of total anergy generation matches the one of the exergy destruction, their sum being very close to zero. One can see that this observation is independent on the turbulence model.

Fig. 3-31b provides the rate of change of the viscous + thermal anergy generation (solid lines), of the exergy destruction (dashed lines) and of their sum (solid lines with symbols). The rate of viscous + thermal anergy generation does not match the one of the exergy destruction, meaning that their sum is negative which is in contradiction with theoretical considerations. Also, there appears to be a ranking between the turbulence models: the less discrepancy is given by the model of *Smith* (–) and the worst from the *SA* model (–).

It has been highlighted that the dissipation of the vortex is not captured by the viscous and thermal anergy terms. The main reason for that is the coarsening of the mesh that prevents the accurate computation of the velocity and temperature gradients whose squared quantities are crucial to the viscous and thermal anergy. The turbulence models that emphasize turbulence (*Menter* and *Smith*) are slightly less inaccurate but all of them require a correction.

3.4.3 Turbulence Model Sensitivity Analysis for Drag Prediction

In order to apply the exergy analysis for the determination of the drag experienced by the body, we shall first determine the wave anergy with the local method. Then, the correction of the viscous and thermal anergy in terms of accuracy is introduced. Finally, the definition of the control volume is made *via* the determination of the distance between the wing and the transverse plane before applying the exergy formulation for the prediction and decomposition of the drag.

3.4.3.1 Local Shock Wave Treatment

As described in details for the NACA 0012 Airfoil in paragraph 3.3.3.3 (p. 86), the local treatment of the shock wave relies on the determination of a surface enclosing the anergy associated with this (theoretically discontinuous) phenomenon. A number of additional cell layers is required to smooth the solution of an initial physical criterion.

(a) Wave anergy.

(b) Sum of the neglected terms.
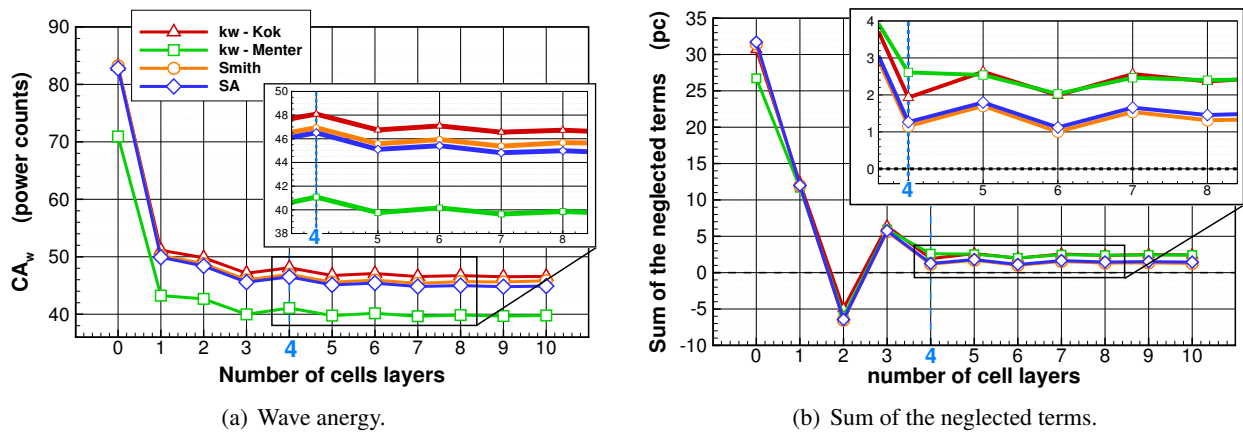
Figure 3-32: 3D rectangular Wing in a transonic flow: local shock wave treatment.

Fig. 3-32a gives the wave anergy for each turbulence model as function of the number of cell layers. One can see that the predicted values are in close agreement, around 46-48 pc except for the k–ω model of *Menter* which gives a wave anergy slightly lower, around 41 pc. Note that these values are consistent with the wave drag predicted from the far-field drag method in Fig. 3-29 (p. 93).

Fig. 3-32b gives the neglected terms for each turbulence model as function of the number of cell layers. One can see that this coefficient is significant for all turbulence models, at least above on power count. This undesirable result is however a second order consideration regarding the definition of the surface; the predominant one being the wave anergy (Fig. 3-32a).

In each case, the viscous and thermal anergy generated within the wave surface is found to be less than 0.01 pc. The wave surface definition, although not perfect, yields wave anergy coefficient in close agreement to the wave drag coefficient from the far-field method of $ffd72$. As a consequence, the treatment of the shock wave is considered satisfactory.

3.4.3.2 Viscous and Thermal Anergy Accuracy Correction

Evaluation of the Error. As we have seen in Fig. 3-31, the rate of anergy generation is lower than the rate of exergy dissipation: all turbulence models fail to capture the dissipation of the vortex. In order to provide the correction described in paragraph 2.5.1.2 (p. 55), we must first determine the *missing* anergy that is not captured $\Delta\dot{\mathcal{A}}$, see Fig. 3-33a.
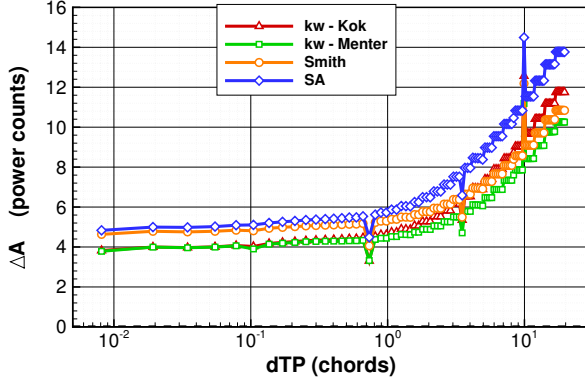
(a) $\Delta\dot{\mathcal{A}}$ in the wake.
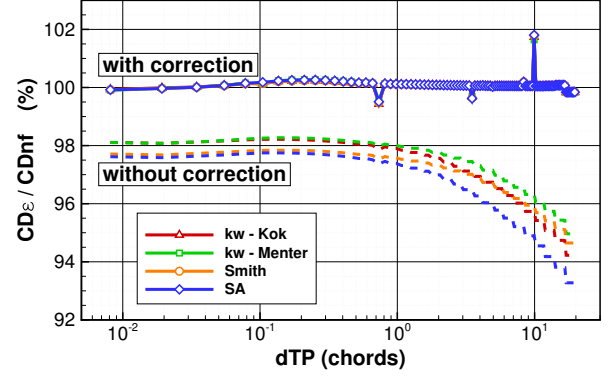
(b) Total drag-power coefficient, with and without correction.

Figure 3-33: 3D rectangular Wing in a transonic flow: $\Delta\dot{\mathcal{A}}$ and total drag-power coefficient, with and without correction.

All turbulence models require a correction of 4 to 6 pc even in mid-field of the wing ($d_{TP} \leq 1$ chord) which suggests that the spatial discretization in the vicinity of the wing is too coarse for accuracy velocity and temperature gradients computation. As we move away from the trailing edge of the wing, the correction rises steeply and is associated with the dissipation of the vortex. As expected from the wake analysis in Fig. 3-31b, the *SA* model (**–**) requires the largest correction and the k–ω model of *Menter* (**–**) the lowest.

Fig. 3-33b illustrates the total drag-power predicted with (solid lines with symbols) and without (dashed lines) correction. Without the correction, the drag prediction is dependent on the turbulence model and is in average *only* about 98% accurate. Also, the drag prediction is highly sensitive to the transverse plane location as it rapidly falls when the plane is pushed in the far-field of the wing. It appears that the correction provides a coefficient in excellent agreement with the near-field drag for all turbulence model which is additionally quasi-independent on the position of the downstream plane. The robustness of the post-processing code is thereby enhanced.

Correction for Viscous and Thermal Anergy. Now that the missing (not captured) anergy generation has been identified, it has to be attributed to each of the two mechanisms:

$$\dot{\mathcal{A}}_{\Phi}^c := \dot{\mathcal{A}}_{\Phi} + \zeta_{\phi}^{wake} \times \Delta\dot{\mathcal{A}} \tag{3.16a}$$

$$\dot{\mathcal{A}}_{\nabla T}^c := \dot{\mathcal{A}}_{\nabla T} + \left[1 - \zeta_{\phi}^{wake}\right] \times \Delta\dot{\mathcal{A}} \tag{3.16b}$$

Physically speaking, the dissipation of the lift-induced vortex is a very long process that can take several minutes for a large aircraft. Judging from Fig. 3-30, we can see that the thermal anergy generation is one order of magnitude lower than the viscous component within the boundary layers. It is assumed that the dissipation of the vortex contributes to the thermal anergy even less than within the boundary layers where the temperature gradients are higher: $\zeta_{\phi}^{wake} \geq \zeta_{\phi}^{BL}$. Given the close agreement between all turbulence models observed in Table 3.9, it is assumed that 95% of the missing anergy would contribute to the viscous anergy.

The corresponding evolution of the viscous (a) and thermal (b) anergy generation with and without correction is illustrated in Fig. 3-34.

(a) Viscous anergy generation.   (b) Thermal anergy generation.
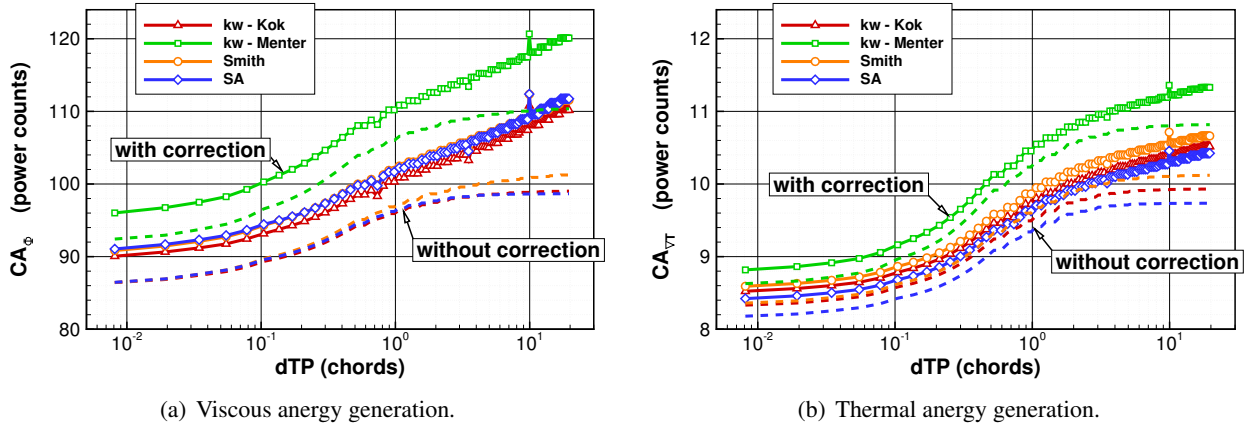
Figure 3-34: 3D rectangular Wing in a transonic flow: viscous anergy generation in the wake, with and without correction.

From the choice of $\zeta_\phi^{wake} = 0.95$, the viscous anergy is greatly impacted by the correction both in the mid-field and in the far-field of the wing while the thermal anergy is only weakly impacted. In terms of drag prediction, it is desirable to choose a location of the TP which minimizes the influence of the correction.

3.4.3.3   Domain of Validity of the Formulation

The control volume is defined by the distance between the trailing edge of the wing and the transverse plane which is determined from the information given in Fig. 3-35.
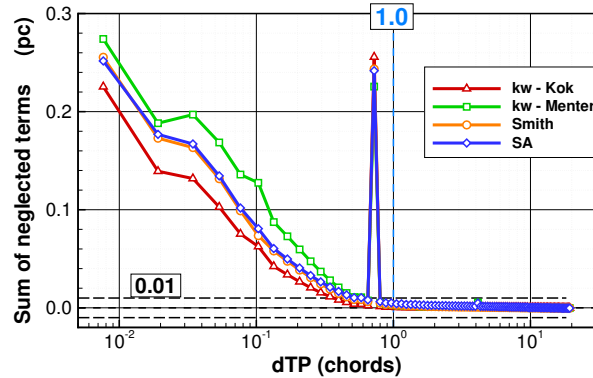
Figure 3-35: 3D rectangular Wing in a transonic flow: domain of validity of the formulation.

Fig. 3-35 provides the evolution of the sum of the neglected terms as the plane is moved aft from the wing for each turbulence model. We observe a very similar decrease from about 0.25 pc to less than 0.01 within less than a chord distance. An unexpected peak at 0.7 chords is observed which has no obvious numerical explanation.

A distance of one chord is chosen as being a good compromise between accuracy in terms of drag prediction and domain of validity of the formulation. The corresponding control volume is depicted in blue in Fig. 3-36 where the wave surface is highlighted in orange on the top-right zoom.

From bottom-right figure we can see that the transverse plane is oriented perpendicular to the freestream, at 3 deg incidence.

98
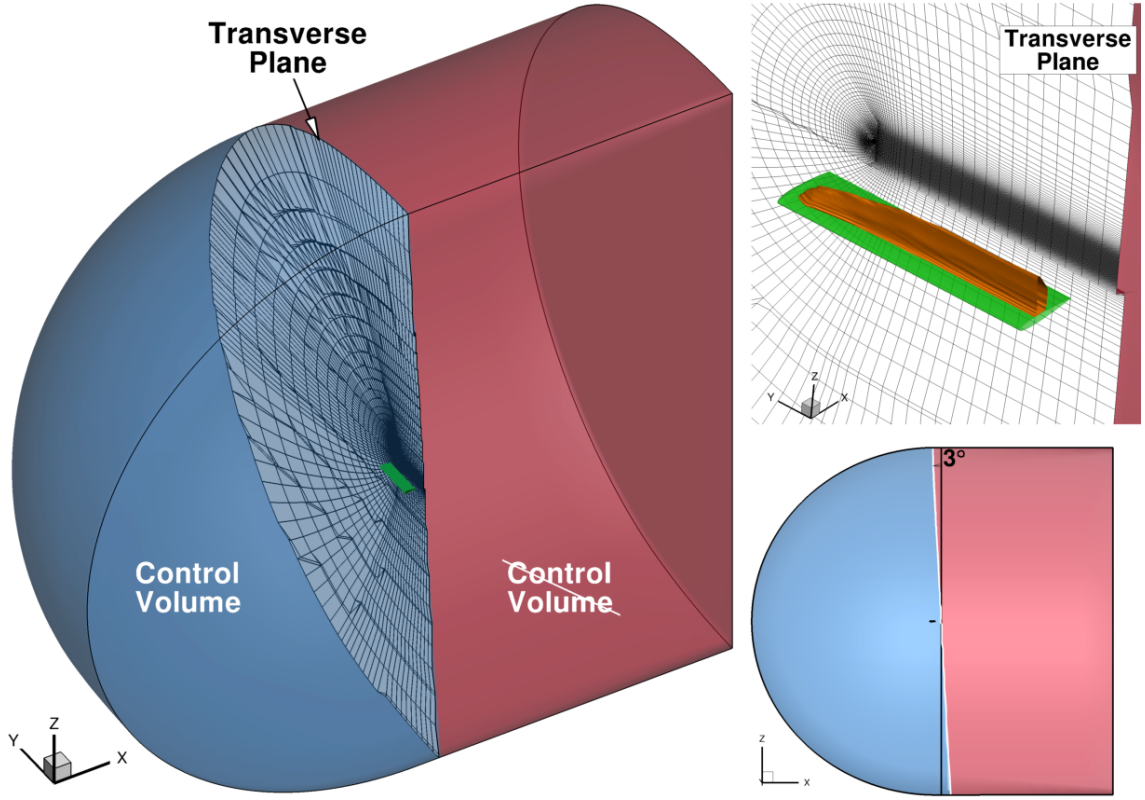
Figure 3-36: 3D rectangular Wing in a transonic flow: control volume definition around the wing (green) and with wave surface (orange).

3.4.3.4 Drag Assessment and Decomposition

For this transonic flow, the complete exergy-based formulation for the drag-power prediction and decomposition is given by:

$$DV_\infty = \dot{\mathcal{E}}_m + \dot{\mathcal{E}}_{th} + \dot{\mathcal{A}}_\phi + \dot{\mathcal{A}}_{\nabla T} + \dot{\mathcal{A}}_w \tag{3.17}$$

Table 3.10 summarizes the coefficients[21] for a plane located one chord downstream of the trailing edge of the wing.

Turbulence	far-field exergy *via ffx*									
Model	$C\dot{\mathcal{E}}_m$	$C\dot{\mathcal{E}}_{th}$	$C\dot{\mathcal{A}}_w$	$C\dot{\mathcal{A}}_\phi$	$C\dot{\mathcal{A}}_\phi^c$	$C\dot{\mathcal{A}}_{\nabla T}$	$C\dot{\mathcal{A}}_{\nabla T}^c$	CD_ε	CD_ε^c	CD_{nf}
k-ω *Kok*	47.66	3.91	48.08	95.92	100.32	9.49	9.72	**205.07**	**209.69**	209.55
k-ω *Menter*	45.22	3.86	41.08	105.99	110.21	10.23	10.45	**206.39**	**210.83**	210.62
Smith	48.01	3.98	46.93	96.22	101.67	9.34	9.63	**204.48**	**210.22**	209.97
SA	47.25	3.87	46.50	96.85	101.90	9.60	9.87	**204.06**	**209.39**	209.18

Table 3.10: 3D rectangular Wing in a transonic flow: coefficients expressed in power counts (10^{-4}) for a plane one chord downstream the body.

As expected from the wake analysis, the correction yields a total drag-power coefficient in close agreement with the near-field drag method, which, in this case, is also in excellent agreement with the near-field drag method (within 0.25 pc). Also, the local treatment of the shock wave yields wave anergy coefficients in excellent agreement with the wave drag coefficients calculated from the far-field drag approach.

---

[21]Note that in terms of execution time, the post-processing code *ffx* takes about 0.02% of the time required to compute the flow solution with the Onera-*elsA* code.

99

It appears that an accurate treatment of a viscous and transonic flow over a 3D wing yields higher grid density requirement than for the classical momentum-based approaches. Yet, with the correction, the post-processing code *ffx* is capable of providing drag predictions with an accuracy comparable to the near-field drag approach.

3.4.4   Summary of the Key Findings

Transonic and viscous flows at $M_\infty = 0.75$ and $Re_c = 1.3 \times 10^6$ have been investigated over a rectangular wing based at $3\,\mathrm{deg}$ incidence. High levels of convergence were achieved for all four turbulence models studied for which the excellent agreement between the near-field and far-field drag approaches suggested that the flow solutions were well resolved.

From a momentum perspective, the generation of a vortex is seen as a loss and therefore as (lift-induced) drag. From the energy (exergy) standpoint on the other hand, the reversible formation of vortices is seen a potential for work generation, *i.e.* a beneficial phenomenon, which is a radically different perspective. The potential for energy recovery is not new yet the exergy analysis appears to provide the rigorous formalism to determine the sources of design improvement in any flow field.

It was shown that the rate of viscous and thermal anergy generation did not match the rate of exergy destruction in the wake. In agreement with existing experience [46, 64], it was suggested that the coarsening of the mesh is the primary reason for not capturing the dissipation of the vortex. As the anergy outflow contains this additional dissipation, a correction of the viscous and thermal anergy coefficients was introduced.

As regards shock waves, the local method for wave anergy was validated as it provided a coefficient in close agreement to the wave drag from the far-field method in $ffd72$.

Finally, the drag predicted without correction for all turbulence model failed to be more accurate than 98% of the total near-field drag value. The correction of the viscous and thermal anergy coefficients enabled obtaining a total drag-power coefficient in close agreement to the near-field drag value, which, in this case, was also close to the far-field drag approach. It has further been validated that the correction is independent of the turbulence models used.

The post-processing code *ffx* is thereby validated for the assessment of transonic flow solutions over 3D lifting bodies. This preliminary step allows the investigation of a transonic flow over a more complex and more realistic 3D configuration.

3.5   Validation for a Wing-Body Aircraft in Cruise Conditions

This last test case of the Chapter builds on the knowledge developed in all three previous applications. Its main objective is to validate the post-processing code *ffx* for an industrially realistic configuration: a wing-body aircraft in cruise conditions. The flow over this three-dimensional geometry will be thoroughly examined in terms of anergy generation. Additionally, a grid convergence study will highlight the benefit of the viscous and thermal anergy correction by achieving an accuracy similar to the near-field drag method.

Application of the exergy method to this test case is the focus of an article submitted for publication to the *AIAA Journal* in December 2014 [14].

3.5.1   Test Case Presentation

3.5.1.1   Context

Drag Prediction Workshops.   The Drag Prediction Workshop (DPW) series was initiated in 2001 by a working group of the AIAA Applied Aerodynamics Technical Committee. The first objective was to assess the state-of-the-art computational methods as practical aerodynamic tools for aircraft drag and moment prediction. Over the years, it has provided an impartial forum for evaluating the effectiveness of existing CFD codes and modeling techniques using *Navier–Stokes* solvers.

The detailed aerodynamic design of the Common Research Model (CRM) used for the fifth DPW was performed by teams from the *Boeing* company. The reference geometry is defined by a mean aerodynamic chord (MAC) of $c = 7.00532$ m, a reference surface area of 383.68956 m^2 (full model), a semispan of 29.38145 m for an aspect ratio $AR = 9$. The general characteristics of the geometry are representative of a Boeing B777-200 [30] without vertical and horizontal stabilizers and without engines, see Fig. 3-37.

(a) CRM geometry.

(b) Japan Airlines B777-200.
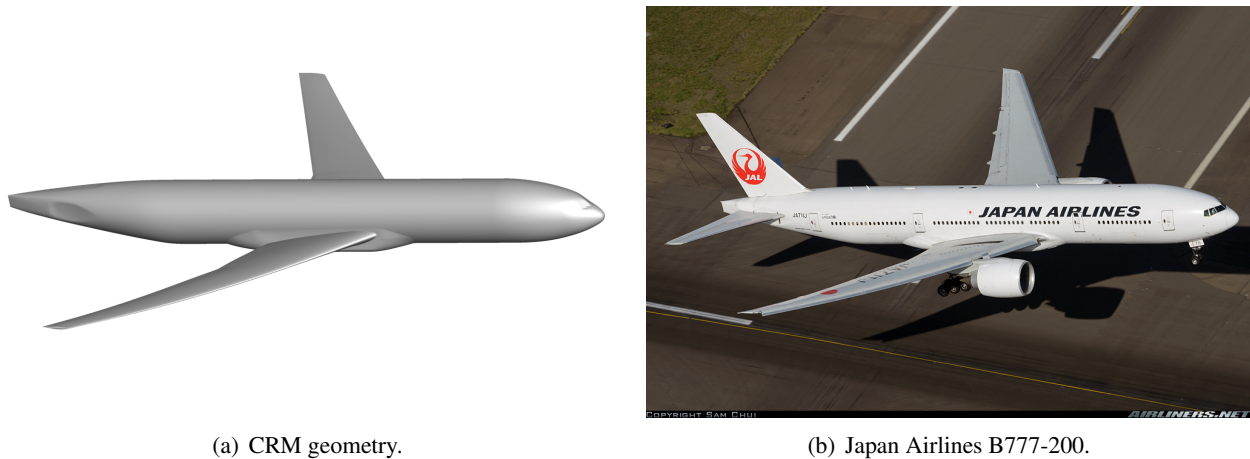
Figure 3-37: 3D Wing-body Configuration in cruise conditions: Common Research Model (CRM) representative of a Boeing B777-200.

Case 1 of DPW-5.   The case 1 of the Fifth Drag Prediction Workshop is a grid-convergence study on the prediction of the drag experienced by the wing-body configuration in cruise conditions: $M_\infty = 0.85$, $CL = 0.5$ and $Re_c = 5 \times 10^6$. All aerodynamic reference conditions are given in Table 3.11 which are in fact representative of wind-tunnel conditions. To obtain a reference value independent on any numerical considerations a wind-tunnel model was fabricated and tested in the National Transonic Facility [136] and at the NASA Ames Research Center [137].

Quantity	Value	Unit	Quantity	Value	Unit
ρ_∞	0.0450	kg.m^3	p_∞	4020	Pa
T_∞	310.79	K	V_∞	300.37	m.s^{-1}
$T_{i,\infty}$	355.63	K	$p_{i,\infty}$	6447	Pa
M_∞	0.85	–	Re_c	5×10^6	–
MAC	7.00352	m	A_{ref}	191.84	m^2

Table 3.11: 3D Wing-body Configuration in cruise conditions: reference aerodynamic conditions.

3.5.1.2 Numerical Considerations

Grids. The DPW Committee provided a family of six self-consistent multiblock and structured grids ranging from 0.64 to 138 millions elements, see Table 3.12, therefore exhibiting a grid-size ratio of 216.

Level	Name	Elements	y^+
L1	Tiny	0.64 M	2.00
L2	Coarse	2.16 M	1.33
L3	Medium	5.11 M	1.00
L4	Fine	17.25 M	0.67
L5	Extra fine	40.89 M	0.50
L6	Super fine	138.02 M	0.33

Table 3.12: 3D Wing-body Configuration in cruise conditions: characteristics of the six multiblock structured grids provided by the DPW Committee.

These meshes are O-type grids and have been created by extrusion of the surface discretization and are made of five structured blocks. Through this strategy, a precise control on grid quality, such as grid spacing, stretching ratio, and grid orthogonality near configuration surfaces, is achieved, see Figs. 3-38 and 3-39. All grids exhibit an extension greater than 100 mean-aerodynamic chords in all directions.

Note the large range of refinement levels provided by the grid family provided by the DPW Committee. It is perfectly suitable for a deep grid-convergence study.

Computation of the Flow Solutions. All flow solutions that will be analyzed for this configuration have been produced by HUE (ONERA) and published in [75]. Structured RANS computations were performed with the ONERA-*elsA* solver [35]. A target lift algorithm has enabled to reach the requested accuracy of the lift coefficient ($CL = 0.5 \pm 0.001$) for all grids. Time integration was carried out by a backward Euler scheme with implicit LU-SSOR relaxation. Spatial discretization was realized using a central *Jameson* scheme with artificial viscosity. Depending on the grid, multigrid techniques were used to accelerate the convergence. All of the flow solutions are fully turbulent with the *Spalart-Allmaras* turbulence model [156].

In terms of convergence, the computations were continued until the near-field fluxes were stable enough to observe a lift and drag variation lower than 0.001 and 0.0001 (one drag count), respectively. This convergence level is lower than the one observed for the previous (more academic) test cases and is more representative of *typical* flow solutions in an industry environment.

3.5.1.3 Momentum-based Drag Method

Before analyzing the flow from an exergy point of view, the drag prediction from the near-field and far-field methods enables an assessment of the flow solutions:

$$D_{nf} = D_p + D_f \quad ; \quad D_{ff} = D_v + D_i + D_w \quad ; \quad D_{sp} = D_{nf} - D_{ff}$$
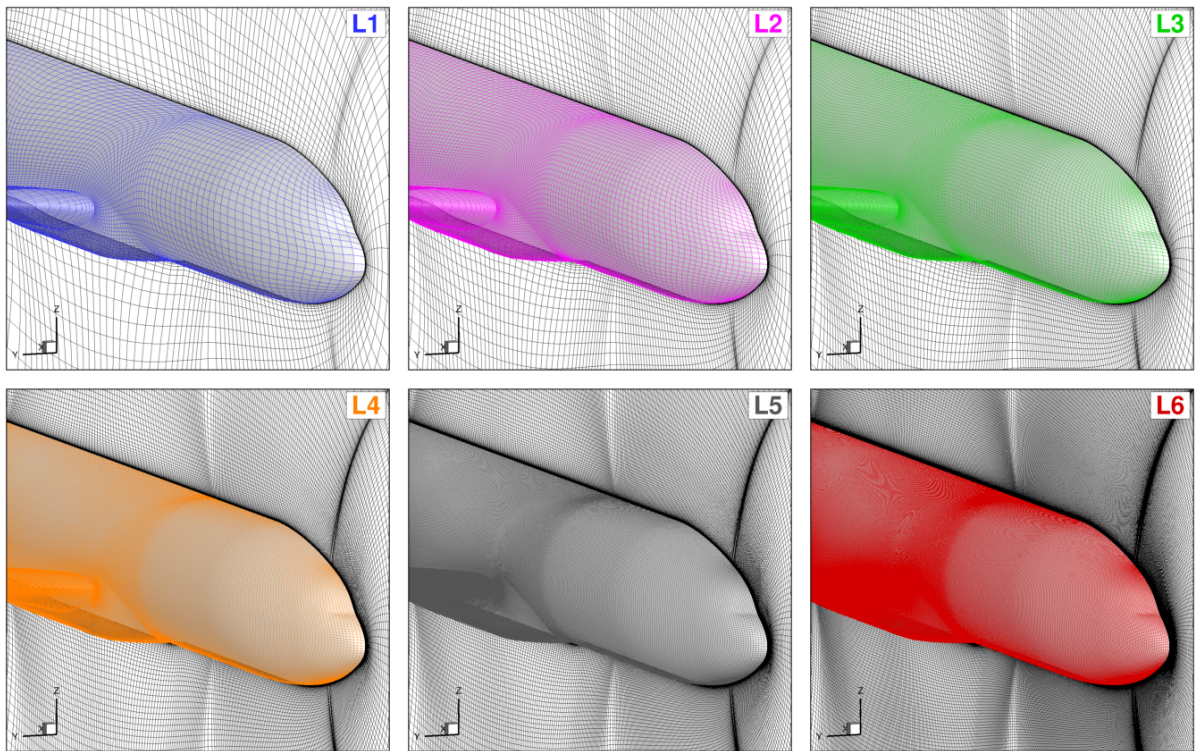
Figure 3-38: 3D Wing-body Configuration in cruise conditions: surface and symmetry plane spatial discretization, zoom on nose.
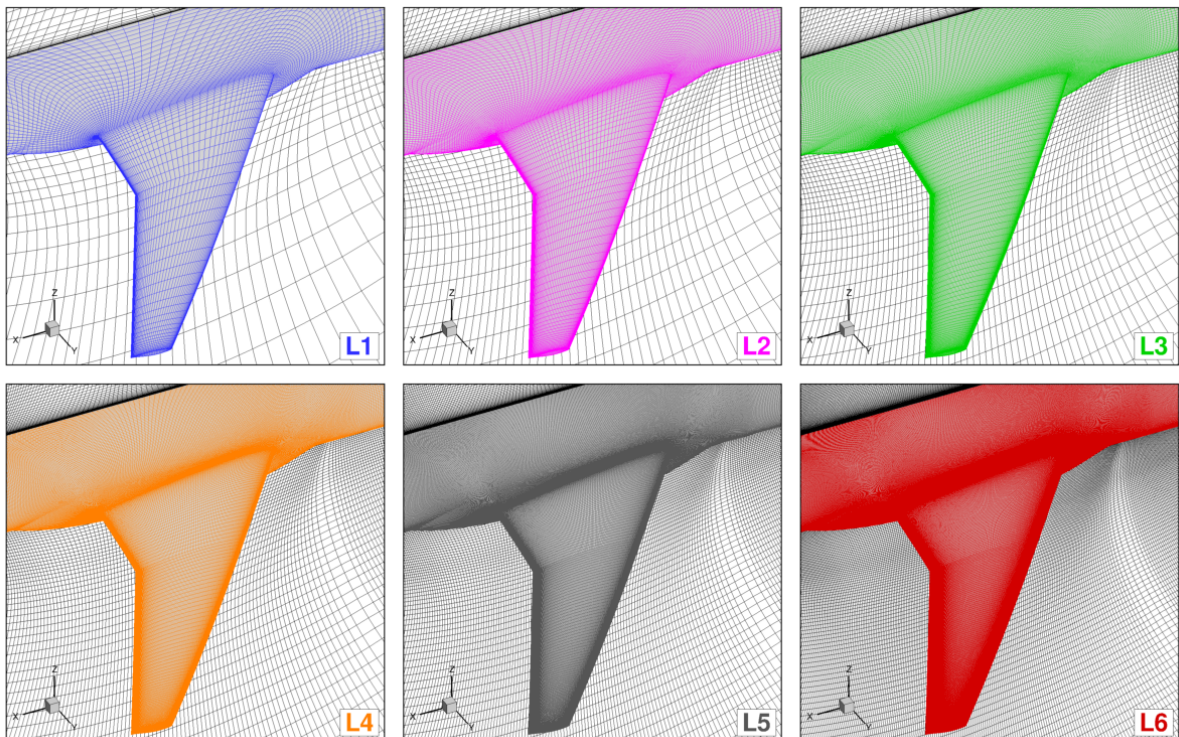
Figure 3-39: 3D Wing-body Configuration in cruise conditions: surface and symmetry plane spatial discretization, zoom on wing.

103

Table 3.13 presents the near-field and far-field drag decomposition from the $ffd72$ code. The line corresponding to L_∞^2 is a second order extrapolation based on the three finest grids[22], it should only be considered as an indication.

Mesh	near-field drag *via* $ffd72$			far-field drag *via* $ffd72$				
	CD_f	CD_p	CD_{nf}	CD_v	CD_i	CD_w	CD_{ff}	CD_{sp}
L1	113.49	146.22	**259.72**	158.95	91.48	4.77	**255.20**	4.52
L2	113.77	139.16	**252.93**	156.43	90.91	3.91	**251.25**	1.68
L3	114.14	137.33	**251.47**	155.86	90.92	3.82	**250.60**	0.87
L4	114.63	135.17	**249.79**	155.35	90.37	3.69	**249.41**	0.39
L5	114.83	135.05	**249.87**	155.24	90.62	3.80	**249.66**	0.21
L6	114.99	134.81	**249.79**	155.16	90.63	3.89	**249.68**	0.12
$\vdots$	$\vdots$	$\vdots$	$\vdots$	$\vdots$	$\vdots$	$\vdots$	$\vdots$	$\vdots$
L_∞^2	115.07	134.67	**249.74**	155.12	90.63	3.93	**249.68**	0.06

Table 3.13: 3D Wing-body Configuration in cruise conditions: near-field and far-field drag components from $ffd72$ with mesh refinement.

Friction drag D_f is underestimated on coarse meshes while pressure drag D_p is overestimated. The total near-field D_{nf} varies very little for the three finest meshes, around 249.80 dc.

The far-field drag approach enables a physical breakdown of drag into a viscous drag D_v, a (lift-)induced drag D_i, and a wave drag D_w. One can see that this latter component is very small, around 4 dc. Lift-induced component accounts for 90 dc while the remaining 155 dc are associated with viscous phenomena. Each component appears well converged with grid refinement. As described by HUE [75], the far-field drag formulation implemented in $ffd72$ is capable of discriminating the spurious (numerical) drag D_{sp} which is below 1 drag count starting from the medium grid (L3).

The overall good agreement between the near-field and far-field drag methods suggest trustworthy flow solutions in terms of numerics. A flow analysis from an exergy standpoint is introduced next before applying the approach in terms of drag prediction.

3.5.2   Flow Field Analysis

A qualitative and quantitative flow analysis is made on the finest mesh (L6), first in terms of exergy outflows and then in terms of anergy generation.

3.5.2.1   Mechanical and Thermal Exergy Outflows

Mechanical Exergy Outflows.   Fig. 3-40 gives the streamwise evolution over the aircraft of the terms composing the mechanical exergy: $\dot{\mathcal{E}}_m = \dot{E}_u + \dot{E}_v + \dot{E}_p$.

The penetration of the aircraft generates perturbations of the flow clearly visible for $0 \le x \le 10$, especially it forces the flow to get round the nose, thereby increasing its transverse kinetic energy ($\dot{E}_v$ **–**). At about $x \approx 15$, all perturbations have been damped. Then the zone of greatest changes is observed in the vicinity of the wing. The flow accelerates (high positive u values) due to lower static pressure (high negative $p - p_\infty$ values), meaning that the pressure boundary-work rate ($\dot{E}_p$ **–**) is largely negative. The acceleration of the flow has increased its streamwise kinetic energy ($\dot{E}_u$ **–**).

One can also observe a (quite) steady increase in the transverse kinetic energy (**–**) up to the wingtip which then stays relatively constant. Right downstream of the wing ($x \approx 50$), the streamwise kinetic energy

---

[22]For example, for the friction drag we plot the coefficient as a function of $1/(n)$, where n is the number of elements of the grid, and get $CD_f(n) = -2\,10^{14}(1/n)^2 - 1\,10^7(1/n) + 115.07$. Now, for n going to *infinite*, we simply get 115.07 dc. We follow the same procedure for the pressure drag and sum the two components to yield the *converged* near-field drag coefficient.
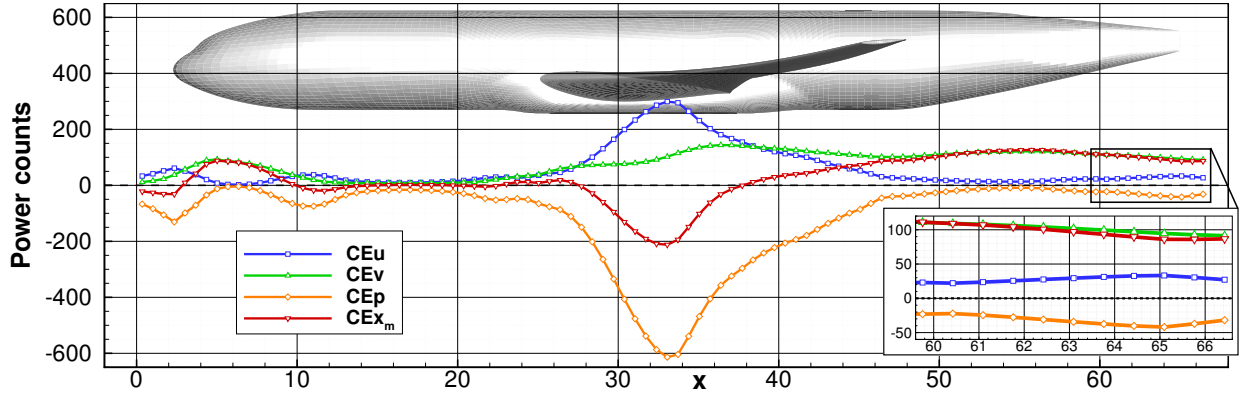
Figure 3-40: 3D Wing-body Configuration in cruise conditions: mechanical exergy distribution over the body. Super-fine mesh (L6).

($-$) and boundary pressure-work ($-$) balance each other and the mechanical exergy ($\dot{\mathcal{E}}_m$ $-$) is only made up of the transverse kinetic energy component, associated with the lift-induced vortices.

Thermal Exergy Outflows. Fig. 3-41 provides the streamwise evolution over the aircraft of the terms composing the thermal exergy: $\dot{\mathcal{E}}_{th} = \dot{\mathcal{E}}_\phi - \dot{\mathcal{A}}_{\nabla T} + \dot{E}_{PV}$. Here the *indirect* decomposition introduced in paragraph 2.3.1.2 (p. 48) is considered more meaningful because it highlights the duality of this thermocompressible term: $\dot{\mathcal{E}}_\phi$ and $\dot{\mathcal{A}}_{\nabla T}$ are *pure* thermal considerations while $\dot{E}_{PV}$ is more related to compressibility effects.
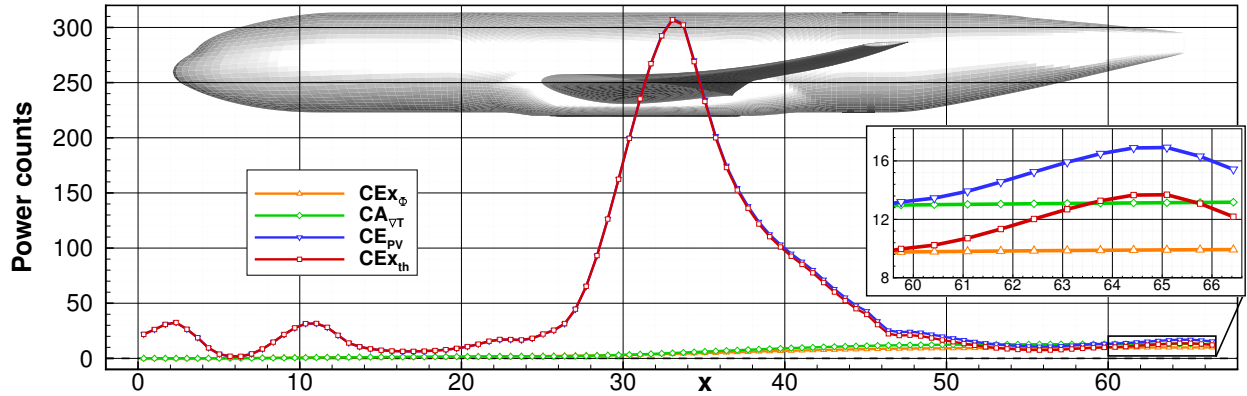
Figure 3-41: 3D Wing-body Configuration in cruise conditions: thermal exergy distribution over the body. Super-fine mesh (L6).

For this highly-compressible flow over an unpowered configuration[23], the predominant term is clearly $\dot{E}_{PV}$ ($-$). This term is mostly impacted around the wing where $p \ll p_\infty$: the fluid expands $\nabla \cdot \mathbf{V} > 0$ and is then recompressed $\nabla \cdot \mathbf{V} < 0$.

The viscous exergy ($-$) and the thermal anergy ($-$) steadily increase towards the end of the fuselage to account for about 10 pc.

Recoverable Exergy. One important aspect of the exergy analysis is to pinpoint any source of improvement in a fluid flow. The object, here the aircraft, has generated perturbations in terms of velocity, pressure and temperature, which, in order to satisfy Second Law requirements, have to be dissipated. Until these

---

[23]A realistic conventional propulsion system would supply thermal exergy, see the first powered application in section 4.2 (p. 122).

deviations from the reference conditions are damped, they represent a potential for improvement because they could be valued. The Exergy-Waste Coefficient has been introduced in paragraph 2.4.1.1 (p. 51) to quantify the relative amount of exergy that is being lost:

$$EWC = \frac{\dot{\mathcal{E}}_{rec}}{\dot{\mathcal{A}}^*} = \frac{\dot{\mathcal{E}}_m + \dot{\mathcal{E}}_{th}}{DV_\infty} \tag{3.18}$$

Fig. 3-42a gives the evolution of this coefficient downstream of the aircraft up to a distance of about 80 mean aerodynamic chords. At a distance of 70 mean aerodynamic chords (490m), the $EWC_{70} \approx 33\%$ represents around 2 MW for a complete aircraft[24]. This estimation is the absolute amount of mechanical work that could be extracted and does not involve any particular system to achieve this recovery.

(a) EWC.

(b) Decomposition of the recoverable exergy.
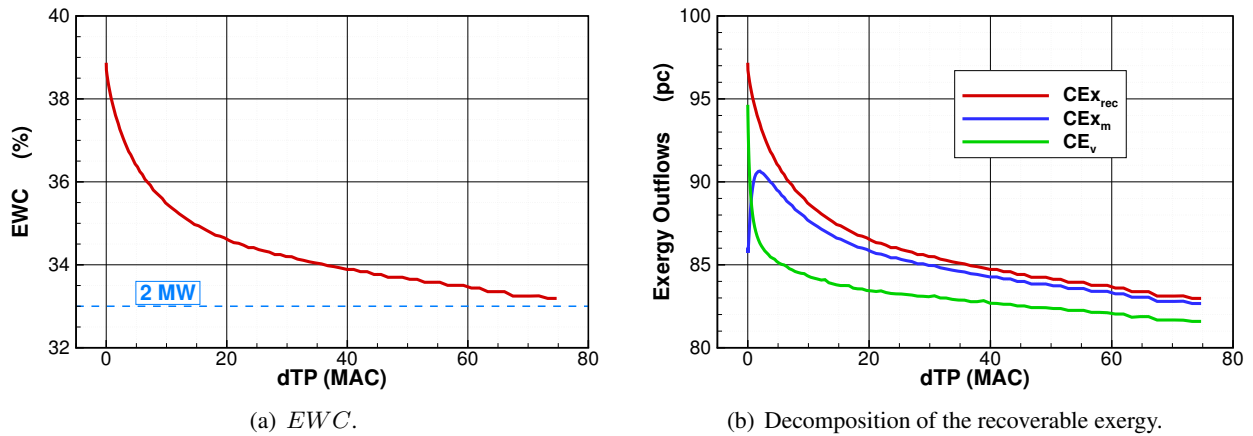
Figure 3-42: 3D Wing-body Configuration in cruise conditions: recoverable exergy in the wake. Super-fine mesh (L6).

From Fig. 3-42b, one can see that the recoverable exergy (–) is mainly in the mechanical form (–) with a thermal exergy outflow therefore rapidly vanishing. As a consequence, the transverse kinetic energy (–), associated with the presence of the lift-induced vortices, see Fig. 3-43, remains the main contributor far from the aircraft.

Figure 3-43: Isosurface of transverse kinetic energy ($v^2 + w^2$) and work potential evaluated 70 mean aerodynamic chords. Super-fine mesh (L6).

3.5.2.2 Anergy Generation

Qualitative Analysis. The anergy field is depicted in Fig. 3-44 on page 107 by the wave surface in red and by iso-surfaces (of same level) of thermal and viscous anergy, respectively in orange and yellow. The threshold chosen to define the isosurfaces is lower on the left and bottom figures.

First, from the bottom picture, we can see that the isosurfaces associated with the dissipation in the wake remains several fuselage lengths downstream of the aircraft, up to the mesh boundaries[25]. The thermal

---

[24]The recoverable exergy is given by $EWC \times DV_\infty = 0.33 \times \frac{1}{2}\rho_\infty V_\infty^3 \, CD_\varepsilon \, A_{ref}$, which, with $CD_\varepsilon \approx 250$ pc and from the geometric data of the airplane, yields 2 MW.

[25]On a coarser grid, these iso-surfaces decline more rapidly: the numerical dissipation overtakes the physical dissipation.
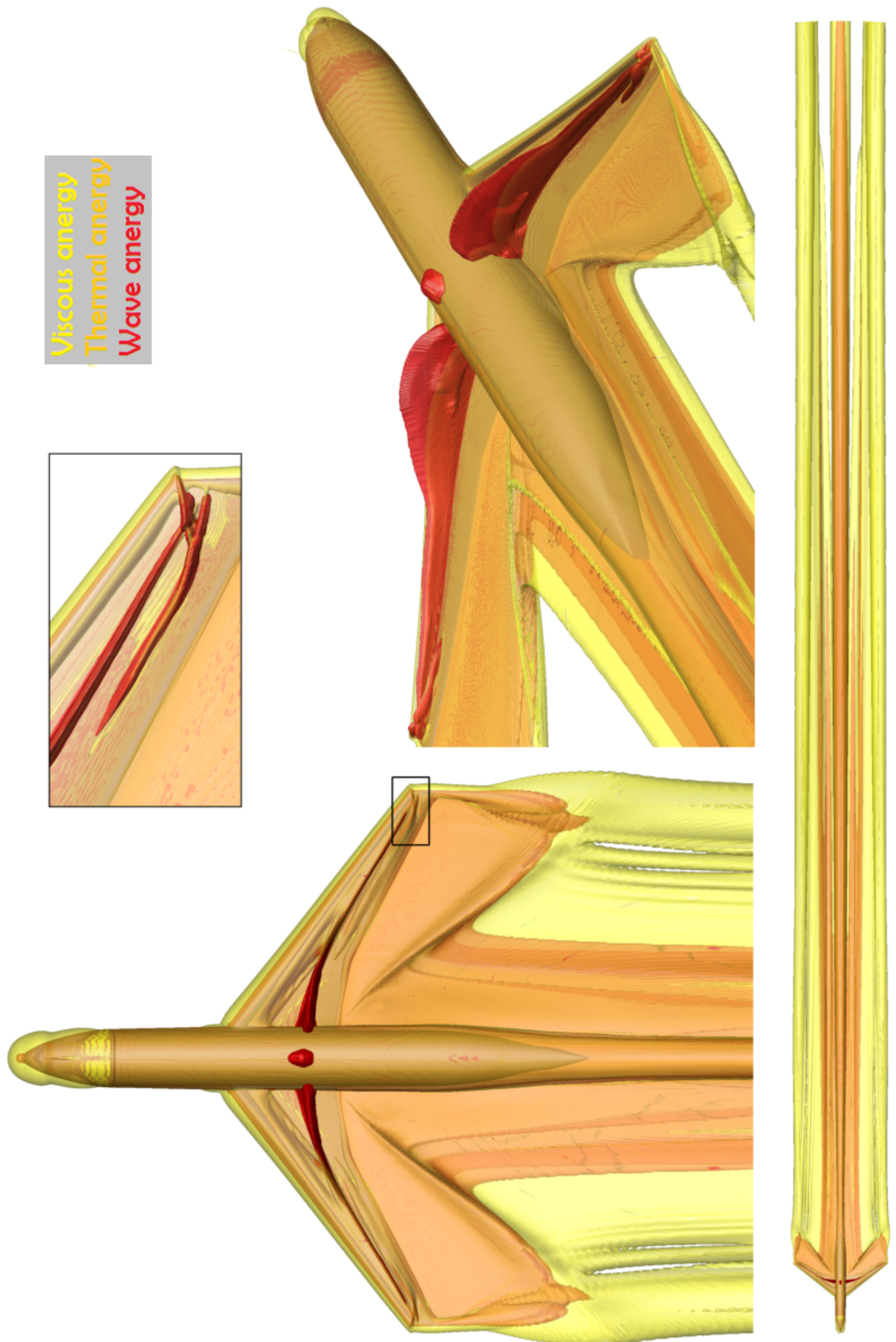
Figure 3-44: 3D Wing-body Configuration in cruise conditions: thermal and viscous anergy iso-surfaces (orange and yellow) with shock wave surface (red). Super fine mesh (L6).

anergy is mostly generated in the wake of the fuselage while the viscous dissipation is clearly connected to lift-induced vortices; the roll-up of the shear layer is clearly visible on the right picture.

From the left Figure, we clearly distinguish the formation of shock waves, with a small contribution above the fuselage. The shock pattern at the wing tip is highlighted in the middle-zoom.

This visualization of the flow from an anergy point of view enables the aircraft designer to pinpoint the location of the losses in the flowfield. By doing so, regions of potential improvement are highlighted and the impact of modifying the configuration can be visually assessed.

Quantitative Analysis. Quantitatively speaking, Fig. 3-45 gives the streamwise and spanwise rate of change of anergy generation with a representation of the aircraft and of the shock surface (yellow).
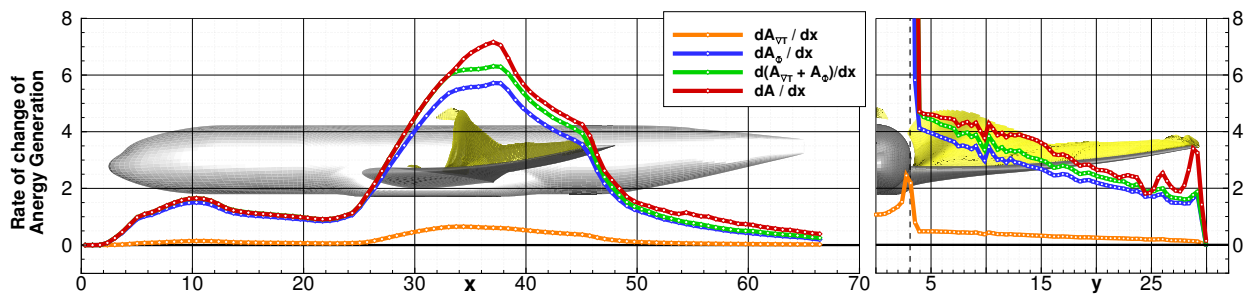
Figure 3-45: 3D Wing-body Configuration in cruise conditions: rate of change of viscous, thermal and total anergy generation. Left: chordwise distribution, right: spanwise distribution. Super-fine mesh (L6).

As regards the streamwise distribution, one can first notice a zone just downstream of the nose which corresponds to the dissipation of the perturbations due to the penetration of the body in the fluid. Then, the predominant source of anergy generation appears to be the wing; the rates rapidly fall towards the wake for all dissipative phenomena. As regards the spanwise distribution, the fuselage involves extremely high rates of anergy generation (above scale) which rapidly reduce over the wing. The total anergy (—) presents bumps (relative to the viscous + thermal anergy —) that are directly related to the three (separate) shocks that are visible on the wing, see Fig. 3-44.

On both distributions, viscous anergy (—) is predominant over the thermal anergy (—). This observation is consistent with the *Mach* number sensitivity analysis in paragraph 3.3.1 (p. 79) and with the qualitative assessment of the Boeing B747-200 in cruise conditions of ALABI *et al.* [6].

This quantitative assessment gives the aircraft designer the magnitude of the losses associated with each dissipative phenomena and is complementary to the flow visualization in Fig. 3-44 (p. 107).

3.5.3   Grid Convergence Study on Drag Prediction

A generic control volume is first introduced, its distance relative to the body is chosen with considerations on the domain of validity of the performance formulation:

$$DV_\infty = \dot{\mathcal{E}}_m + \dot{\mathcal{E}}_{th} + \dot{\mathcal{A}}_\phi + \dot{\mathcal{A}}_{\nabla T} + \dot{\mathcal{A}}_w \qquad (3.19)$$

Afterwards, an analysis of the wake shows that the correction of the viscous and thermal anergy generation is required. Finally, the efficiency of the correction is highlighted for an accurate drag prediction and a few comments are made regarding its benefits.

3.5.3.1 Generic Control Volume Definition

Geometric Considerations. The control volume is custom-made and based on geometric considerations. As depicted in blue in Fig. 3-46 for the medium mesh (L3), the outer boundary extends upstream and laterally up to the mesh boundary. The transverse plane (white) is close to the aircraft in order to avoid the spurious dissipation of the vortices highlighted in the previous test case. The remaining part of the volume (red) is outside of the control volume. The distance d_{TP} needs to be determined in agreement with the domain of validity of the formulation and with considerations on the accuracy of the drag prediction.
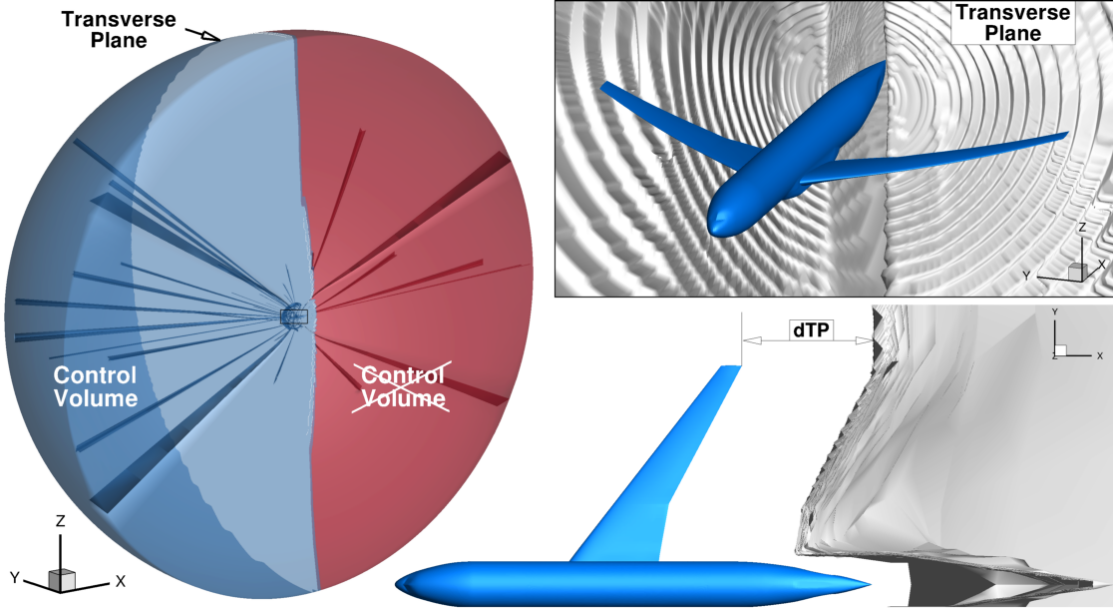
Figure 3-46: 3D Wing-body Configuration in cruise conditions: control volume definition for drag prediction. Medium mesh (L3). Radial lines are due to the visualization software.

Domain of Validity. In order to determine the distance between the transverse plane and the body (d_{TP}), we must consider the domain of validity of relation (3.19), *i.e.* the distance at which the neglected terms are effectively negligible, see paragraph 2.5.1.3 (p. 56). Fig. 3-47 gives the evolution of the sum of the neglected terms in the wake of the body.
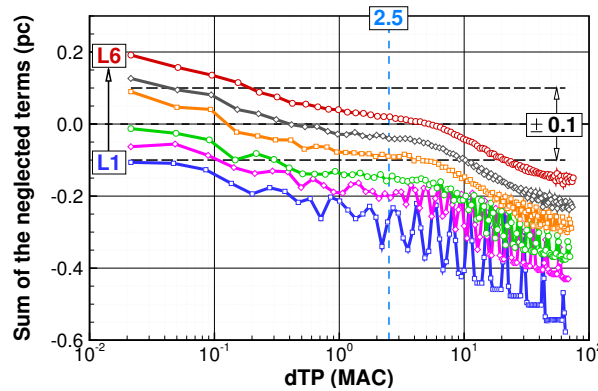
Figure 3-47: 3D Wing-body Configuration in cruise conditions: sum of the neglected terms of the approximated formulation, with grid refinement.

The sum of the neglected terms ranges from -0.3 (L1) to +0.2 (L6) right downstream of the aircraft to -0.6 (L1) to -0.25 (L6) at a hundred mean aerodynamic chords. A distance of 2.5 mean aerodynamic chords appears to be an acceptable location for the transverse plane: the sum of the neglected terms is very close to 0.00 pc for the finest grid and acceptable for the coarsest grid.

3.5.3.2 Shock Wave Treatment

The numerical treatment of the shock wave relies on the definition of a shock surface with two main criteria given for each grid in Fig. 3-48.

(a) Wave anergy.

(b) Sum of the neglected terms.
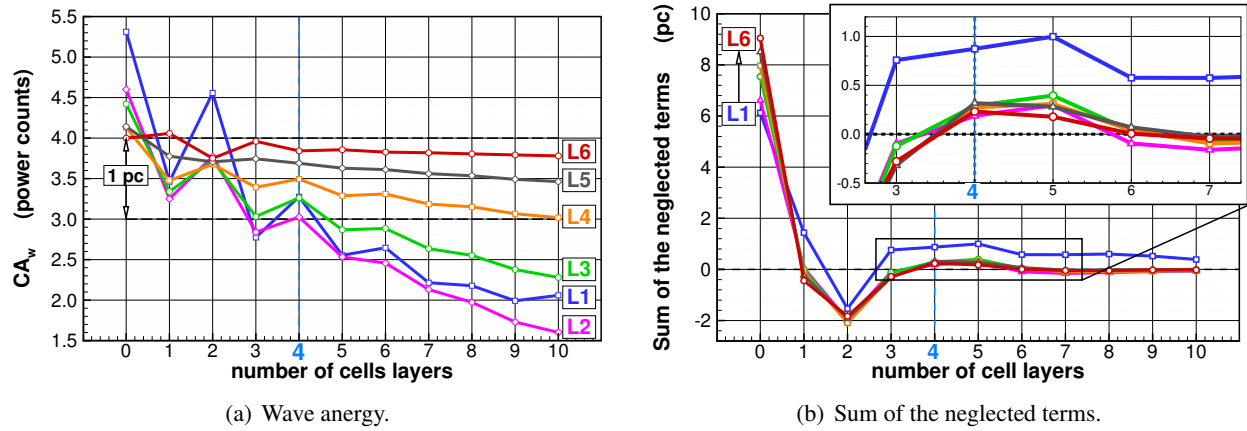
Figure 3-48: 3D Wing-body Configuration in cruise conditions: wave anergy versus the number of cell layers, with grid refinement.

From Fig. 3-48a one can observe a close agreement between all grids close to 3.5 pc, in agreement with those from the far-field drag method given in Table 3.13. As the grid is refined, the sensitivity of the wave anergy to the number of layers clearly reduces. The sum of the neglected terms is given in Fig. 3-48b where one can see that it may account for a few tenths of power counts. From these two graphics, 4 cell layers are added to define the shock surface[26], see Fig. 3-49.
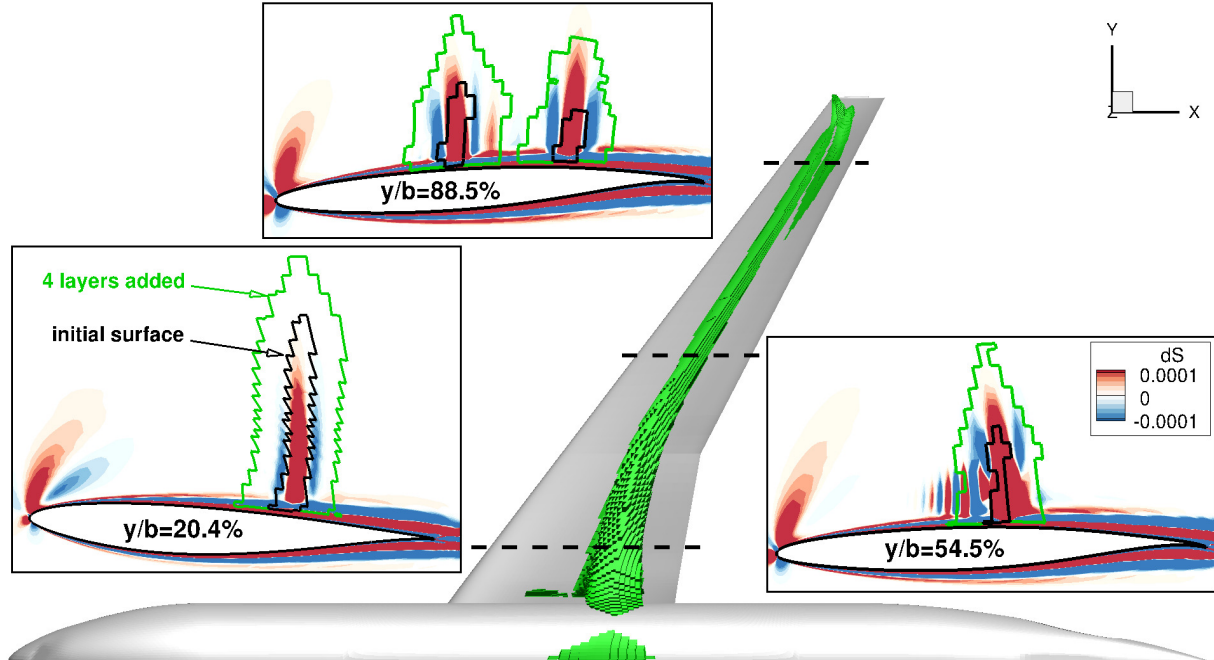
Figure 3-49: 3D Wing-body Configuration in cruise conditions: initial shock wave surface (black) and with 4 cell layers added (green), with field of entropy increase (red) and reduction (red). Medium mesh (L3).

Note that the viscous and thermal anergy integrated within the wave volume selected account each for less than 10^{-4} pc. As a consequence, the determination of the wave anergy has no impact on the other drag

---

[26]A value of 3 cell layers could also have been chosen.

components, as opposed to some momentum-based approaches [170]. For these methods, the choice of the surface $\mathcal{S}_w$ involves some sharing between the viscous drag and the wave drag. This problem is completely absent in the present implementation of the exergy method, which represents a numerical (and theoretical) advantage.

3.5.3.3 Wake Analysis in Terms of Anergy Generation and Exergy Destruction

In agreement with theoretical considerations established in Chapter 2 (p. 27), Eq. (3.19) is theoretically valid for any (closed) outer boundary $\mathcal{S}_O$ enclosing the body. As the transverse plane is moved away from the body, we *scan* the wake in terms of anergy generation and exergy destruction to evaluate the consistency of the theoretical balance:

$$\frac{\mathrm{d}}{\mathrm{d}x_{\mathcal{TP}}} \cancel{DV_\infty} = \frac{\mathrm{d}}{\mathrm{d}x_{\mathcal{TP}}}\dot{\mathcal{E}}_m + \frac{\mathrm{d}}{\mathrm{d}x_{\mathcal{TP}}}\dot{\mathcal{E}}_{th} + \frac{\mathrm{d}}{\mathrm{d}x_{\mathcal{TP}}}\dot{\mathcal{A}}_\phi + \frac{\mathrm{d}}{\mathrm{d}x_{\mathcal{TP}}}\dot{\mathcal{A}}_{\nabla T} + \frac{\mathrm{d}}{\mathrm{d}x_{\mathcal{TP}}}\cancel{\dot{\mathcal{A}}_w}$$
$$0 = \frac{\mathrm{d}}{\mathrm{d}x_{\mathcal{TP}}}\dot{\mathcal{E}}_m + \frac{\mathrm{d}}{\mathrm{d}x_{\mathcal{TP}}}\dot{\mathcal{E}}_{th} + \frac{\mathrm{d}}{\mathrm{d}x_{\mathcal{TP}}}\dot{\mathcal{A}}_\phi + \frac{\mathrm{d}}{\mathrm{d}x_{\mathcal{TP}}}\dot{\mathcal{A}}_{\nabla T} \tag{3.20a}$$

where we note that the rate of drag work and the wave anergy are independent on the transverse plane location. This relation can be rearranged into

$$0 = \frac{\mathrm{d}}{\mathrm{d}x_{\mathcal{TP}}}\left(\dot{\mathcal{E}}_m + \dot{\mathcal{E}}_{th}\right) + \frac{\mathrm{d}}{\mathrm{d}x_{\mathcal{TP}}}\left(\dot{\mathcal{A}}_\phi + \dot{\mathcal{A}}_{\nabla T}\right) \tag{3.20b}$$

In other words, the rate of decrease in exergy outflows should match the rate of anergy generation. Fig. 3-50 gives the information for assessing the numerical (in)consistency of this relation in the wake of the body.
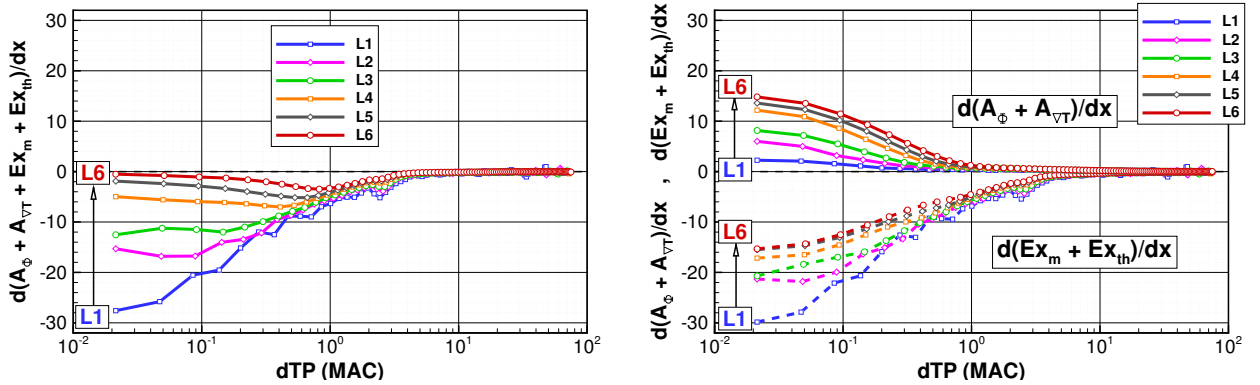
(a) Rate of change of the sum of anergy generation and exergy destruction, *i.e.* Eq. (3.20a).

(b) Rate of change of viscous + thermal anergy generation and rate of change of exergy destruction, *i.e.* Eq. (3.20b).

Figure 3-50: 3D Wing-body Configuration in cruise conditions: rates of change of anergy generation and exergy destruction versus transverse plane chordwise position, with grid refinement.

Fig. 3-50a gives the rate of change of the sum of (viscous + thermal) anergy generation and exergy destruction versus the distance expressed in mean aerodynamic chords (MAC). The theoretical equality of Eq. (3.20a) is not numerically verified: the sum is negative up to a few mean-aerodynamic chord distance downstream of the body. As the grid is refined, the balance is better verified.

Fig. 3-50b gives the two right-hand side terms of Eq. (3.20b), *i.e.* the rate of anergy generation (solid lines) and the rate of exergy destruction (dashed lines). On the coarsest grid the rate of exergy destruction is highest (negative) and the rate of anergy generation is lowest (positive), leading to the worst balance

observed in Fig. 3-50a. As the grid is refined, the rate of exergy destruction diminishes, and simultaneously the rate of anergy generation increases, thereby providing a better agreement of the overall balance.

To conclude, the exergy destruction downstream of the body is not captured by the terms responsible for anergy production. The viscous and thermal anergy are functions of respectively velocity and temperature gradients-squared. The calculation of these gradients suffer from inaccuracy due to (too coarse) spatial discretization. This study additionally highlights the region where the grid is considered too coarse to numerically satisfy the physical laws: on the finest grid (L6 –), this region extends up to a few mean aerodynamic chords downstream of the aircraft with a peak error located at d_{TP} = 0.9 MAC. As expected from the previous test cases, the post-processing of these flow solutions for accurate drag prediction requires a correction for the anergy generation.

3.5.3.4 Viscous and Thermal Anergy Accuracy Correction

It has been highlighted that the theoretical balance between anergy generation and exergy destruction is not numerically verified in the wake of the aircraft. The viscous and thermal anergy calculation are therefore corrected with the method introduced in paragraph 2.5.1.2 (p. 55).

Error Estimation. The first step consists in determining the amount of missing anergy (not captured)

$$\Delta \dot{\mathcal{A}} = T_\infty \int_{\mathcal{S}_O} \rho \, \delta s \, (\mathbf{V} \cdot \mathbf{n}) \, \mathrm{d}\mathcal{S} - (\dot{\mathcal{A}}_\phi + \dot{\mathcal{A}}_{\nabla T} + \dot{\mathcal{A}}_w + \dot{\mathcal{A}}_{qO}) \tag{3.21}$$

as a function of the transverse plane location, see Fig. 3-51a.

| (a) Missing anergy $\Delta \dot{\mathcal{A}}$. | (b) Total drag-power coefficient with or without correction. |
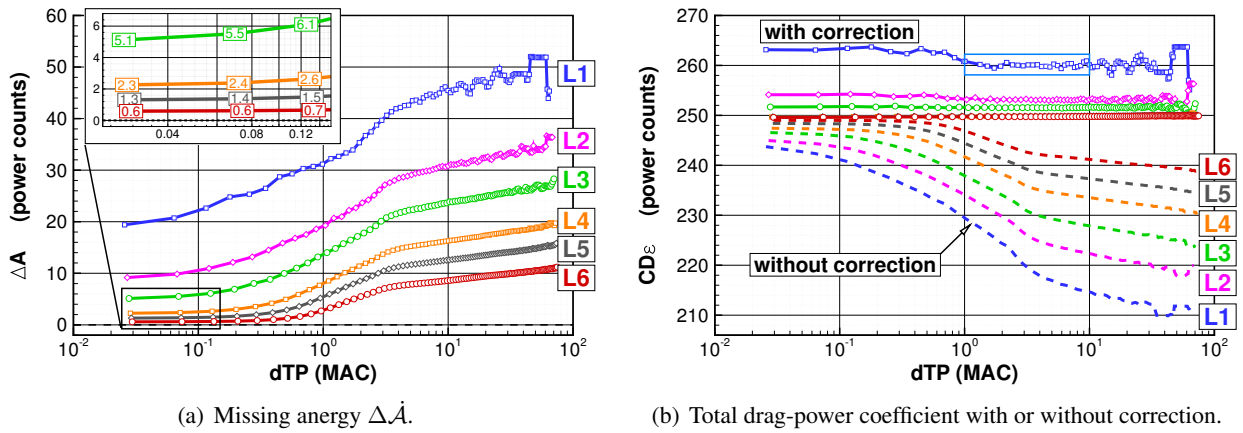
Figure 3-51: 3D Wing-body Configuration in cruise conditions: determination of the accuracy correction.

Immediately downstream of the body, the correction reaches 20 pc for the coarsest mesh (L1 –), and drastically diminishes with grid refinement: 2.3, 1.3 and 0.6 pc correction on the three finest grids (L4 –, L5 – and L6 –). From Fig. 3-51b, one can see that the correction is very effective in providing a total drag-power coefficient independent of the transverse plane position (solid lines). From the coarsest grid, we observe that for $d_{TP} \leq 1$ mean aerodynamic chord the total drag predicted seems slightly overestimated while for $(10 \leq d_{TP})$ the coefficient starts oscillating due to spurious entropy variation. In the mid-field of the body $1 \leq d_{TP} \leq 10$, the total drag power coefficient is relatively stable and therefore this represents the region of confidence in the application of the correction (light blue box). Without correction (dashed lines), depending on the grid density, this coefficient drops by 14 to 2.5 pc within a distance of only one mean aerodynamic chord.

The magnitude of the anergy not captured $\Delta\dot{\mathcal{A}}$ in the (very) near-field of the body (for $d_{TP} < 10^{-1}$ MAC) is a direct indication of the incapacity of the coarse grids to allow for accurate temperature and thermal gradients in the vicinity of the airplane. For the finest grids, the correction mainly accounts for the dissipation of the lift-induced vortices that is not captured in the far-field.

Viscous and Thermal Anergy Correction. Now that the total anergy not captured has been identified and effectively improves the total drag-power predicted, it has to be distributed between the viscous and the thermal anergy. An analysis shows that the dissipation within the boundary layers is due 91% of the viscous dissipation[27]. From the argument that $\zeta_\phi^{wake} \geq \zeta_\phi^{BL}$, a constant value of $\zeta_\phi^{wake} = 95\%$ is chosen[28], giving the following corrected anergy values:

$$\dot{\mathcal{A}}_\phi^c = \dot{\mathcal{A}}_\phi + 0.95 \times \Delta\dot{\mathcal{A}} \qquad ; \qquad \dot{\mathcal{A}}_{\nabla T}^c = \dot{\mathcal{A}}_{\nabla T} + 0.05 \times \Delta\dot{\mathcal{A}} \qquad (3.22)$$

Fig. 3-52 gives the corresponding evolution of the viscous (a) and thermal (b) anergy generation with or without correction in the wake.

(a) Viscous anergy.
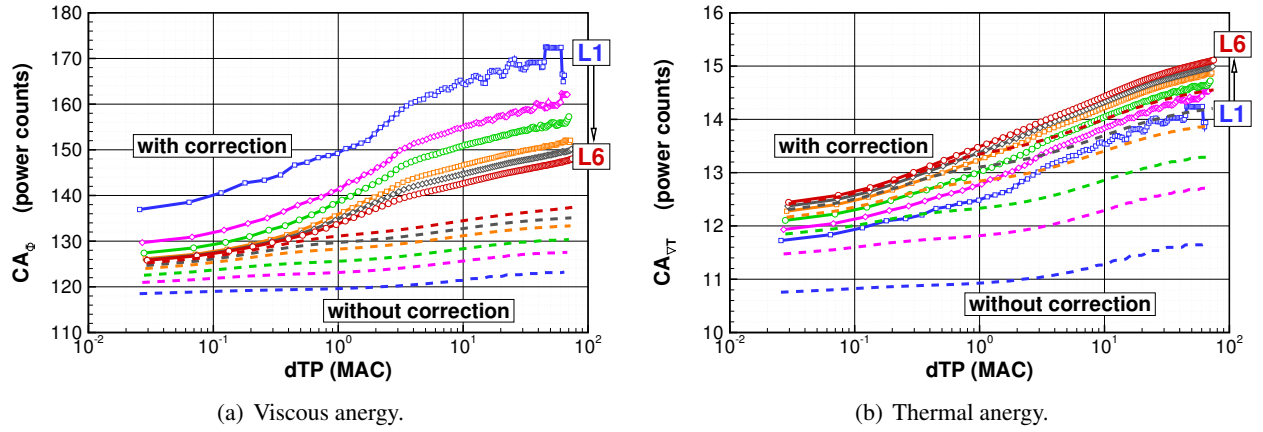
(b) Thermal anergy.

Figure 3-52: 3D Wing-body Configuration in cruise conditions: viscous and thermal anergy generation in the wake, with or without correction.

Without correction (dashed lines), the coefficient is almost flat: the primary value only depending on the grid density. The correction yields coefficients (solid lines) that converge smoothly towards higher values. For the viscous component (a), we observe an overestimation: $\dot{\mathcal{A}}_\phi$ is (much) greater on the coarse grid than on the fine grid. As regards the thermal exergy, from the value of $\zeta_\phi^{wake} = 95\%$ chosen, little impact is to be observed.

3.5.3.5 Drag Assessment and Decomposition

To highlight the benefit of the numerical correction for accurate total drag-power prediction, results from the code *ffx* with or without correction are presented. The methodology for an efficient post-processing of the flow solution with or without correction is slightly distinct and leads to the definition of a different control volume.

Without Correction. From the wake study in Fig. 3-51, one can see that, as the transverse plane is located closer to the wing, the drag calculated without correction becomes more accurate. As a consequence, in

---

[27]L1: 91.7%, L2: 91.6%, L3: 91.1%, L4: 91.1%, L5: 91.0%, L6: 91.0%.

[28]It could also have been simply assumed that 100% of the dissipation occurring in the wake contribute to viscous anergy and none to thermal anergy.

terms of total drag-power prediction, one could consider locating the TP as close as possible to the body, as depicted in Fig. 3-53b. The reference CV illustrated in Fig. 3-53a simply corresponds to the one depicted in Fig. 3-46 (p. 109).

(a) Reference control volume.

(b) Alternative control volume (lower d_{TP}).
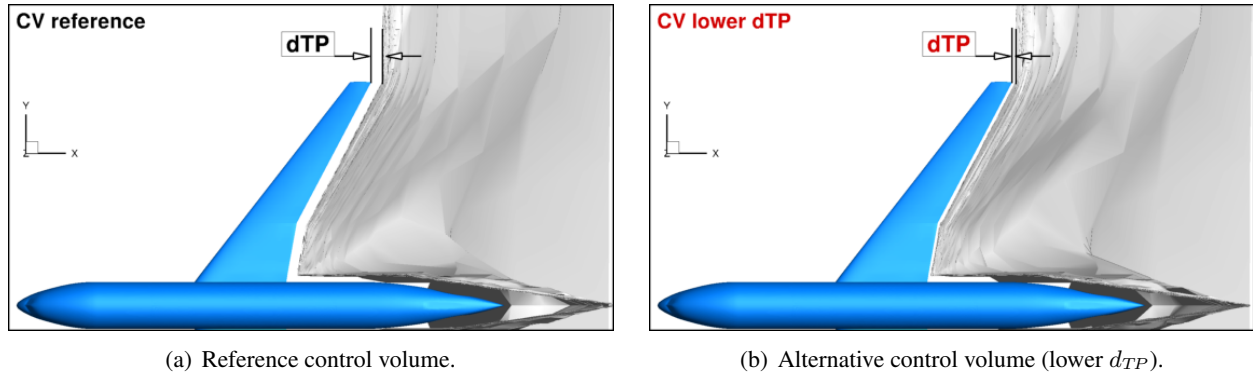
Figure 3-53: 3D Wing-body Configuration in cruise conditions: alternative control volume definitions for drag assessment without correction.

The drag breakdown for the alternative control volume of Fig. 3-53b is given in Table 3.14. The impact of the correction is given as additional information.

Mesh	far-field exergy *via ffx*									
	$C\dot{\mathcal{E}}_m$	$C\dot{\mathcal{E}}_{th}$	$C\dot{\mathcal{A}}_w$	$C\dot{\mathcal{A}}_\phi$	$C\dot{\mathcal{A}}_\phi^c$	$C\dot{\mathcal{A}}_{\nabla T}$	$C\dot{\mathcal{A}}_{\nabla T}^c$	CD_ε	CD_ε^c	CD_{nf}
L1	71.58	40.90	3.28	118.17	135.05	10.72	12.60	**244.65**	**263.41**	259.72
L2	69.23	41.35	3.03	120.37	128.31	11.40	12.28	**245.38**	**254.20**	252.93
L3	68.23	41.63	3.26	121.85	126.31	11.77	12.27	**246.74**	**251.70**	251.47
L4	66.93	41.73	3.49	123.23	125.20	12.07	12.29	**247.45**	**249.64**	249.79
L5	66.75	41.86	3.69	123.88	125.02	12.21	12.34	**248.39**	**249.66**	249.87
L6	66.49	41.93	3.84	124.40	124.92	12.31	12.37	**248.97**	**249.55**	249.79
$\vdots$	$\vdots$	$\vdots$	$\vdots$	$\vdots$	$\vdots$	$\vdots$	$\vdots$	$\vdots$	$\vdots$	$\vdots$
L_∞^2	66.35	41.96	3.91	124.66	124.88	12.36	12.38	**249.24**	**249.48**	249.74

Table 3.14: 3D Wing-body Configuration in cruise conditions: exergy-based drag power breakdown from *ffx* and mesh refinement, without correction methodology. The near-field drag coefficient serves as reference.

As regards the mechanical and thermal exergy outflows, it appears that these two coefficients are well converged and vary only by a few tenths of power counts on the three finest mesh. This fact was also suggested by the wake study in Fig. 3-50b, which highlights the cumulative chordwise error that is made: the closer from the body, the lower the error between different grids.

Without correction, the total drag only varies by 4.6 pc with grid refinement: quite accurate results are obtained even on the coarsest grids, which is satisfactory. However, the total drag prediction on the finest mesh is too low and fails to reach 249 pc. In other words, the grid density on the finest mesh (138 millions elements) is not enough to allow convergence of the exergy approach.

With correction[29], the total drag varies by 13.9 pc which is much higher, that is because the transverse plane is located outside of the zone of confidence identified in Fig. 3-51b. However, for the fine grids, it enables to predict a value closer to the momentum based methods: 249.55 pc for the finest grid.

At the expense of a challenging definition of the control volume, relatively accurate results could be obtained, even for the coarse grids. However, if accuracy requirements is important, high grid density are

---

[29]The correction applied considers that ζ_ϕ^{wake} = 95% of the dissipation in the wake is attributed to viscous anergy, and 5% to thermal anergy.

needed for accurate flow solutions. In this case, even the finest grid fails to reach a total drag prediction with an accuracy greater than 0.50 pc. The numerical correction of the viscous and thermal anergy appears therefore well adapted to obtain more accurate results.

With Correction. If the correction is applied, the main criteria are to 1) be in the region of confidence determined in Fig. 3-51b and 2) respect as much as possible the domain of validity of the formulation depicted in Fig. 3-47. As a consequence, the transverse plane is here located at a distance of 2.5 MAC, see Fig. 3-54a.

(a) Reference control volume with correction.   (b) Alternative control volume with correction.
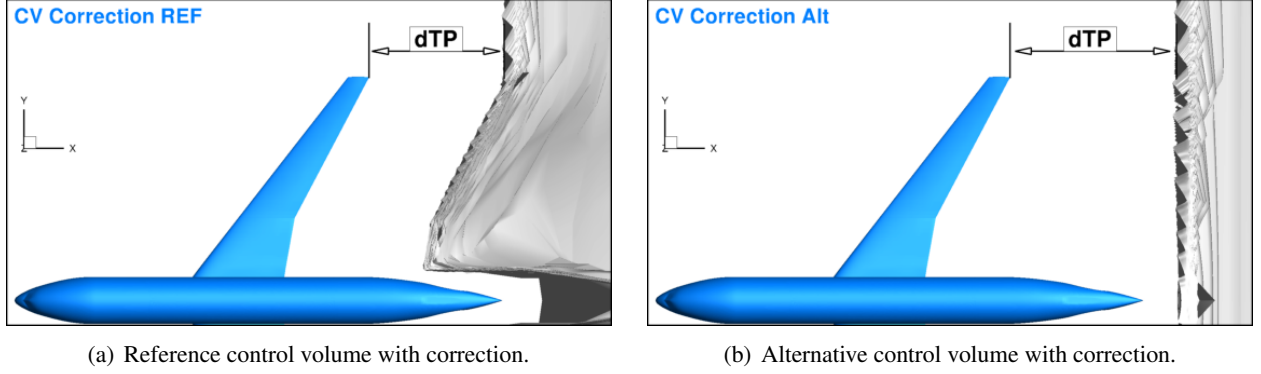
Figure 3-54: 3D Wing-body Configuration in cruise conditions: alternative control volume definitions for drag assessment with correction.

The coefficients given in Table 3.15 corresponds to the reference control volume depicted in Fig. 3-54a. For such complex geometries, the definition of the control volume is a challenging and time-consuming task. Another advantage of the correction is to be effective regardless of the definition of the control volume: a very similar *corrected* total drag-power[30] would be obtained by defining the transverse plane as shown in Fig. 3-54b. As a consequence, the post-processing with the code *ffx* of any flow solution becomes more robust and effective.

| Mesh | far-field exergy *via ffx* | | | |
	$C\dot{\mathcal{E}}_m$	$C\dot{\mathcal{E}}_{th}$	$C\dot{\mathcal{A}}_w$	$C\dot{\mathcal{A}}_\phi$	$C\dot{\mathcal{A}}_\phi^c$	$C\dot{\mathcal{A}}_{\nabla T}$	$C\dot{\mathcal{A}}_{\nabla T}^c$	CD_ε	CD_ε^c	CD_{nf}
L1	85.04	3.38	3.28	120.09	155.32	11.01	12.86	222.79	**259.88**	259.72
L2	86.12	3.36	3.03	122.16	147.38	11.66	13.18	226.26	**253.07**	252.93
L3	87.31	3.41	3.26	126.36	144.19	12.47	13.41	232.81	**251.58**	251.47
L4	88.21	3.44	3.49	129.10	141.03	12.99	13.62	237.24	**249.79**	249.79
L5	89.29	3.50	3.69	130.61	139.62	13.27	13.74	240.36	**249.84**	249.87
L6	90.35	3.56	3.84	132.18	138.15	13.54	13.85	243.47	**249.75**	249.79
⋮	⋮	⋮	⋮	⋮	⋮	⋮	⋮	⋮	⋮	⋮
L_∞^2	90.90	3.59	3.91	133.00	137.38	13.68	13.91	245.08	**249.69**	249.74

Table 3.15: 3D Wing-body Configuration in cruise conditions: exergy-based drag power breakdown from *ffx* and mesh refinement, with correction ($\zeta_\phi^{wake} = 95\%$). The near-field drag coefficient serves as reference.

The drag predicted *without correction* for this control volume *far* from the body is largely underestimated as expected from Fig. 3-51b. More relevant is the total drag-power predicted *with correction* which is in excellent agreement with the near-field drag coefficient given in the last column.

Note the much lower thermal exergy for this control volume ($C\dot{\mathcal{E}}_{th} \approx 3$ pc) compared to the one closer to the body ($C\dot{\mathcal{E}}_{th} \approx 41$ pc, see Table 3.14). In terms of physical assessment, the former value is more

---

[30]The balance between the various terms of Eq. (3.19) would be different.

representative of the perturbations generated by the aircraft in terms of thermal aspects, see thermal exergy distribution Fig. 3-41 (p. 105). The higher magnitude is associated with the transient region right downstream of the body where thermocompressible and mechanical aspects are highly coupled. Similar remarks can therefore be made regarding the mechanical exergy outflows whose magnitude is much closer to the lift-induced drag determined by the far-field drag method, see Table 3.13 (p. 104).

Comparison to Momentum-based Methods. The results from the drag assessment with or without correction are graphically represented in Fig. 3-55 with reference to the DPW5 CFD Median value of 249.6 dc and a standard deviation of 5.3 dc [92]. As mentioned in the introduction, experimental wind-tunnel testing campaign were made in two different facilities yielding a total drag coefficient of 248 dc (NTF [136]) and 241 dc (Ames [137]). The difference between the NTF and Ames data is about seven counts which is similar to the standard deviation of the CFD data. Comparison of the results to wind-tunnel data is reasonable, within about four counts to the median solution[31].

Also shown for reference are the total drag predicted from the two momentum-based methods implemented in the code $ffd72$.

(a) Near-/far-field drag and exergy-based total drag coefficients with grid refinement compared to DPW5 CFD median.

(b) Exergy coefficients variation with grid refinement and with reference to the extrapolated *converged* values (L_∞^2).
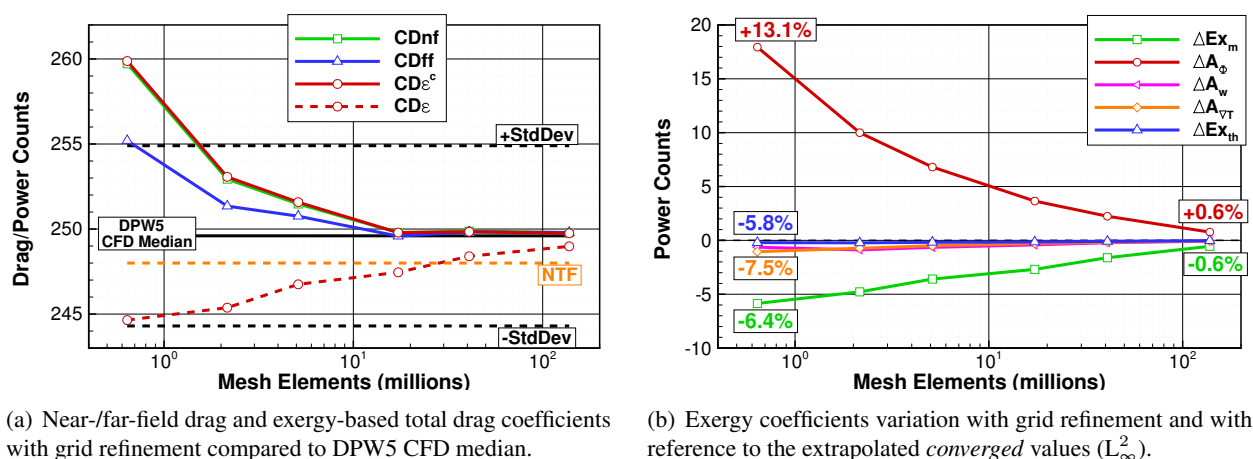
Figure 3-55: 3D Wing-body Configuration in cruise conditions: exergy-based drag-power breakdown from $ff\chi$ with mesh refinement.

All methods converge precisely towards the DPW CFD median value and are well within the standard deviation, the far-field drag method (CD_{ff} –) being the most efficient approach. The best results obtainable without correction (CD_ε – –) are within the standard deviation but, as expected, fail to converge even on the finest grid. With correction, the total drag predicted (CD_ε^c –) is found to be as sensitive to grid density as the near-field drag method (CD_{nf} –).

It has been shown in paragraph 3.5.3.3 (p. 111) that on the coarse grids, the missing anergy $\Delta\dot{A}$ accounts for excessive exergy destruction (or equivalently spurious entropy generation) and thereby leads to an overestimation of the total drag experienced by the body comparable to the near-field drag method. Consequently, an enhancement of the correction could be to subtract from the missing anergy the spurious drag D_{sp} identified by the far-field drag method. By doing so, an accuracy similar to the far-field drag method of VAN DER VOOREN and DESTARAC [46, 174] would be obtained. However, because this spurious drag is identified thanks to a very different approach, this additional correction is not adopted here.

Greater details of the results obtained from the exergy analysis with numerical correction are given in Fig. 3-55b where the variations of the main terms are given with mesh refinement and with reference to the

---

[31]According to LEVY, since the wind-tunnel test and CFD problem setups are inherently different, there is some question as to how well they should agree [92].

second order extrapolated *converged* values (L^2_∞). Although the total drag-power coefficient appears stable after the fourth grid (L4), each component is not that well converged and each is at least 5.8% from the (L^2_∞) value. In magnitude, the two predominant terms are the viscous anergy ($\Delta \dot{\mathcal{A}}_\phi$ −) and the mechanical exergy ($\Delta \dot{\mathcal{E}}_m$ −). Note that these variations are much greater than those observed for the near-field and far-field drag coefficients given in Table 3.13 (p. 104).

3.5.4 Summary of the Key Findings

An industry-realistic test case has been investigated corresponding to the NASA Common Research Model (CRM) which is representative of a Boeing B777-200. The airplane was studied in cruise conditions: transonic regime at cruise $CL = 0.5$. These settings correspond to Case 1 of the Fifth Drag Prediction Workshop (DPW) whose Committee provided a family of six multiblock and structured grids for drag convergence study. As the workshop brought together more than 50 participants, a solid numerical (and experimental) database for validation is available. All flow solutions post-processed here were made by HUE (ONERA) and published in [75]. A satisfactory level of convergence was achieved for all grid densities. The drag assessment based on momentum considerations predict on the finest grid a total drag of 249.79 dc (near-field) and of 249.68 dc (far-field) which are both very close to the CFD DPW median value of 249.6 dc.

As regards the exergy analysis, the flow field was first investigated in terms of exergy variations around the airplane with the post-processing code[32] *ffx*. The recoverable exergy in the wake, mainly due to the transverse kinetic energy of the lift-induced vortices, represents about 2MW at a distance of about 80 mean aerodynamic chords (560m)[33]. Secondly, the three dissipative phenomena (viscous, thermal and wave) were qualitatively identified in the flow field. Quantitatively speaking, zones directly downstream of the nose and around the wing were seen to be the two main regions responsible for exergy destruction.

As regards drag assessment, a reference control volume was defined to be close to the body. A wake analysis showed that the theoretical balance between exergy destruction and anergy production is not well numerically satisfied; this observation being worsened with grid coarsening. As a consequence, the correction of the numerical accuracy of the viscous and thermal anergy was adopted and calibrated by considering that 95% of the dissipation in the wake would contribute to viscous anergy and only 5% to thermal anergy. Also, the shock wave treatment yielded coefficients in good agreement with the far-field drag method. An additional advantage comes from the independence of the other anergy components to the selection of the wave surface: there is no interaction as opposed to some other drag prediction methods [170].

The total drag-power predicted without correction failed to converge to within 0.50 pc of the well-tried momentum-based methods. With correction of the viscous and thermal anergy generation, an accuracy similar to the near-field drag method was achieved and the robustness of the code was improved. These satisfactory results enable to validation[34] of the exergy-based formulation and its numerical implementation in the code *ffx* for the drag prediction of transonic flows over complex three-dimensional geometries.

---

[32]In terms of execution time, it represents a third order contribution to the computational time of the flow solutions (CFD-RANS).

[33]The performance evaluation at such a large distance from the body involves some uncertainty, even on the finest grid available. The value of 2MW should be considered as an order of magnitude rather than an exact estimation.

[34]With respect to experimental wind-tunnel testings data acquired at National Transonic Facility [136] and at NASA Ames [137].

3.6   Chapter Summary

This chapter was devoted to the validation of the numerical implementation of the aerodynamic performance assessment of unpowered configurations. The methodology that has been followed considered geometries and flow regimes of increasing complexities on a step-by-step basis: from a 2D airfoil in a subsonic flow to a 3D wing-body configuration in a transonic flow. The last test case allowed the validation of the post-processing code *ffx* for the accurate assessment of the aerodynamic performance of transonic flows over three-dimensional configurations, thereby fulfilling the primary objective of this chapter. Additional objectives were to precisely characterize the various terms of the formulation with *Mach* and *Reynolds* numbers. The thermal aspects are second order contributors to the drag experienced by the body, even at transonic regimes. The viscous and thermal anergy are caused at least 60% by turbulence (90% for the thermal mixing).

The viscous and thermal anergy generation are functions of squared-gradients of respectively velocity and temperature. Their accurate calculation sets grid density requirements that are higher than for more classical momentum-based methods. The increase in computational capabilities in the future could mitigate this drawback. In the meantime, a correction was introduced to ensure consistency with the flow solution. This correction is calibrated by considering that the anergy generation in the wake is less due to thermal mixing than in the boundary layers where the temperature gradients are highest. The correction provides a total drag-power prediction that is 1) less sensitive to the definition of the control volume, which can be a challenging and time-consuming task for complex configurations, 2) in excellent agreement with the near-field drag approach. The shock surface $\mathcal{S}_w$ enables the accurate calculation of the wave anergy which has no interaction with the two other anergy components.

For subsonic and transonic flows, the *Moore* and *Moore* model [108] is for entropy generation what the *Spalart–Allmaras* model [156] is for RANS flow solutions: a simple and efficient model adapted for external and mean steady flows. The model was validated for typical *Reynolds* numbers of aerospace applications in the order of a few millions. Such a detailed validation of the *Moore* and *Moore* model for mean entropy production [108] was not reported in the literature review. No sensitivity to the turbulence model used for computing the flow solution was observed in terms of direct exergy assessment and numerical correction for accurate drag prediction.

One drawback of the exergy analysis is the lack of a clear identification of the drag associated with the lift-induced vortices, which is provided by the far-field drag method of VAN DER VOOREN and DESTARAC [46, 174]. One must however recognize that a clear distinction between the overall wake and the vortex is not straightforward because the lift-induced vortex has a very global impact on the flow [103]. One could imagine discriminating the vortex from the overall wake from a criterion based on vorticity, and associate the corresponding mechanical and thermal exergy outflow to a separate coefficient.

Generally speaking, neither the formulation nor its numerical implementation is as mature as the far-field drag method of DESTARAC and VAN DER VOOREN and the code *ffd*72 which relies on decades of experience. However, the intention is not to discard these capabilities for aerodynamic flows, but to investigate the kind of configurations that can not be satisfactorily treated with an approach based on momentum considerations only. Among these *unconventional* configurations are those analyzed in the next Chapter: a simplified blended wing-body aircraft with boundary layer ingestion in section 4.4 (p. 143) as well as the integration of a heat exchanger on an aircraft in section 4.5 (p. 160).

Chapter 4

Numerical Applications for the Aero-thermo-propulsive Performance Assessment of Powered Configurations

This chapter focuses on the application of the formulation to powered configurations. In order to demonstrate the capabilities of the post-processing code ffx as a multidisciplinary tool for aircraft design in terms of aerothermoproulsive performance, different test cases are examined to gradually increase interactions between the subsystems. The benefit of having a single performance metric for the analysis of these various systems is highlighted and all terms of the exergy balance are further physically characterized for each application. Also, the relevance of the performance indicators based on exergy considerations is emphasized when investigating the concept of wake-ingestion.

4.1   Methodology and Test Cases Introduction

A powered configuration is a system that exchanges either mechanical or thermal energy with the flowing fluid. For the most complex system, the full Eq. (2.34) derived in 2.1 (p. 28) must be considered:

$$\dot{\mathcal{E}}_{prop} + \dot{\mathcal{E}}_q = F_x V_\infty + \dot{\mathcal{E}}_m + \dot{\mathcal{E}}_{th} + \dot{\mathcal{A}}_\phi + \dot{\mathcal{A}}_{\nabla T} + \dot{\mathcal{A}}_w \tag{4.1}$$

Exergy is supplied to the fluid either by convection through a permeable surface $\dot{\mathcal{E}}_{prop}$ or by conduction at a solid surface of the body $\dot{\mathcal{E}}_q$. This amount of exergy is generally delivered to generate a net force whose rate of work is $F_x V_\infty$. Residual mechanical $\dot{\mathcal{E}}_m$ and thermal energy $\dot{\mathcal{E}}_{th}$ outflows are dissipated over time by viscous $\dot{\mathcal{A}}_\phi$ and thermal $\dot{\mathcal{A}}_{\nabla T}$ anergy generation. The presence of a shock wave would represent an additional destructive phenomenon $\dot{\mathcal{A}}_w$.

This exergy balance is applied to four test cases gradually deviating from conventional systems, see Fig. 4-1 and Table 4.1. All flow solutions have been computed with the ONERA-*elsA* flow solver [35] and all the performance data that are presented are delivered by the post-processing code *ffx* developed (and validated[1]) in the framework of this thesis.
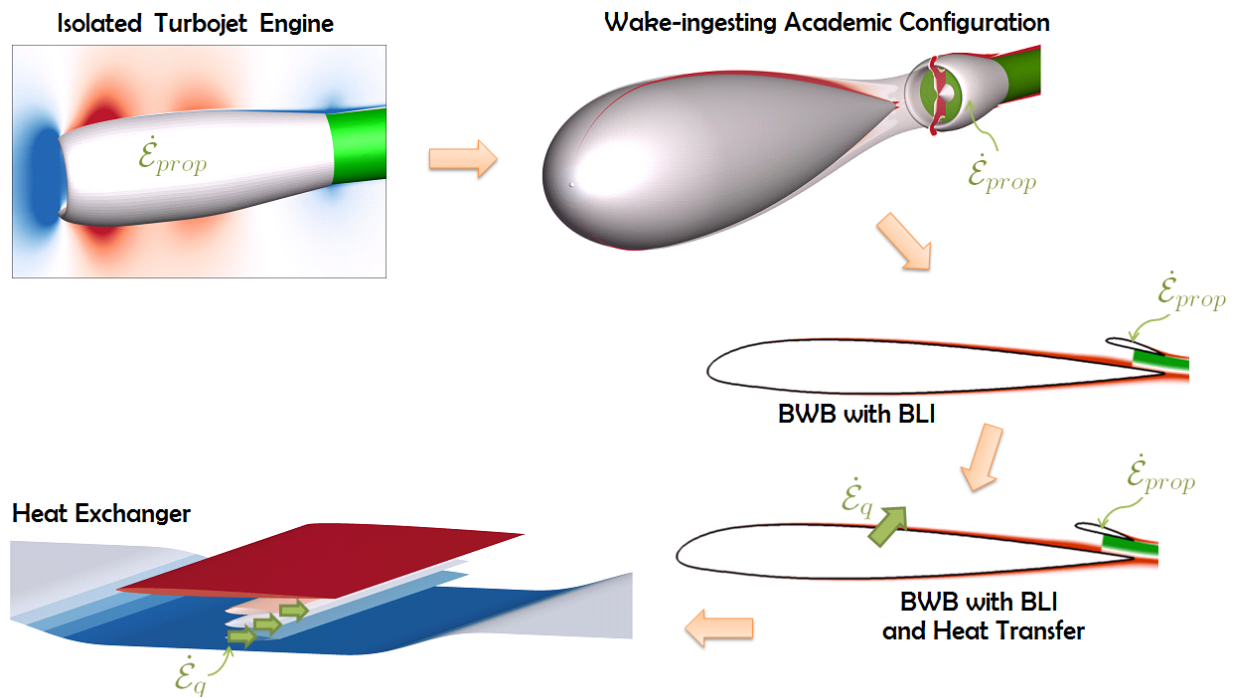
Figure 4-1: Chapter 4: methodology and introduction to the test cases investigated.

Section	Configuration	Drag/Thrust Distinction	Heat Transfer	2D/3D
4.2	Isolated Engine	✓	✗	3D
4.3	Wake-ingesting Configuration	≈	✗	2D-axi
4.4	BWB BLI	✗	✗ / ✓	2D
4.5	Heat Exchanger	–	✓	2D

Table 4.1: Chapter 4: main characteristics of the four test cases of powered configurations.

---

[1]This code, described in paragraph 2.5.2.2 (p. 58), has been validated in the previous chapter 3 (p. 63) for the performance prediction of three-dimensional configurations immersed in transonic flows, with the help of a numerical correction that ensures an accuracy similar to the near-field drag method.

– The first application in section 4.2 (p. 122) considers an isolated engine which supplies exergy only through its propulsive system. It represents the engine of a conventional aircraft with which we assume no interactions. The study will be made at transonic regime in order to be representative of cruise flight conditions. In this test case, it will be highlighted that the exergy balance (4.1) is almost insensitive to the definition of the propulsive surface, unlike the main performance metric for a momentum analysis which is thrust.

– In the second application in section 4.3 (p. 133), the propulsive device is placed immediately downstream of a simplified fuselage in order to investigate the concept of wake ingestion from an exergy point of view. This academic configuration will enable us to draw major conclusions regarding the physical underlying principle responsible for the overall benefit of such architectures.

– Based on these two analyses, section 4.4 (p. 143) focuses on a simplified (2D) blended wing-body (BWB) with a propulsion system placed on the top-rear of the configuration so as to ingest the boundary layer that develops on the upper surface (BLI). It will be shown that application of the traditional drag/thrust bookkeeping becomes excessively ambiguous. The full performance characteristics of this architecture are evaluated from an exergy point of view and it will be shown that very little exergy is wasted in its jet/wake.

This test case makes a perfect candidate for the investigation of thermopropulsive interactions. A cold/hot temperature is imposed on the surface just upstream of the propulsion system in order to alter the boundary layer that is ingested. The benefit of having a single performance metric for such multidisciplinary system will be emphasized.

– The last test case in section 4.5 (p. 160) investigates the integration of a heat exchanger on an aircraft with a simplified geometry (2D). The capability of the exergy approach to provide meaningful information about the integration of such sub-system will be compared to a more traditional approach based on momentum considerations only.

Except for the isolated engine, the aero-thermo-propulsive performance assessment of all configurations investigated in this chapter was not possible prior to the development of the multidisciplinary tool *ffx* which allow the quantification of the interactions between the various subsystems.

While thermal aspects were second order aspects for the performance assessment of unpowered configurations examined in the previous chapter, we will see that these considerations become more significant in the following test cases.

4.2 Verification of the Formulation for an Isolated Turbojet Engine

The benefit of the exergy analysis for a better understanding of propulsive devices (and thereby for a more efficient design) has been mentioned in the literature review [47, 132, 141]. The objective of the present test case is therefore not to make a deep analysis of a propulsive system but rather to gradually introduce the newly-developed performance formulation for the case of a classic powered configuration. Care will be taken to validate the approach with reference to classic momentum approaches for an isolated engine and the consistency of the proposed exergy balance with conventional drag/thrust bookkeepings [42, 53] will be shown. Additionally, a complete characterization of all terms involved in the formulation will be made for this illustrative example, with a special emphasis on thermal considerations.

4.2.1 Test Case Presentation

The geometry comes from the propulsion system of the DLR-F6 configuration. This airplane was studied both from CFD and wind-tunnel testings in the second Drag Prediction Workshop[2]. It is simplified representation of an Airbus A300, see Fig. 4-2.
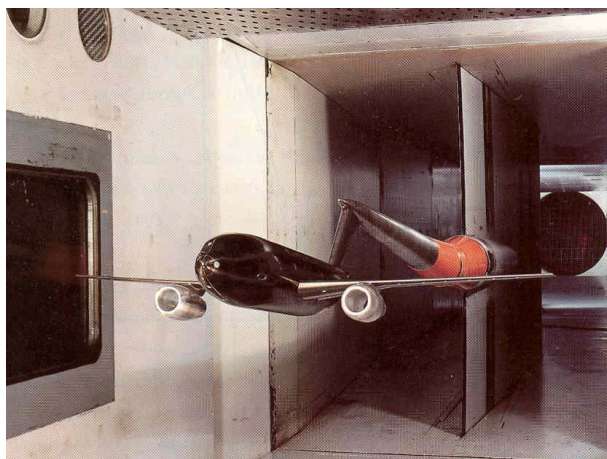
(a) DLR-F6 wind-tunnel model.

(b) Airbus A300 operated by Novespace (CNES).

Figure 4-2: 3D Isolated Nacelle: DLR-F6 wind-tunnel model representative of an Airbus A300.

Several authors have considered the exergy efficiency of an engine for a complete flight, from take-off to landing [47]. They particularly emphasized the need for properly defining the reference conditions as the system changes its altitude during the flight [52]. The following analysis is restricted to a steady cruise phase because it is the predominant one for a long range airplane.

We consider here a viscous flow ($Re_c = 6.49 \times 10^6$) at cruise *Mach* number ($M_\infty = 0.82$) and zero incidence, see Table 4.2. The reference atmosphere is representative of an altitude of 35,000ft. The reference surface is $A_{ref} = 102.56\text{m}^2$ which corresponds to the DLR-F6 model scaled to match the A300 geometry characteristics.

4.2.1.1 Numerical Considerations

Grid and Boundary Conditions. The nacelle studied here is a CFM-56 like type with a long duct [32]. The structured grid, depicted in Fig. 4-3a, has been generated by MÉHEUT (ONERA) and used in an

---

[2]Since the first Drag Prediction Workshop (DPW) held in 2001, the DPW series gather industry, academia and research centers to assess the state-of-the-art computational methods as practical aerodynamic tools for aircraft drag (and moment) prediction.

Quantity	Value	Unit	Quantity	Value	Unit
ρ_∞	0.3828	kg.m^3	p_∞	24037	Pa
T_∞	218.81	K	V_∞	243.14	m.s^{-1}
$T_{i,\infty}$	248.24	K	p_{i_∞}	37383	Pa
M_∞	0.82	–	Re_c	6.49×10^6	–
α	0	degree	A_{ref}	102.56	m^2

Table 4.2: 3D Isolated Nacelle: reference aerodynamic conditions.

optimization process [163]. It contains 64 blocks for a total of 916,480 elements. The grid extends 5 nacelle lengths upstream, 6 downstream and 2 laterally.

(a) 3D Overview.

(b) Slice and zoom on the nacelle.
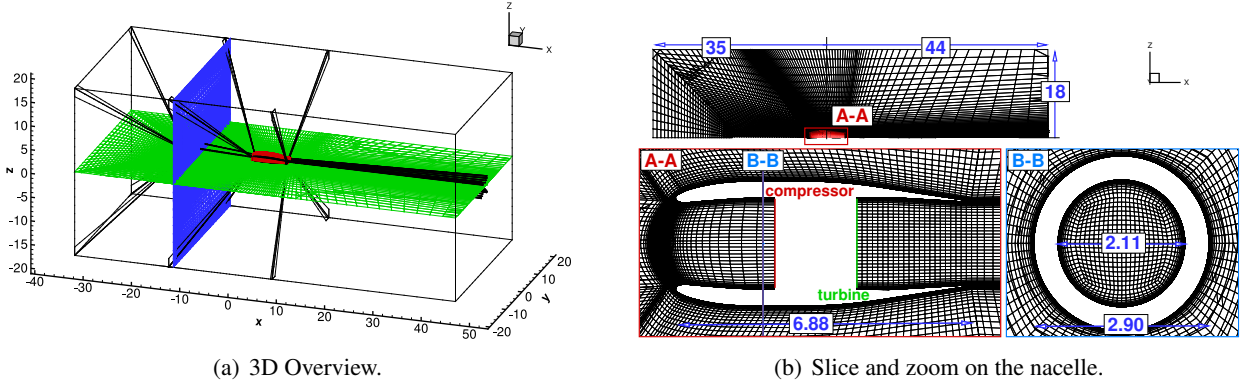
Figure 4-3: 3D Isolated Nacelle: overview of the mesh and zoom on the nacelle.

The primary components for a gas-turbine comprise compressor, combustor, and turbine and the ideal cycle is the *Brayton* cycle. A jet engine supplies heat to the flow in the combustion chamber by burning fuel. This addition of thermal energy is then converted into thrust. The core of the engine is a highly complex system which is out of the scope of the present analysis and is therefore modeled by a set of two boundary conditions[3]. The first one corresponds to the compressor, highlighted in red — in Fig. 4-3a, for which we impose the surface mass flow rate to be ingested by the engine. The second boundary conditions represents the turbine (–) for which impose both the mass flow rate and a jump in total enthalpy compared to the freestream reference. This ratio corresponds to the energy being released by the fuel combustion and supplied to the flow. For the present test case, the mass flow rate is set at 249.4 kg.s^{-1} and the total enthalpy ratio to $h_{i,turbine}/h_{i,\infty} = 2.7$.

Convergence. The convergence of the flow solution is depicted in Fig. 4-4. 2500 iterations were run with multigrid techniques to reach a convergence of the near-field drag better than 0.01 dc. This corresponds to a residual reduction of the energy equation of more than 3 orders. This satisfactory convergence level is lower than academic test cases investigated in the previous chapter but is less costly and is closer to typical convergence levels in industry.

---

[3]Another set of boundary conditions was traditionally used. It consists in the input of two parameters: the total enthalpy and total pressure ratios between the compressor and the turbine planes. Given the choice of these two parameters, potentially non-physical solutions can be obtained which do not satisfy basic Second Law requirements. Consider the *Gibbs* equation:

$$\exp^{(s_{out}-s_{in})/c_p} = \left(\frac{T_{i,out}}{T_{i,in}}\right) \cdot \left(\frac{p_{i,out}}{p_{i,in}}\right)^{\frac{1-\gamma}{\gamma}} \quad \text{so that if} \quad \left(\frac{T_{i,out}}{T_{i,in}}\right) < \left(\frac{p_{i,out}}{p_{i,in}}\right)^{\frac{\gamma-1}{\gamma}} \quad \text{then} \quad \boxed{s_{out} < s_{in}} \quad (4.2)$$

which does not make sense if we consider the case of a streamline of the flow entering the engine compressor plane and leaving the engine through the turbine plane.

(a) Near-field drag coefficient.

(b) Residual energy equation.
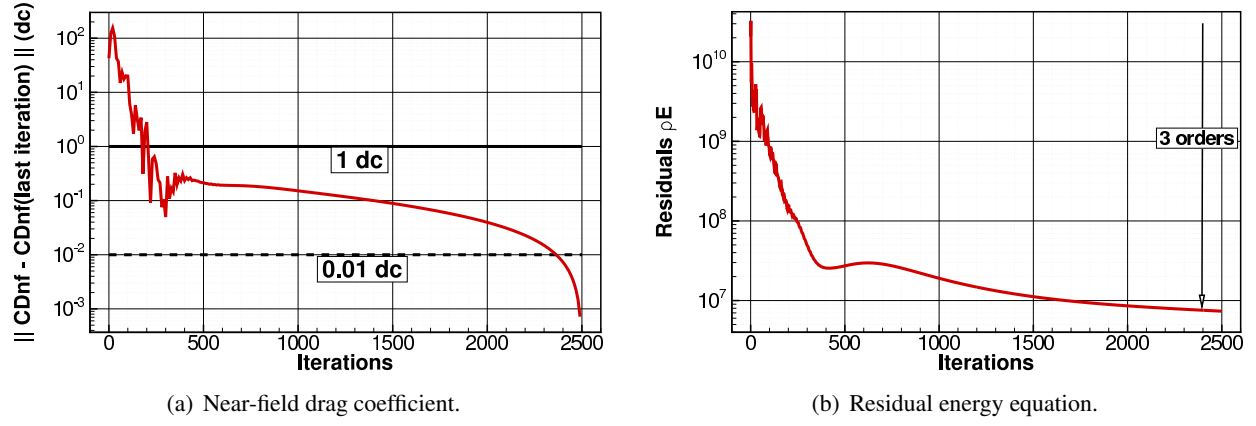
Figure 4-4: 3D Isolated Nacelle: convergence history.

4.2.1.2 Flow Description

The corresponding flow field is depicted in Fig. 4-5 in terms of *Mach* number (top) and static pressure (bottom). The flow entering the engine is slowed down to $M_{inlet} \approx 0.64$ and the static pressure is increased. An efficient inlet design is generally assessed in terms of total pressure loss meaning that the slowing process of the fluid was not reversible: the static pressure increase is lower than the drop in kinetic energy; a portion having been converted into heat (thereby producing entropy). In the nozzle, the increased static pressure is gradually converted into a higher *Mach* number. At the exhaust, the static pressure is close to freestream.
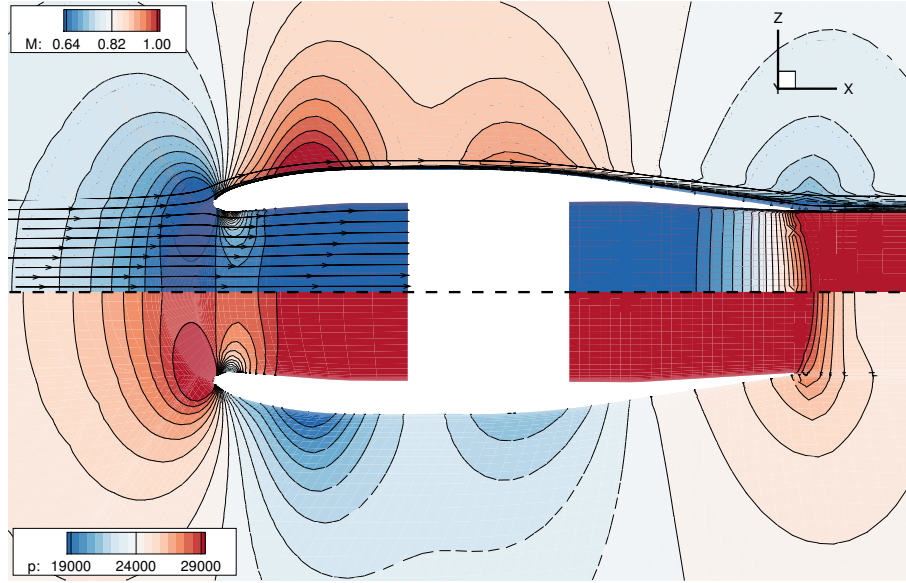
Figure 4-5: 3D Isolated Nacelle: overview of the flow field with the *Mach* number (top) and relative pressure $p - p_\infty$ (bottom).

The simulated fan pressure ratio is $FPR = p_{i,out}/p_{i,in} = 1.98$ which is in fact representative of a low bypass ratio turbofan engine. The non-dimensionalized mass flow rate[4] $MFR_\% = 76.1\%$ which is also

---

[4]It is a comparison between the actual mass flow rate through the engine and the mass flow rate that *would have* occurred through the same area at freestream conditions:

$$MFR_\% = \frac{\int_{\mathcal{S}_P} \rho(\mathbf{V} \cdot \mathbf{n}) \, \mathrm{d}\mathcal{S}}{\int_{\mathcal{S}_P} \rho_\infty (\mathbf{V}_\infty \cdot \mathbf{n}) \, \mathrm{d}\mathcal{S}}$$

representative of a turbofan in cruise conditions.

Note that the streamlines stop at the compressor surface and do not exit from the turbine plane: information is lost. This aspect will become more important in the wake ingestion studied in section 4.3 (p. 133).

Momentum Analysis. From the code $ffd72$, the characteristics of the engine can be determined by a momentum analysis. Because of an excellent agreement between the near-field and far-field methods, for simplicity, only the near-field approach is given. The default settings define the propulsive surface directly on the boundary condition, *i.e.* the compressor and turbine surfaces (highlighted respectively in red and green in Fig. 4-3b). The resultant axial force is equal to 607.76 dc meaning a large forward[5] net force:

$$F_x = T - D \tag{4.3}$$

provided by a thrust of 698.26 dc with a pressure and friction drag on the nacelle of respectively 69.70 and 20.79 dc. This amount of thrust is relatively high if one considers a typical airplane like the CRM configuration examined in section 3.5 (p. 101) with a drag coefficient in cruise conditions of about 250 dc; the thrust produced by this engine is more than twice as large[6].

4.2.2 Thermopropulsive Performance Assessment

Restriction of Eq. (2.34) to this case with adiabatic surfaces and in a subsonic flow reads:

$$\dot{\mathcal{E}}_{prop,nf} = \underbrace{W\dot{\Gamma} + \dot{\mathcal{E}}_m + \dot{\mathcal{E}}_{th} + \dot{\mathcal{A}}_\phi + \dot{\mathcal{A}}_{\nabla T}}_{\dot{\mathcal{E}}_{prop,ff}} \tag{4.4}$$

The left-hand side term results from a near-field integration on the propulsive surface while all right-hand side terms are integrated within the control volume or on the outer boundary of the domain. Before applying this equation for the determination of the performance of the engine, one has to define the control volume in which the analysis is made through its two boundary surface. The propulsive surface $\mathcal{S}_P$ is first defined and then the outer boundary is chosen.

4.2.2.1 Propulsive Surface Definition

In order to evaluate the sensitivity of the performance prediction to the definition of the propulsive surface, we use a tuning option of the post-processing code *ffx*. It consists in the automatic addition of a number of cell layers to define the propulsive surface. Each term integrated on this surface is then computed and written in an output data file. If a second tuning option is activated, the corresponding cell layers can be written in a data and loaded in Tecplot360[TM] for visualization purpose, as shown by Fig. 4-6.

In total, 22 cell layers have been iteratively added to the initial definition of the propulsive surface which corresponds to those of the engine boundary condition that are supplied as input data to the code, see paragraph 2.5.2.2 (p. 58).
The main quantities calculated for each iteration are given in Fig. 4-7.

Fig. 4-7a gives the main mechanical characteristics in terms of propulsion with the field of *Mach* number around the nozzle in top figure. The propulsive power (**–**, thrust power) remains constant until the nozzle area reduces at $x \approx 3.5$ at which point a decrease is observed up to the exhaust.

---

[5]In the aircraft reference frame (flight path direction).

[6]Neglecting the slightly different flow conditions in terms of *Mach* and *Reynolds* numbers.
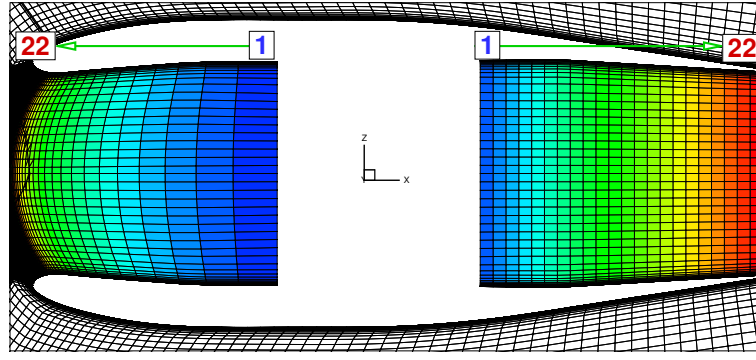
Figure 4-6: 3D Isolated Nacelle: propulsive volume with increasing cell number.

(a) Main mechanical characteristics.

(b) Propulsive exergy.
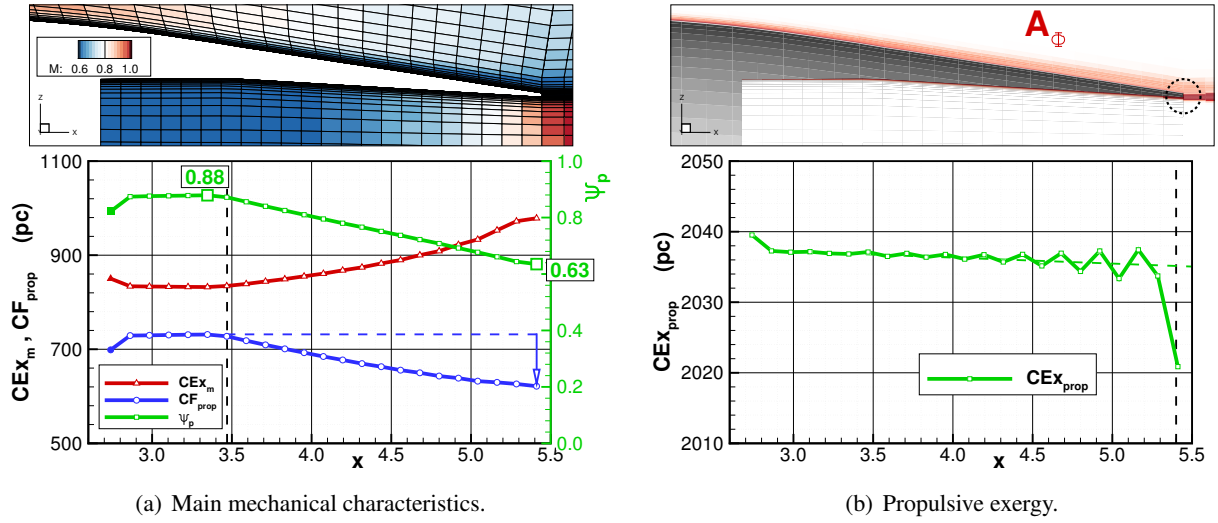
Figure 4-7: 3D Isolated Nacelle: influence of the addition of a few cell layers in the nacelle nozzle for the determination of the propulsive surface.

Similarly, because the flow is accelerated towards the exhaust, the mechanical exergy (–) increases. Consequently, the mechanical efficiency (ψ_m –) drops from 88% to 63%.

Fig. 4-7b provides the (direct) integration of the propulsive exergy on the propulsive surface $\mathcal{S}_P$. One can see that this coefficient is well independent of the number of cell layers added: it varies about 5 pc, which, compared to the average value of 2,036 pc, represents variations lower than 0.25%. The small negative slope of the curve is due to the destruction of exergy by viscous and thermal dissipation within the nozzle. Also, a drop is observed for the last data point. This reduction in exergy is due to a larger generation of anergy right at the exhaust as circled in the field of viscous anergy (top).

The (in-)sensitivity of this term to the definition of the propulsive surface is very different to the one exhibited by the thrust (power, – in Fig. 4-7a). This latter coefficient drops from 740 pc to 620 pc, which represents a much larger variation of 16%.

The performance from a momentum perspective is based on the evaluation of the thrust as the rate of change of momentum between the inlet and outlet surfaces. It has been shown that this performance metric is highly sensitive to the definition of the number of cell layers, even for this simplified example. On the other hand, the main performance metric from an exergy point of view is the exergy delivered by the propulsive device, see Eq. (4.4). It appears that this propulsive exergy is almost insensitive to the definition of the propulsive surface, which is a great advantage.

Finally, note that for all four quantities presented in Fig. 4-7, the direct integration on the boundary conditions *i.e.* with no additional layers (first data points with filled symbols), is not as precise as if a few cells are added.

4.2.2.2 Overall Balance

In order to evaluate the performance relation (4.4), one must first define the control volume. As illustrated in Fig. 4-8, the outer surface $\mathcal{S}_O$ extends up to the mesh boundaries upstream and laterally, and the transverse plane is located at 0.15 nacelle length downstream of the body.

From the description of the flow in paragraph 4.2.1.2, we consider that the nacelle inlet and nozzle are part of the propulsive device. As a consequence, the propulsive surface extends from the nacelle inlet up to its exhaust and 22 cell layers are added to the default definition of the propulsive surface. The propulsive volume is excluded from the control volume, see Fig. 4-8b.

(a) Overview.

(b) Zoom around the nacelle.
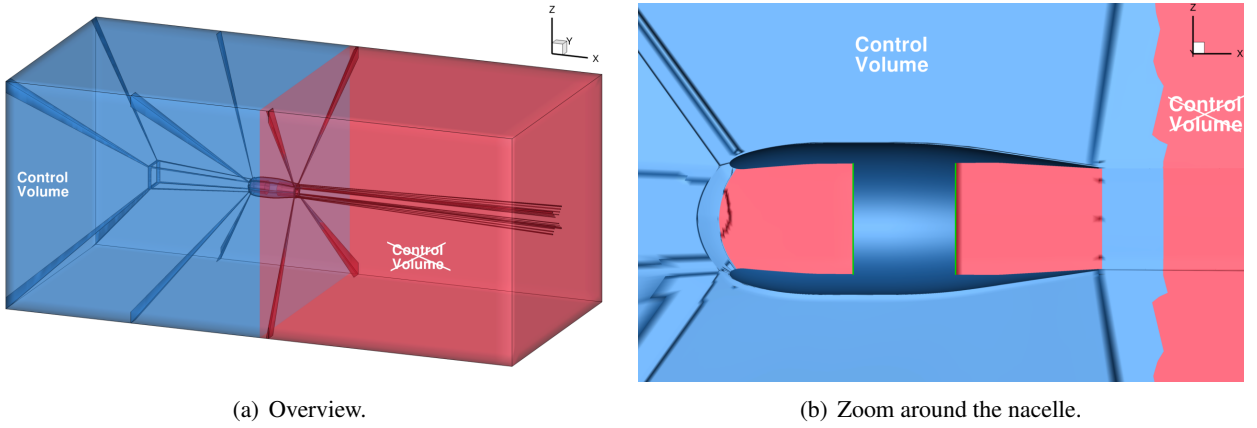
Figure 4-8: 3D Isolated Nacelle: control volume definition for performance prediction.

Table 4.3 provides the value for each term of Eq. (4.4) for this control volume.

	Exergy Balance						
$C\dot{\mathcal{E}}_{prop,nf}$	$CW\dot{\Gamma}$	$C\dot{\mathcal{E}}_m$	$C\dot{\mathcal{E}}_{th}$	$C\dot{\mathcal{A}}_\phi$	$C\dot{\mathcal{A}}_{\nabla T}$	$C\dot{\mathcal{E}}_{prop,ff}$	$\Delta\dot{\mathcal{E}}_{prop}$
2020.87	608.09	360.09	1021.64	19.89	21.46	2031.17	+0.51%

Table 4.3: 3D Isolated Nacelle: verification of the exergy balance.

In a few words, the propulsive device has supplied 2,021 pc of exergy to the flow. Only a relatively small portion has been converted to effectively generate a (great amount of) thrust to apply a net forward force of 608.09 pc, which is in excellent agreement with the momentum analysis (607.76 dc). Large amounts of excess of mechanical and thermal exergy are flowing out of the control volume. Finally, note that the thermal and viscous anergy generation coefficients are of same magnitude.

The sum of all right-hand side terms yields a propulsive exergy slightly higher than the near-field calculation. Yet, with a discrepancy $\Delta\dot{\mathcal{E}}_{prop}$ lower than one percent, satisfactory results are considered. Application of the numerical correction introduced in paragraph 2.5.1.2 (p. 55) reduces this value below 0.001%.

4.2.3 Near-field and Far-field Analyses

4.2.3.1 Fuel Exergy Breakdown

As introduced in paragraph 2.2.1 (p. 39), the propulsive exergy can be broken down to yield additional relevant characteristics of the propulsive device.

Figure 4-9: 3D Isolated Nacelle: fuel exergy decomposition

Fig. 4-10 gives the breakdown of the fuel exergy $\dot{\mathcal{E}}_{fuel}$ down to the generation of thrust.
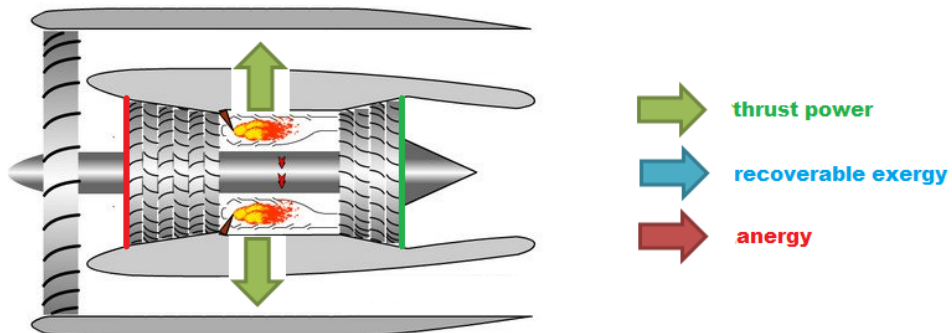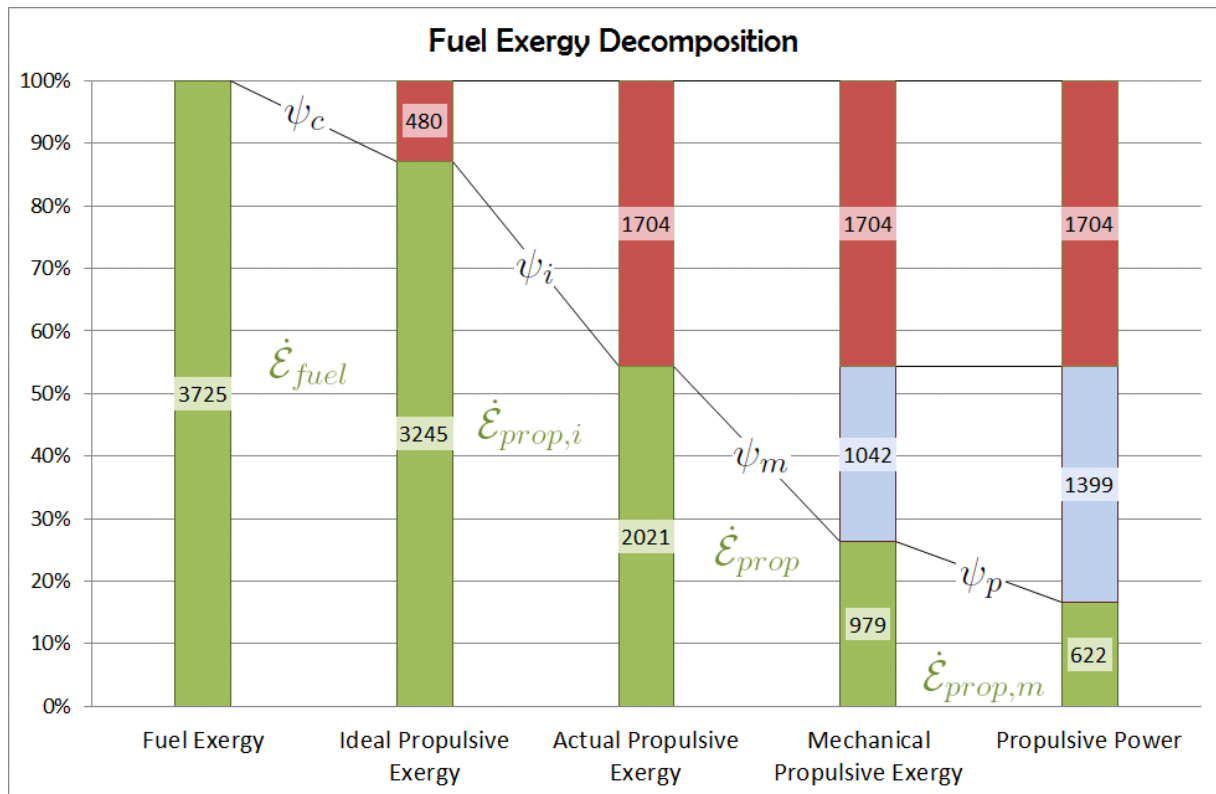
Figure 4-10: 3D Isolated Nacelle: decomposition of the fuel exergy supply.

ψ_c = 87.1%: for a turbojet, the energy supplied to the fluid is delivered by the combustion of fuel, usually jet-A

kerosene. The energy stored in the fuel comes from its chemical deviation from the reference state. The latter must be defined according to the conditions in which the system is operating, *i.e.* the atmosphere at the altitude of flight[7]. To the leading order, we can consider that the exergy content of the fuel is equal to its energy content [47, 114]: $\dot{\mathcal{E}}_{fuel} = \dot{\mathcal{H}}_{prop}$.

$\psi_c = 87.1\%$ is associated with combustion and is equal to the *Carnot* efficiency, only dependent on the temperature at which the fuel is burnt. We have assumed here an ideal[8] combustion temperature of 1,700K, which with an ambient temperature of $T_\infty = 218.8$K, directly yields $\psi_c = 87.1\%$.

$\psi_i = 62.3\%$: this efficiency represents the portion of the ideal exergy delivered by the fuel combustion that is effectively available to generate thrust. It is associated with the *internal* or *intrinsic* losses that have occurred within the engine due to irreversible phenomena like shock waves.

$\psi_m = 48.4\%$: this efficiency represents the portion of the actual (available) propulsive exergy which is in mechanical form; the remaining part being of thermal nature (light blue area, 1042 pc) and therefore not directly transformable into a force.

$\psi_p = 63.5\%$: this efficiency represents the proportion of mechanical exergy that has been converted into useful work, *i.e.* thrust power; the remaining part, being mainly excess kinetic energy as will be seen from Fig. 4-11a, increases the wasted exergy (greater light blue area).

If we multiply all these efficiencies we obtain the engine efficiency ψ_ε

$$\psi_\varepsilon := \psi_p \times \psi_m \times \psi_i \times \psi_c = \frac{F_{prop} V_\infty}{\dot{\mathcal{E}}_{fuel}} = \frac{622}{3725} = 16.7\% \tag{4.5}$$

which corresponds to the rational efficiency introduced by CLARKE and HORLOCK in 1975 [40]. 16.7% is a very low performance indicator which is consistent with other similar studies [47, 139]. In other words, 83.4% of the exergy initially stored in the fuel has been destroyed by internal irreversibilities (45.7%) and lost in the jet (37.6%).

The *Brayton* cycle, on which all gas turbines for propulsion are based, involves the ejection of exhaust gases at high temperatures and velocities to produce thrust [52]. This high exhaust loss, which is specific to the aerospace engine, leads to low exergy efficiencies. This analysis yields absolute figures of merit that do not take into account the specific characteristics of the *Brayton* cycle and more information figures of merit exist for the engine designer, among which the thrust work potential and the gas horsepower [131, 132, 141]. These concepts are however out of the scope of the present analysis.

4.2.3.2 Far-field Outflows Analysis

The preceding paragraph indicated that a large portion of the exergy initially stored in the fuel and released to the flow was actually lost in the jet. These aspects are examined in more detail next.

Mechanical and Thermal Exergy.   Fig. 4-11 gives (a) the mechanical and (b) the thermal exergy outflows in the jet downstream of the nacelle up to 4 body length downstream[9]. Qualitatively speaking, from the pictures on top of the curves, one can see that the jet is well defined by a large streamwise velocity (a) as well as by a much higher static temperature (b).

---

[7] In reality, these conditions vary with time and space, but to simplify we assume a standard reference atmosphere.

[8] Ideal is here considered in the sense of no *unburnt hydrocarbons*. Also, the order of magnitude of the combustion temperature chosen here is correct [41]. In any case, it should be taken as an illustrative example.

[9] The *step*-like shape of the curves is due to the increasing cell sizes in the wake: more than one data point is calculated in the same cell.

(a) Mechanical aspects.

(b) Thermal aspects.
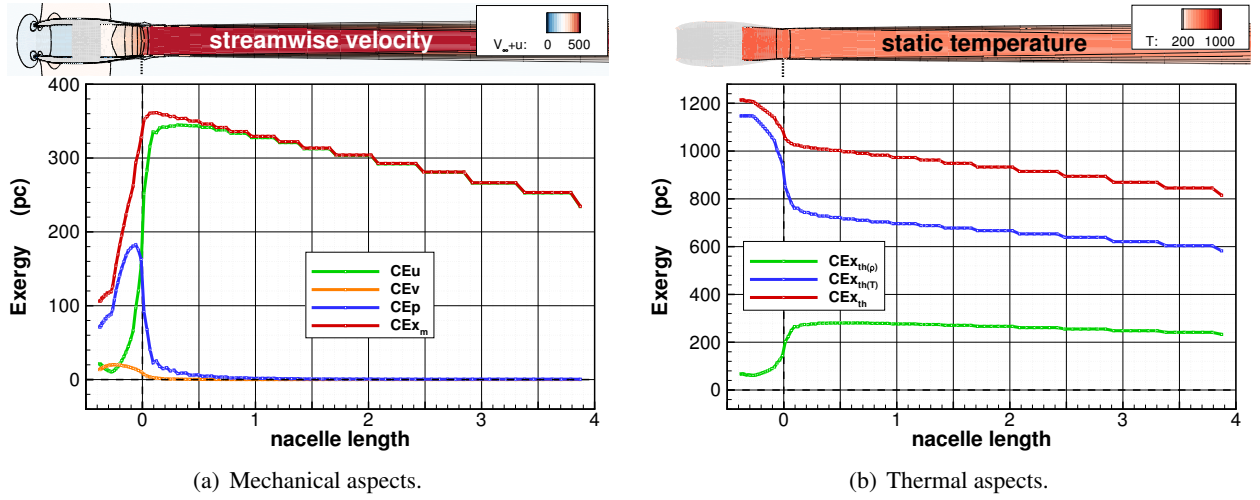
Figure 4-11: 3D Isolated Nacelle: (a) mechanical and (b) thermal exergy outflow in the jet downstream of the nacelle.

Fig. 4-11a gives the decomposition of the mechanical exergy into the streamwise kinetic power, the transverse kinetic power and the pressure boundary-work rate:

$$\dot{\mathcal{E}}_m = \dot{E}_u + \dot{E}_v + \dot{E}_p \tag{4.6}$$

Little transverse kinetic energy ($\dot{E}_v$ −) is observed in the nozzle of the nacelle. This region is designed to convert the higher static pressure into axial velocity of the jet in order to produce thrust. This energy exchange is clearly visible noting that the boundary pressure work ($\dot{E}_p$ −) is converted into streamwise kinetic energy ($\dot{E}_u$ −). Because the nacelle is almost perfectly expanded ($p_{exhaust} \simeq p_\infty$), all the energy input is ultimately converted into streamwise kinetic energy which forms the mechanical exergy ($\dot{\mathcal{E}}_m$ −).

Fig. 4-11b provides the decomposition of the thermocompressible exergy into its pure thermal and compressible components:

$$\dot{\mathcal{E}}_{th} = \dot{\mathcal{E}}_{th(\rho)} + \dot{\mathcal{E}}_{th(T)} \tag{4.7}$$

The adjective *thermocompressible* introduced in paragraph 2.2.2.3 (p. 43) makes perfect sense for this test case. One can see that the predominant form in the jet exhaust is the one associated with compressibility $\dot{\mathcal{E}}_{th(\rho)}$ (−). In the exhaust nozzle, a portion of this component is converted into the purely thermal component $\dot{\mathcal{E}}_{th(T)}$ (−) as the fluid rapidly expands.

Recoverable Exergy and Dissipation. The mechanical and thermal exergy outflows have been characterized. According to Second Law considerations, these two quantities have to be dissipated in order to bring the system back to mechanical and thermal equilibrium with the atmosphere. Fig. 4-12

Fig. 4-12a provides the evolution of the three main dissipation terms in the jet. First, note that the thermal anergy ($\dot{\mathcal{A}}_{\nabla T}$ −) rapidly becomes more significant than the viscous anergy ($\dot{\mathcal{A}}_\phi$ −) and is already more than twice as high only two nacelle length downstream of the body.

Second, the difference between the energy ($\dot{E}_\phi$ −) and the anergy associated with viscous dissipation is highlighted. While little discrepancy between the two coefficients is visible in the boundary layers around the nacelle ($x \leq 0$), in the jet, the distance between the two curves increases. In other words, viscous dissipation at higher temperature generates lower levels of anergy $\dot{\mathcal{A}}_\phi = T_\infty/T \times \dot{E}_\phi$. This observation is consistent with the idea that dissipation at high temperature is less crucial [31].

130

(a) Anergy generation.

(b) Recoverable exergy.
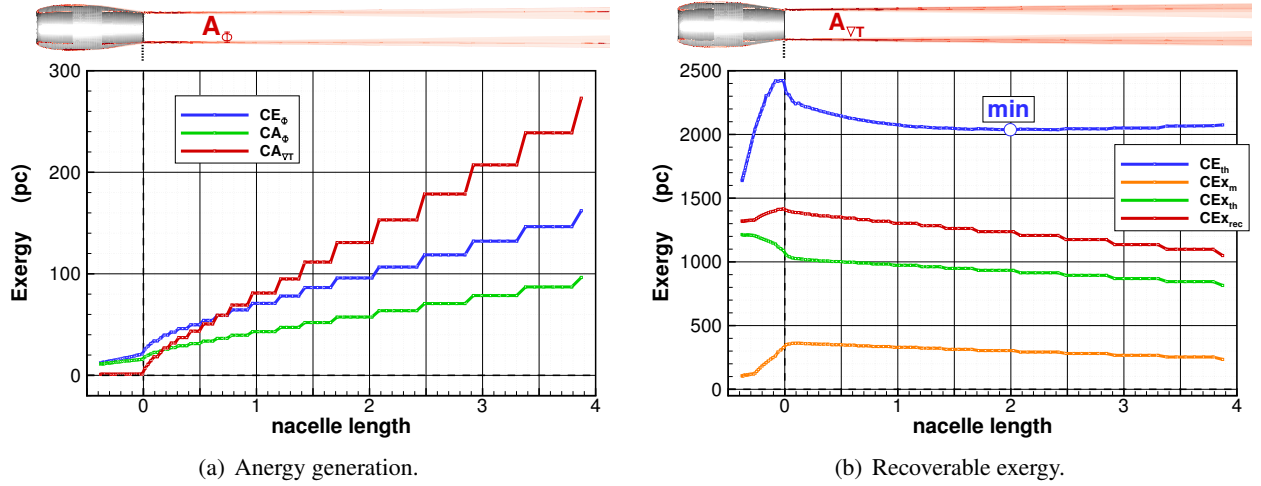
Figure 4-12: 3D Isolated Nacelle: dissipation terms and recoverable exergy in the jet of the nacelle.

Fig. 4-12b gives some additional information on the recoverable exergy; two comments should be made.

First, the thermal energy $\dot{E}_{th}$ (–) increases steeply in the nozzle where the fluid expands up to the exhaust. Then, this form of energy decreases to reach a minimum at about two nacelle lengths downstream of the body, which corresponds to a mid-field transient *reequilibrium*, and then increases again. In fact, this component will continue to grow as the transverse plane is moved away from the nacelle because of the increasing dissipation ($\dot{E}_{\phi}$, – in Fig. 4-12a) in the wake which converts mechanical energy into thermal energy.

This thermal energy has a very different behavior than the *pure*[10] thermal exergy (–) which is monotonically decreasing (downstream of the exhaust). In other words, although the total amount of thermal energy increases, its practical value (exergy) vanishes as we move aft from the nacelle.

Second, note that in the nozzle, the thermocompressible exergy (–) is converted into mechanical exergy (–) thereby leading to a maximum recoverable exergy (–) at the exhaust $\dot{\mathcal{E}}_{rec} = \dot{\mathcal{E}}_m + \dot{\mathcal{E}}_{th}$. The negative slopes for all exergy terms makes it clear that their work potential is decreasing.

The recoverable exergy, or more exactly the exergy *wasted*, is made of residual mechanical energy and of thermal exergy which at 3 nacelle lengths downstream represents about 1,200 pc or $EWC_3 = 59.4\%$ of the exergy delivered to the fluid by the propulsive device. It would however be wrong to consider that the streamwise kinetic energy downstream of the jet engine should be recovered: the underlying principle of the *Brayton* cycle of a gas turbine is to accelerate the flow to produce thrust.

However, the exergy analysis tells us that reducing the magnitude of the perturbations improves the efficiency. One way to reduce the velocity of the jet, for a given amount of thrust to be delivered, is to accelerate a greater mass flow. This increase in the bypass ratio is known to enhance the propulsive efficiency of turbofan engines.

4.2.4 Summary of the Key Findings

An isolated turbojet in cruise conditions ($M_\infty = 0.82$) was investigated. The core of the engine is modeled by a set of two boundary conditions which set the input the mass flow through the engine, and the jump in total enthalpy at the exhaust which represents the total energy released from the combustion of fuel.

---

[10]Thermal exergy at constant volume, see derivation in paragraph 2.2.2.3 (p. 43).

In the case of more traditional propulsion systems integration, the propulsive exergy term can be decomposed to express the propulsive thrust power and therefore the approach proposed here could fit conventional drag/thrust bookkeepings [42, 53]. Also, the evaluation of the thrust was proven highly sensitive to the number of cell layers added for the definition of the propulsive volume. As a consequence, an additional benefit of the exergy balance comes from the low sensitivity of the main performance metric (propulsive exergy) to the definition of the propulsive surface.

The formulation allows the determination of the full characteristics of the propulsive device. It was notably highlighted that, as opposed to all unpowered configuration examined in the previous chapter 3 (p. 63), for realistic propulsion systems that are thermally representative, the thermal aspects (exergy and anergy) become predominant in the overall performance balance.

Higher fidelity models of the propulsion sub-system would be required to yield more convincing arguments as to the ability of the formulation and of the code *ffx* to assess the loss generation mechanisms at a component level, as proposed by CLARKE and HORLOCK [40] in 1975 and revisited in the 1980-90's [44, 112, 150].

4.3 Wake-ingesting Academic Configuration

The aim of this numerical application is to demonstrate the benefit of the formulation for a physical flow analysis. It is also a first step towards the investigation of a realistic boundary layer ingestion (BLI) propulsion systems placed on top of a blended-wing body in section 4.4 (p. 143).

This study has been presented at the 32nd AIAA Applied Aerodynamics Conference in Atlanta (GA) in June 2014, see [11].

4.3.1 Test Case Presentation

4.3.1.1 Background

The present study follows recent numerical and experimental aerodynamic investigations of BLI at ONERA [16]. The test case has been developed for validating both numerical simulations and experimental methodologies that will be necessary for the design of a future transport aircraft incorporating a BLI propulsive system. It consists in a rather academic configuration made up of a simplified fuselage geometry and a nacelle enclosing a fan. The fuselage has been designed to produce a wake whose diameter matches the one of the engine inlet, so that a 100% wake ingestion is achievable, see Fig. 4-13.

(a) 3D view.

(b) XZ-Plane view.
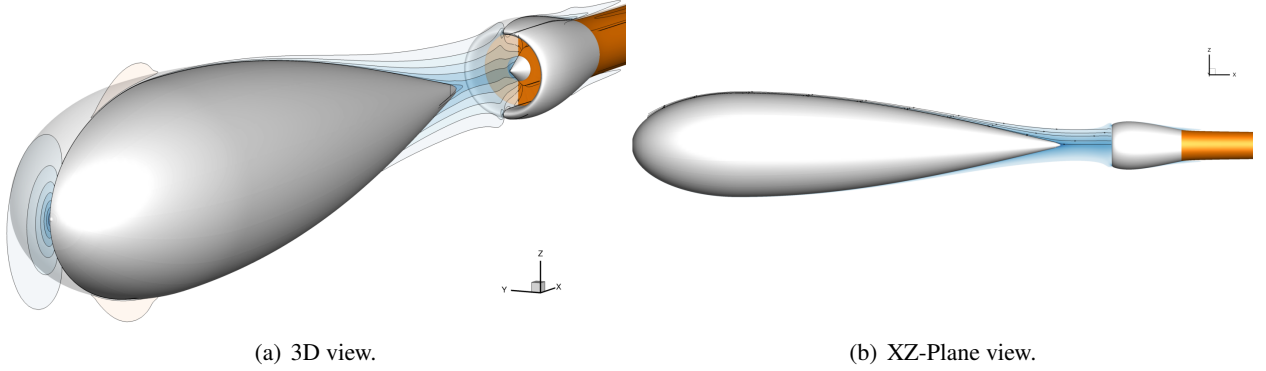
Figure 4-13: 3D representation of the BLI configuration ingesting the fuselage wake.

The *Reynolds* number is set at $Re = 4.58 \times 10^6$ based on a unit reference length. No incidence is considered and a low-speed *Mach* number of $M_\infty = 0.20$ is set, so that the flow is in the low-compressible range.

4.3.1.2 Reference and BLI Configurations

Two configurations will be compared to determine the benefit of the BLI arrangement:

- A **BLI configuration** which corresponds to the case where the nacelle is placed at a given distance downstream of the fuselage ($\Delta x = 0.20$ for a fuselage length of 1.50). The aim being for the nacelle to ingest the entire wake of the fuselage and leaving no wake is downstream of the entire configuration, see Fig. 4-14. This configuration will be referred to as BLI.

  Strictly speaking it is more a wake ingestion rather than a boundary layer ingestion, but the acronym BLI is used for convenience.

- A **reference configuration** which corresponds to the case where the fuselage and the nacelle are assumed to be sufficiently far from each other so that we can neglect any interaction between the two solids, see Fig. 4-15. This configuration represents a typical commercial aircraft architecture and will be referred to as REF.
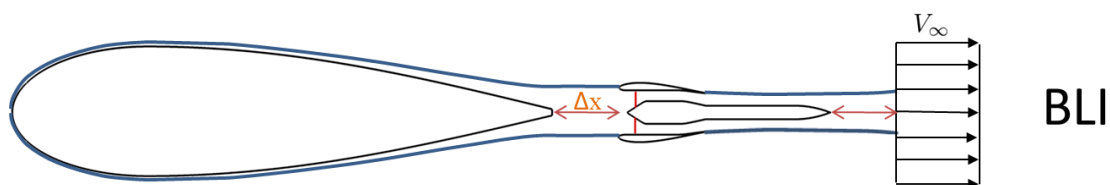
Figure 4-14: 3D wake-ingesting configuration: simplified representation of the ideal BLI configuration.
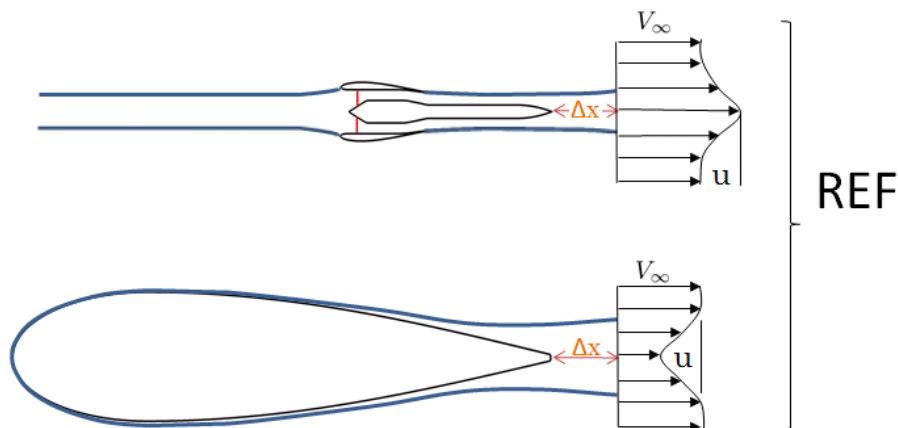
Figure 4-15: 3D Wake-ingesting Configuration: simplified representation of the reference configuration being the combination of the isolated nacelle (top) and of the isolated fuselage (bottom).

4.3.1.3 Numerical Settings

Grids. According to the methodology described, three grids have been generated, by GRENON (ONERA). First, an isolated fuselage with 172,000 nodes and an isolated nacelle with 533,000 nodes. This ensures the absence of interactions between the two bodies. Secondly, a [fuselage + nacelle] configuration with 694,000 nodes. In order to reduce the computational time, only an angular portion (16° or 18°) of the 3D configuration (360°) is represented. All grids are structured, axisymmetric, multiblocks and extend about 10 reference lengths in all three dimensions, see Figs. B-8, B-9 and B-10 in appendix B.3 (p. 195).

Because these meshes are relatively coarse, the absolute performance coefficients that can be extracted from the flow solutions may be affected. However, as we are interested in comparing two configurations (REF and BLI) that have approximately the same level of inaccuracy, the difference between the coefficients will be meaningful.

Boundary Condition. Different models can be applied to represent the propulsion system with different level of fidelity. For turbofans, the thrust is mainly produced by the fan itself so that modeling its impact on the flow is a satisfactory approximation. Actuator disks are therefore used in the present analysis. They are relatively average-fidelity as they (only) model the mechanical aspect of the propulsion system. It consists in the addition of a uniform total pressure jump $\Delta p_i = p_{i,out} - p_{i,in}$ across the discontinuity, see Fig. 4-16.

The main advantage of this boundary condition is that the flow downstream is affected by the state of the flow upstream of it. Its main drawback is that it does not take into account the flow distortions present in the boundary layer. As a consequence, we implicitly assume that the inlet fan distortion does not modify the fan operating conditions, which is a relatively strong assumption [127]. Further improvements of this boundary condition formulation are necessary to take into account those distortions [80].
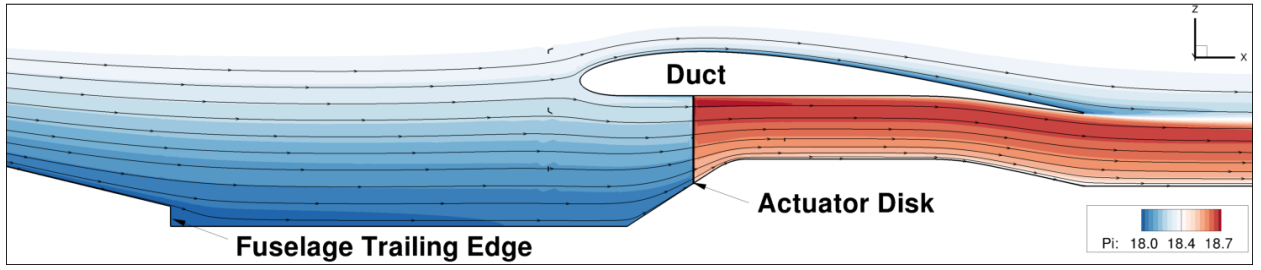
Figure 4-16: 3D Wake-ingesting Configuration: wake ingestion and actuator disk position. Contours of total pressure and streamlines.

Flow Computations. All computations are made using the Onera-*elsA* code [35]. No multigrid techniques are used to accelerate the convergence and all computations are performed in fully turbulent conditions using the *Spalart–Allmaras* model [156]. For the BLI computations, the flow is initialized with a first computation where the nacelle and the fuselage are interacting but the actuator disk is inactive. 60,000 iterations are made to get a 6-order residual reduction, which is considered satisfactory, see Fig. 4-17. Then 60,000 additional iterations are run to provide again a 6-order residual reduction with the actuator disk active.
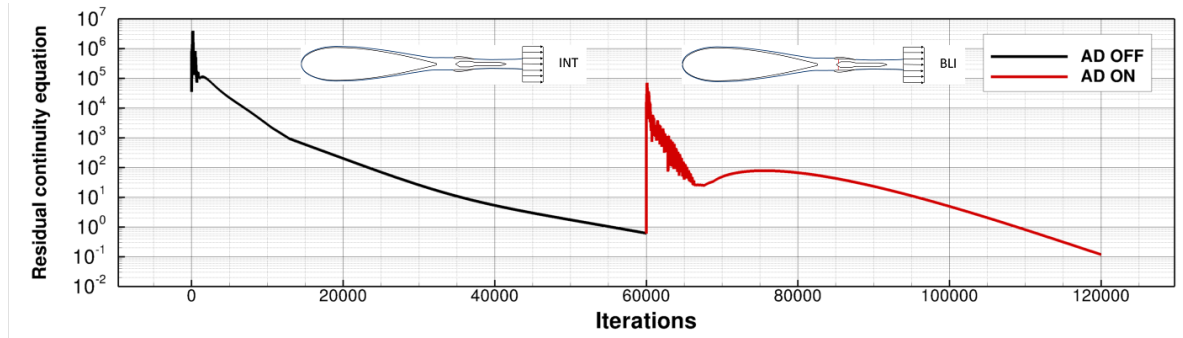
Figure 4-17: 3D Wake-ingesting Configuration: typical residuals reduction. Black line: actuator disk inactive, red line: actuator disk active.

A total of 54 computations with various pressure jump across the actuator disk was performed: 27 for the isolated nacelle (REF configuration) and 27 computations for the BLI configuration, as illustrated in Fig. 4-18.
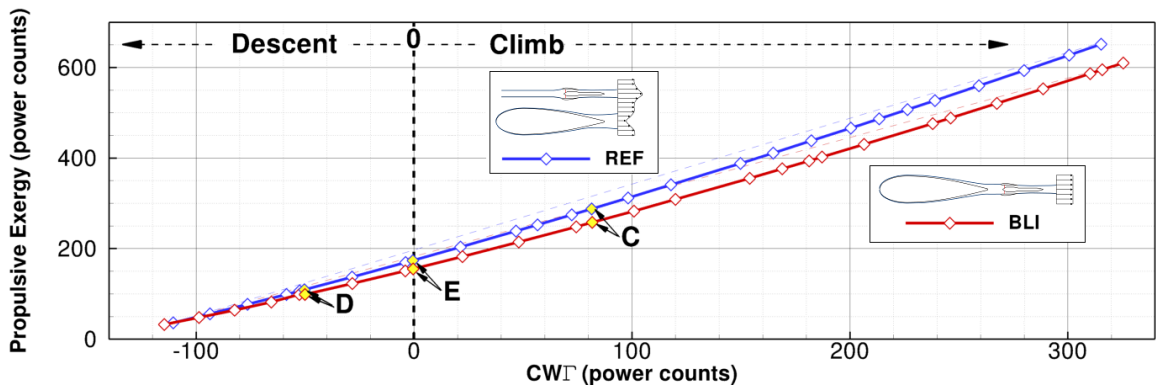
Figure 4-18: 3D Wake-ingesting Configuration: propulsive exergy versus net force acting on the configuration for the REF configuration (blue) and for the BLI configuration (red).

In the following, emphasis will be put on three REF and three BLI cases characterized by an equal net force acting on the configuration which is respectively negative, zero and positive: case **D** when the aircraft is in descent, case **E** in equilibrium and case **C** when in climb.

135

4.3.2 Aeropropulsive Performance Assessment

The investigation considers the 4 following steps:

1. Evaluation of the recoverable exergy and EWC of the reference configuration in paragraph 4.3.2.1,

2. Performance comparison of three selected REF/BLI cases in 4.3.2.2,

3. Characterization of the outflow for the case at equilibrium in 4.3.2.3,

4. Quantification of the overall BLI benefit in 4.3.2.4.

4.3.2.1 Nacelle-Jet and Fuselage-Wake Recovery Potential

According to the methodology described above, the first step consists of determining the recoverable exergy from the reference configuration. The recoverable exergy is defined as the mechanical (and in a lesser extent thermal) exergy flowing out of the control volume. It is crucial to note that both a jet and a wake represent a potential for improvement: the kinetic energy associated is independent on whether the flow is locally faster or slower than the freestream velocity: as soon as the flow is not in equilibrium with its environment ($u \neq u_\infty$), exergy exists. Viscous (and thermal) anergy will have to be generated to dissipate this work potential. It is therefore important to evaluate how much recovery potential exists. Fig. 4-19 represents the outflow's recoverable exergy destruction when moving the outer boundary downstream of the nacelle-jet[11] (a) and the fuselage-wake (b). For the nacelle, the *step*-like shape of the curve is due to increasing mesh cell size.

(a) A typical propulsive nacelle-jet. (b) The fuselage-wake.
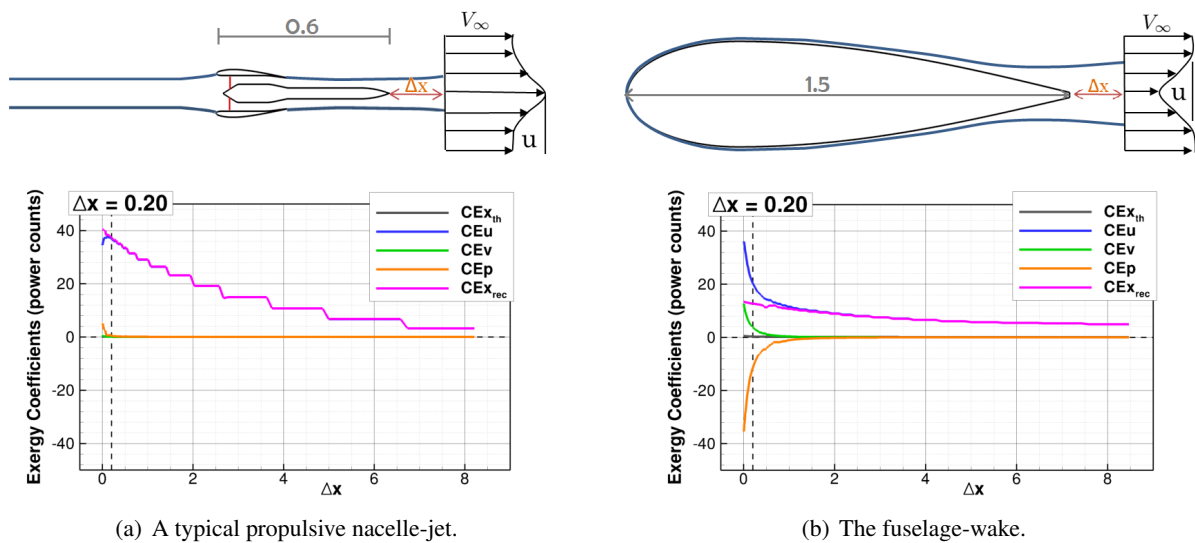
Figure 4-19: 3D Wake-ingesting Configuration: outflows recoverable exergy destruction when moving the outer boundary downstream the body.

For both bodies, the thermal exergy (–) is very negligible, as expected, and the pressure-work (–) and transverse kinetic energy (–) rapidly reduce to zero, leaving the streamwise kinetic energy (–) as the largest contributor to recoverable exergy (–).

The exergy recovery potential and the EWC are represented in Fig. 4-20 for a downstream plane located at a given distance downstream of the configuration $\Delta x = 0.20$.

As regards recoverable exergy, the fuselage contribution (–) is constant[12] while the nacelle contribution

---

[11] The general characteristics of the jet have been examined for the isolated nacelle in section 4.2 (p. 122).

[12] Around 13 pc which represents around 10% of its drag.
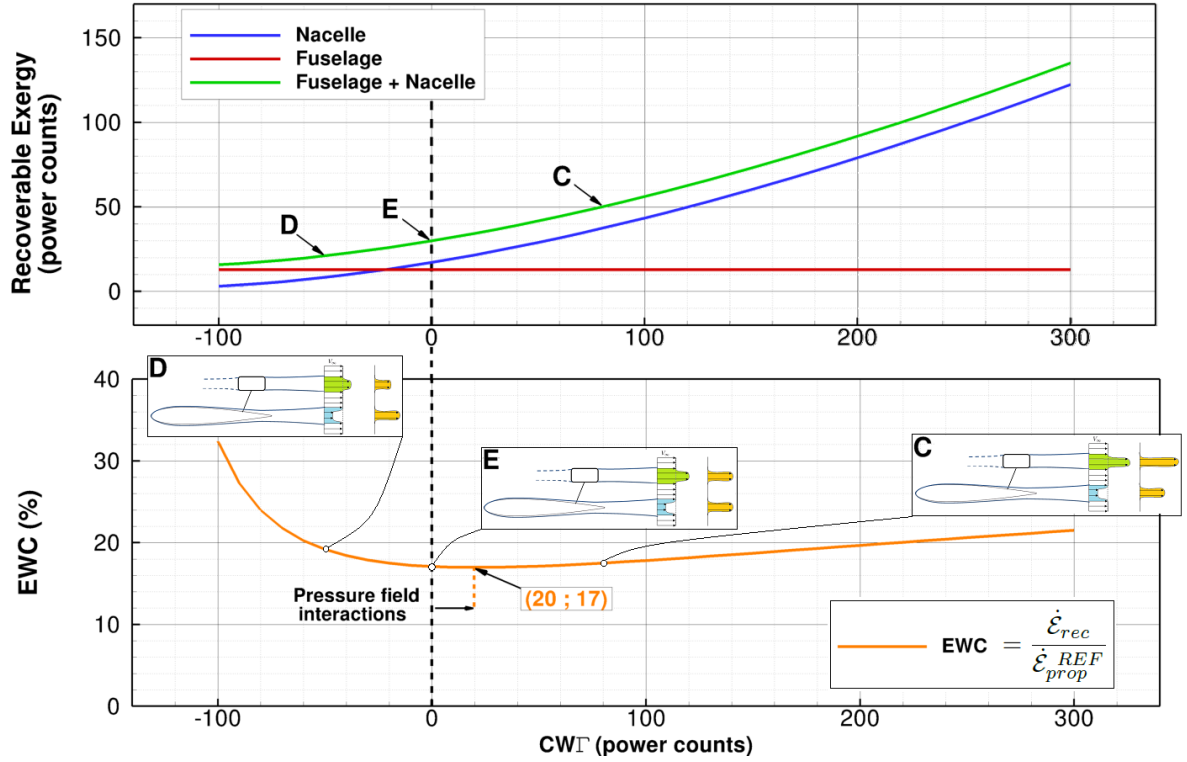
Figure 4-20: 3D Wake-ingesting Configuration. Top: extrapolated recoverable exergy at $\Delta x = 0.20$ versus net force acting on the reference configuration. Bottom: EWC versus net force acting on the configuration.

(–) increases with increasing thrust. By non-dimensionalizing the total recoverable exergy by the propulsive exergy, we get the EWC (–). The curve exhibits a minimum value close to equilibrium which makes the separation between an overall wake ($u - u_\infty < 0$) and an overall jet ($u - u_\infty > 0$). Besides from values extrapolation, pressure field interactions ($\dot{E}_p$ – in Fig. 4-19b) are likely to be the cause of shifting from strict equilibrium.

The higher values on the right are associated with the exergy supplied[13] in excess at greater thrust levels and moderated by higher propulsive exergy. As opposed, the higher values reached at descent are associated with the wake when low levels of thrust are generated and emphasized by low levels of propulsive exergy.

In the following analysis, the nacelle will be located $\Delta x = 0.20$ downstream the fuselage. This distance is also the shortest one at which pressure field interactions are negligible according to wind-tunnel testings.

4.3.2.2 Far-Field Exergy Comparison

Now that the recoverable exergy and EWC have been determined, it is possible to compare the BLI configurations to the reference configurations. Qualitatively, the benefit of the BLI configuration is illustrated in Fig. 4-18 (p. 135) by the vertical distance between the REF curve in blue and the BLI curve in red: for a given net force acting on the configurations, the BLI requires less propulsive exergy.

Quantitatively speaking, Table 4.4 presents the far-field exergy terms with or without BLI for the three cases mentioned, D, E, and C. The values for REF are the sum of those for the nacelle and for the fuselage, at the same downstream location of the outer boundary S_O ($\Delta x = 0.20$). For the BLI cases, the nacelle is located at $\Delta x = 0.20$ downstream the fuselage and the outer boundary is located at $\Delta x = 0.20$ downstream the nacelle.

---

[13]In the form of kinetic energy.

	Configuration	$CW\dot{\Gamma}$	$C\dot{\mathcal{E}}_{rec}$	$C\dot{\mathcal{A}}_{tot}$	$C\dot{\mathcal{E}}_{prop}$	EWC	ERC	ESC
	REF	-50.3	20.9	138.6	109.0	19.2%	–	–
D	BLI	-50.1	2.4	146.1	98.6	–	50.7%	9.7%
	BLI - REF	+0.2	-18.5	**+7.5**	**-10.6**	–	–	–
	REF	-0.5	30.4	144.7	174.6	17.4%	–	–
E	BLI	-0.4	3.5	152.4	155.5	–	62.8%	10.9%
	BLI - REF	+0.1	-26.9	**+7.7**	**-19.1**	–	–	–
	REF	81.5	50.1	156.0	287.3	17.4%	–	–
C	BLI	81.8	10.2	164.5	258.1	–	58.3%	10.2%
	BLI - REF	+0.3	-39.9	**+8.5**	**-29.2**	–	–	–

Table 4.4: 3D Wake-ingesting Configuration: far-field exergy terms comparison with or without BLI for a downstream plane located at $\Delta x = 0.20$. All exergy coefficients are expressed in power counts.

The following comments can be made:

- From the fist column of results ($CW\dot{\Gamma}$), we can effectively consider that the same force is acting on the two configurations, within 0.3 power counts.

- From the second column we have the recoverable exergy of the reference configuration (Fig 4-20). Note the great reduction in the recoverable outflows with the BLI configuration. This point will be described in greater details in the following section.

- The third column indicates the anergy generated within the control volume, or equivalently, the exergy destroyed. We observe a non-negligible increase with the BLI configuration meaning that some of the initial recovery potential has been destroyed by the interaction between the two solids. For case E for example, if this *interaction anergy* was negligible, the exergy saving would rise from 19.1 to 26.8, thereby improving the ERC from 62.8% to ERC* = 88% and the ESC up to 15.3%.

- The fourth column represents the exergy delivered by the propulsion system and is the sum of the three previous terms, see Eq. (2.34). We observe a large reduction of the propulsive exergy for the BLI configuration.

The exergy-waste coefficient (EWC) is around 18% which is a relatively high figure due to the ingestion of the entire fuselage-wake. The exergy-recovery coefficient (ERC) ranges from 50% to 60% meaning that about half of the initial potential was effectively recovered, the rest being lost or destroyed by interaction. This figures yield a global exergy-saving coefficient (ESC) of about 10%.

A rapid estimation of the EWC_{BLI} can be made for the BLI arrangement from the data available in Table 4.4. Only 2-4% of the propulsive exergy would be recoverable at a downstream location of $\Delta x = 0.20$ meaning that placing a second nacelle downstream the first one would not make sense. This low figure equivalently signifies that more than 96% of the propulsive exergy was used wisely.

4.3.2.3 Outflow Characterization for the Case at Equilibrium

The BLI benefit having been clearly quantified, it appears that the exergy saving is mainly due to a great reduction of the various recoverable outflows. Therefore Table 4.5 provides more detailed information about the outflows downstream of the configurations for case E.

From the first column ($C\dot{E}_u$) we can see that the streamwise kinetic energy has nearly vanished downstream of the BLI configuration. Also, the second and third columns indicate that the transverse kinetic energy and boundary pressure-work have been noticeably reduced, being almost negligible for the BLI configuration. The thermal exergy is clearly negligible compared to the mechanical terms.

Configuration	Body	$C\dot{E}_u$	$C\dot{E}_v$	$C\dot{E}_p$	$C\dot{\mathcal{E}}_{th}$	$C\dot{\mathcal{E}}_{rec}$
	Fuselage	20.6	3.8	-11.7	0.6	13.3
REF	Nacelle	16.6	0.1	0.3	0.1	17.1
	Nacelle + Fuselage	37.2	3.9	-11.4	0.7	30.4
BLI	Nacelle + Fuselage	3.8	0.6	-1.2	0.3	3.5
BLI - REF	Nacelle + Fuselage	-33.4	-3.3	+10.2	-0.4	-26.9

Table 4.5: 3D Wake-ingesting Configuration: detailed far-field exergy outflows comparison with or without BLI for case E and a downstream plane located at $\Delta x = 0.20$. All exergy coefficients are expressed in power counts.

Except for the streamwise kinetic energy, the outflows downstream of the BLI configuration are comparable to those downstream of the isolated nacelle, see lines 2 and 4. In other words, to the leading order, the BLI arrangement is almost equivalent to having removed the fuselage wake. By doing so, the anergy (entropy [120]) that would have been required to bring the velocity perturbation back to equilibrium is avoided: because less exergy is destroyed, less exergy needs to be supplied.

Although, it appears that the overall benefit comes from various source, the largest exergy form that is dealt with in this application is the flow streamwise kinetic energy $\dot{E}_u$ and of the boundary pressure work rate $\dot{E}_p$. Fig. 4-21 presents the evolution of the streamwise kinetic energy outflow (–) and of the boundary pressure-work rate (–) when the plane of the outer boundary S_O is moved over the nacelle. By doing so, we *scan* the configuration and can pinpoint the location of great variations. The thick lines represent the isolated nacelle of the reference case, *i.e.* when the bodies are assumed sufficiently far from each other that we can simply sum the separate terms. The thin and dotted lines represent the BLI case.

Qualitatively speaking, from the relative velocity-squared field on top of Fig. 4-21, one can see that there is very little kinetic energy in the jet of the nacelle, suggesting that this case is close to the ideal one where no exergy, in the form of kinetic energy, is wasted, see sketch in Fig. 4-22.

Quantitatively speaking, comparing the evolution of $\dot{E}_u$ and $\dot{E}_p$ for the isolated nacelle and the BLI configuration, one can see that:

- For the BLI case, we observe non-zero values ($\pm\,40\,pc$) which indicate perturbations generated by the fuselage, *i.e.* its wake.

- For both cases, the flow is slowed down when approaching the engine inlet: there is a conversion of kinetic energy into pressure energy.

- The dramatic decrease of the kinetic energy around $x = 0.0$ is associated with the acceleration of the flow around the duct leading edge[14]. Afterwards, the velocity is increased due to a reduction of the channel area (incompressible flow) around the actuator disk (— —). The difference between the isolated nacelle and BLI configuration is more significant regarding the $\dot{E}_p$ term.

- The (total) pressure jump across the actuator disk (clearly visible on the $\dot{E}_p$ curve) is then converted into kinetic energy through the engine's exhaust. As a consequence, the axial velocity increases up to the nacelle exhaust and at about half the nacelle length the velocity nearly matches the one of the freestream at which point the kinetic energy exhibits a minimum value.

- The flow is further accelerated in both cases and remains relatively constant for the isolated nacelle in which case the kinetic energy will be dissipated by viscous dissipation. On the other hand, the BLI kinetic energy is rapidly reduced by simple interaction with the $\dot{E}_p$ term. The same process can not

---

[14]The flow velocity gets closer to the freestream and therefore its kinetic energy reduces.
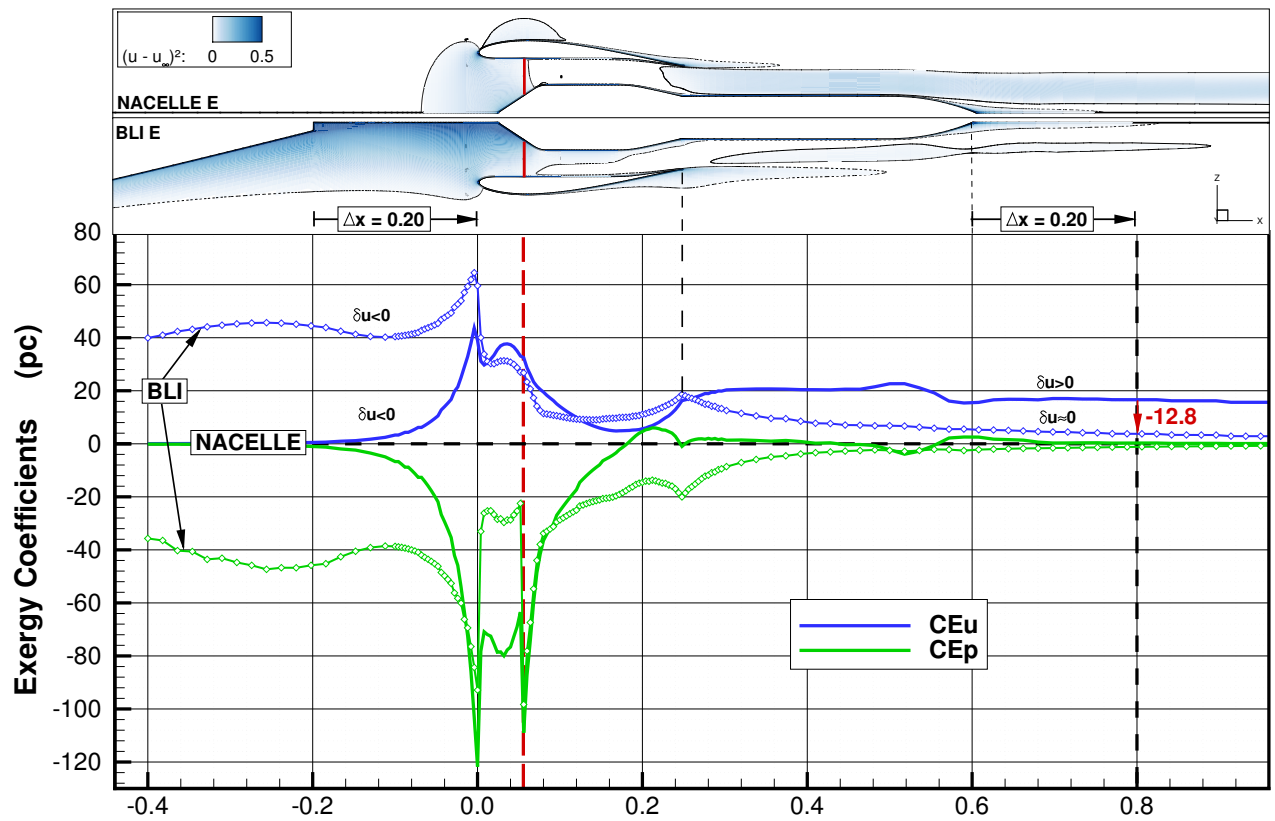
Figure 4-21: 3D Wake-ingesting Configuration. Top: contours of relative velocity squared for the nacelle and BLI when at equilibrium (Case E). Dashed line enclose regions of negative relative axial velocity (deficit) while solid line enclose regions of positive relative axial velocity (excess). Bottom: Comparison of $C\dot{E}_u$ and $C\dot{E}_p$ with or without wake ingestion. Thick lines indicate the reference configuration while the thin and dotted lines indicate the BLI configuration
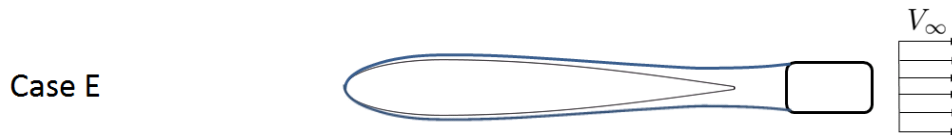
Figure 4-22: 3D Wake-ingesting Configuration: Case E (at equilibrium) is close to the ideal BLI configuration.

occur for the isolated nacelle as $C\dot{E}_p^{nacelle} \simeq 0$. As a consequence, at $\Delta x = 0.20$, there is a 12.8 pc reduction compared to the reference.

Note that the mass flow rate of the internal flow (through the engine) is reduced by roughly 12% which is the reason for lower energy (exergy) supply to the flow.

4.3.2.4 BLI Benefit Overview

A summary of the points that have been made in the above sections is provided by Fig. 4-23 which gives the variation of the three coefficients that quantify the BLI benefit.

The exergy delivered by the propulsive system (top) and the ESC (bottom) are plotted in Fig. 4-23a. Again, the direct benefit of the BLI configuration can be observed by the vertical distance between the two curves. Note that they nearly cross at $C\dot{W}\dot{T} = -100\ pc$: there is an overall negative impact when the propulsive system does not generate great levels of thrust. In other words, the two bodies have a negative impact when placed close from one another: there is an increase in exergy destruction.
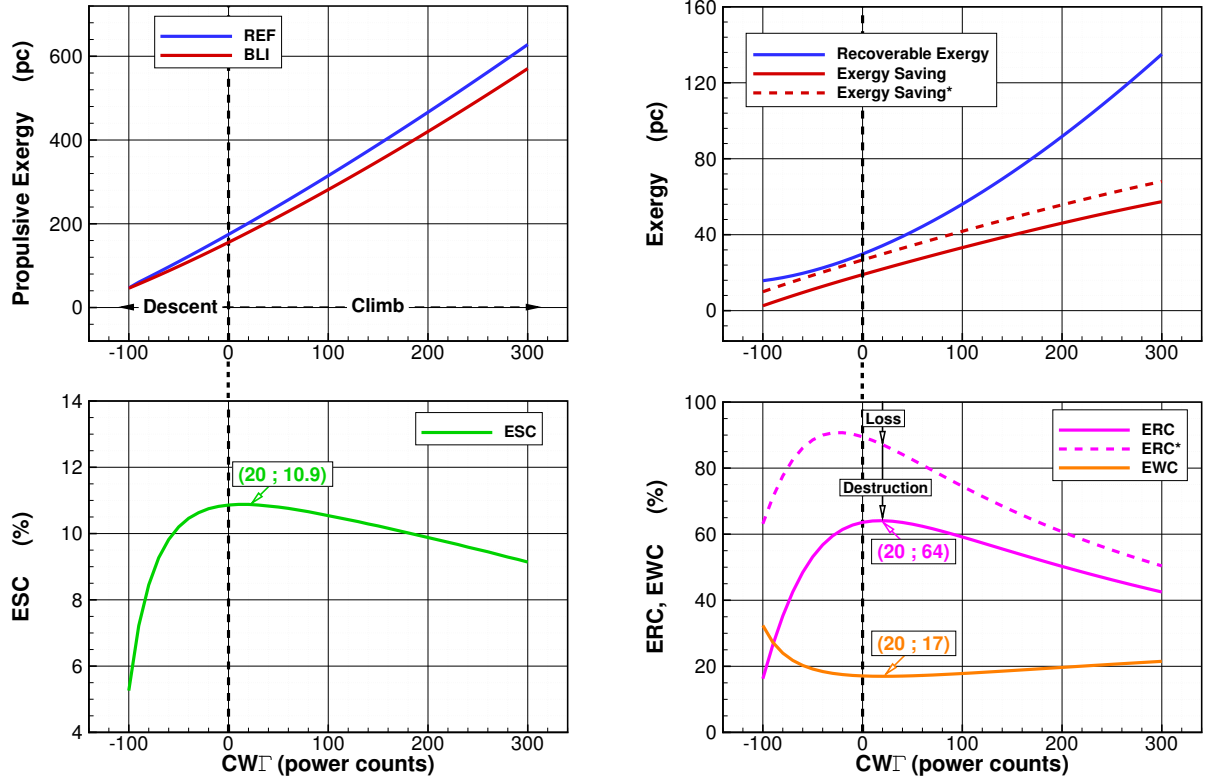
(a) Top: total power coefficients for reference configuration (blue) and BLI configuration (red) versus change in energy height. Bottom: ESC versus change in energy height.

(b) Top: recoverable exergy (blue), actual and possible exergy saving (red) versus change in energy height. Bottom: EWC, ERC and ERC* versus change in energy height.

Figure 4-23: 3D Wake-ingesting Configuration: BLI performance coefficients summary

However, it appears that the BLI arrangement presents a benefit over a wide range of $CW\dot{\Gamma}$: the ESC (–) ranges from 5 to 11% at descent, but more importantly exhibits a maximum of ESC_{max} = 10.9% near equilibrium and stays relatively constant for climb cases. As more thrust is generated, the ESC drops down to 9% at $CW\dot{\Gamma}$ = 300 pc. As mentioned earlier, this figure of merit is critical as it directly indicates how much fuel could be saved. However, in a design perspective, this coefficient does not tell the designer how much improvement was in fact achievable.

Fig. 4-23b gives more information about how much improvement was possible and how efficient was the recovery of the initial potential. Top figure recalls the recoverable exergy (–), which, divided by the propulsive exergy, yields the EWC (–). This coefficient exhibits a minimum EWC_{min} = 17% near equilibrium. As we have seen, the higher values on the right are associated with the exergy supplied in excess (in the form of kinetic energy) at greater thrust levels and moderated by higher propulsive exergy. As opposed, the higher values reached at descent are associated with the wake when low levels of thrust are generated and magnified by low levels of propulsive exergy.

Top figure also gives the exergy effectively recovered (–) and the exergy that could have been recovered in the absence of *interaction anergy* (– –). Bottom figure shows that ERC (–) exhibits a maximum of ERC_{max} = 64% at $CW\dot{\Gamma}$ = 20 pc. There are two identified reasons for not recovering 100% of the recoverable exergy. First, part of it has been destroyed by interaction anergy, *i.e.* the additional exergy destroyed due to the interaction of the two bodies, see ERC* (–). The second reason is the loss of that potential because the presence of the engine has modified the initial flow field downstream of the fuselage. In descent, the destruction is the most important cause while at climb the loss appears predominant.

141

Interestingly, the maximum exergy saving (ESC) occurs when the improvement potential (EWC) is the lowest but its recovery (ERC) is the highest. As a consequence, it would not make sense to simply focus on the situation where the potential (EWC) is highest.

4.3.3   Summary of the Key Findings

The formulation was applied to an academic BLI configuration to investigate the benefit of wake ingestion with high fidelity (CFD) tools and realistic engine conditions. A simplified fuselage was used to generate a wake subsequently ingested by a propulsion system. An actuator disk boundary condition was applied to model the effects of a fan on a low-speed flow (M_∞ = 0.20). It has been shown that the boundary pressure-work may be as important as the streamwise kinetic energy to explain the benefit of this principle.

The *common currency* aspect of the exergy analysis could facilitate the development of such concepts that are multidisciplinary. First, from an exergy standpoint, the potential benefit associated with the wake downstream the fuselage can be clearly identified and quantified. An exergy-waste coefficient (EWC) has been evaluated to determine the potential for improvement of the reference configuration. Loss and destruction of that recoverable exergy due to interaction (between the two bodies) have been quantified through an exergy-recovery coefficient (ERC). Overall, for the present configuration, a net benefit (ESC) in the range of 10%-11% is found for a complete wake ingestion using a simple actuator disk to model a propeller.

Physically speaking, the underlying principle of the wake ingestion can be stated as: *less exergy has to be supplied with the BLI configuration because less exergy is destroyed to bring the wake/jet back to thermodynamic equilibrium with its environment than if viscous dissipation was the mechanism involved.*[15]

---

[15]It is also interesting to note that the interpretation of this concept based on the mechanical energy analysis of DRELA ends up requiring some kind of thermodynamic (entropy generation) considerations [120].

4.4 Blended Wing-Body Architecture with Boundary Layer Ingestion

The objective of this test case is to investigate a typical unconventional configuration for which it will be highlighted that the complex characteristics of the flow makes the application of the drag/thrust bookkeeping challenging. The benefit of having a single performance metric (in the form of exergy destruction) for the aerothermopropulsive assessment will also be underlined when considering heat transfer at the aircraft surface.

Application of the exergy method to this test case is the focus of an article submitted for publication to the *AIAA Journal* in November 2014 [13].

4.4.1 Test Case Presentation

As mentioned in the introduction, a number of studies have focused on the design of blended wing-body architectures following the early detailed analysis of LIEBECK [95]. Two examples are reminded in Fig. 4-24 where one can see that the main feature of this concept is to have wings merged with the fuselage, as opposed to the conventional *tube-and-wing* architecture. The design philosophy of current airplane is about 60 years old and is based on the idea of carrying a payload in a fuselage, producing lift with wings and getting thrust from a propulsion system. Among the advantages of the blended wing-body concept is a higher aerodynamic efficiency (lift-to-drag ratio). Such architecture is also a very good candidate for implementing the ingestion of the boundary layer that develops on top of the wing.

(a) MIT-Cambridge SAX-40 concept [72].   (b) NASA N3-X concept [54, 55].
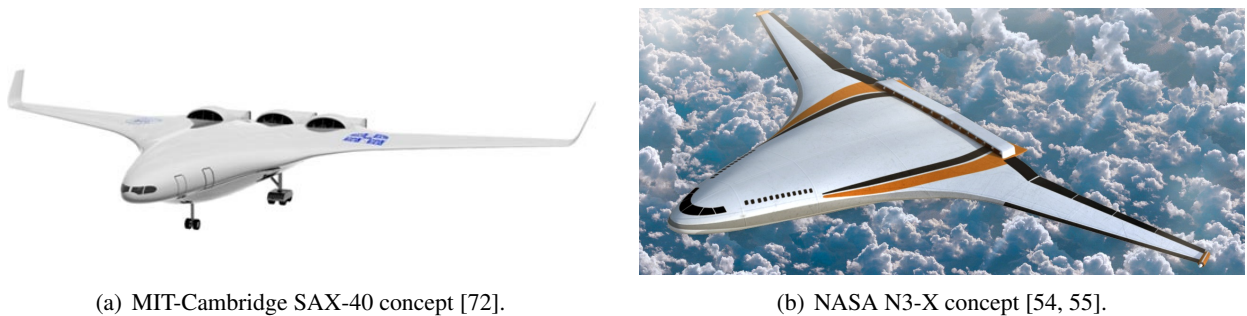
Figure 4-24: Typical studies of Blended Wing-Body (BWB) configurations with Boundary Layer Ingestion (BLI).

The MIT-Cambridge SAX-40 concept [72] is a design driven for low noise emission by placing the propulsion system on top of the upper surface which allows the use of the aircraft as a noise shield, see Fig. 4-24a.

The NASA N3-X concept (Fig. 4-24b) has been studied for a 2030+ timeframe where advanced technologies could become mature [54, 55]. It utilizes superconducting electrically driven, distributed low-pressure-ratio fans with power provided by two remote superconducting electric generators based on a conventional turbofan core engine design [15].

The following study takes part in the framework of a recent European effort of a low TRL[16] project called DisPURSAL[17] [76] to better understand challenges faced by such concepts that highly departs from existing aircraft design knowledge.

---

[16]Technology Readiness Level.

[17]DisPURSAL stands for Distributed Propulsion and Ultra-high By-Pass Rotor Study at Aircraft Level. The project is coordinated by the Bauhaus Luftfahrt e.V. with partnerships with CIAM (Russia) and Airbus Group Innovations (Germany).

4.4.1.1 Numerical Considerations

Geometry and Grid. We consider here a 2D simplified representation of possible future aircraft configurations which contains many of the challenges faced by such a design. The grid has been generated by Graduate student P. Toniato and is depicted in Fig. 4-25a. It contains 27 blocks and extends 50 reference chords in both directions for a total of 97,700 elements. This mesh is too coarse to allow for accurate performance in terms of absolute magnitude. Yet, as the analysis mainly consists of comparisons, the difference between two configurations is considered meaningful and sufficient for determining performance improvement or degradation.

(a) Overview.   (b) Slice and zoom on the boundary layer ingestion.
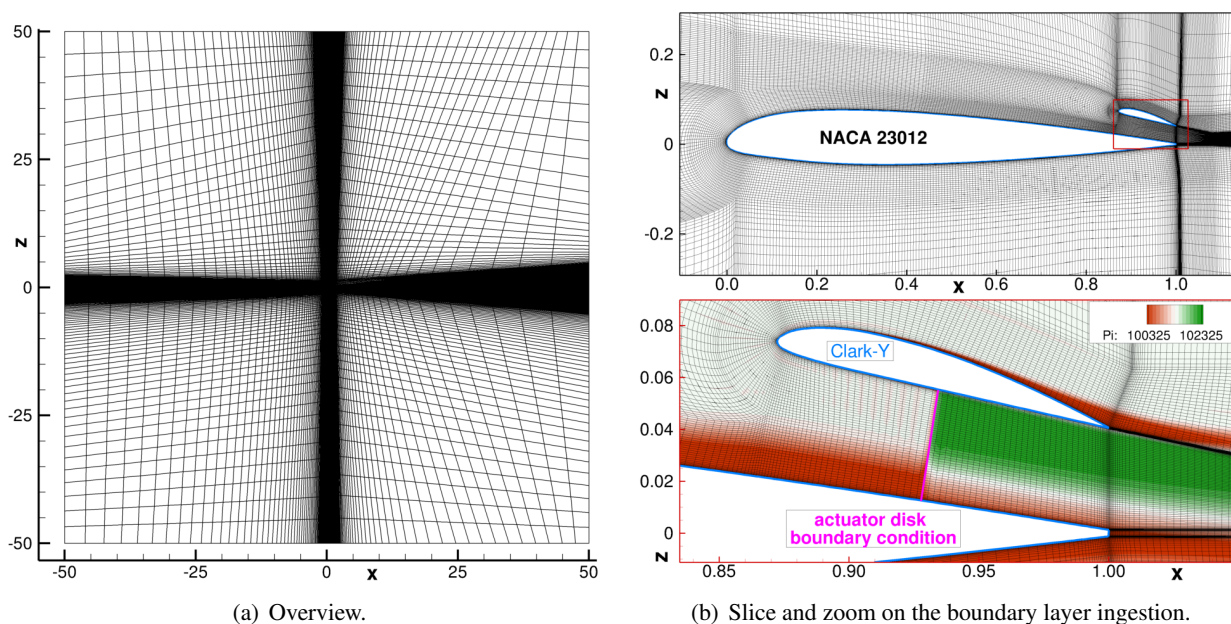
Figure 4-25: 2D BWB with BLI: geometry and grid.

The geometry illustrated in 4-25b is purposely academic: the blended wing-body is represented by a NACA 23012 Airfoil with a chord length of 1.0. The nacelle of the engine is represented by a Clark-Y Airfoil which has the specificity of providing a flat lower surface. The vertical space between the two airfoils forms a propulsive *channel* around the boundary condition modeling the propulsion.

The field of total pressure is illustrated in Fig. 4-25b where red and green contours represent respectively lower and higher values than the freestream reference. One can observe that the history of the boundary layer ingested by the propulsion is conserved: the boundary layer of total pressure field is reduced downstream of the propeller.

Boundary Conditions and Limitations. The boundary condition used here is an actuator disk where the input data is the force to be applied on the surface. It is representative of a fan that could be powered by an electrical energy source itself produced by a remote generator, as for the NASA N3-X concept. Regarding the propulsion, no thermal aspects are accounted for: the boundary condition is purely mechanical, which is consistent with an electrical fan.

Also, flow distortions are not accounted for: the efficiency of the engine does not depend on the instabilities of the incoming flow. Flow distortions (either steady or unsteady) can cause significant problems to the engine operation, performance and even integrity. As mentioned in the previous application in paragraph 4.3.1.3 (p. 134), further improvements of the boundary condition are necessary to take into account those distortions which are estimated to yield a $\approx 2\%$ loss [60, 80, 151, 159].

Flow Computations. Three freestream *Mach* numbers have been considered: a low-subsonic flow at $M_\infty = 0.20$, a high-subsonic flow at $M_\infty = 0.50$ and a transonic flow at $M_\infty = 0.70$. The *Reynolds* number ranges from 4 to 12 millions. The reference conditions for each flow regime are given in Table 4.6 for which the total enthalpy and pressure are constant and representative of wind-tunnel atmosphere: $T_{i,\infty} = 300$ K and $p_{i,\infty} = 101325$ Pa.

Quantity	Value	Unit	Quantity	Value	Unit
α	0	degree	A_{ref}	1	m^2
$T_{i,\infty}$	300	K	$p_{i,\infty}$	101325	Pa
M_∞	0.20	–	Re	4.36×10^6	–
ρ_∞	1.15	kg.m^3	T_∞	297.62	K
p_∞	98538	Pa	V_∞	69.16	m.s^{-1}
M_∞	0.50	–	Re	9.95×10^6	–
ρ_∞	1.04	kg.m^3	T_∞	285.71	K
p_∞	85419	Pa	V_∞	169.41	m.s^{-1}
M_∞	0.70	–	Re	12.62×10^6	–
ρ_∞	0.93	kg.m^3	T_∞	273.22	K
p_∞	73048	Pa	V_∞	231.93	m.s^{-1}

Table 4.6: 2D BWB with BLI: aerodynamic reference conditions.

For each flow regime, a large number of computations were made to cover a wide range of net force acting on the configuration. All these computations exhibit a convergence similar to the one depicted in Fig. 4-26.

(a) Near-field axial net force.

(b) Residuals energy equation.
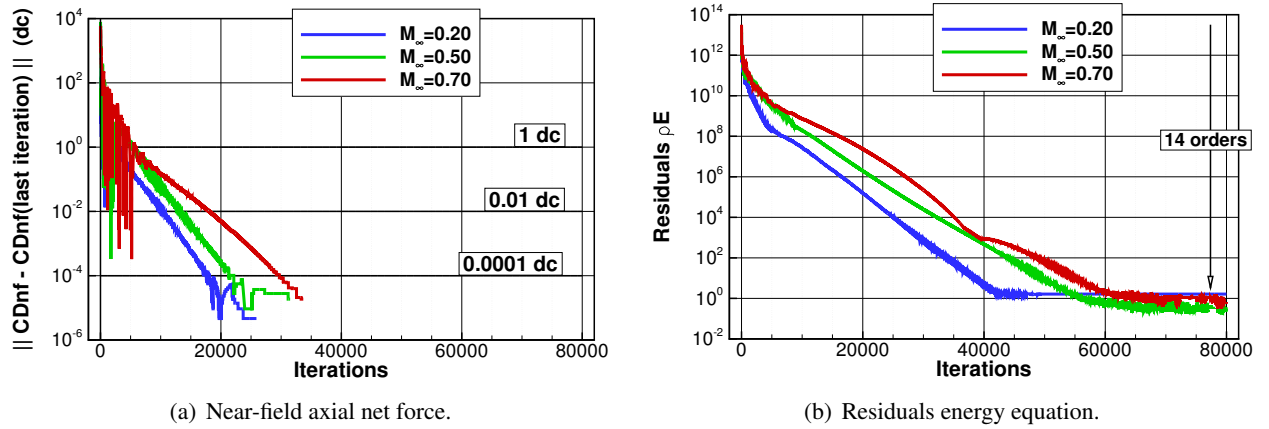
Figure 4-26: 2D BWB with BLI: convergence history at $M_\infty = 0.20$ (—), $M_\infty = 0.50$ (—) and $M_\infty = 0.70$ (—).

Although the (near-field) force acting on the configuration required less than 40,000 iterations to reach a convergence greater[18] than 10^{-5} dc, see Fig. 4-26a, 80,000 iterations were run to achieve a 14 orders reduction of all residuals as shown in Fig. 4-26b for the energy equation.

4.4.1.2 Drag-Thrust Bookkeeping Issues

The first comment that should be made about such configuration is that the flow is very different than the one dealt with conventional architectures. Three main drag-thrust bookkeeping issues are described next.

---

[18]A drag coefficient expressed in drag counts (10^{-4}) that is below a magnitude of 10^{-5} represents data below 10^{-9} which exceeds the precision of the data extracted from the flow solution. This explains the vanishing curves for iterations greater than 30,000 in Fig. 4-26a.

Pressure Field Interactions.   Fig. 4-27 illustrates the (relative[19]) pressure field around the configuration without active propulsion for the subsonic flow regime.
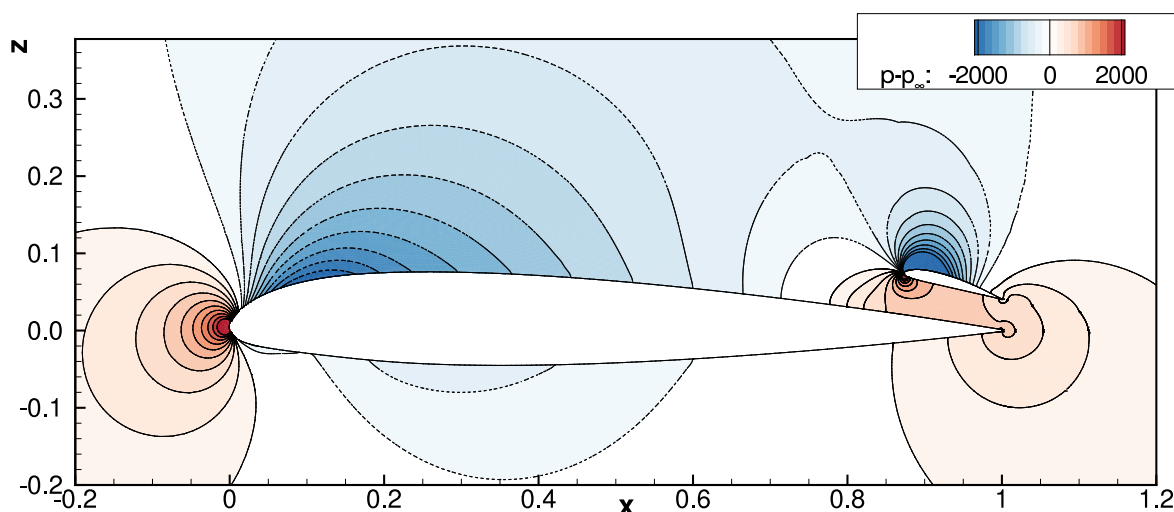
Figure 4-27: 2D BWB with BLI: field of pressure relative to freestream without active propulsion at $M_\infty = 0.20$.

One can see that the presence of the nacelle duct (Clark-Y Airfoil) has a great influence on the pressure force experienced by the main body (NACA Airfoil). Likewise, the large body modifies the pressure force experienced by the nacelle duct. This pressure interaction between the two solids is generally referred to as *buoyancy* [157] or *potential effect* [146]. The straightforward integration of this near-field pressure force for each separate body would yield a force which could not be strictly referred to as the *drag* of each body.

Internal/External Flow Distinction.   Traditional drag-thrust bookkeepings [42, 53, 157, 161] are based on the distinction between the flow that enters the propulsion system and the flow that does not: the former is called *internal* and the latter is named *external* and is associated with the flow over the airframe. It is considered that both flows can be investigated separately because we assume no interactions between them. As mentioned by KAWAI *et al.* [78], such distinction becomes challenging when dealing with boundary layer ingestion as illustrated in Fig. 4-28 which shows the *Mach* number field around the configuration with an active propulsion[20].

The location of the strong shock wave (highlighted in green) would suggest a treatment by the airframe design team. Even if an efficient design of a blended wing-body aircraft could prevent the formation of such phenomena, the point raised here is that the state of the flow through the engine may be greatly influenced by the design of the airframe which is usually made by experts of a different design team/company.

Similarly, the jet of the propulsion mixes very shortly with the airframe wake, making the definition of a post-exit streamtube hardly possible, see appendix A.1 (p. 178).

Propulsion to Aerodynamic Interactions.   Furthermore, it should be emphasized that the propulsion system may also greatly influence the state of the upstream flow, as highlighted by comparing Fig. 4-28 and Fig. 4-29. The only difference is that the engine is inactive on the latter image.

Because the stronger shock wave observed in Fig. 4-28 is due to a higher velocity flow generated by a greater thrust level, this increase in shock intensity is throttle-dependent and the question arises: to whom should this increase in wave drag (or wave anergy[21]) be associated with? the airframer or the engine

---

[19]Relative to freestream, $\delta p = p - p_\infty$.

[20]Note the large boundary layer separation that occurs on the upper surface of the Clark-Y Airfoil.

[21]From 3.7 to 21.3 pc according to the code *ffx*.

146
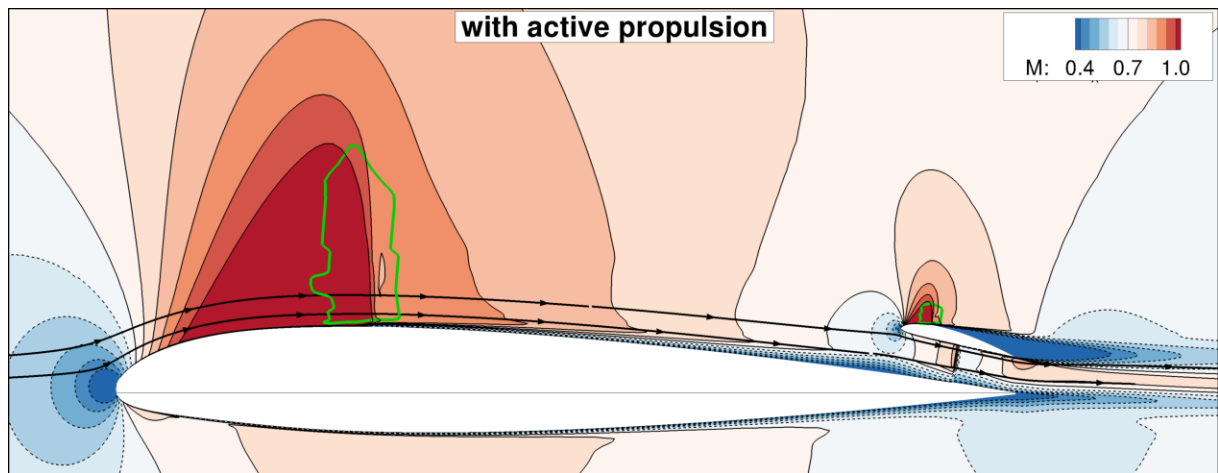
Figure 4-28: 2D BWB with BLI: field of *Mach* number and shock surface (green) with active propulsion.
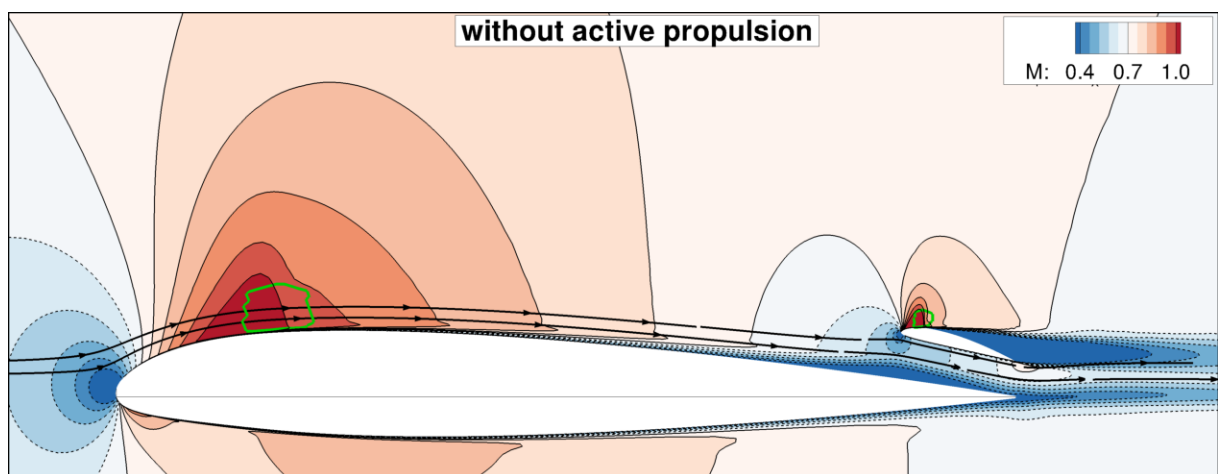
Figure 4-29: 2D BWB with BLI: field of *Mach* number and shock surface (green) without active propulsion.

manufacturer? Both answers could be argued. Also, the higher intensity of the shock wave destroyed a greater amount of exergy in the streamtube, or equivalently increased the stagnation pressure losses, which, in turn, may impact the operating conditions of the engine.

Drag/Thrust Distinction. Finally, the definition of the thrust is itself tricky. One could consider the *thrust* as the momentum change across the inlet and outlet of the duct. In practice however, this is not a convenient definition because thrust is then strongly dependent on intake/exhaust geometry [157], as observed in the case of the isolated nacelle in section 4.2 (p. 122). The only combination of surface that appears valid[22] is those of the boundary condition. It could also be a force measurable in wind-tunnel testing with a dedicated equipment. This force could not be strictly referred to as *thrust*, but rather to a *propulsive (fan) force*.

From a force balance perspective, if the distinction between thrust and drag becomes ambiguous, the only meaningful force is the net force acting on the configuration. This overall force is however of very little interest to the aircraft designer because it does not provide information about what physical phenomena may be involved and therefore no clue on how to improve the current configuration.

---

[22]An alternative entry interface could be the engine face, but again in this case, thrust would be very dependent on intake conditions. Moreover, it may be difficult to measure the stream force at this station since the flow is often non-uniform and unsteady.

Clearly, the complexity of the flow and of the propulsive integration makes the concept of thrust and drag less defined and introduce possible arbitrariness into the traditional drag-thrust bookkeeping. For all the aforementioned reasons, a global design perspective must be adopted to reach an aircraft with optimal performance. The one proposed here is based on the analysis of the flow in terms of exergy management.

4.4.2 Aeropropulsive Performance Assessment

The aeropropulsive performance of the configuration is assessed for the three flow regimes considered. First, a few comments are made on the numerical verification of the theoretical formulation. Then, the efficiency of the aircraft is given from an exergy point of view.

4.4.2.1 Near-field / Far-field Integration

Restriction of the global exergy balance Eq. (2.34) to this case with adiabatic surfaces reads:

$$\dot{\mathcal{E}}_{prop,nf} = \underbrace{W\dot{\Gamma} + \dot{\mathcal{E}}_m + \dot{\mathcal{E}}_{th} + \dot{\mathcal{A}}_\phi + \dot{\mathcal{A}}_{\nabla T} + \dot{\mathcal{A}}_w}_{\dot{\mathcal{E}}_{prop,ff}}$$

(4.8)

The left-hand side term results from a near-field integration of the propulsive exergy $\dot{\mathcal{E}}_{prop,nf}$ on the propulsive surface while all right-hand side terms are integrated within the control volume or on the outer boundary of the domain and thereby forms a far-field expression which is noted $\dot{\mathcal{E}}_{prop,ff}$.

A numerical comparison of both approaches is made for the configuration at mechanical equilibrium in the transonic regime. To do so, the propulsive exergy is calculated by the two methods for an increasing number of propulsive layers, as introduced for the isolated nacelle treated in 4.2.2.1 (p. 125). As illustrated in purple in Fig. 4-30a, as the number of cell layers increases (up to 32), the propulsive surface $\mathcal{S}_P$ goes away from the boundary condition (white line).

(a) Increasing number of propulsive cell layers.

(b) Field of viscous anergy in the vicinity of the propulsion system.
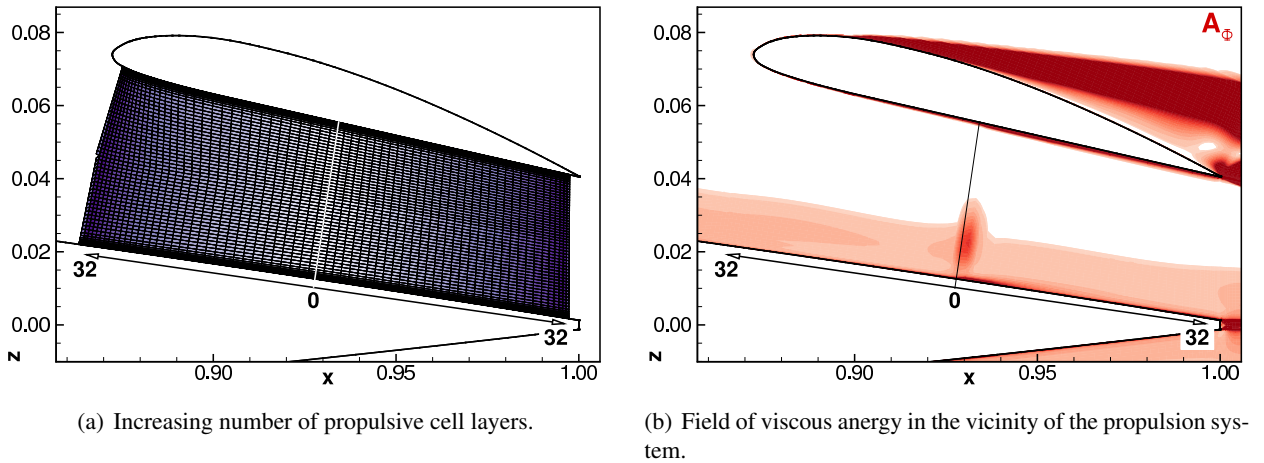
Figure 4-30: 2D BWB with BLI: field visualization of the addition of cell layers around the propulsive boundary conditions.

The corresponding near-field and far-field integration of the propulsive exergy is given in Fig. 4-31a. The decreasing of the propulsive exergy is due to the destruction (within the channel) by the viscous (and thermal) anergy around the boundary conditions, see Fig. 4-30b.

The near-field integration exhibits an oscillatory behavior over a mean value corresponding to the far-field integration[23]. From Fig. 4-31b we see that the oscillations comes from the total enthalpy inflow which

---

[23] The transverse plane is located at 1.5 reference chord downstream of the body. At this distance an accuracy correction of the

(a) Near-field and far-field integration of the propulsive exergy.

(b) Near-field total enthalpy inflow.
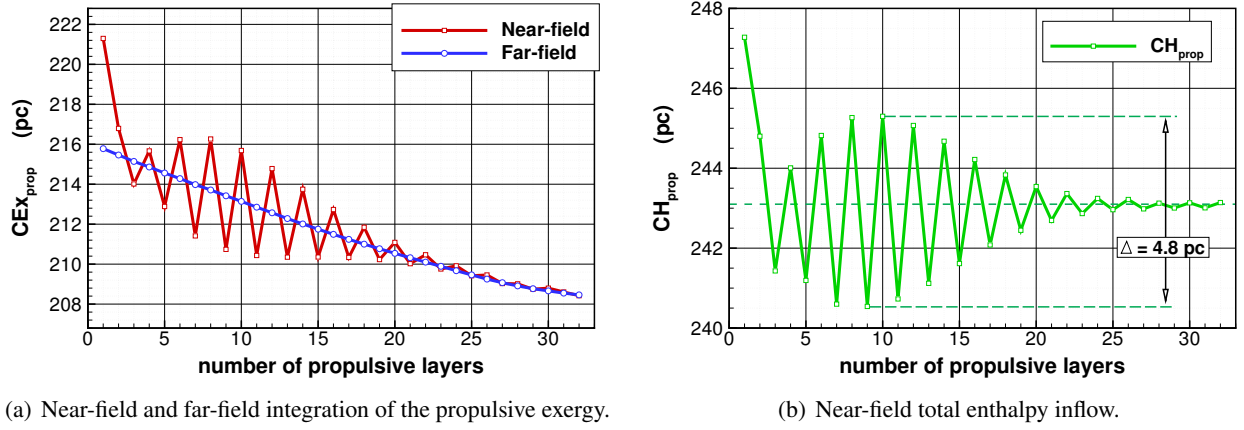
Figure 4-31: 2D BWB with BLI: near-field and far-field propulsive exergy integration versus the number of cell layers.

requires more than 20 cell layers to converge within 0.5 pc. The maximum deviation accounts for 2.5 pc which represents about one percent of the mean value. Note that the same observations were made regarding the rate of momentum change across the propulsive surface.

As a consequence, the far-field integration presents a numerical advantage over the straightforward near-field integration by being less dependent on the numerical treatment of the boundary conditions (more robust).

4.4.2.2 Anergy Generation

In the description of the test case, the interactions between the external (aerodynamic) flow and the internal (propulsive) flow were highlighted. Fig. 4-32 gives the necessary information to quantify the influence of the propulsion on the anergy generation. The first data point corresponds to the case where the propulsion is inactive: no thrust is delivered and the unpowered configuration experiences drag.

Fig. 4-32a provides the change in the production of viscous anergy. For the subsonic flows, a reduction is observed for low levels of propulsive exergy supply, typically before reaching mechanical equilibrium (filled symbols) as for $M_\infty = 0.50$. Once the transonic regime is reached, there seems to be no more gain from interactions with the propulsion system: as greater level of thrust is provided, the viscous anergy generated increases.

Fig. 4-32b gives the variation of the thermal anergy for which no gain can be observed. A small increase is observed for the subsonic flows at which regime this component is low, see *Mach* number dependency studied in paragraph 3.3.1 (p. 79). In the transonic conditions, the activation of the propulsion system involves a steady increase of the thermal anergy generation up to the equilibrium and then rises more steeply.

Fig. 4-32c illustrates the change in the production of the anergy associated with the shock wave (absent in the two subsonic flows). The influence of the propulsion on this term is even more significant: the greater mass flow through the engine accelerates the flow and thereby the shock intensity.

The considerable influence of the propulsion system on the overall flow, that was qualitatively observed by comparing Fig. 4-28 and Fig. 4-29, has been quantitatively assessed for the generation of anergy.

---

viscous and thermal anergy by $\Delta \dot{\mathcal{A}} \approx 7$ pc is required. Refer to paragraph 2.5.1.2 (p. 55) for the description of the correction method.

(a) Viscous anergy.

(b) Thermal anergy.

(c) Wave anergy.
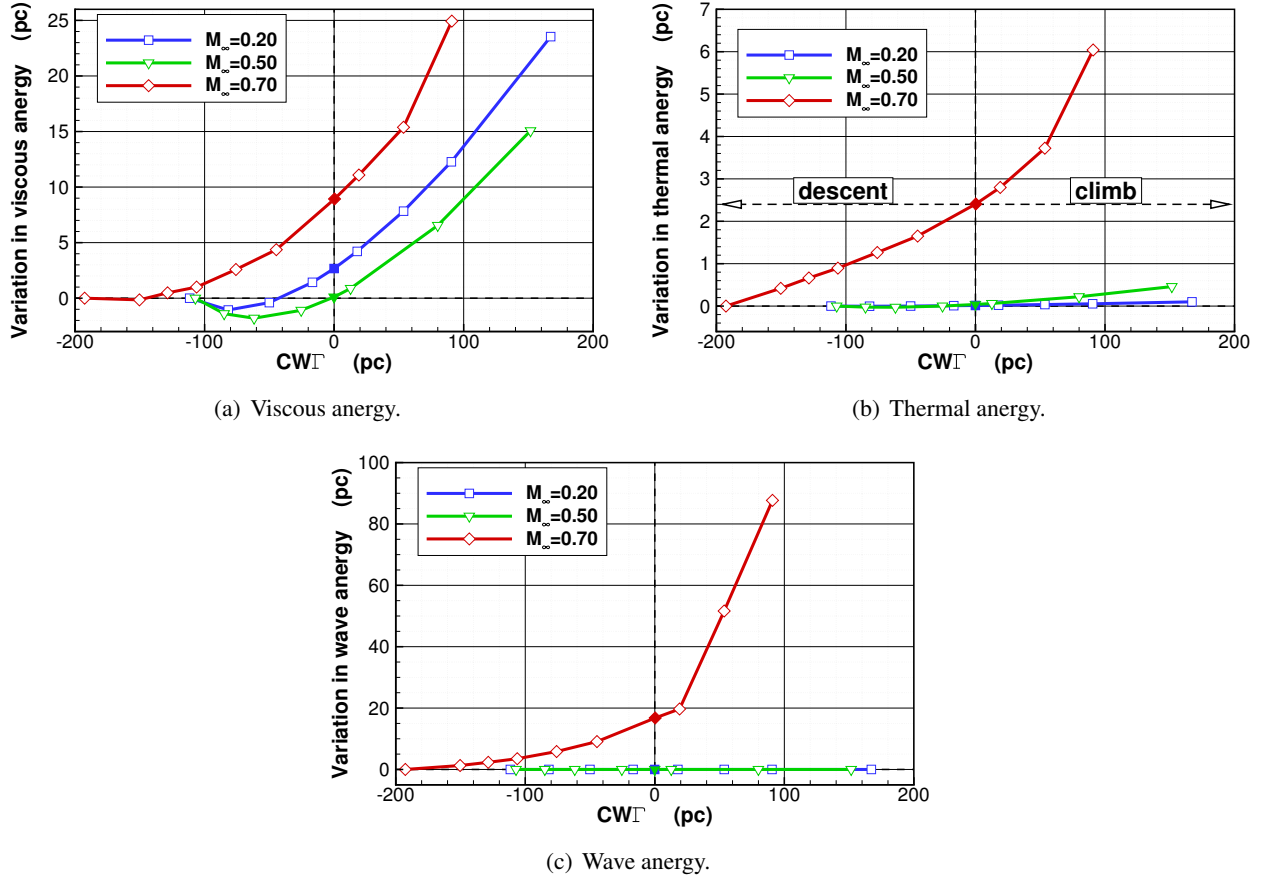
Figure 4-32: 2D BWB with BLI: change in the viscous (a), thermal (b) and wave (c) anergy generation as the propulsion system delivers more exergy.

4.4.2.3 Recoverable Exergy

Mechanical and Thermal Exergy Outflows. The second key aspect of the performance formulation Eq. (B) is the mechanical and thermal exergy outflows. These two components form the exergy potentially recoverable in the wake/jet of the configuration: $\dot{\mathcal{E}}_{rec} = \dot{\mathcal{E}}_m + \dot{\mathcal{E}}_{th} = \dot{E}_u + \dot{E}_v + \dot{E}_p + \dot{\mathcal{E}}_{th}$. Fig. 4-33 provides the decomposition of this recoverable exergy in the wake of a configuration in mechanical equilibrium ($\dot{W\Gamma} = 0$) at $M_\infty = 0.20$ and $M_\infty = 0.70$.
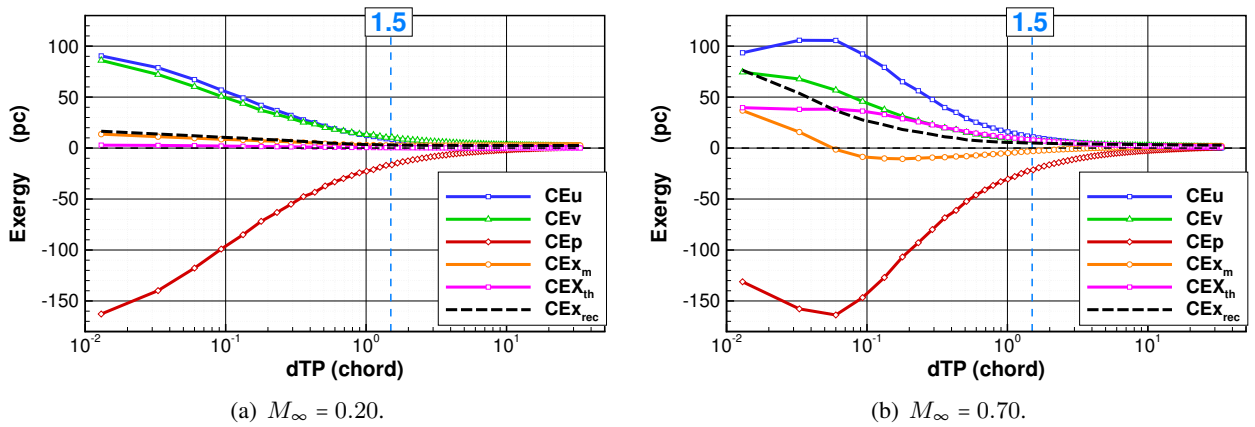
(a) $M_\infty = 0.20$.

(b) $M_\infty = 0.70$.

Figure 4-33: 2D BWB with BLI: evolution of the recoverable exergy downstream of the body at mechanical equilibrium $\dot{W\Gamma} = 0$ in a flow at (a) $M_\infty = 0.20$ and (b) $M_\infty = 0.70$.

One clearly notice that for both flow regimes the transverse kinetic energy (–), associated with lift, has the same order of magnitude as the streamwise kinetic energy (–) associated with the wake/jet; it would therefore be wrong to neglect this component. Also, the pressure boundary-work term (–) exhibits a high (negative) magnitude which leads to a relatively small recoverable exergy (–).

The thermal exergy (–), while being low in the subsonic regime becomes non-negligible for the transonic flow. As discussed in paragraph 2.2.2.3 (p. 43), a more appropriate terminology would be *thermocompressible* exergy as it is made up of these two aspects. For a (highly) compressible flow, there is a transient region right downstream of the body where exchanges between the mechanical and thermal energy take place. This phenomenon is clearly visible in the mid-field of the configuration ($d_{TP} \leq 2$) on Fig. 4-33b where the mechanical exergy is even negative. The total (mechanical + thermal) exergy[24] (– –) is always positive and steadily decreasing towards zero as the transverse plane is moved away from the configuration.

Influence of the Propulsion. As for the anergy generation, we now look at the impact of the propulsion system on the mechanical and thermal exergy outflows with reference to the unpowered configuration. Fig. 4-34 gives this information for the three flow regimes considered when the recoverable exergy is evaluated 1.5 chord downstream of the body versus $W\dot{\Gamma}$.

(a) Mechanical part of the recoverable exergy.   (b) Thermal part of the recoverable exergy.
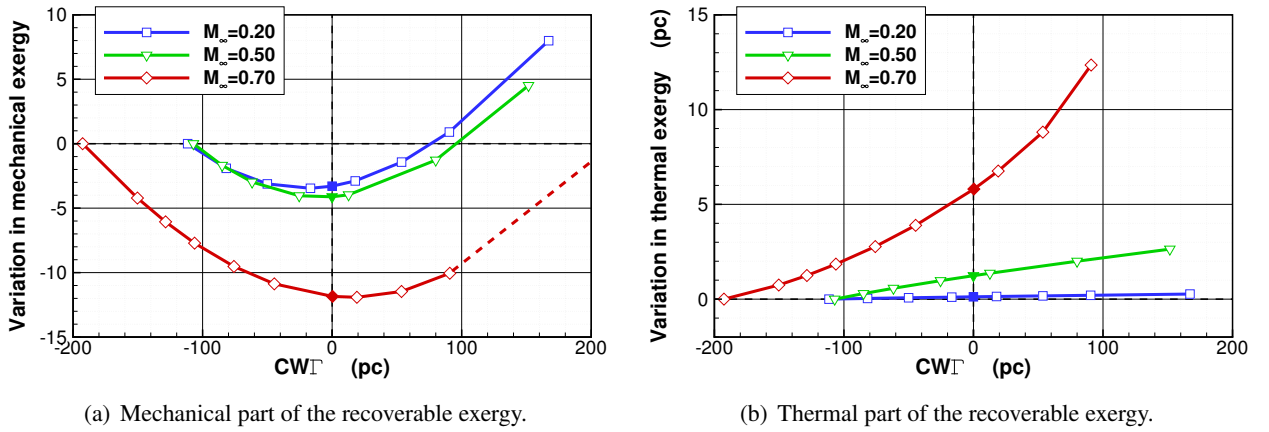
Figure 4-34: 2D BWB with BLI: change in the mechanical (a) and thermal (b) part of the recoverable exergy evaluated at 1.5 chord downstream of the body.

Fig. 4-34a gives the change in mechanical exergy. For all three flow conditions, the mechanical exergy reduces as propulsive exergy (and thereby thrust) is delivered. This trend is observable up to a maximum reduction which occurs very near the mechanical equilibrium of the configuration (filled symbols). For higher thrust levels, exergy is supplied in excess and therefore the mechanical exergy recoverable at 1.5 chord downstream of the body increases.

In the two subsonic regimes, the exergy in the jet becomes eventually greater than the exergy in the wake of the unpowered configuration. This phenomenon is not observed in the transonic condition for which the propulsion reduces the exergy potentially recoverable. An adverse impact is likely to be only observed for large climb rates ($CW\dot{\Gamma} > 200$ pc, see extrapolation – –).

Fig. 4-34b provides the change in thermal exergy, which increases for all three flow conditions. As the freestream *Mach* number gets higher, the influence of the propulsion becomes more significant, but is almost negligible at $M_\infty = 0.20$. The thermocompressible exergy rises (quite) linearly at $M_\infty = 0.50$ and more rapidly at $M_\infty = 0.70$.

---

[24]It is crucial to consider all components of the mechanical and thermal exergy and to not restrict the analysis to the streamwise kinetic energy.

As we have seen from Fig. 4-33, the decomposition of the recoverable exergy into its mechanical and thermal components can be misleading at high *Mach* numbers if evaluated *too* close to the body. This is because immediately downstream of a configuration, there is a transient region where the flow *reequilibrates* itself following the disturbance caused by the body. As a consequence, a better indicator of the performance is the total recoverable exergy which is given for increasing propulsive exergy supply in Fig. 4-35.
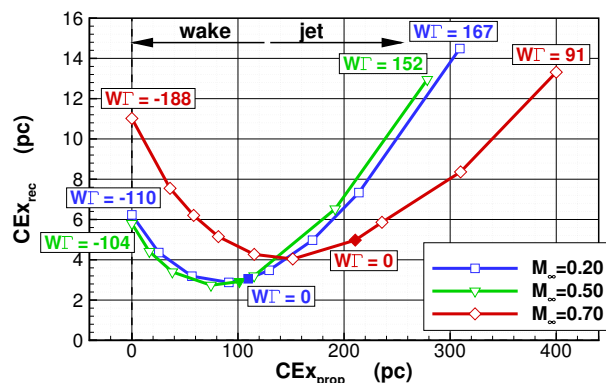
Figure 4-35: 2D BWB with BLI: recoverable exergy determined 1.5 chord downstream of the body versus propulsive exergy.

We observe very similar trend and magnitude for the curves corresponding to the subsonic flows: without propulsion (first data point of each curve), there is about 6 pc of recoverable exergy. Equilibrium of the configuration ($W\dot{\Gamma} = 0$) is reached for a propulsive exergy slightly greater than 100 pc. It is interesting to note that this value corresponds to the rate of work of the drag experienced by the unpowered configurations ($W\dot{\Gamma} = -104$ pc at $M_\infty = 0.50$ and $W\dot{\Gamma} = -110$ pc at $M_\infty = 0.20$). In other words, the propulsion system has only supplied as much exergy as was required to balance the rate of exergy destruction by the airframe alone; no additional losses are generated. On top of that, the configuration at equilibrium wastes less exergy in the wake than without propulsion.

In the transonic regime, this observation does not hold any more: at equilibrium, the exergy supplied by the propulsion system is greater (210 pc) than the rate of work of the drag alone (188 pc). As illustrated in Fig. 4-34c, this increase is likely to be due to a higher shock intensity. The propulsion has a negative impact for this particular configuration which was not designed for transonic operation.

The critical point here is that as the propulsive exergy supplied increases, the recoverable exergy reduces to reach a minimum at which point the deficit of streamwise velocity has been gradually brought closer to the freestream reference. The minimum is not strictly equal to zero because the velocity profile is not perfect: there are some regions of deficit and some of excess of momentum, as sketched in Fig. 4-36.
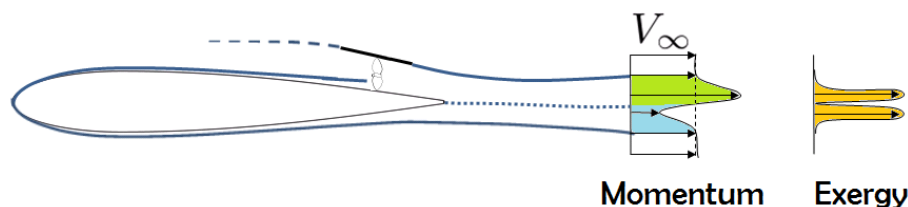
Figure 4-36: 2D BWB with BLI: sketch of a non-ideal, yet realistic, boundary layer ingestion for a configuration at equilibrium.

Then, as the propulsive force continues to rise, so does the axial velocity; it eventually exceeds the freestream reference and the jet (excess) represents recoverable exergy, again.

4.4.2.4 Exergy-Waste Coefficient

A powerful indicator of the degree of perfection of a given architecture introduced in paragraph 2.4.1.1 (p. 51) is the exergy-waste coefficient that quantifies the relative magnitude of the exergy loss in the wake/jet:

$$EWC = \frac{\dot{\mathcal{E}}_{rec}}{\dot{\mathcal{E}}_m + \dot{\mathcal{E}}_{th} + \dot{\mathcal{A}}_{tot}} \tag{4.9}$$

Fig. 4-37 gives the necessary information to assess the performance of the configuration for the three flow regimes considered.

(a) EWC versus propulsive exergy.

(b) EWC versus net force acting on the configuration.
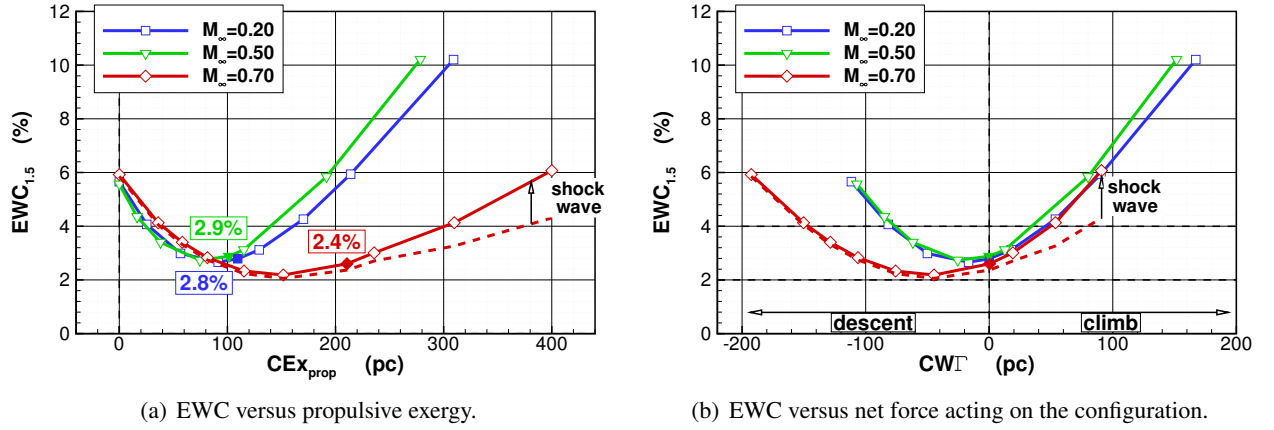
Figure 4-37: 2D BWB with BLI: exergy-waste coefficient evaluated at 1.5 reference chord downstream of the body.

Fig. 4-37a provides the EWC versus the propulsive exergy supplied. We observe first that all curves have a very similar starting point at about 5.8% and that at equilibrium (colored symbols), this coefficient has been divided by two, $EWC_{1.5} \simeq 2.8\%$. In other words, we have recovered half of the recoverable exergy, *i.e.* about 100% of the upper boundary layer, where the propulsion system is integrated. One could therefore imagine that if a second propulsion system was placed on the lower surface, the ideal case of no exergy wasted in the wake could be reached.

Fig. 4-37b gives the EWC versus the change in energy height of the aircraft. For all flow regimes, we have $2 \leq EWC \leq 4\%$ over a large range of net force acting on the configuration (descent and climb). Because of its independence relative to the flow regime, EWC appears to be a relevant characteristic of the configuration under study, which is an appreciable feature of this coefficient.

In the transonic regime, the impact of the shock wave on the overall performance of the configuration is clearly visible: its reduction (cancellation) would obviously improve the EWC.

These low values indicate a highly efficient architecture where very little exergy is left in the wake of the body: about 97% of the propulsive exergy has been used to balance the anergy generated within the boundary layers and by the shock wave. This efficiency analysis gives the aircraft designer the information that this configuration does not represent a great potential of improvement in terms of wake recovery. Efforts, and thereby investment, should be put on other sub-systems.

4.4.3   Aerothermopropulsive Performance Assessment

The goal of the exergy approach to the design of complex systems is to determine how to take advantage of the interactions between their various sub-systems. As an example, we study here the impact of capturing or delivering heat to the surrounding flow by one surface of the body in order to favor thermopropulsive interactions, see Fig. 4-38.
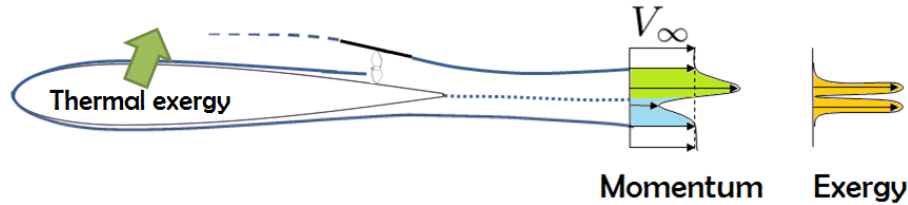
Figure 4-38: 2D BWB with BLI: sketch of the analysis of the thermopropulsive interactions test case.

Aero-thermodynamic interactions were considered as early as 1920's when it was found that the careful design and location of engine and oil cooling radiators could yield dramatic improvements in the overall drag characteristics of the aircraft [177]. Also, some studies indicate that surface heating, if the temperature distribution is carefully tailored, can be a viable means of not only heat dissipation but also boundary layer control[25] [88]. The latter objective could also be achievable by using cryogenic fuels to cool the wing, as suggested by LEE [91].

In order to obtain thermocompressible interactions, only the highest *Mach* number flow $M_\infty = 0.70$ is considered next.

4.4.3.1   Test Case Presentation

Description.   To investigate this transonic test case with heat transfer, the complete exergy balance (2.34) is required:

$$\dot{\mathcal{E}}_{prop} + \dot{\mathcal{E}}_q = W\dot{\Gamma} + \dot{\mathcal{E}}_m + \dot{\mathcal{E}}_{th} + \dot{\mathcal{A}}_\phi + \dot{\mathcal{A}}_{\nabla T} + \dot{\mathcal{A}}_w \tag{4.10}$$

Despite a simplified configuration, this test case represents the typical multi-disciplinary problem which could benefit from the *single currency* provided by the exergy analysis. The thermal and mechanical energies can be simultaneously accounted for with a special emphasis on the real engineering/practical value of the thermal energy.

Isothermal Wall.   The analysis is made for configurations at equilibrium (constant axial net force) $W\dot{\Gamma} = 0.00 \pm 0.05$ pc and a fixed temperature T_w is applied on the surface upstream of the propulsion system, see Fig. 4-39. A temperature range of $90 \le T_w \le 1185$K is imposed keeping in mind that the averaged temperature observed for the adiabatic case is $\overline{T}_{w,adiab} = 296$K $\approx 1.10 \times T_\infty$. Higher or lower wall temperatures had a very limited impact on the convergence of the flow solutions.

The goal is to determine under what conditions there may be a benefit in the interactions between purely thermal (heat transfer) and purely mechanical (propulsion) aspects.

Thermal and Viscous Boundary Layers.   The difference in temperature imposed at the surface has an influence on the viscous and thermal boundary layers [147], as illustrated in Fig. 4-40 for one section at $x = 0.80$ (dotted lines) and one at the engine inlet (solid lines).

---

[25]The authors also found experimentally that a heated airfoil exhibited a longer zone of transition, suggesting that the addition of heat, through density and viscosity changes, alters the character of the instabilities which cause transition.

(a) Cold surface: T_w = 163K (= $0.55 \times \bar{T}_{w,adiab}$).

(b) Hot surface: T_w = 430K (= $1.45 \times \bar{T}_{w,adiab}$).
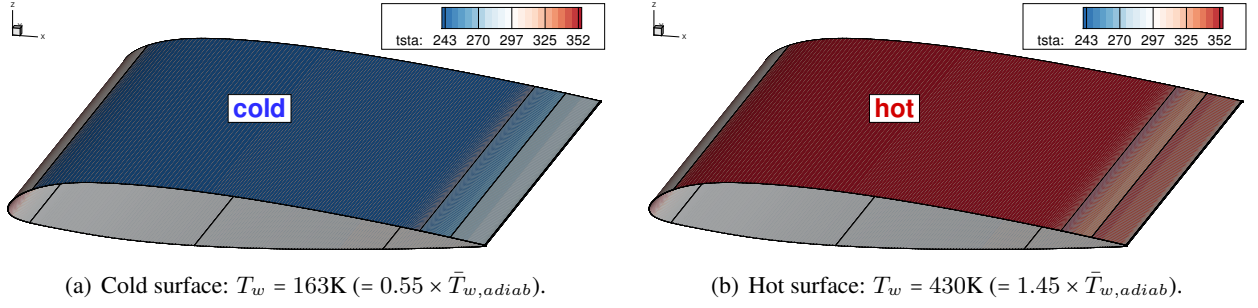
Figure 4-39: 2D BWB with BLI: representation of the surface used for heat transfer in the cold (a) and hot (b) case.

(a) Streamwise velocity.

(b) Static temperature.
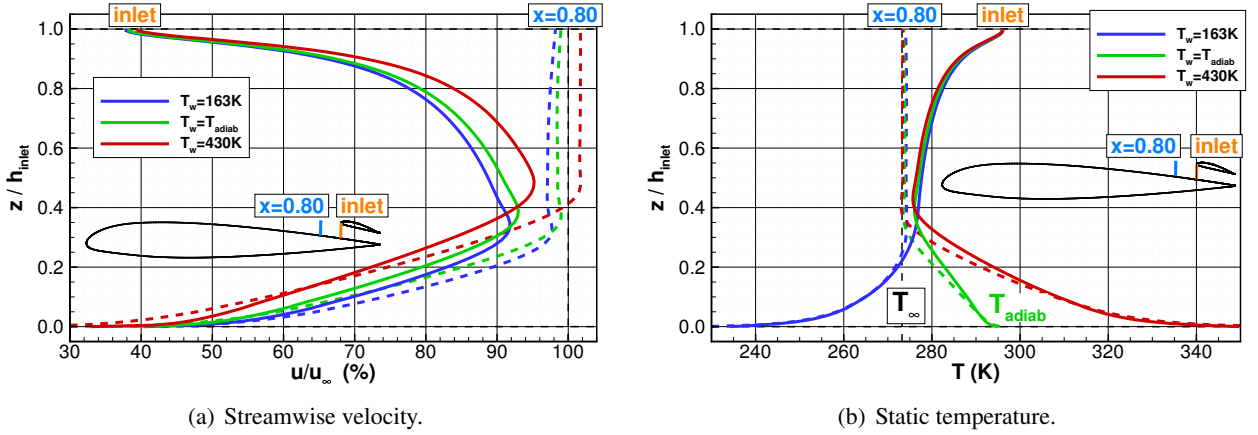
Figure 4-40: 2D BWB with BLI: velocity and static temperature profiles at x = 0.80 (dashed) and at the engine inlet (solid) for the cold (T_w = 163K, —), adiabatic (—) and hot (T_w = 430K, —) cases.

Fig. 4-40a gives the streamwise velocity profile in the boundary layers. For both stations, the wall temperature has a large impact on the viscous boundary layer. One can see that the viscous boundary layer is thickened with the higher temperature. This information could be valuable for the engine manufacturer which could eventually modify the state of the flow entering the engine, especially in terms of distortions.

Fig. 4-40b provides the static temperature profile in the boundary layers. For the first section (dashed lines) one can see the temperature resumes to the freestream reference[26] within a vertical distance of about $0.3h_{inlet}$. The temperature profile is slightly more tilted at the engine inlet: even for the cold case, once outside of the thermal boundary layer, the temperature is higher than freestream ($0.4 \leq z/h_{inlet} \leq 0.8$). One can observe the presence of a thermal boundary layer above 0.8 where the temperature resumes to the adiabatic reference.

The (higher or lower) wall temperature has almost no influence on the temperature profile outside of the boundary layer ($0.4 \leq z/h_{inlet}$).

Thermal and viscous boundary layers exhibit very similar thicknesses, about 40% of the inlet height, in agreement with a *Prandtl* number near unity [147].

The wall temperature has therefore an impact of the mass flow rate through the engine. Overall, the non-dimensionalized mass flow rate ($\rho[V_\infty + u]/\rho_\infty V_\infty$) is slightly reduced when increasing the wall temperature, from 96.3% at T_w = 163K to 92.7% at T_w = 430K.

---

[26]It is precisely the thermal mixing which damps the deviations from the reference conditions (T_∞) and allows this equilibrium process.

In terms of the post-processing of these flow solutions, this modification of the thermal and viscous boundary layers has an impact on the y^+ because the same grid is used for all these flow computations. This, in turns, has an impact on the thermal and viscous dissipation calculated. A higher fidelity analysis should take this effect into account by adapting the grid to the wall temperature imposed.

Energy, Exergy and Anergy Distribution. For the two cold (163K) and hot (430K) cases, the distribution over the configuration of energy (–), anergy (–) and exergy (–) is depicted in Fig. 4-41, with reference to the adiabatic case (dashed lines). The peaks observed at $x \approx 0.3$ is due to the shock wave.

(a) Cold surface, $T_w = 163$K ($= 0.55 \times \bar{T}_{w,adiab}$).   (b) Hot surface, $T_w = 430$K ($= 1.45 \times \bar{T}_{w,adiab}$).
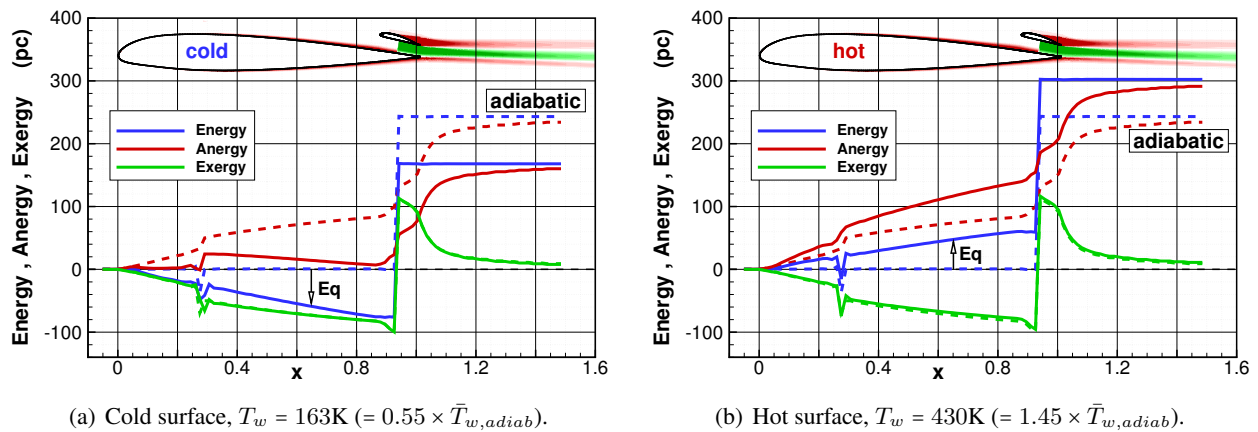
Figure 4-41: 2D BWB with BLI: distribution of energy (–), anergy (–) and exergy (–), with reference to the adiabatic case (dashed lines).

Heat energy is being either taken from (a) or supplied to (b) the surrounding fluid. In the first case, lower energy (–) and anergy (–) compared to the adiabatic case are exhibited.

As regards the engine inlet, intuitively, one could imagine that the lower level of anergy provided by the cold surface could be advantageous because it should be a *cleaner* flow. On the other hand, a flow with a higher energy could also be valuable. Here again, refined models of the propulsion system could take advantage from this information.

Laminar and Turbulent Anergy Generation. In order to better understand the influence of heat transfer on the dissipation mechanisms, a decomposition of the viscous and thermal anergy production into their laminar and turbulent component is given in Fig. 4-42. We focus here on the dissipation impacted by the wall temperature, *i.e.* the one occurring on the upper surface of the NACA Airfoil. The stagnation point varying slightly, the distinction between the lower and upper surface is made by a simple geometric criterion: if $z_{elmt} \geq 0$ then the dissipation within the element considered is accounted for. The rise observed at $x = 1.0$ is associated with the boundary layer separation observed on the upper surface of the Clark-Y Airfoil.

Fig. 4-42a gives the decomposition for the viscous anergy production. Increasing the wall temperature reduces both the laminar and the turbulent viscous anergy generation. The two mechanisms seem more sensitive to a cooling (–) than to a heating (–).

Fig. 4-42b provides the decomposition for the thermal anergy production. For this component, any (large) deviation from the adiabatic case increases the magnitude of the temperature gradients and thereby the thermal dissipation. Noteworthy, up to the trailing edge of the configuration ($x = 1.0$), the laminar dissipation for the cold surface (– –) is larger than the dissipation associated with turbulence (–).

(a) Viscous anergy.
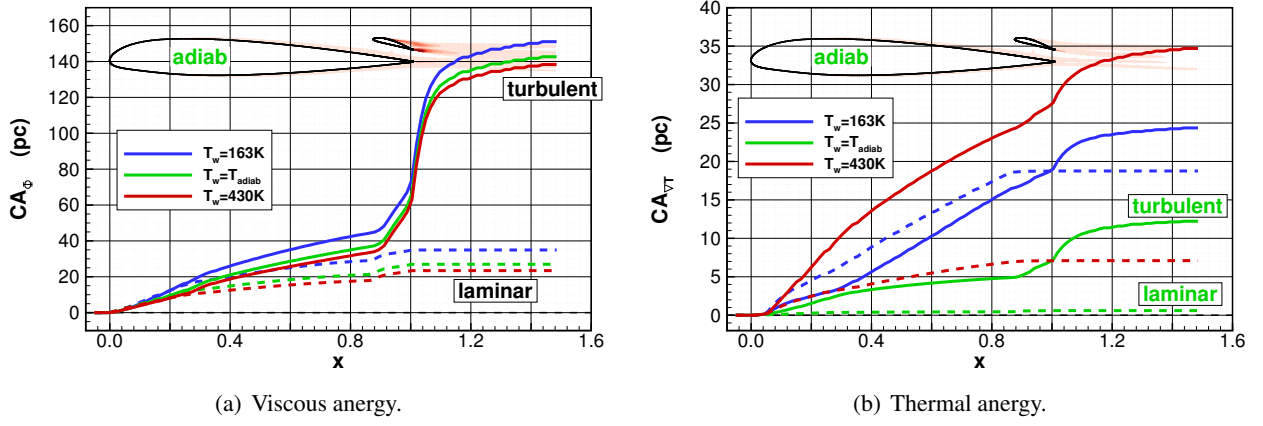
(b) Thermal anergy.

Figure 4-42: 2D BWB with BLI: laminar (dashed) and turbulent (solid) viscous and thermal anergy generation, with cold ($T_w = 163$K, —), adiabatic (—) and hot ($T_w = 430$K, —) surfaces.

4.4.3.2 Propulsive Exergy

Performance Benefit. The thermal energy and exergy transferred[27] to the fluid are depicted respectively as $\dot{E}_q$ (—) and $\dot{\mathcal{E}}_q$ (—) in Fig. 4-43a. The energy transferred is negative for $T_w < \bar{T}_{w,adiab}$ while the thermal exergy is positive regardless of the temperature relative to the adiabatic reference. If $T_w < \bar{T}_{w,adiab}$, the surface represents a sink which could be used to improve a CARNOT cycle efficiency. In fact, a cold surface rapidly represents a large potential. The exergy transferred ranges from 0 to 170kW for a surface of exchange of about 0.82m^2 for a unit span configuration.

(a) Thermal energy and exergy transfer.

(b) Change in propulsive exergy relative to the adiabatic case.
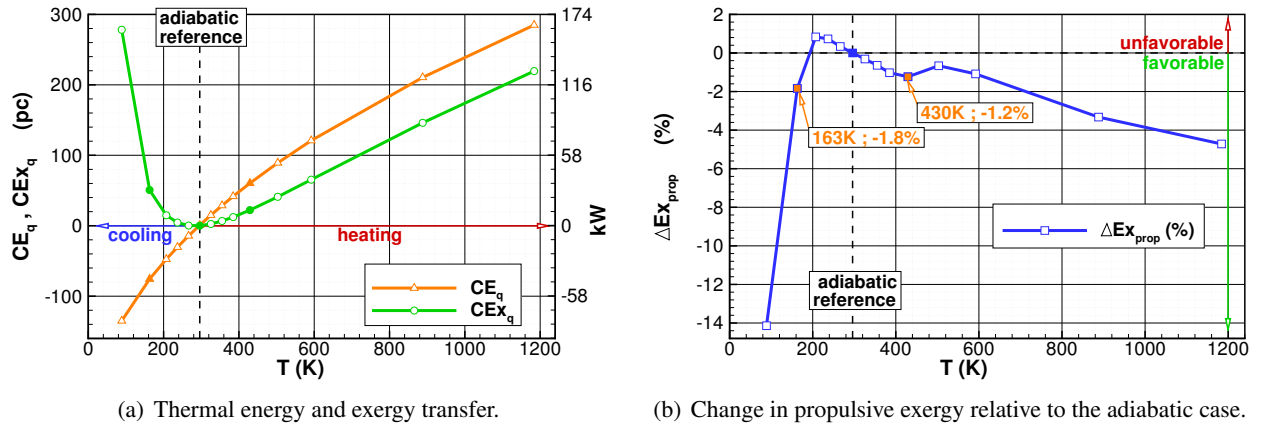
Figure 4-43: 2D BWB with BLI: aerothermopropulsive performance assessment with cold and hot surfaces.

The corresponding change in propulsive exergy relative to the adiabatic reference is presented in Fig. 4-43b. The adiabatic case is actually representative of the blended wing-body configuration *plus* a distant heat exchanger that would deliver/capture the same amount of energy. The latter system would have no influence on the exergy delivered by the propulsion system. One can see that except for a small unfavorable region when the wall temperature T_w is slightly less than the adiabatic value, there is an overall benefit of the thermopropulsive interactions. The highest benefit of -14% is obtained for the lowest temperature of

---

[27]Note that the sharing between exergy and anergy associated with the heat transfer is function only of the temperature at which the heat transfer occurs:

$$\dot{\mathcal{E}}_q = \left(1 - \frac{T_\infty}{T_w}\right)\dot{E}_q = \dot{E}_q - \frac{T_\infty}{T_w}\dot{E}_q = \dot{E}_q - \dot{\mathcal{A}}_q \tag{4.11}$$

As the temperature increases, the portion of anergy reduces and the *usefulness* of the heat transfer in terms of mechanical performance increases.

89K (= $0.3 \times \bar{T}_{w,adiab}$). Also noticeable are a 1.8% and 1.2% propulsive exergy reduction obtained for a wall temperature of respectively 163K (= $0.55 \times T_{w,adiab}$) and 430K (= $1.45 \times \bar{T}_{w,adiab}$).

Physical Breakdown. Fig. 4-44 gives a phenomenological breakdown of the overall reduction in propulsive exergy supply where variations of viscous ($\Delta\dot{\mathcal{A}}_{\phi}$ –), thermal ($\Delta\dot{\mathcal{A}}_{\nabla T}$ –) and wave ($\Delta\dot{\mathcal{A}}_w$ –) anergy and of the recoverable exergy ($\Delta\dot{\mathcal{E}}_{rec}$ –) evaluated at d_{TP} = 1.5 are illustrated.
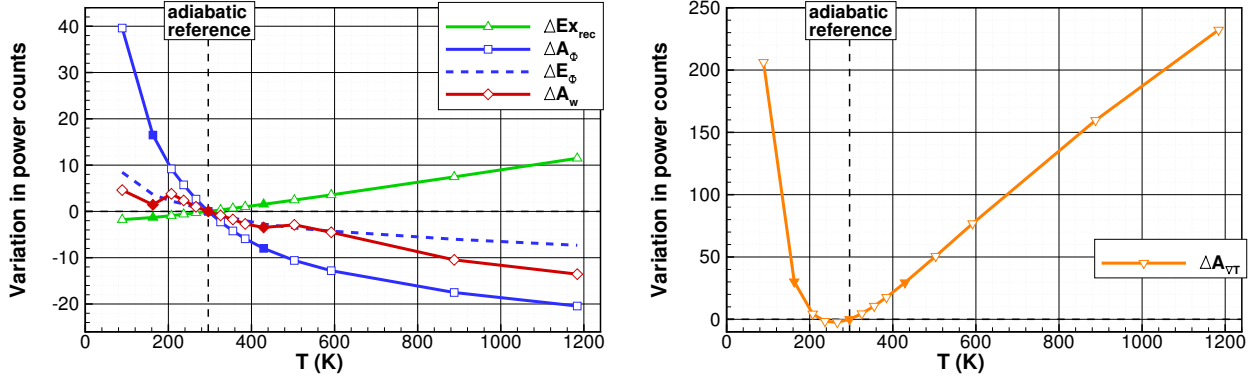
(a) Recoverable exergy as well as dissipation associated with viscous and wave phenomena.

(b) Thermal anergy.

Figure 4-44: 2D BWB with BLI: change in the terms composing the propulsive exergy with wall temperature increase.

Not surprisingly, the recoverable exergy (–) increases with the thermal exergy delivered to the fluid. We can also observe that a higher temperature allows a reduction of the intensity of the shock wave and therefore in the anergy (–) associated with this phenomenon: for a given flow velocity, a higher static temperature increases the speed of sound and thereby reduces the shock *Mach* number.

Also, the viscous dissipation (– –) is reduced as the wall temperature is increased. From the velocity profile depicted in Fig. 4-40a, one can infer lower velocity gradients within the boundary layer when the temperature is higher. This mechanism is emphasized for the anergy (–) associated with viscous dissipation due to the presence of the temperature ratio ($\dot{\mathcal{A}}_{\phi} = T_{\infty}/T \times \dot{E}_{\phi}$).

For wall temperatures just below the adiabatic one, a reduction in the thermal anergy generated (–) is observed. Looking back to the temperature profile depicted in Fig. 4-40b, one can imagine that if the wall temperature is closer to the reference (T_{∞}), less dissipation (anergy) will be required within the thermal boundary layer to bring the fluid back to thermal equilibrium.
The more we deviate from the reference temperature, the more thermal anergy will be required.

The overall reduction in propulsive exergy (fuel burn) is due to several mechanisms that can be quantified:

$$\Delta\dot{\mathcal{E}}_{prop} = \dot{\mathcal{E}}_{prop}^{heat\ transfer} - \dot{\mathcal{E}}_{prop}^{adiab} = \Delta'\dot{\mathcal{E}}_q + \Delta\dot{\mathcal{E}}_{rec} + \Delta\dot{\mathcal{A}}_{\phi} + \Delta\dot{\mathcal{A}}_{\nabla T} + \Delta\dot{\mathcal{A}}_w \quad (4.12)$$

The exergy associated with heat transfer has been placed right-hand side to isolate the propulsive exergy. Table 4.7 gives the value of each term of this relation for three wall temperatures: 163K, 207K, and 430K.

One can see that there is a large possible reduction by supplying heat, and that, the greater the temperature difference, the greater the potential. But this exergy supply has an impact on the different flow mechanisms responsible for flight power requirements. There is an overall benefit only if this net impact is lower than the exergy supply. Lower wall temperatures (relative to the adiabatic reference) reduce the

T_w (K)	propulsive exergy breakdown					
	$\Delta'\dot{\mathcal{E}}_q$	$\Delta\dot{\mathcal{E}}_{rec}$	$\Delta\dot{\mathcal{A}}_\phi$	$\Delta\dot{\mathcal{A}}_{\nabla T}$	$\Delta\dot{\mathcal{A}}_w$	$\Delta\dot{\mathcal{E}}_{prop}$
163	-50.67	-1.31	+16.49	+30.18	+1.43	**-3.88**
207	-14.80	-0.91	+9.19	+4.39	+3.81	**+1.68**
430	-22.15	+1.54	-8.00	+29.44	-3.46	**-2.63**

Table 4.7: 2D BWB with BLI: breakdown of the change in propulsive exergy for two cooling conditions (T_w = 163K and T_w = 207K) and one heating condition (T_w = 430K).

recoverable exergy, but increase all dissipative phenomena. There is only a gain for significantly lower temperatures for which the exergy supply $\dot{\mathcal{E}}_q$ becomes rapidly predominant. A higher wall temperature increases the recoverable exergy and the thermal mixing while reducing the viscous anergy and the shock intensity.

4.4.4 Summary of the Key Findings

A two-dimensional simplified representation of possible future aircraft concepts has been investigated. One of its main feature is the ingestion of the boundary layer that develops on its upper surface. It has been shown that the interactions between the internal and external flows are such that a clear separation between the airframer and engine designer's task is not obvious. A global design approach must be adopted for which the proposed formulation provides detailed and unambiguous information of the aeropropulsive performance.

Placing the propulsion on top of the blended wing-body configuration effectively enabled an improvement by 50% of the overall performance of the airplane. In fact, the exergy-waste coefficient evaluated at 1.5 reference chord was reduced to about 2.8%. This extremely low value means that about 97% of the exergy delivered by the propulsion system was destroyed in the direct vicinity of the body and very little in its wake. This information tells the aircraft designer that efforts, and thereby investment, should be put on sub-systems other than the architecture itself.

This test case was also the opportunity to characterize the impact of the wall temperature on the viscous and thermal anergy generation and on their laminar and turbulent production mechanisms. It was found that a higher temperature within the boundary layer reduces both the laminar and turbulent viscous dissipation. As regards to thermal mixing, for temperature that differs from the freestream reference, an increase in both the laminar and turbulent mechanisms was observed. Overall, the rise in thermal mixing exceeds the reduction in viscous dissipation: a higher temperature means a higher overall dissipation.

Clear benefit of the *single currency* aspect of the exergy analysis has been highlighted when considering heat transfer at the body surface just upstream of the propulsion system. The interactions between the purely thermal subsystem (heat exchanger) and the purely mechanical propulsion system (as modeled by the boundary condition), were studied[28]. The aerothermopropulsive performance of the configuration showed that a reduction in propulsive exergy of 1-2% should be possible by cooling or heating the surface by 45% of the reference temperature (±130K). In addition, the impact of heat transfer on each physical mechanisms identified in the exergy balance can be quantified separately.

---

[28] It would be desirable to develop/use a higher fidelity boundary condition which would account for thermal energy. It would also be required to adapt the mesh according to the wall temperature imposed in order to obtain the desired $y^+ \approx 1$.

4.5 Heat Exchanger Integration on Aircraft

At the crossroad between the tasks of the aircraft aerodynamic designer and air system designer lies the integration of heat exchanger. The benefit of the exergy analysis, or more precisely, of the Entropy Generation Minimization (EGM) approach, for the design of thermal systems in itself is well covered by BEJAN [18, 21, 24] and will not be investigated in the present test case. Rather, we study more deeply the integration of such a system on a commercial aircraft. The aerothermodynamic aspects of the formulation enables the multi-disciplinary approach suggested by this test case.

4.5.1 Test Case Presentation

Heat exchangers are required on any commercial airplane to ensure the cooling of various systems like electronics and for providing air conditioning to the cabin. As an example for the Airbus A320, one can see the inlet (green circles) and the exhaust (red squares) on Fig. 4-45.

(a) Bottom view.

(b) Zoom on the inlet (green circles) and exhaust (red squares).
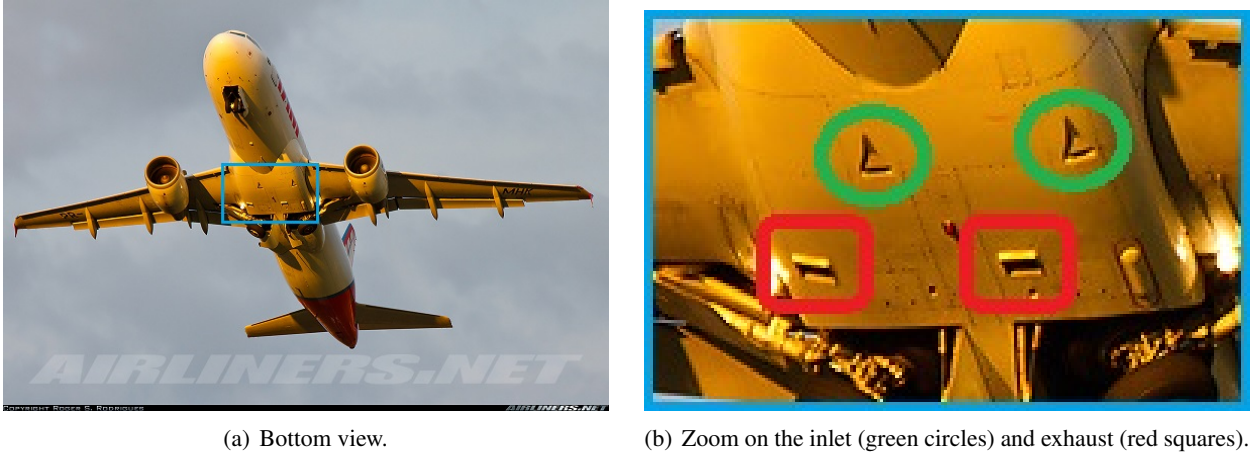
Figure 4-45: 2D Heat Exchanger: Airbus A320 air system view.

4.5.1.1 Design Considerations

The duty of the aerodynamicist would be to integrate this air system in such a way as to minimize perturbations to the initial aircraft design while ensuring the desired heat exchange. Even a small improvement could provide an overall benefit to the aircraft. Traditionally, the quality of such integration has been evaluated with (mechanical) considerations of total pressure loss, as described by HOERNER [74].

Alternatively here we consider exergy management which is a more comprehensive approach. The exergy balance for this subsonic flow with heat transfer at the body surface reads:

$$\dot{\mathcal{E}}_q = F_x V_\infty + \dot{\mathcal{E}}_m + \dot{\mathcal{E}}_{th} + \dot{\mathcal{A}}_\phi + \dot{\mathcal{A}}_{\nabla T} \tag{4.13}$$

The question asked is: for a given amount of thermal energy $\dot{E}_q$ that the system must evacuate and deliver to the fluid, how to maximize the net rate of change of momentum F_x? Would a careful integration even allow to generate (a little amount of) thrust? The design objective is therefore to convert as much as possible the thermal energy associated with the heat transfer into useful mechanical work. To do so, one must try to reduce as much as possible the exergy outflow and destruction, *i.e.* all right-hand side terms.

4.5.1.2 Numerical Considerations

Grids and Geometries. An overview of the system is given in Fig. 4-46. The mesh extends 10 chords upstream, 20 downstream and 10 chords vertically for a total number of 252,000 elements.
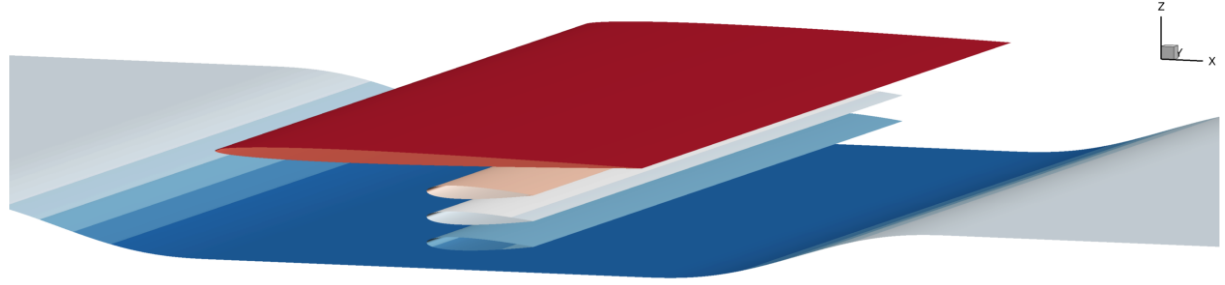
(a) Overview of the system.
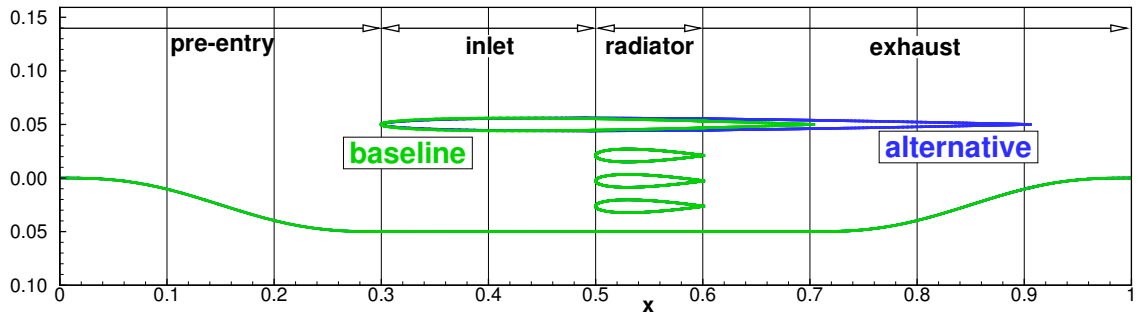
(b) Difference between the baseline and the alternative designs.

Figure 4-46: 2D Heat Exchanger: overview of the grid extension and highlight of the geometrical differences between the baseline and the alternative designs.

The air system is represented by three NACA 0012 Airfoils of same length that are placed under the duct which is a stretched NACA 0012, see Fig. 4-46b. The total surface of exchange is $3 \times 0.2057 \approx 0.62 \mathrm{m}^2$. In order to determine the sensitivity of the design, two geometries of the duct have been considered. Compared to the baseline design (–), the alternative geometry (–) has a greater extension of its duct up to $x_{TE}^{alt} = 0.9$ instead of $x_{TE}^{base} = 0.7$. Both grids have been generated by O. Atinault (ONERA).

The system can be divided into four zones: 1) the pre-entry, 2) the inlet, 3) the radiator (NACA 0012) and 4) the exhaust.

Flow Computations. As for the previous test case, a wall temperature is imposed on the three NACA Airfoils. This temperature ranges from adiabatic ($\bar{T}_{w,adiab} \approx 235\mathrm{K}$) to 500K. A flow regime at zero incidence, $Re = 5 \times 10^6$ and $M_\infty = 0.65$ has been considered, see Table 4.8.

Quantity	Value	Unit	Quantity	Value	Unit
ρ_∞	0.3796	kg.m^3	p_∞	23841	Pa
T_∞	218.81	K	V_∞	192.73	m.s^{-1}
$T_{i,\infty}$	237	K	p_{i_∞}	31668	Pa
M_∞	0.65	–	Re	5.12×10^6	–
α	0	degree	A_{ref}	10	m^2

Table 4.8: 2D Heat Exchanger: reference aerodynamic conditions.

The choice of *Mach* number is dictated by compressibility effects. On one hand, at lower *Mach* numbers, the interactions between the thermal energy and the mechanical aspects are negligible. In other words, the

supply of thermal energy to the fluid would not alter its mechanical characteristics, mainly the rate of change of momentum. On the other hand, a higher *Mach* number would be more representative of cruise conditions but may also involve the formation of shock waves in the channel. This greater complexity of the flow would however not present any major advantage in terms of heat transfer analysis.

The convergence of the computations is illustrated in Fig. 4-47. 50,000 iterations were run to provide a convergence of the near-field force below 0.0001 dc, as illustrated for the middle NACA Airfoil in Fig. 4-47a. This also corresponds to a residual reduction of about 6 orders, as shown in Fig. 4-47b for the energy equation.

(a) Near-field net force acting on the NACA 2 Airfoil.

(b) Equation of energy residuals reduction.

(c) Heat transfer coefficient for the baseline (dashed) and alternative (solid) designs.
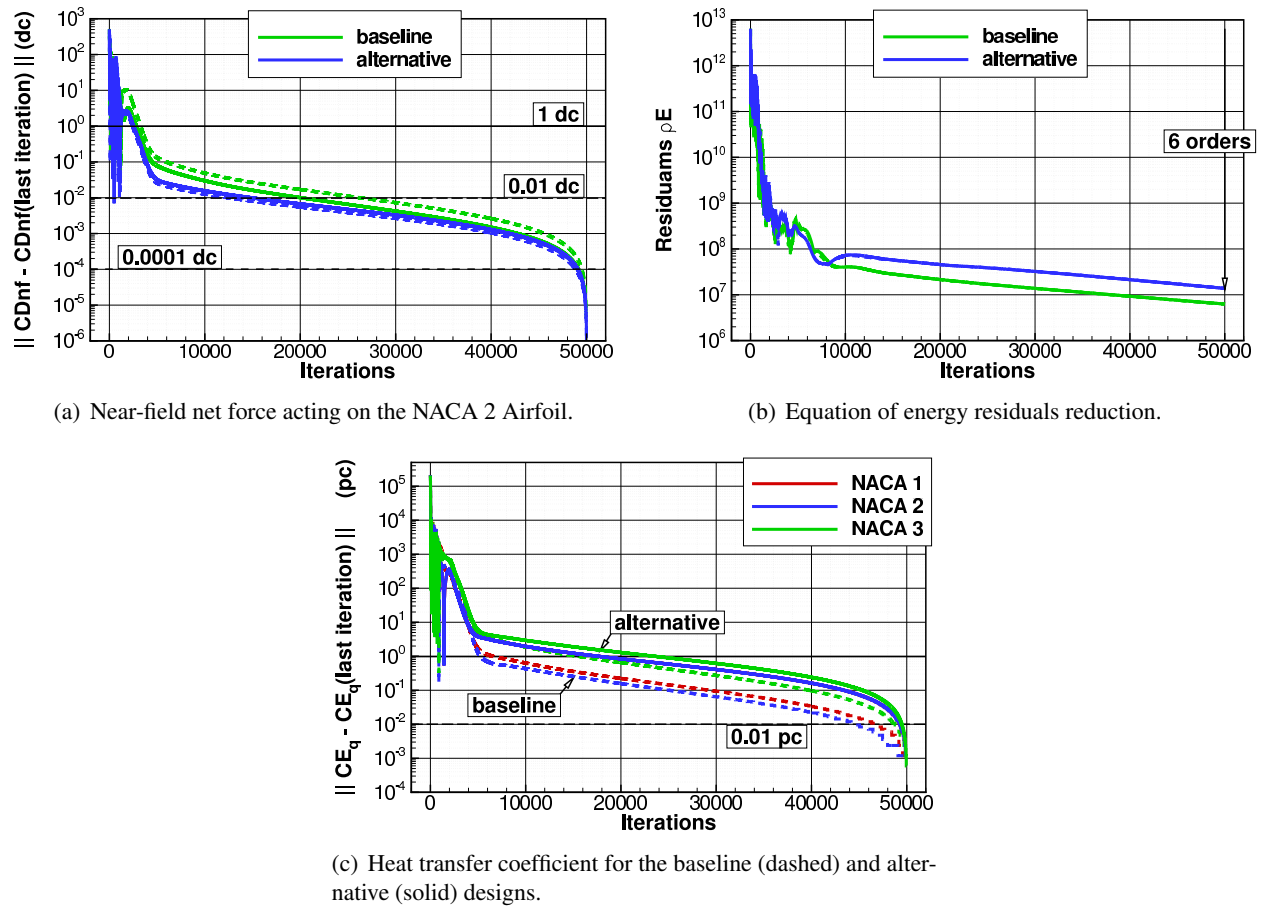
Figure 4-47: 2D Heat Exchanger: convergence history for both geometries with the adiabatic surface (dashed lines) and for T_w = 450K (solid lines).

The convergence of the heat transfer coefficient for all three NACA Airfoils also exhibits a convergence higher than 0.01 pc for both geometries, see Fig. 4-47c. Note that the coefficient corresponding to the third NACA (lowermost location) is slightly less converged.

No major influence on the convergence from the isothermal wall condition was observed. As regards the first grid-point y^+, values slightly lower than unity were measured one the largest part of the system and were only weakly affected by higher temperatures.

Flow Solutions. The main characteristics of the flow in the system are given by the *Mach* number field depicted for both geometries in Fig. 4-48.

One can notice the appearance of a *recirculation* in the pre-entry zone in the case of the alternative geometry. The convergence of the flow solution is therefore impacted which explains the slightly lower rate of convergence observed in Fig. 4-47c for the NACA 3 Airfoil.

(a) Baseline geometry.

(b) Alternative geometry.
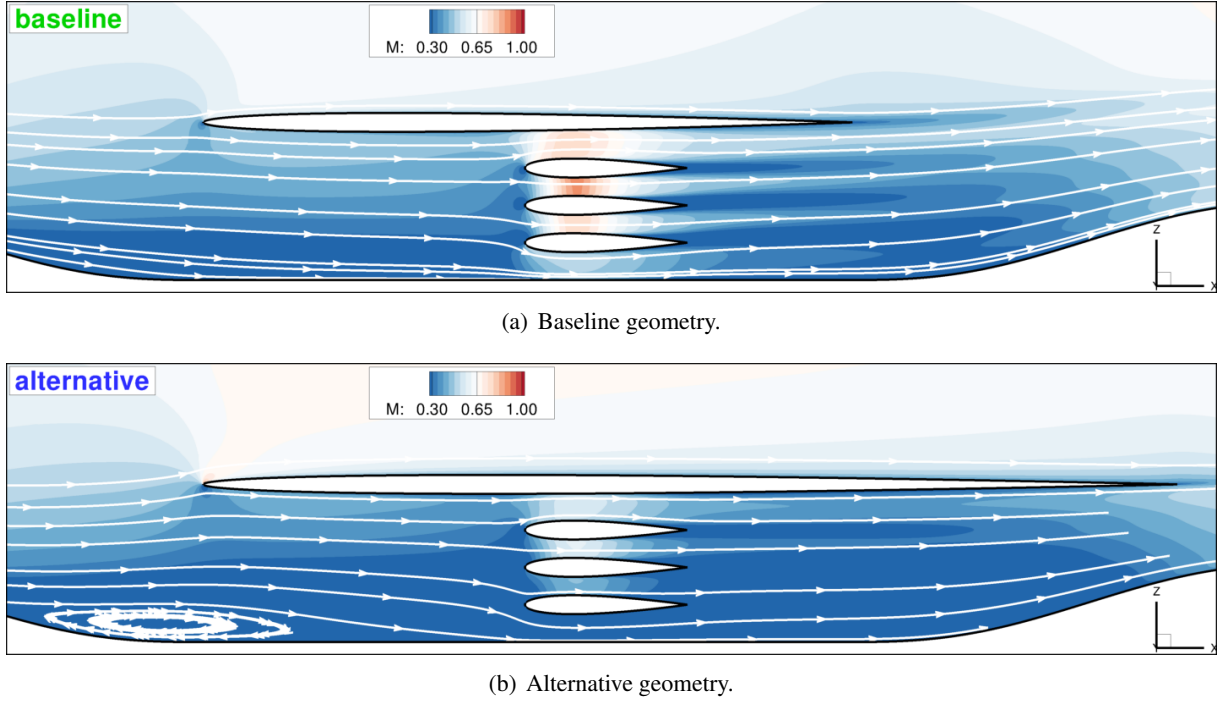
Figure 4-48: 2D Heat Exchanger: *Mach* number fields with streamlines for the two geometries at T_w = 450K.

Also, there is a boundary layer separation on all NACA Airfoils which involve additional losses.

4.5.2 Aerothermodynamic Performance Assessment

In order to determine the quality of the integration of the system, we first describe the flow in terms of heat transfer and (streamwise) momentum change. Then, the analysis is made with regard to exergy supply and destruction. All the following data have been extracted from the code *ffx* only.

4.5.2.1 Flow Description

Mass flow and Heat Transfer. The non-dimensionalized surface mass flow rate ($\rho[V_\infty + u]/\rho_\infty V_\infty$) evaluated in a slice located a half NACA-chord distance upstream of the leading edge is given in Fig. 4-49.
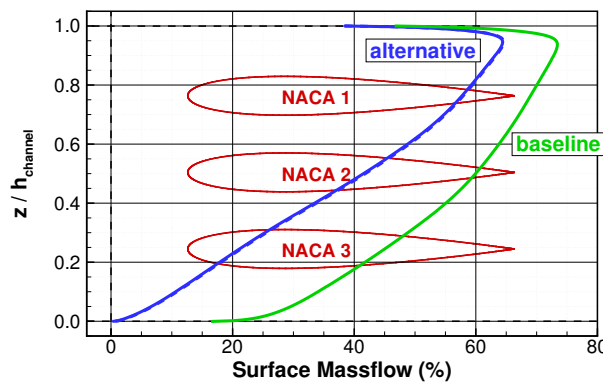
Figure 4-49: 2D Heat Exchanger: mass flow rate through the channel for the baseline design at T_w = 450K (**—**) and for the alternative geometry at T_w = 450K (**— —**) and at T_w = 500K (**—**).

One can see that, in agreement with the flow described in Fig. 4-48, the flow in the channel is far from being uniform. A large deficit is observed in the bottom half of the channel, especially for the alternative

design which involves a large recirculation zone in the pre-entry zone. Note that the presence of the boundary layer could be removed by a careful design of the system [48, 74].

The non-uniform mass flow in the channel thus generates discrepancies in the heat transfer because the greater the mass flow, the larger the energy transferred to the fluid, see Table 4.9.

	Baseline ($T_w = 450K$)			Alternative ($T_w = 450K$)			Alternative ($T_w = 500K$)		
	$C\dot{E}_q$	$C\dot{\mathcal{A}}_q$	$C\dot{\mathcal{E}}_q$	$C\dot{E}_q$	$C\dot{\mathcal{A}}_q$	$C\dot{\mathcal{E}}_q$	$C\dot{E}_q$	$C\dot{\mathcal{A}}_q$	$C\dot{\mathcal{E}}_q$
NACA 1	6.03	2.93	3.10	5.40	2.63	2.77	6.51	2.85	3.66
NACA 2	5.58	2.71	2.87	4.79	2.33	2.46	5.77	2.52	3.25
NACA 3	5.44	2.65	2.79	3.93	1.91	2.02	4.79	2.09	2.70
Total	**17.05**	8.29	8.76	**14.13**	6.87	7.26	**17.06**	7.47	9.61

Table 4.9: 2D Heat Exchanger: heat transfer coefficients ($\dot{E}_q = \dot{\mathcal{A}}_q + \dot{\mathcal{E}}_q$) for the three NACA 0012 Airfoils, expressed in power counts.

Due to a lower mass flow rate for the alternative geometry, less energy is transferred to the flow for the same wall temperature of 450K, 14.13 pc versus 17.05 pc[29]. This observation is also valid for an isolated NACA: the uppermost airfoil (NACA 1) is the one that transfers the greatest amount of energy.

In a design perspective, the amount of energy that *must* be released to the flow is likely to be a constraint. As a consequence, in order to reach the same quantity of energy transfer for a given geometry, one has to increase the wall temperature up to 500K (last column). Because the temperature has been raised, so has the proportion of exergy: $\dot{\mathcal{E}}_q = (1 - T_\infty/T_w)\dot{E}_q = 0.56\dot{E}_q$ instead of $0.51\dot{E}_q$ at 450K.

Looking back at Fig. 4-49, one may notice that the surface mass flow distribution for the alternative geometry with a wall temperature of 500K, represented by the solid blue line (–), is almost identical to the case at 450K (– –). In other words, the wall temperature has only a weak impact on the mass flow, the primary driver being the outlet geometry.

Momentum Analysis. As a first look, it is worth considering the change in streamwise momentum around the system. This information is given with a large view by Fig. 4-50a and with a zoom around the heat exchanger in Fig. 4-50b.

(a) Large view.

(b) Zoom on the system.
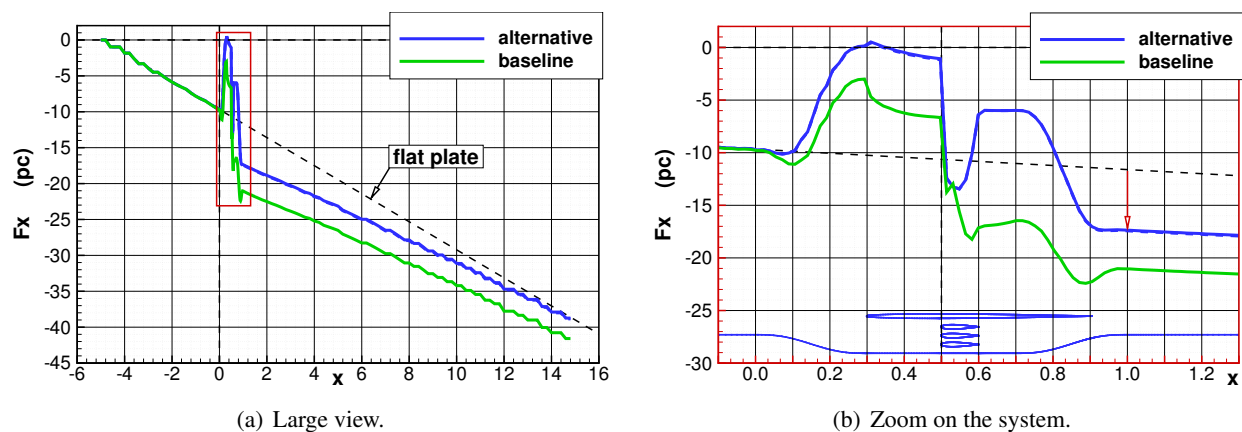
Figure 4-50: 2D Heat Exchanger: chordwise momentum change for the baseline geometry at $T_w = 450K$ (–) as well as for the alternative design at $T_w = 450K$ (– –) and at $T_w = 500K$ (–).

---

[29]For an Airbus A320 airplane with a wing area of roughly $A_{ref} = 100$ m^2, the thermal energy evacuated by this 1m-wide system would represent about 2 kW.

Fig. 4-50a shows the rate of change of momentum from x_{min} = −5 to x_{max} = 15 reference (air system's) length. The dashed black line represents the drag that would be experienced in the absence of the heat exchanger, *i.e.* in the case of a simple flat plate, which serves as a reference. Most noticeable is the change in slope upstream and downstream of the system. After a sudden drop, the rate of momentum change is reduced compared to the flat plate. Yet, up to a distance of 15 chords the presence of the heat exchanger has worsened the drag compared to a simple flat plate case. One can see that the alternative design (**–**) presents a less negative impact on the drag than the baseline (**–**), even with a slightly greater wetted surface (and thereby greater friction drag).

Fig. 4-50b allows a detailed analysis of the two geometries. In the pre-entry (a), the momentum change is positive which means that the drag is reduced. The effect is more pronounced for the alternative design (**–**) which eventually reaches (slightly) positive values of F_x (at x = 0.30), meaning *thrust*. The biggest difference is observed in the region of heat exchange ($0.5 \leq x \leq 0.6$): while the baseline geometry yields a drop in momentum, the alternative design provides a large increase. This difference of 3.5 dc is kept at the exhaust of the channel. Note that this benefit is observed regardless of the two wall temperatures for the alternative design.

In terms of mechanical considerations, an effective integration can be assessed in terms of momentum loss. The (direct) drag involved by the heat exchanger, if defined as the loss in momentum between x = 0.0 and x = 1.0, is equal to 11.3 dc for the baseline design. Yet, because the system modifies the external flow the analysis appears slightly more complex. In fact, one can consider that this loss of momentum is slightly overestimated because the presence of the system involves a reduced momentum loss downstream of the system, see 4-50a. As a consequence, if one considers its overall impact on the flow, he could suggest that the presence of the heat exchanger does not involve a much larger penalty compared to a flat plate (+5 dc at x = 10).

These observations are even more valid for the alternative design whose the longer duct enables to reduce the direct momentum loss by 30%, from 11.3 to 7.8 dc. For an Airbus A320 airplane, it represents about 10 times less, *i.e.* around 1 dc.

4.5.2.2 Exergy Analysis

Now let's have a look at the destruction of exergy around the system for the two geometries and with reference to an hypothetical flat plate. Fig. 4-51 gives more detailed information on the heat exchanger in terms of exergy evolution (a) and rate of change of exergy (b). The latter representation makes the regions of large changes more visible.

As opposed to the momentum change depicted in Fig. 4-50a, there is no major change in exergy in the pre-entry zone ($x \leq 0.3$). One can see a greater drop in exergy for the alternative geometry (**–**) than for the baseline (**–**) at $x \approx 0.3$ which is due to the greater anergy generation around the duct leading edge deduced from Fig. 4-48. This loss could be largely reduced by a better design and is not considered critical. More important is the discrepancy observed around the radiator ($0.5 \leq x \leq 0.6$):

– the baseline geometry exhibits a net destruction of exergy despite the supply from the heat transfer.

– the alternative geometry on the other hand can maintain a constant level at T_w = 450K (**– –**) or even provide a net (local) gain in exergy at the highest temperature of 500K (**–**).

For a given energy to be evacuated to the surrounding fluid, the baseline design appears to destroy more exergy than the amount supplied by heat transfer. Fig. 4-52 gives an overall view on the exergy evolution. With reference to the loss of momentum depicted in Fig. 4-50b (same y scale), one can see that the destruction of exergy is lower. This is because, the loss of momentum is not strictly speaking a *loss* in the exergy analysis; fundamentally speaking, only irreversible phenomena involve losses.

(a) Zoom on the system: exergy.

(b) Zoom on the system: rate of change of exergy.
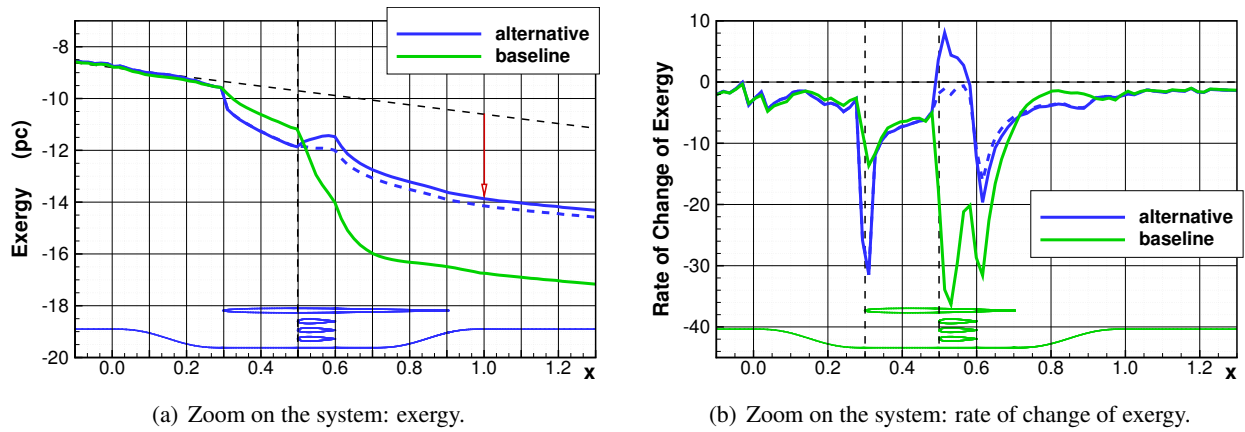
Figure 4-51: 2D Heat Exchanger: exergy evolution and rate of change of exergy for the two geometries.
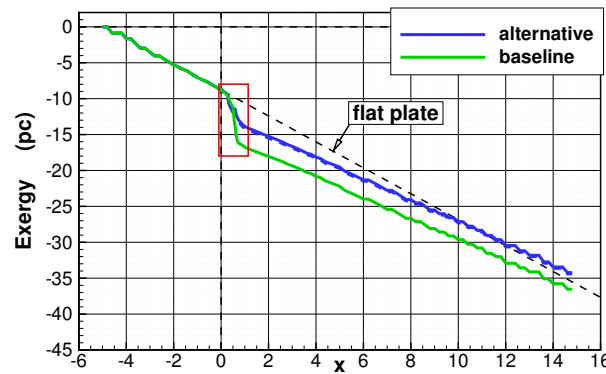
Figure 4-52: 2D Heat Exchanger: large view of the exergy distribution for the two geometries.

In a similar fashion to the momentum evolution, it appears that the system has a beneficial impact on the flow downstream. For the alternative design (–), at a distance of 10 reference lengths, the overall impact in terms of exergy destruction is equivalent to the simple flat plate suggesting that there is no major performance penalty resulting from the integration of such a system.

4.5.2.3 Anergy Generation

The rate of change of the viscous and thermal anergy generation around the system is given in Fig. 4-53 for the two geometries.

Fig. 4-53a focuses on the viscous dissipation. The additional dissipation associated with the poor design of the duct at $x = 0.3$ is highlighted and emphasized for the alternative design (–). More interesting is the radiator section where one can see that there is a viscous dissipation about twice as high for the baseline geometry (–) compared to the improved design. For this latter geometry, we observe very little influence of the wall temperature: the two curves ($T_w = 450k$ – – and $T_w = 500k$ –) are practically identical.

In the exhaust, the baseline configuration resumes more rapidly to the flat plate reference because its trailing edge duct is located at $x_{TE}^{base} = 0.7$ instead of $x_{TE}^{alt} = 0.9$ for the alternative design.

Fig. 4-53b focuses on the thermal dissipation. First notice that the production is almost entirely located at the radiator, as opposed to the viscous component (Fig. 4-53a). If the same temperature is set at the

(a) Viscous anergy.
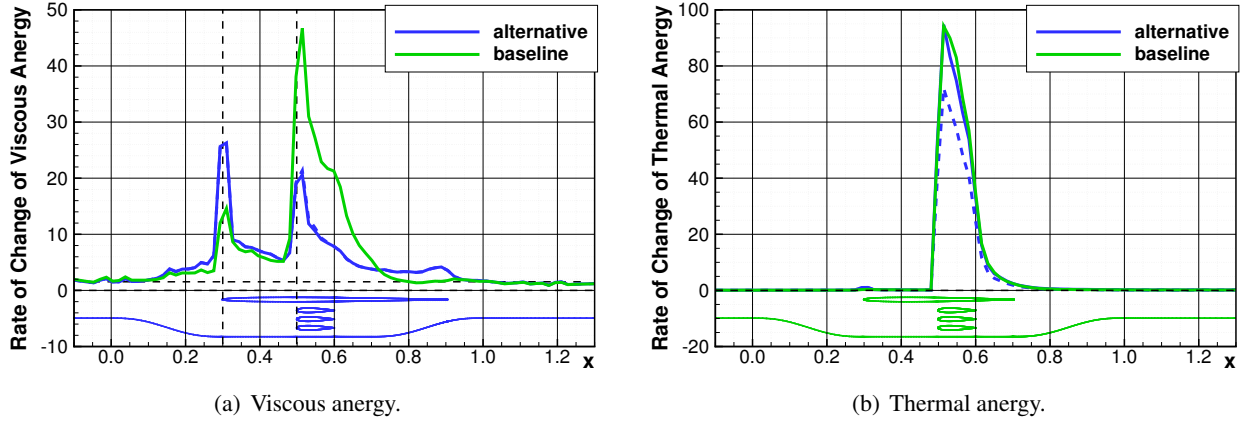
(b) Thermal anergy.

Figure 4-53: 2D Heat Exchanger: rate of change of viscous and thermal anergy generation for the two geometries.

wall, the alternative design exhibits a lower dissipation. A higher temperature of 500K must be used to reach a comparable level of thermal mixing.

Judging from the very little difference between the two geometries, one can infer that the thermal dissipation is only a weak function of the mass flow through the channel. To leading order, it appears to be a characteristic of the geometry and of the wall temperature.

4.5.2.4 Design Considerations

Once again, we have adopted the idea that the integration of any system on an aircraft should be done in such a way as to minimize exergy destruction. As a consequence, the heat exchanger should ideally deliver more exergy to the fluid than its integration has destroyed. Table 4.10 gives the information required to assess the quality of the integration of the heat exchanger. It contains the value of all the terms present in Eq. (4.13)

$$\dot{\mathcal{E}}_q + DV_\infty = \dot{\mathcal{E}}_m + \dot{\mathcal{E}}_{th} + \dot{\mathcal{A}}_\phi + \dot{\mathcal{A}}_{\nabla T} \tag{4.14}$$

for a control volume extending from $x_{min} = 0.0$ to $x_{max} = 1.0$ and vertically to $z_{max} = 0.8$.

Geometry	T_w (K)	$C\dot{\mathcal{E}}_q$	CD_ε	$C\dot{\mathcal{E}}_m$	$C\dot{\mathcal{E}}_{th}$	$C\dot{\mathcal{A}}_\phi$	$C\dot{\mathcal{A}}_{\nabla T}$	$C\dot{\mathcal{E}}_{rec}$
Baseline	450	8.76	11.27	2.11	1.32	7.48	9.10	3.43
Alternative	450	7.26	7.75	1.39	1.01	5.89	6.67	2.40
Alternative	500	9.60	7.68	1.37	1.26	5.86	8.74	2.63

Table 4.10: 2D Heat Exchanger: value of the terms of the exergy balance Eq. (4.13), expressed in power counts.

From Fig. 4-53b we can conclude that the thermal anergy is almost entirely associated with the heat transferred by the radiator. One can therefore look at the ratio of thermal exergy supply and thermal anergy generation $\dot{\mathcal{E}}_q/\dot{\mathcal{A}}_{\nabla T}$ and notice that this ratio is lower[30] for the baseline geometry than for the alternative design. These values suggest that the latter design is more efficient in terms of exergy management.

Noting that $\dot{\mathcal{E}}_q$ is dependent on the mass flow and on the temperature while $\dot{\mathcal{A}}_{\nabla T}$ is almost independent on the mass flow, an efficient integration of a heat exchanger could be inspired by the following guidelines. For a given amount of energy to be transferred, the exergy content should be as high as possible. In other words, the temperature at which the heat transfer occurs should be highest so as to minimize the anergy portion. This temperature may also by influenced by other considerations associated with the source of

---

[30]Even lower than one.

the thermal energy. Once this temperature is chosen, the mass flow required to obtain the desired energy transfer must be determined. Then, the system must be designed such as to minimize the exergy destruction, *i.e.* thermal (and viscous) anergy production.

4.5.3 Summary of the Key Findings

The main challenges faced by the integration of an air system on an aircraft were investigated in this test case. The heat exchanger considered is representative of an air system integrated on an Airbus A320. A high subsonic flow at M_∞ = 0.65 was considered in order to enable interactions between the mechanical and thermal aspects of the flow. Two slightly different geometries have been analyzed in order to determine guidelines for an efficient integration of the subsystem in terms of exergy management.

It has been highlighted that the presence of the air system may have an overall positive impact on the flow. This observation is made with comparison to a simple flat plate. The heat exchanger, although involving loss in momentum and exergy in its direct vicinity, leads to a lower generation of anergy downstream. This analysis suggests that for a long fuselage (more than 15 times the length of the air system), the presence of the air system does not involve any performance penalty.

If a more detailed analysis of the system was necessary, it is important to note that the approach adopted here is fully consistent with well-tried methods for the design of heat exchangers introduced by BEJAN [21].

Furthermore, this test case could be treated by a multi-disciplinary optimization problem to maximize the net rate of change of momentum F_x for a given amount of thermal energy to be evacuated. The optimizer would probably tend to reduce the surface of exchange to raise the temperature and thereby the exergy delivered to the fluid. As suggested[31] by DRELA, the optimizer would also favor reduced velocities over the heat-transfer surfaces, since heat transfer rates scale roughly as V, while the losses or anergy production scales roughly as V^3.

---

[31]Through the review of the document.

4.6   Chapter Summary

The objective of this chapter was to demonstrate the ability of the proposed formulation and of the post-processing code *ffx* to provide a multidisciplinary tool in terms of aerothermopropulsive performance. Test cases that deviate from the conventional configurations with interactions between the subsystems have been gradually introduced for which all the data were extracted by the code *ffx*.

The approach was first applied to an isolated nacelle representing a turbojet engine similar to the propulsion system of the Airbus A300. This test case enabled to characterize all terms of the formulation with an emphasis on the thermal exergy which becomes predominant for that type of realistic propulsive device. Consistency with traditional bookkeepings was demonstrated. Additional benefit comes from the higher robustness of the exergy balance compared to the definition of thrust and drag, even for this simple geometry.

The concept of wake ingestion was then investigated through an academic configuration made up of a simple fuselage that generates a wake of about the size of an engine inlet located close downstream of the fuselage. A simple mechanical boundary condition was applied to model the effect of a fan on the flow. It was highlighted that the basic (mechanical) principle is to *reenergize* the flow in order to bring its velocity closer to the freestream reference. By doing so, less anergy needs to be produced to bring the system back to thermodynamic equilibrium than if the two subsystems were isolated (and therefore not interacting). In this latter case, viscous dissipation would be required and therefore anergy would be produced.

A third application was the aeropropulsive assessment of a simplified blended wing-body architecture with a propulsion system ingesting the boundary layer that develops on the upper surface. This architecture, for which conventional drag-thrust bookkeepings become ambiguous, was found very effective by wasting less than 4% of the propulsive exergy in its wake, regardless of the flow regime (subsonic or transonic). This simple geometry was also used to investigate the interactions between a purely thermal system (heat exchanger) and a purely mechanical (propulsion system, as modeled here). The proposed formulation allows one to determine the overall aerothermopropulsive performance of such configuration which eventually could reduce its exergy consumption by almost 2%. The heat transfer by the body surface upstream of the propulsion system could also be a way to control the state of the boundary layer that is ingested.

Finally, the integration of a heat exchanger representative of an air system was examined. Two slightly different designs have been analyzed which allowed the definition of a few guidelines in terms of exergy efficiency. This test case could greatly benefit from an optimization process that would seek at maximizing the rate of momentum change (reduce drag) for a given amount of thermal energy to be evacuated.

The benefit of having a single performance metric for all these various test cases, in terms of exergy management, has been highlighted. Also, the robustness and maturity of the post-processing code *ffx* has been demonstrated.

Chapter 5

Summary, Conclusions and Perspectives

Summary

The thesis consisted in the theoretical development, numerical implementation, validation and application of a formulation dedicated to the aero-thermo-propulsive performance assessment of civil aircraft by an exergy analysis of high-fidelity CFD-RANS flow solutions.

First, the theoretical development of the formulation was introduced. It consists of a fluid flow analysis based on the first and second law of thermodynamics combined with momentum considerations. The output of the derivation process is an exergy balance between the exergy supplied by a propulsion system or by heat transfer, the mechanical equilibrium of the aircraft, and the exergy outflow and destruction within the control volume. Restriction of the formulation to aerodynamic flows over unpowered configurations shows that the underlying theory of many well-tried far-field drag methods can be related to exergy considerations.

The formulation was subsequently numerically implemented in a Fortran code named *ffx* which is dedicated to the post-processing of high-fidelity CFD-RANS flow solutions. Adaptation of the theoretical formulation to numerical considerations was made, especially regarding the numerical treatment of theoretically-discontinuous shock waves. Also, the underlying principle of a correction for the accurate calculation of the viscous and thermal anergy production was introduced.

Then, the post-processing code *ffx* was validated for the prediction of the aerodynamic performance of various unpowered configurations. The methodology adopted was to consider flow phenomena and bodies of increasing complexity, ranging from a low-subsonic flow over a two-dimensional airfoil to a transonic flow over a wing-body configuration. It was highlighted that the calculation of the velocity and temperature gradients was underestimated, especially for coarse grids. As a consequence, a numerical correction was introduced and calibrated by evaluating the anergy not captured and by distributing this *missing* anergy to the viscous and to the thermal anergy generation. The sharing is based on the suggestion that the thermal term contributes relatively less than in the boundary layers.

Rigorous comparison to well-tried near-field and far-field drag prediction methods enabled the validation of the accuracy of the drag-power predicted from the newly-derived exergy relation. In fact, an accuracy similar to the straightforward near-field drag method was obtained with the numerical correction. A turbulence model sensitivity analysis was additionally performed to demonstrate the robustness of the post-processing for assessing flow solutions. Validation against wind-tunnel experimental measurements was made when considering the wing-body configuration for which acceptable accuracy was exhibited.

Subsequently, the formulation was applied for the aerothermopropulsive performance assessment of powered configurations. Here again, a step-by-step methodology was adopted to gradually increase subsystem interactions and thermal aspects. First, an isolated turbojet engine was examined to highlight the capability of the formulation to assess a conventional propulsive system. Then, the concept of wake-ingestion was investigated *via* an academic configuration at low-speed. This test case enabled us to demonstrate the pertinence of the exergy analysis to provide physically informative indicators on the performance of such concept that favors aeropropulsive interactions: less anergy *is to be* generated in the absence of jet/wake to bring the system back to thermodynamic equilibrium with the environment than if viscous dissipation was the mechanism involved.

Finally, a 2D-simplified blended wing-body with a propulsion system ingesting a portion of the boundary layer was analyzed from an exergy standpoint. It was shown that this type of architecture wastes very little exergy in its wake (about 3% at equilibrium). Thermopropulsive interactions were triggered by imposing heat (energy and exergy) transfer at the surface just upstream of the propulsion system. The impact of heat transfer on each flow phenomenon has been quantified separately. It was found that a 1-2% reduction in the exergy supplied by the propulsion system was achievable. Finally, the integration on a civil aircraft of a heat exchanger was investigated. For this test case which involves aerothermodynamic interactions, the idea was to determine guidelines for the effective integration of such a system so as to limit the degradation of performance of an initial design.

The benefit of having a single performance metric, in terms of exergy management, for the performance assessment of all these very different subsystems was thereby demonstrated.

Conclusions

All the objectives and requirements stated in the Introduction (p. 4) have been fulfilled:

✓ *Rely on a formulation that is not based on a drag/thrust bookkeeping in order to be applicable for aircraft with boundary layer-ingesting propulsion systems,*

> This crucial point was theoretically introduced in the derivation of the exergy balance in chapter 2 (p. 27) and numerically validated for the simplified blended wing-body architecture examined in section 4.4 (p. 143). For this test case, it was shown that application of the traditional drag/thrust bookkeepings would be excessively ambiguous. On the other hand, a very detailed performance assessment of the configuration was obtained from the exergy balance.

✓ *The compatibility of the formulation to assess conventional configurations for which such approach is applicable would be a plus,*

> This point was theoretically introduced in the derivation of the formulation in paragraph 2.2.1 (p. 39) and numerically validated for the isolated turbojet engine investigated in section 4.2 (p. 122). In addition, the higher robustness of the exergy balance with the definition of the propulsive surface, compared to more traditional *thrust*, is a clear advantage.

✓ *The formulation should allow for the assessment of aerothermopropulsive performance of civil aircraft,*

> This point was validated for each powered configurations analyzed in chapter 4 (p. 119) with a special emphasis on the last two test cases dealing with thermal aspects. The exergy balance provides a consistent framework from which the energy interactions between the subsystems can be quantified.

✓ *The formulation should also provide a phenomenological identification of the main flow phenomena responsible for fuel consumption,*

> This point was validated for each unpowered configuration analyzed in chapter 3 (p. 63). The exergy balance provides a physical decomposition into clearly-identified destructive mechanisms associated with viscous dissipation, thermal mixing, and shock wave.

✓ *The post-processing code should involve a computational cost a few orders of magnitude lower than the one of the CFD computation,*

> This point was validated for each unpowered configurations investigated in chapter 3 (p. 63). It represents a third order compared to the time required for computing the RANS flow solution.

✓ *The accuracy of the code should be within standards, i.e. typically within one drag count (10^{-4}) of the reference value,*

> This crucial point was validated for all four unpowered test cases analyzed in chapter 3 (p. 63) and especially for the last wing-body configuration in cruise conditions. The accurate drag prediction required the introduction of a numerical correction to balance the underestimated viscous and thermal anergy production. An accuracy similar to the near-field drag method was demonstrated and validation was made with experimental wind-tunnel data when available.

✓ *The code should be capable of treating any kind of turbulence models with a particular emphasis on the popular Spalart-Allmaras turbulence model,*

> This point was validated for all four turbulence models examined to compute the transonic flows around a rectangular wing in section 3.4 (p. 91). The weak dependency observed was adjusted with the application of the numerical correction of the viscous and thermal anergy generation.

✓ *For validation purpose and flow analysis, the visualization in the flow-field of all terms involved in the theoretical formulation should be possible,*

> Dedicated options were implemented in the post-processing code *ffx* to allow flow visualization that were extensively used for each application analyzed in the framework of this thesis.

Additional benefit comes from the characterization of the exergy flowing out of the control volume as a *wasted* or *recoverable* exergy which highlights the potential for improvement associated with any given aerospace vehicle. Also, such a detailed validation of the *Moore* and *Moore* model for mean entropy production [108] in terms of *Reynolds* and *Mach* numbers had not been reported in the literature.

Perspectives

The perspectives can be separated into three distinct sections relative to the theoretical formulation, to the numerical implementation, and to the application of the code *ffx* to other configurations.

Theoretical Formulation

Aircraft Design Methodology. The performance formulation proposed in this work is expected to fit the radically new propositions for the design of aerospace vehicle exhibited in the literature review. Further developments are necessary to gather these various suggestions into a consistent framework for the conceptual and preliminary design of civil commercial airplanes. For example, a map[1] of the exergy distribution and destruction for an entire airplane from the aircraft system-level down to the component-level has not been reported in the literature review and could help assess the interactions between the subsystems and thereby potential performance gain for the system (airplane). Additionally, thermoeconomic analysis [89, 166] could be directly incorporated in the definition of the design process.

Lift-induced Vortices. The precise relation between the exergy distribution within the flow field and the lift-induced drag is yet to be determined [105]. It is unclear whether the key parameter is the peak exergy value or eventually its mean value evaluated on a plane downstream of the wing. Also, a low overall exergy integrated on the downstream plane could suggest a low vorticity field and therefore a low lift-induced drag. However, this conclusion may be erroneous as a higher viscous (and thermal) anergy may have been generated upstream of the point of evaluation. Further studies should be made to better understand the minimum drag associated with an elliptically (aerodynamically) loaded wing from an exergy standpoint.

Total Pressure Loss and Exergy Destruction. The loss in total pressure is a well-used indicator of loss in any aerodynamic flow. It is felt that the total pressure is an indicator unable to *quantify* the loss as opposed to exergy destruction, but the precise interpretation remains somewhat difficult. The *Gibbs* equation provides a relation between the total enthalpy, the total pressure and the relative entropy, see appendix A.5 (p. 182), which could be starting point to derive a relationship between exergy and total enthalpy loss.

Unsteady Flows. The present formulation is restricted to the assessment of steady mean flows but extension to unsteady flows should also be considered. The exergy approach could be combined with the ongoing research conducted at ONERA by TOUBIN and BAILLY [164] to extend the far-field drag method of VAN DER VOOREN and DESTARAC [46, 174] for decomposing the drag into physical mechanisms (viscous drag, vortex drag, and wave drag).

Power Balance. The differences and similarities between the proposed exergy balance and the mechanical energy analysis of DRELA [49] have been theoretically examined in chapter 2 (p. 27). This author also went further in the quantification of the BLI benefit [67] which could be inspirational for the exergy method. Also, the extension to supersonic and unsteady flows of the formulation could benefit from this existing work as well as for the adaptation of the exergy balance for wind-tunnel testings [171].

Impact of Turbulence. What has been referred to *laminar* and *turbulent* anergy production was investigated both for the viscous dissipation and for the thermal mixing. Further work could be carried to relate these results to existing dissipation coefficients such as those described by DENTON [44]. A better fundamental understanding of the underlying physics could be informative in terms of entropy generation [102]. Additionally, higher fidelity models for entropy generation based on $k-\epsilon$ turbulence models have been reported in the literature [81, 82]; they could be investigated to determine if more accurate drag prediction would be reachable.

---

[1]*Grassman* diagrams are typically used to represent energy systems [26, 45].

Post-processing Code *ffχ*

Memory Allocation.   The post-processing code *ffχ* has been validated on a number of unpowered and powered configurations but can still be considered as a *prototype*. Improvements of the current capabilities include a better memory treatment (allocation/deallocation) of the variables to further reduce the computational time. Also, the treatment in parallel of specific blocks of the whole computational solution would greatly reduce the post-processing time. In order to fit gradient-based optimization processes, additional routines should be developed to compute the gradients of (all) the terms involved in the formulation. All these improvements require a significant effort.

Gradients Calculation.   The evaluation of the viscous and thermal anergy production requires the calculation of velocity and temperature gradients. It has been highlighted by the various unpowered applications that the calculation of these terms produced underestimation. Their computations is currently made by determining the average quantity at each cell interface and by dividing by the volume of the element, see Eq. (2.110). Alternative ways of calculating the fluxes other than simple averaging should be considered. Another possibility would be to extract these quantities directly from the flow solver (ONERA-*elsA*).

Accuracy Improvements.   Due to weaker viscous and thermal anergy production, the drag prediction from the *ffχ* code is underestimated. To improve this weakness the numerical correction introduced was able to provide a performance prediction consistent with the near-field drag method. However, this method contains what is generally referred to as *spurious* drag. It was suggested that the spurious drag identified by the code *ffd72* could be removed from the correction, thereby providing an accuracy similar to this more powerful method. This technique has not been adopted in the present work because it comes from very different considerations. An alternative way of improving the accuracy would be to use mesh refinement techniques that could be based on the evaluation of the anergy not captured due to coarse regions of the grid.

Thermal Exergy.   It has been shown in the numerical applications that the direct and indirect methods for thermal exergy calculation, although theoretically rigorously equivalent, can yield very different values. A more detailed comparison of the direct and indirect methods for thermal exergy calculation would enable to identify the numerical cause of the discrepancy observed for the indirect method. Focus should be put on the computation of the compressible term $\dot{E}_{PV}$. This study would also bridge the (numerical) gap between the exergy balance and the *Power Balance* proposed by DRELA.

CFD Numerical Settings.   There are various numerical settings that are required for an effective computation of a flow solution. For all the test cases investigated in the framework of this thesis, *standard* settings have been applied. They correspond to the *good practice recommendation* followed in the research unit. Yet, one must recognize that every user has his own set of parameters that he feels are the most appropriate. As a consequence, another part of validation would be required to assess the sensitivity of the post-processing code to those set of parameters in terms of accuracy of the drag predicted (and decomposition). It is possible that the accuracy of the temperature and velocity gradients might be improved by a careful selection of the numerical parameters. As a consequence, this study may help defining the most appropriate numerical parameters for an accurate drag prediction with the code *ffχ*.

Aerospace Applications

Optimizations. It would be interesting to perform optimization of simple aerospace geometries like a simple wing or of a more realistic wing-body aircraft (CRM) in terms of exergy considerations. Various objectives should be considered such as minimum anergy production, minimum or maximum exergy outflow, etc. Influence on the overall flow should be assessed and the results should be compared with more traditional performance metrics (drag) to determine any potential improvements. This study could be made in combination with a better understanding of the lift-induced drag suggested in the theoretical part of the perspectives.

Wind-tunnel Tests. CFD is essentially the only tool for the aerothermopropulsive performance assessment of civil aircraft in the preliminary design phase. However, as the overall design is better defined, experimental wind-tunnel testing provide additional valuable information. Application of the proposed formulation for wind-tunnel measurement should be considered. At low speed, considering the thermal aspects to be negligible, no additional equipment should be required. In the compressible range however, measurements of both the static and total temperatures are desirable.

Boundary-Layer Ingestion Concept. One of the key aspects of the formulation is its ability to evaluate the overall performance of an aircraft with a propulsion system ingesting a boundary-layer. This concept is currently investigated through several internal projects at ONERA among the project which constituted the framework of the present thesis. An innovative architecture has been developed by WIART (ONERA), see Fig. 5-1, for which the post-processing code *ffx* should demonstrate its full potential.
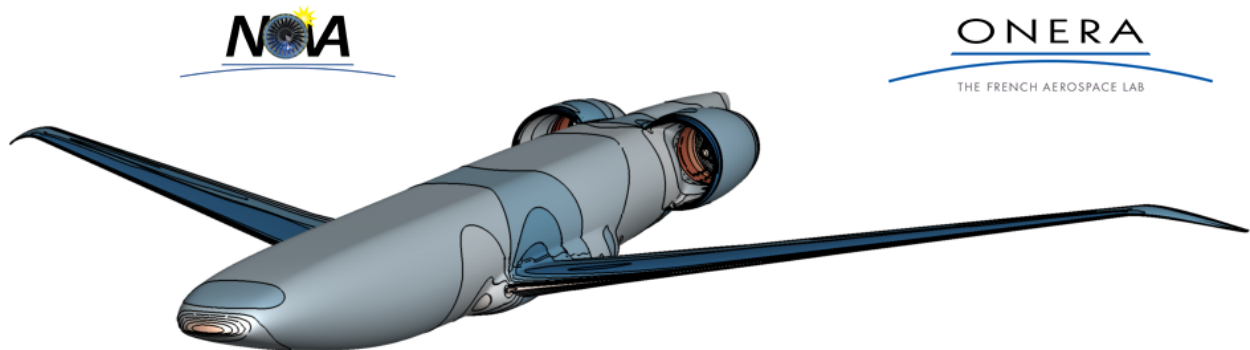
Figure 5-1: ONERA Project: overview of the aircraft with boundary layer ingestion, image credit WIART (ONERA).

Propulsion Systems. The literature review emphasized that the greatest benefit of the exergy approach in aerospace has been observed both historically and recently for the analysis of propulsion systems. As a consequence, application of the exergy balance for a propulsion system at a component-level as proposed by DENTON [44] could provide a more consistent framework for an effective design.

Corner Flows. As suggested by SATO [146], the investigation of a configuration with intersections such as wing/fuselage junctions could provide valuable information and replace the performance estimation currently based on empirical correlations. It was also reported by ALABI *et al.* that the thermal anergy in this region was much higher than in the remaining part of the flow [6]. An exergy point of view could provide additional information as to the improvement of this region responsible for interference drag.

Appendix A

Theoretical Appendices

A.1   Drag/thrust Bookkeeping Methodology

In a simple approach, fuel is consumed by the engine to produce a forward force, called *thrust*, which makes it possible to gain speed, and as a consequence, to produce lift. The amount of thrust needed is directly dependent on how much the aircraft resists to move forward due to the aerodynamic force called *drag*. Drag is the heart of the aerodynamic design, under the responsibility of the airframe manufacturer, while thrust is the engine manufacturer's task.

A.1.1   A Few Examples of Drag Performance

Many examples of the consequence of drag variations are found in the literature which show the importance of the field:

- A one percent increase in the lift-to-drag ratio (L/D) during takeoff is equivalent to a 2,800 lb (1,270 kg) increase in payload for a generic twin engine subsonic transport airplane on a long-range mission or approximately 200 lb (90 kg) in payload (or 1 passenger) per drag count (CD = 0.0001) [173].

- An average slope of approximately 18,750 lb (8,500 kg) in takeoff weight per drag count is found for a supersonic civil transport airplane [173].

- A 1% drag reduction can have dramatic implications:

  - It would save 4,000,000 liters of fuel over the lifetime of a military large cargo aircraft [8].

  - For the giant A380, it corresponds to 1.6 tonnes and roughly to 16 more passengers for a given trip [8].

  - For the C-5 in cruise configuration, it is equivalent to 0.40% of the total drag and to a reduction in payload of 1,000 lb (450 kg) for the design mission. [173].

A.1.2   Requirements for Drag/Thrust Bookeeping

Most textbooks focusing on aircraft design tackle the drag and thrust analyses in two distinct chapters [9, 77, 138]. The challenge faced by their clear definition is often eluded.

In 1979, the Ministry-Industry Drag Analysis Panel (MIDAP) Study Group of the Advisory Group for Aerospace Research & Development (AGARD) defined the basic requirements for a practical bookkeeping system [157]:

1. It must be free from ambiguity.

2. It must, so far as possible, provide for the separate study of engine and airframe performance by the respective manufacturers, both in preliminary paper projects and in any subsequent model and/or flight testing.

3. It must include clear definition of the interfaces where the engine and airframe responsibilities meet, and facilitate a proper understanding of any zones where responsibilities overlap.

4. It must assist in planning model and flight testing in such a way as to provide the information required for design and performance evaluation at minimum total cost.

5. It must recognize practical limitations in experimental and theoretical techniques.

A.1.3 Thrust Definitions

One could expect a unique definition of thrust such as being the force applied by the propulsion system to the airframe. However, this definition is not really helpful in the analysis and in fact, the thrust of an aircraft propulsion system may be defined as *the change of the integrated momentum impulse plus the integrated viscous stresses between the entry and exit stations*. There are at least three possibilities for the definition of these interfaces, and hence three corresponding thrusts. The usefulness of the various definitions is strongly influenced by practical considerations. The presentation given here follows the one given in [157].
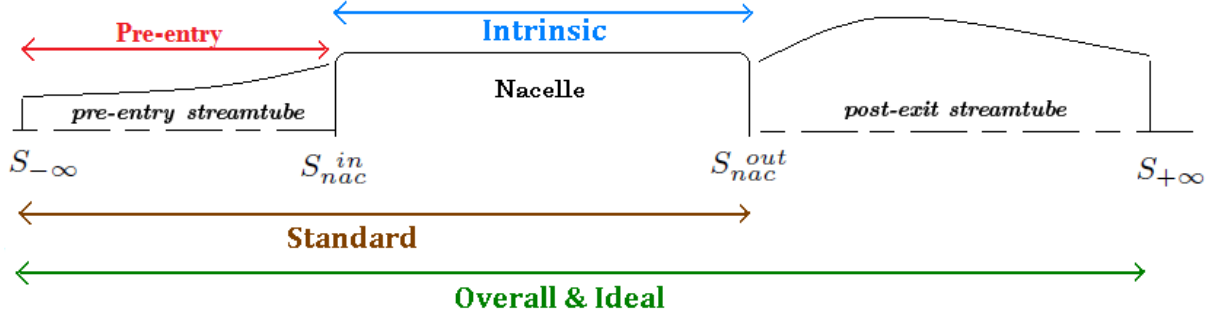
Figure A-1: Three Net Thrusts Representation.

A.1.3.1 Intrinsic Net Thrust

At first sight it might seem appropriate to locate the interfaces at the inlet and outlet of the nacelle. This defines the *intrinsic net thrust* which is the actual thrust on the internal nacelle surfaces.

$$T_{int} = -\int_{S_{nac}^{in}} \left[\rho u(\mathbf{V} \cdot \mathbf{n}) + (p - p_\infty)n_x - \bar{\bar{\tau}} \cdot \mathbf{n}\right] \, \mathrm{d}\mathcal{S} - \int_{S_{nac}^{out}} \left[\rho u(\mathbf{V} \cdot \mathbf{n}) + (p - p_\infty)n_x - \bar{\bar{\tau}} \cdot \mathbf{n}\right] \, \mathrm{d}\mathcal{S} \quad \text{(A.1)}$$

In practice however, this is not a convenient definition because thrust is then strongly dependent on intake geometry. This means that the engine manufacturer would not be able to express performance in a compact way applicable to all installations. An alternative entry interface could be the engine face, but again in this case, thrust would be very dependent on intake conditions. Moreover, it may be difficult to measure the stream force at this station since the flow is often non-uniform and unsteady.

A.1.3.2 Standard Net Thrust

A far more convenient entry interface is the undisturbed freestream located at upstream *infinity*, *i.e.* at station $-\infty$, where $p = p_\infty$ and the fluid can be considered inviscid ($\bar{\bar{\tau}} = \bar{\bar{0}}$). In this case, the *standard net thrust* is defined:

$$T_{std} = -\int_{S_{-\infty}} \rho u(\mathbf{V} \cdot \mathbf{n}) \, \mathrm{d}\mathcal{S} - \int_{S_{nac}^{out}} \left[\rho u(\mathbf{V} \cdot \mathbf{n}) + (p - p_\infty)n_x - \bar{\bar{\tau}} \cdot \mathbf{n}\right] \, \mathrm{d}\mathcal{S} \quad \text{(A.2)}$$

This corresponds to what the engine manufacturer usually define as the *total thrust* of the engine. This interface satisfies all the basic bookkeeping requirements because it can be defined precisely in terms of aircraft velocity and is the only possible upstream station free from any disturbance by the aircraft. Standard net thrust, forms the basis of most thrust/drag accounting systems and many engine brochures. Note that the difference between the standard net thrust and the intrinsic net thrust is called the *pre-entry thrust*.

A.1.3.3   Overall Net Thrust

The exit interface could be located at downstream *infinity* where $p = p_\infty$. The fluid cannot be considered inviscid due to momentum diffusion. This corresponds to the definition of the net *overall* or *fully-expanded* *thrust*.

$$T_{overall} = -\int_{S_{-\infty}} \rho u (\mathbf{V} \cdot \mathbf{n})\, \mathrm{d}\mathcal{S} - \int_{S_{+\infty}} \left[\rho u (\mathbf{V} \cdot \mathbf{n}) - \bar{\bar{\tau}} \cdot \mathbf{n} \right]\, \mathrm{d}\mathcal{S} \tag{A.3}$$

The post-exit thrust component would require integrating the actual forces acting in the jet expansion. Assuming that the jet expansion is isentropic, although representing an *ideal* case gives the *ideal net thrust*:

$$T_{ideal} = -\dot{m}(V_{+\infty,is} - V_{-\infty}) \tag{A.4}$$

Note that these thrust definitions rely on the clear identification of the streamtube of air flowing through the engine.

A.2   Aircraft Force Balance

A force balance of a flying aircraft is the result of taking into account the mechanical equilibrium of the airplane. This force balance is made in the Earth reference frame in which we consider the aircraft as a mass moving at velocity V_∞. We assume that the thrust and the drag act in the flight path direction; the net resultant axial force being noted F_x. A popular result is that a general force balance [85, 112] yields:

$$\boxed{F_x V_\infty = (T - D)V_\infty = W \frac{\mathrm{d}}{\mathrm{d}t}\left(H_A + \frac{V_A^2}{2} \right) = W\dot{\Gamma}} \tag{A.5}$$

where we consider the aircraft weight W to be constant, H_A and V_A are respectively the aircraft altitude and speed. As a consequence, if more thrust T is provided than drag D, we have that $F_x V_\infty > 0$. This *excess power* represents a potential for a gain in aircraft mechanical energy, *i.e.* an increase in height and/or velocity. If $F_x = 0$, the propulsion system provides as much thrust as the drag of the configuration and the aircraft is in mechanical equilibrium[1], $W\dot{\Gamma} = 0$ and there is no potential for acceleration.

A.3   Vortex Drag Power for Inviscid Flows

Let us examine flow over a three-dimensional wing and consider a theoretical case of a fluid that is: inviscid, calorically perfect, and incompressible. As a consequence, the exergy-based drag-power relation Eq. (2.71) reduces to:

$$DV_\infty = \dot{\mathcal{E}}_m \tag{A.6}$$

Choosing the outer boundary $\mathcal{S}_O$ as being only a *Trefftz* plane[2] $\mathcal{TP}$ yields the following expression for $\dot{\mathcal{E}}_m$:

$$\dot{E}_u + \dot{E}_v + \dot{E}_p = \int_{\mathcal{S}_{\mathcal{TP}}} \frac{1}{2}\rho \left(u^2 + v^2 + w^2 \right) (V_\infty + u)\, \mathrm{d}\mathcal{S} + \int_{\mathcal{S}_{\mathcal{TP}}} (p - p_\infty) u\, \mathrm{d}\mathcal{S} \tag{A.7}$$

Inserting the pressure defect in low-speed flow according to the *Bernoulli* relation:

$$p - p_\infty = -\frac{1}{2}\rho(V^2 - V_\infty^2) = -\rho V_\infty u - \frac{1}{2}\rho \left(u^2 + v^2 + w^2 \right) \tag{A.8}$$

---

[1] We consider that all forces have the same point of application, that point being the aircraft center of gravity, so that there is no torque imbalance.

[2] On which $\mathbf{V} \cdot \mathbf{n} = (V_\infty + u)$.

yields the following expression:

$$\dot{\mathcal{E}}_m = \int_{\mathcal{S}_{\mathcal{TP}}} \frac{1}{2}\rho \left(v^2 + w^2 - u^2\right) V_\infty \, d\mathcal{S} \tag{A.9}$$

Similarly, inserting Eq. (A.8) into the far-field drag expression Eq. (2.9b) yields:

$$\mathrm{D}_i V_\infty = \int_{\mathcal{S}_{\mathcal{TP}}} \frac{1}{2}\rho \left(v^2 + w^2 - u^2\right) V_\infty \, d\mathcal{S} \tag{A.10}$$

Comparing Eqs. (A.9 & A.10) proves that, in the conditions of application of BERNOULLI relation, *i.e.* for an adiabatic and inviscid (isentropic) and incompressible flow, $\dot{E}_u + \dot{E}_v + \dot{E}_p$ is equal to the total drag power of an unpowered configuration, *i.e.* the power of the vortex drag.

A.4 Exergy-based Range Equation

This appendix presents the derivation of the exergy-based range equation which is obtained in a very similar manner as for the *Power Balance* method [67]. During the flight, the time rate of change of weight is linked to the time rate of weight of fuel burnt $\dot{W}_f$:

$$-\frac{dW}{dt} = \dot{W}_f \tag{A.11}$$

One can define an *exergy specific fuel consumption ESFC* as:

$$ESFC := \frac{\dot{W}_f}{\dot{\mathcal{E}}_{prop}} \tag{A.12}$$

and therefore re-write Eq. (A.11) as:

$$-\frac{dW}{dt} = ESFC \, \dot{\mathcal{E}}_{prop} \tag{A.13}$$

Considering the aircraft to be in a steady level flight, we have that $W = L$ where L is lift. If we consider adiabatic surfaces, according to Eq. (2.34), we have that $\dot{\mathcal{E}}_{prop} = \dot{\mathcal{A}}^* := \dot{\mathcal{A}}_{tot} + \dot{\mathcal{E}}_{rec}$ is the sum of the anergy generated and all outflows. Therefore, one can write:

$$\dot{\mathcal{E}}_{prop} = \dot{\mathcal{A}}^* = \dot{\mathcal{A}}^* \frac{W}{L} \tag{A.14}$$

and re-write Eq. (A.13) as:

$$-\frac{dW}{dt} = \frac{ESFC}{(L/\dot{\mathcal{A}}^*)} W \tag{A.15}$$

Assuming $L/\dot{\mathcal{A}}^*$ and $ESFC$ to be constant along the flight path, one can write:

$$-\frac{dW}{W} = \frac{ESFC}{(L/\dot{\mathcal{A}}^*)} dt \tag{A.16}$$

and integrate to get a relation of the weight W at a given time t and the initial weight W_0:

$$-\ln\left(\frac{W}{W_0}\right) = \frac{ESFC}{(L/\dot{\mathcal{A}}^*)} (t - 0) \tag{A.17}$$

For the final time t_f of the flight we have, introducing the final weight W_1:

$$t_f = \frac{1}{ESFC} \frac{L}{\dot{\mathcal{A}}^*} \ln\left(\frac{W_0}{W_1}\right) \tag{A.18}$$

Therefore, the (exergy-based) range $\mathcal{R}_\varepsilon$ flown at a given flight velocity V_∞ during the flight time t_f is simply:

$$\mathcal{R}_\varepsilon := V_\infty \times t_f = \frac{1}{ESFC} \frac{L V_\infty}{\dot{\mathcal{A}}^*} \ln\left(\frac{W_0}{W_1}\right) \tag{A.19}$$

which, introducing the non-dimensionalized lift and anergy power coefficients yields:

$$\mathcal{R}_\varepsilon = \frac{1}{ESFC} \left(\frac{CL}{C\dot{\mathcal{A}}^*}\right) \ln\left(\frac{W_0}{W_1}\right) \tag{A.20}$$

or equivalently

$$\mathcal{R}_\varepsilon = \frac{1}{ESFC} \left(\frac{CL}{C\dot{\mathcal{A}}_{tot} + C\dot{\mathcal{E}}_m + C\dot{\mathcal{E}}_{th}}\right) \ln\left(\frac{W_0}{W_1}\right) \tag{A.21}$$

From $ESFC = \dot{W}_f/\dot{\mathcal{E}}_{prop}$ and $\dot{\mathcal{E}}_{prop} = \dot{\mathcal{A}}_{tot} + \dot{\mathcal{E}}_m + \dot{\mathcal{E}}_{th}$, we can also obtain the following condensed form:

$$\mathcal{R}_\varepsilon = \left(\frac{CL}{\dot{W}_f}\right) \ln\left(\frac{W_0}{W_1}\right) \tag{A.22}$$

As the fuel consumption $\dot{W}_f$ tends to zero, the range tends to *infinity*.

A.5 Gibbs Equation in Terms of Stagnation Quantities

This appendix provides the derivation of the GIBBS relation with respect to stagnation pressure and stagnation temperature. Introducing $\rho = p/RT$ into Eq. (2.52) we have:

$$\delta\mathsf{s} = c_v \left[(1-\gamma)\ln\left(\frac{p}{p_\infty}\right) + \gamma\ln\left(\frac{T}{T_\infty}\right)\right] \tag{A.23}$$

Or equivalently:

$$\exp\left(\delta\mathsf{s}/c_v\right) = \left(\frac{p}{p_\infty}\right)^{1-\gamma} \cdot \left(\frac{T}{T_\infty}\right)^{\gamma} \tag{A.24}$$

Using the following stagnation relations:

$$p = \frac{p_i}{\left(1 + \frac{\gamma-1}{2}M^2\right)^{\frac{\gamma}{\gamma-1}}} \tag{A.25a}$$

$$T = \frac{T_i}{\left(1 + \frac{\gamma-1}{2}M^2\right)} \tag{A.25b}$$

where M is the local Mach number and the subscript i denotes stagnation values, Eq. (A.24) can be written as:

$$\exp\left(\delta\mathsf{s}/c_v\right) = \left(\frac{p_i}{p_{i_\infty}}\right)^{1-\gamma} \cdot \left(\frac{T_i}{T_{i_\infty}}\right)^{\gamma} \tag{A.26}$$

To finally get:

$$\exp\left(\delta\mathsf{s}/c_p\right) = \left(\frac{T_i}{T_{i_\infty}}\right) \cdot \left(\frac{p_i}{p_{i_\infty}}\right)^{\frac{1-\gamma}{\gamma}} \tag{A.27}$$

A.6   Nearby-Strong Shock Losses

As described in the literature review (p. 8), DRELA [49] originally defined the losses associated with *nearby-strong shocks* as given by the stagnation pressure drop across the wave surface:

$$\dot{E}_w^o := \int_{\mathcal{S}_w} \left(p_i - p_{i_\infty}\right) (\mathbf{V} \cdot \hat{\mathbf{n}}) \, \mathrm{d}\mathcal{S} \tag{A.28}$$

The connection between the two expressions is provided by the GIBBS equation expressed in terms of stagnation quantities, see appendix A.5 (p. 182):

$$\exp\left(\delta\mathsf{s}/c_p\right) = \left(\frac{T_i}{T_{i_\infty}}\right) \cdot \left(\frac{p_i}{p_{i_\infty}}\right)^{\frac{1-\gamma}{\gamma}} \tag{A.29}$$

Considering the shock wave as an adiabatic and inviscid phenomenon means that here is no stagnation enthalpy change across the shock wave. Eq. (A.29) is therefore equivalent to:

$$\exp\left(\delta\mathsf{s}/c_p\right) = \left(1 + \frac{(p_i - p_{i_\infty})}{p_{i_\infty}}\right)^{\frac{1-\gamma}{\gamma}} \tag{A.30}$$

which, applying the logarithm and assuming small perturbations in stagnation pressure, leads to:

$$\delta\mathsf{s}/c_p \simeq \frac{1-\gamma}{\gamma} \frac{(p_i - p_{i_\infty})}{p_{i_\infty}} \tag{A.31}$$

which, can be manipulated to isolate the entropy as:

$$\delta\mathsf{s} \simeq -\frac{R}{p_{i_\infty}}(p_i - p_{i_\infty}) \tag{A.32}$$

Multiplying this relation by $\rho(\mathbf{V} \cdot \hat{\mathbf{n}})$ and integrating over the wave surface $\mathcal{S}_w$ yields the wave anergy $\dot{\mathcal{A}}_w$ (left-hand side) as well as the following *alternative* stagnation pressure-based loss estimation of transonic shock waves:

$$\dot{\mathcal{A}}_w \simeq \dot{E}_w^a := \int_{\mathcal{S}_w} \rho\frac{R}{p_{i_\infty}}(p_i - p_{i_\infty}) (\mathbf{V} \cdot \hat{\mathbf{n}}) \, \mathrm{d}\mathcal{S} \tag{A.33}$$

CFD computations shows that Eq. (A.33) is much more accurate than Eq. (A.28).

A.7 Alternative Expression for the Effective Viscous Dissipation

From White [179], another way to compute Φ, using only squared terms is:

$$(\bar{\bar{\tau}} \cdot \nabla) \cdot \mathbf{V} = \left[\begin{pmatrix} \tau_{xx} & \tau_{xy} & \tau_{xz} \\ \tau_{yx} & \tau_{yy} & \tau_{yz} \\ \tau_{zx} & \tau_{zy} & \tau_{zz} \end{pmatrix} \cdot \begin{pmatrix} \frac{\partial}{\partial x} \\ \frac{\partial}{\partial y} \\ \frac{\partial}{\partial z} \end{pmatrix} \right] \cdot \begin{pmatrix} u \\ v \\ w \end{pmatrix}$$

(A.34)

$$= \tau_{xx}\frac{\partial u}{\partial x} + \tau_{xy}\frac{\partial u}{\partial y} + \tau_{xz}\frac{\partial u}{\partial z} + \tau_{yx}\frac{\partial v}{\partial x} + \tau_{yy}\frac{\partial v}{\partial y} + \tau_{yz}\frac{\partial v}{\partial z} + \tau_{zx}\frac{\partial w}{\partial x} + \tau_{zy}\frac{\partial w}{\partial y} + \tau_{zz}\frac{\partial w}{\partial z}$$

$$= \tau_{xx}\frac{\partial u}{\partial x} + \tau_{yy}\frac{\partial v}{\partial y} + \tau_{zz}\frac{\partial w}{\partial z} + \tau_{xy}\left(\frac{\partial u}{\partial y} + \frac{\partial v}{\partial x}\right) + \tau_{xz}\left(\frac{\partial u}{\partial z} + \frac{\partial w}{\partial x}\right) + \tau_{yz}\left(\frac{\partial v}{\partial z} + \frac{\partial w}{\partial y}\right)$$

With

$$\tau_{xx}\frac{\partial u}{\partial x} = \frac{2}{3}\mu\left(2\frac{\partial u}{\partial x} - \frac{\partial v}{\partial y} - \frac{\partial w}{\partial z}\right)\frac{\partial u}{\partial x} = \frac{2}{3}\mu\left[2\left(\frac{\partial u}{\partial x}\right)^2 - \left(\frac{\partial v}{\partial y}\frac{\partial u}{\partial x} + \frac{\partial w}{\partial z}\frac{\partial u}{\partial x}\right)\right]$$

$$\tau_{yy}\frac{\partial v}{\partial y} = \frac{2}{3}\mu\left(2\frac{\partial v}{\partial y} - \frac{\partial w}{\partial z} - \frac{\partial u}{\partial x}\right)\frac{\partial v}{\partial y} = \frac{2}{3}\mu\left[2\left(\frac{\partial v}{\partial y}\right)^2 - \left(\frac{\partial w}{\partial z}\frac{\partial v}{\partial y} + \frac{\partial u}{\partial x}\frac{\partial v}{\partial y}\right)\right]$$

$$\tau_{zz}\frac{\partial w}{\partial z} = \frac{2}{3}\mu\left(2\frac{\partial w}{\partial z} - \frac{\partial u}{\partial x} - \frac{\partial v}{\partial y}\right)\frac{\partial w}{\partial z} = \frac{2}{3}\mu\left[2\left(\frac{\partial w}{\partial z}\right)^2 - \left(\frac{\partial u}{\partial x}\frac{\partial w}{\partial z} + \frac{\partial v}{\partial y}\frac{\partial w}{\partial z}\right)\right]$$

$$\tau_{xy}\left(\frac{\partial u}{\partial y} + \frac{\partial v}{\partial x}\right) = \mu\left(\frac{\partial u}{\partial y} + \frac{\partial v}{\partial x}\right)\left(\frac{\partial u}{\partial y} + \frac{\partial v}{\partial x}\right) = \mu\left(\frac{\partial u}{\partial y} + \frac{\partial v}{\partial x}\right)^2$$

$$\tau_{xz}\left(\frac{\partial u}{\partial z} + \frac{\partial w}{\partial x}\right) = \mu\left(\frac{\partial u}{\partial z} + \frac{\partial w}{\partial x}\right)\left(\frac{\partial u}{\partial z} + \frac{\partial w}{\partial x}\right) = \mu\left(\frac{\partial u}{\partial z} + \frac{\partial w}{\partial x}\right)^2$$

$$\tau_{yz}\left(\frac{\partial v}{\partial z} + \frac{\partial w}{\partial y}\right) = \mu\left(\frac{\partial v}{\partial z} + \frac{\partial w}{\partial y}\right)\left(\frac{\partial v}{\partial z} + \frac{\partial w}{\partial y}\right) = \mu\left(\frac{\partial v}{\partial z} + \frac{\partial w}{\partial y}\right)^2$$

(A.35)

So that, rearranging the three first terms to make $a^2 + b^2 + c^2 + 2ab + 2bc + 2ac = (a + b + c)^2$ appear:

$$\tau_{xx}\frac{\partial u}{\partial x} + \tau_{yy}\frac{\partial v}{\partial y} + \tau_{zz}\frac{\partial w}{\partial z}$$

$$= \frac{2}{3}\mu\left[2\left(\frac{\partial u}{\partial x}\right)^2 + 2\left(\frac{\partial v}{\partial y}\right)^2 + 2\left(\frac{\partial w}{\partial z}\right)^2\right] - \frac{2}{3}\mu\left[2\left(\frac{\partial u}{\partial x}\frac{\partial v}{\partial y}\right) + 2\left(\frac{\partial u}{\partial x}\frac{\partial w}{\partial z}\right) + 2\left(\frac{\partial v}{\partial y}\frac{\partial w}{\partial z}\right)\right]$$

$$= -\frac{2}{3}\mu\left[-3\left(\frac{\partial u}{\partial x}\right)^2 - 3\left(\frac{\partial v}{\partial y}\right)^2 - 3\left(\frac{\partial w}{\partial z}\right)^2 + \left(\frac{\partial u}{\partial x}\right)^2 + \left(\frac{\partial v}{\partial y}\right)^2 + \left(\frac{\partial w}{\partial z}\right)^2\right]$$

$$\qquad - \frac{2}{3}\mu\left[2\left(\frac{\partial u}{\partial x}\frac{\partial v}{\partial y}\right) + 2\left(\frac{\partial u}{\partial x}\frac{\partial w}{\partial z}\right) + 2\left(\frac{\partial v}{\partial y}\frac{\partial w}{\partial z}\right)\right]$$

(A.36)

$$= \mu\left[2\left(\frac{\partial u}{\partial x}\right)^2 + 2\left(\frac{\partial v}{\partial y}\right)^2 + 2\left(\frac{\partial w}{\partial z}\right)^2\right]$$

$$\qquad - \frac{2}{3}\mu\left[\left(\frac{\partial u}{\partial x}\right)^2 + \left(\frac{\partial v}{\partial y}\right)^2 + \left(\frac{\partial w}{\partial z}\right)^2 + 2\left(\frac{\partial u}{\partial x}\frac{\partial v}{\partial y}\right) + 2\left(\frac{\partial u}{\partial x}\frac{\partial w}{\partial z}\right) + 2\left(\frac{\partial v}{\partial y}\frac{\partial w}{\partial z}\right)\right]$$

$$= \mu\left[2\left(\frac{\partial u}{\partial x}\right)^2 + 2\left(\frac{\partial v}{\partial y}\right)^2 + 2\left(\frac{\partial w}{\partial z}\right)^2\right] - \frac{2}{3}\mu\left[\frac{\partial u}{\partial x} + \frac{\partial v}{\partial y} + \frac{\partial w}{\partial z}\right]^2$$

And finally, inserting the results of Eqs. (A.35 & A.36) into Eq. (A.34) leads to:

$$(\bar{\bar{\tau}} \cdot \nabla) \cdot \mathbf{V} = \mu \left[2\left(\frac{\partial u}{\partial x}\right)^2 + 2\left(\frac{\partial v}{\partial y}\right)^2 + 2\left(\frac{\partial w}{\partial z}\right)^2 + \left(\frac{\partial u}{\partial y} + \frac{\partial v}{\partial x}\right)^2 + \left(\frac{\partial u}{\partial z} + \frac{\partial w}{\partial x}\right)^2 + \left(\frac{\partial v}{\partial z} + \frac{\partial w}{\partial y}\right)^2 \right]$$
$$- \frac{2}{3}\mu \left[\frac{\partial u}{\partial x} + \frac{\partial v}{\partial y} + \frac{\partial w}{\partial z}\right]^2 \tag{A.37}$$

The $-2\mu/3$ term in front of the last squared term ensures the viscous dissipation to be strictly positive. It has been introduced by G. G. STOKE in 1845 and has no other rational explanation than having found to be experimentally correct. It is considered as *an excellent approximation* [147].

A.8 OSWATITSCH's Development without Small Perturbations Assumption

The development hereafter[3] is largely inspired from the one made by OSWATITSCH in 1956 [118]. It consists in replacing both integrands of the far field drag expression Eq. (2.10) in two steps:

$$DV_\infty = -\int_{\mathcal{S}_O} \left[\rho\, u V_\infty\, (\mathbf{V} \cdot \mathbf{n}) + (p - p_\infty)(\mathbf{V}_\infty \cdot \mathbf{n})\right]\, \mathrm{d}\mathcal{S} \tag{A.38}$$

First, note that:

$$u V_\infty = \frac{1}{2}\left[(V^2 - V_\infty^2) - u^2 - v^2 - w^2\right] \tag{A.39}$$

which, inserted into Eq. (A.38) yields

$$\begin{aligned} DV_\infty &= -\int_{\mathcal{S}_O} \frac{1}{2}\rho\left[(V^2 - V_\infty^2) - u^2 - v^2 - w^2\right]\,(\mathbf{V} \cdot \mathbf{n})\, \mathrm{d}\mathcal{S} - \int_{\mathcal{S}_O}(p - p_\infty)\,(\mathbf{V}_\infty \cdot \mathbf{n})\, \mathrm{d}\mathcal{S} \\ &= \dot{E}_u + \dot{E}_v - \int_{\mathcal{S}_O}\frac{1}{2}\rho(V^2 - V_\infty^2)\,(\mathbf{V} \cdot \mathbf{n})\, \mathrm{d}\mathcal{S} - \int_{\mathcal{S}_O}(p - p_\infty)\,(\mathbf{V}_\infty \cdot \mathbf{n})\, \mathrm{d}\mathcal{S} \end{aligned} \tag{A.40}$$

Adding and subtracting $\int_{\mathcal{S}_O}(p - p_\infty)\,(\mathbf{V} \cdot \mathbf{n})\, \mathrm{d}\mathcal{S}$ gives

$$DV_\infty = \dot{E}_u + \dot{E}_v + \int_{\mathcal{S}_O}\frac{1}{2}\rho(V^2 - V_\infty^2)\,(\mathbf{V} \cdot \mathbf{n})\, \mathrm{d}\mathcal{S} + \dot{E}_p - \int_{\mathcal{S}_O}(p - p_\infty)\,(\mathbf{V} \cdot \mathbf{n})\, \mathrm{d}\mathcal{S} \tag{A.41}$$

Secondly, we invoke the GIBBS equation (2.18) to rearrange the last integral of Eq. (A.41):

$$T\, \mathrm{d}\mathsf{s} = \mathrm{d}h - \frac{1}{\rho}\, \mathrm{d}p \tag{A.42}$$

We consider the case where the surface enclosing the body is sufficiently far from it that we can neglect viscous stresses and consider that all local flow properties are near the freestream values. We can therefore linearize Eq. (A.42) and get:

$$T_\infty\,(\mathsf{s} - \mathsf{s}_\infty) = (h - h_\infty) - \frac{1}{\rho_\infty}\,(p - p_\infty) \tag{A.43}$$

and isolate the pressure terms to get:

$$(p - p_\infty) = \rho_\infty(h - h_\infty) - \rho_\infty T_\infty\,(\mathsf{s} - \mathsf{s}_\infty) \tag{A.44}$$

---

[3]With corrections from A. Bonnet (ISAE).

Inserting Eq. (A.44) into Eq. (A.41) yields

$$
\begin{aligned}
DV_\infty = \dot{E}_u + \dot{E}_v + \dot{E}_p &- \int_{\mathcal{S}_O} \frac{1}{2}\rho(V^2 - V_\infty^2)\,(\mathbf{V}\cdot\mathbf{n})\,\mathrm{d}\mathcal{S} \\
&- \int_{\mathcal{S}_O} \rho_\infty \delta h\,(\mathbf{V}\cdot\mathbf{n})\,\mathrm{d}\mathcal{S} + \int_{\mathcal{S}_O} \rho_\infty T_\infty\,\delta\mathsf{s}\,(\mathbf{V}\cdot\mathbf{n})\,\mathrm{d}\mathcal{S}
\end{aligned}
\tag{A.45}
$$

which, considering $\rho \simeq \rho_\infty$, can be rearranged to read:

$$
DV_\infty = \dot{E}_u + \dot{E}_v + \dot{E}_p - \int_{\mathcal{S}_O} \rho_\infty\,\delta h_i\,(\mathbf{V}_\infty\cdot\mathbf{n})\,\mathrm{d}\mathcal{S} + T_\infty \int_{\mathcal{S}_O} \rho_\infty\,\delta\mathsf{s}\,(\mathbf{V}_\infty\cdot\mathbf{n})\,\mathrm{d}\mathcal{S}
\tag{A.46}
$$

In viscous flows without powered engines (and with adiabatic surfaces), the second integral is usually very negligible [64, 118], so that for airframe cases we have:

$$
DV_\infty = \dot{E}_u + \dot{E}_v + \dot{E}_p + T_\infty \int_{\mathcal{S}_O} \rho_\infty\,\delta\mathsf{s}\,(\mathbf{V}\cdot\mathbf{n})\,\mathrm{d}\mathcal{S}
\tag{A.47}
$$

which, can be rewritten by invoking the divergence therorem as:

$$
\boxed{DV_\infty = \dot{E}_u + \dot{E}_v + \dot{E}_p + \dot{\mathcal{A}}_\phi + \dot{\mathcal{A}}_{\nabla T} + \dot{\mathcal{A}}_w}
\tag{A.48}
$$

This derivation is simply made to highlight the presence of the three mechanical terms $\dot{E}_u$, $\dot{E}_v$ and $\dot{E}_p$.

Appendix B

Numerical Appendices

B.1 Entropy Flow Field over a NACA 0012
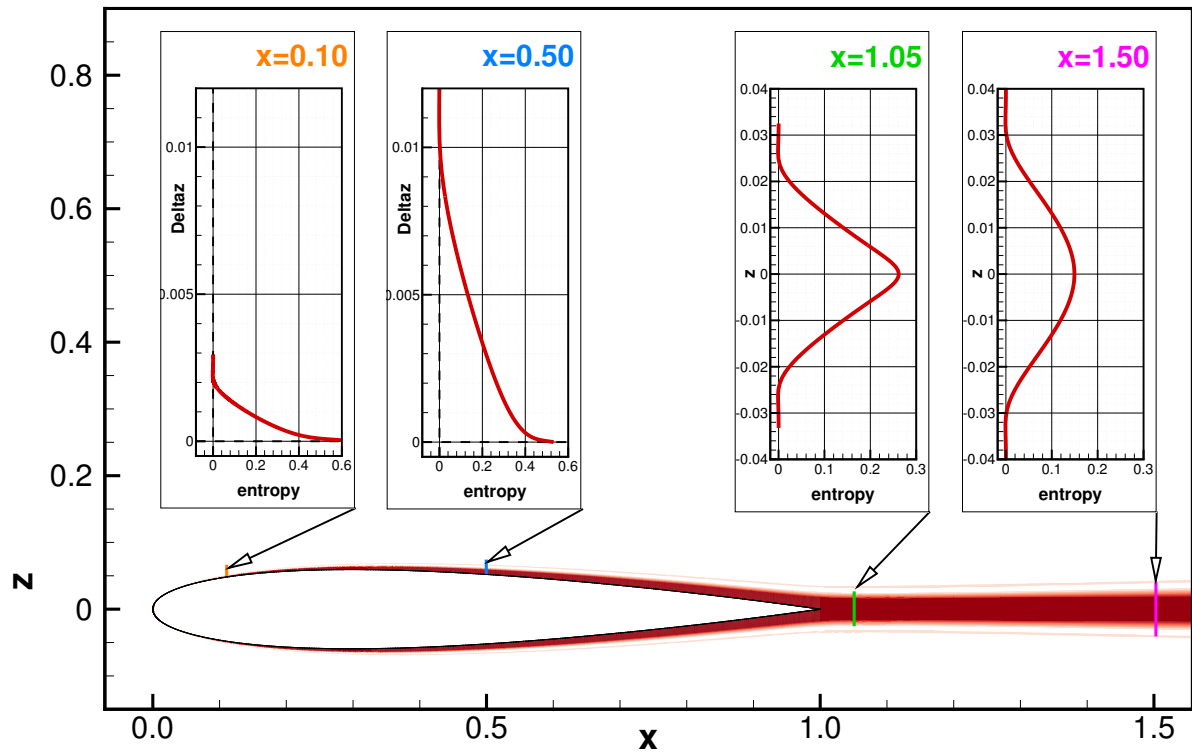
Figure B-1: 2D NACA 0012 Airfoil in a subsonic: entropy flow field. Medium mesh.
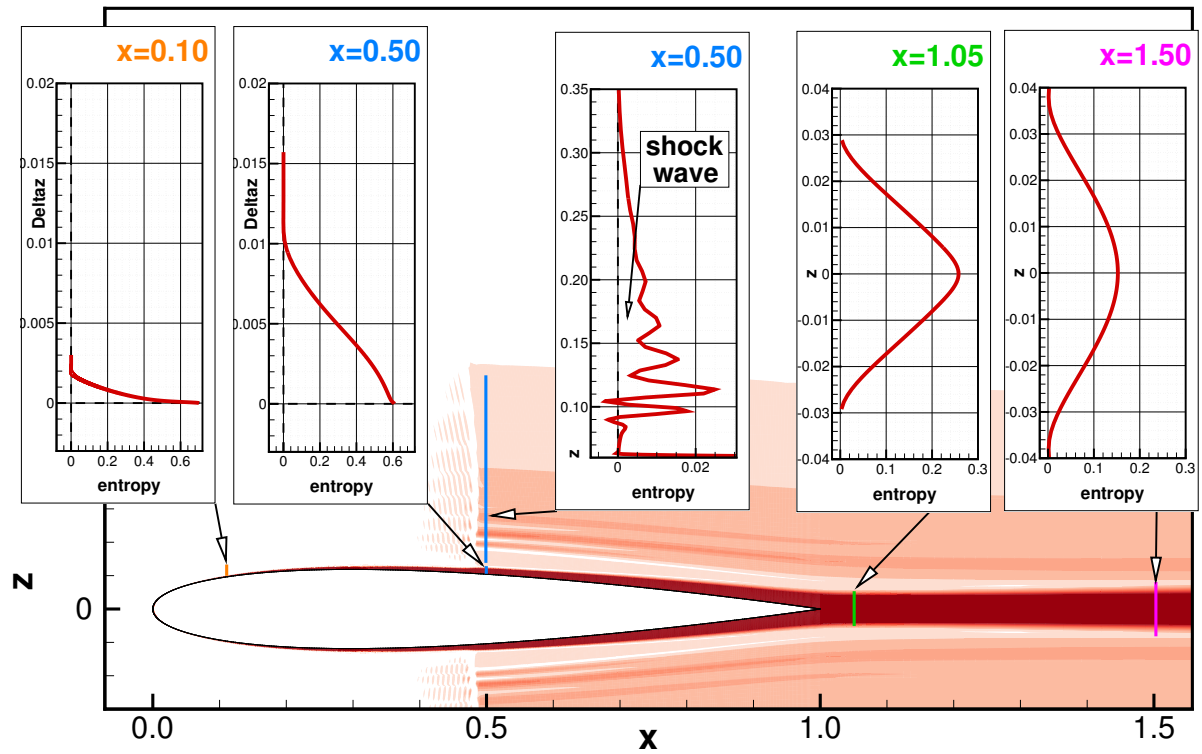
Figure B-2: 2D NACA 0012 Airfoil in a transonic flow: entropy flow field. Medium mesh.

B.2 Validation for the Lift-induced Vortices in 3D Subsonic Flows

The objective of this test case is to investigate only the lift-induced vortices through the analysis of an inviscid and calorically-perfect subsonic flow over a three-dimensional wing. After some theoretical and numerical considerations regarding the grid convergence study, momentum-based drag prediction are given with a comparison to a theoretical reference value given by a theoretically elliptical aerodynamic loading. Then, for the exergy-based formulation, a wake analysis is first performed to determine the most-suitable chordwise position of the transverse plane. Once the control volume is defined, the drag prediction is provided with additional comments on the mechanical and thermal exergy outflows.

B.2.1 Theoretical and Numerical Considerations

B.2.1.1 Theoretical Considerations

For an inviscid and calorically perfect fluid, there is neither viscous dissipation nor thermal mixing. Also, considering a subsonic flow, there is no shock wave. As a consequence, the flow is isentropic and there is no anergy generation within this flow field meaning that Eq. (2.71) reduces to:

$$DV_\infty = \dot{\mathcal{E}}_m + \dot{\mathcal{E}}_{th} + \cancel{\dot{\mathcal{A}}_\phi} + \cancel{\dot{\mathcal{A}}_{\nabla T}} + \cancel{\dot{\mathcal{A}}_w} \tag{B.1}$$

Also, according to the indirect thermal exergy definition: $\dot{\mathcal{E}}_{th}^i = \cancel{\dot{\mathcal{A}}_\phi} - \cancel{\dot{\mathcal{A}}_{\nabla T}} + \dot{E}_{PV}$, meaning that the thermocompressible exergy is here only due to compressibility effects and should be zero for a perfectly incompressible flow. If the indirect method is used, then Eq. (B.1) is equal to the *Power Balance* method of DRELA [49].

In addition to the two momentum-based methods, comparison will be made to a *reference* value given by the theoretical elliptical loading of the wing:

$$CD_{ref} = \frac{CL^2}{\pi AR} \tag{B.2}$$

where CL is the lift coefficient and AR is the wing aspect ratio.

B.2.1.2 Numerical Considerations

The wing geometry is based on the NACA 0012 Airfoil provided by VASSBERG and JAMESON [176]. The wing has been generated by DESTARAC to provide a theoretical elliptical (aerodynamic) loading. Starting from an initial medium monoblock-grid, two additional densities have been generated by dividing and refining the number of nodes by two in each direction: $(n_i, n_j, n_k) = (64, 64, 32)_{coarse}$ and $(256, 256, 128)_{fine}$. These three meshes contain respectively 131,000, 1 million and 8.4 millions elements, see Table B.1. All O-type meshes extend 150 chords in all three dimensions as shown in Fig. B-3 for the coarse and fine grids.

Name	n_i	n_j	n_k	Elements	Extension
Coarse	64	64	32	0.13 M	150 c
Medium	128	128	64	1.05 M	150 c
Fine	256	256	128	8.39 M	150 c

Table B.1: 3D elliptical Wing in inviscid and subsonic flows at $6\,\deg$ incidence: characteristics of the three monoblock structured grids.

A low-subsonic flow ($M_\infty = 0.20$) and a high-subsonic flow ($M_\infty = 0.50$) are considered with an incidence set at $\alpha = 6\,\deg$. Artificial viscosity was introduced in the *Jameson* scheme: $\chi_2 = 0.5$ and

(a) Coarse grid.
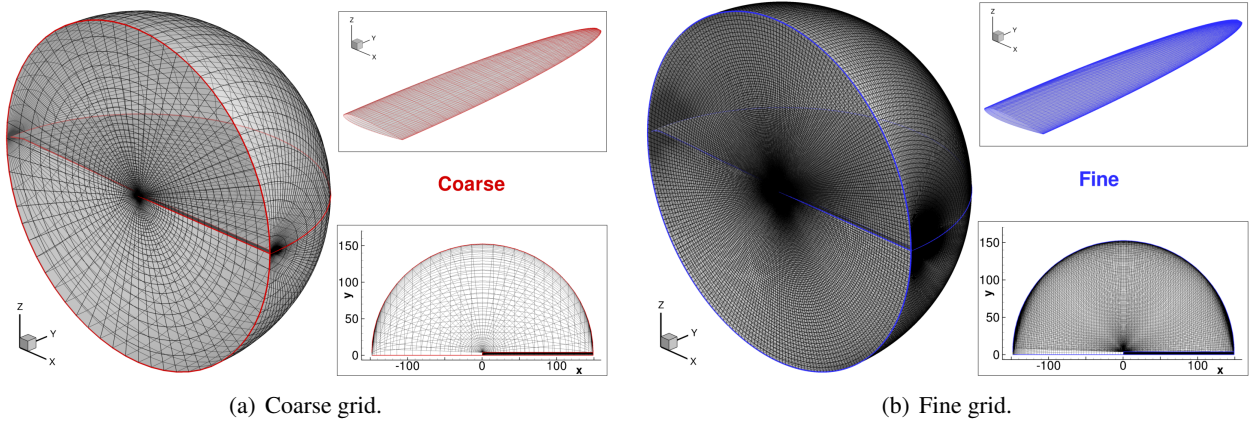
(b) Fine grid.

Figure B-3: 3D elliptical Wing in inviscid and subsonic flows at $6\,\mathrm{deg}$ incidence: coarse and fine grids with 150 root chords extension and wing surface discretization.

$\chi_4 = 0.008$. The convergence is reached when the near-field drag coefficient has variations lower than 0.0001 drag count, see Fig. B-4a. Simultaneously, the residuals of the energy equation reaches a plateau, see Fig. B-4b.

(a)

(b)
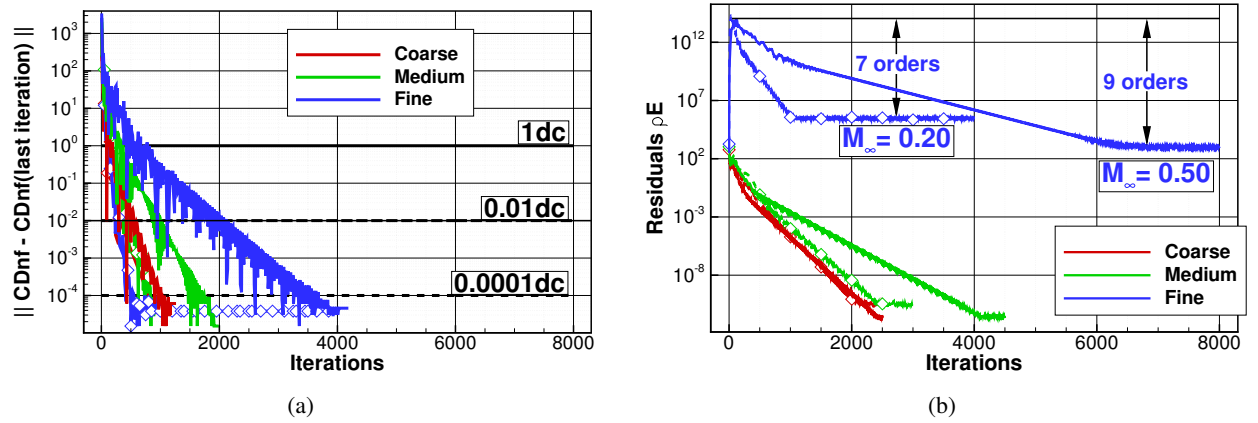
Figure B-4: 3D elliptical Wing in inviscid and subsonic flows at $6\,\mathrm{deg}$ incidence: convergence history with grid refinement.

While the coarse and medium grids provide a convergence to *machine zero*, the fine grid (only) allows for a 7- and 9-orders residuals reduction at respectively $M_\infty = 0.20$ and $M_\infty = 0.50$.

B.2.2 Grid Convergence Study

The accuracy of the implemented exergy-based formulation is compared to the two more conventional drag formulations based on momentum considerations.

B.2.2.1 Momentum-based Drag Methods

Results of the two momentum-based methods are given in Table B.2. In this case, the near-field drag coefficient reduces to the pressure term $CD_{nf} = CD_p$ while the far-field drag coefficient reduces to the lift-induced term $CD_{ff} = CD_i$. As CL is flow-dependent, there is one value of CD_{ref} for each grid[1].

---

[1]The aspect ratio $AR \simeq 9.6$ is also weakly dependent on the wing surface discretization.

				$ffd72$		
M_∞	Mesh	CL	CD_{ref}	CD_{nf}	CD_{ff}	CD_{sp}
	Coarse	0.554	**101.64**	157.01	100.28	56.73
0.20	Medium	0.560	**103.59**	119.54	103.03	16.51
	Fine	0.562	**104.14**	108.27	104.22	4.13
	Coarse	0.596	**117.33**	219.50	115.95	103.56
0.50	Medium	0.615	**125.05**	156.98	124.51	32.47
	Fine	0.624	**128.62**	137.07	128.62	8.45

Table B.2: 3D elliptical Wing in inviscid and subsonic flows at $6\deg$ incidence: near-field and far-field drag coefficients expressed in drag counts (10^{-4}) with grid refinement.

The near-field drag method gives a coefficient that exhibits extremely large variations between the coarse and fine grids: -45% and -60% at respectively M_∞ = 0.20 and M_∞ = 0.50. Even on the finest mesh it is about 4% greater than the (theoretical) reference value.

The far-field drag method provides a coefficient that varies much less with grid refinement and which is always close to the reference values, and almost identical for the finest mesh. It is also able to eliminate the spurious drag component which is twice as high at M_∞ = 0.50 as at M_∞ = 0.20. The high values exhibited in the coarsest meshes[2] are reduced by a factor of about 4 by each grid refinement step, but still represent more than 4% for the finest grids.

From these results, we can expect high levels of numerical dissipation.

B.2.2.2 Exergy-based Drag Method

In order to apply the exergy-based approach for drag prediction, a wake analysis is performed to determine the evolution of each term of the formulation. Then, the direct and indirect methods for thermal exergy calculation are investigated. Finally, the control volume is defined and the drag prediction is made with an emphasis on the outflow decomposition.

1) Wake Analysis. Fig. B-5 illustrates all main terms of the exergy analysis when the plane is moved downstream of the wing up to a 100 root chord-distance. Terms corresponding to the coarse, medium and fine grid are represented with respectively the triangle, square and circle symbols. The data are from the flow at M_∞ = 0.20, but very similar trends were observed at M_∞ = 0.50.

The (direct) thermal exergy outflow ($\dot{\mathcal{E}}_{th}$ −) appears low compared to both the axial kinetic energy deposition rate ($\dot{E}_u$ −) and to the the boundary pressure-work rate ($\dot{E}_p$ −). As expected, all three terms converge towards zero within a few body length as highlighted on the x-log scale in the lower box. As a consequence, the total drag-power (D_ε −) rapidly reduces to the transverse kinetic energy deposition rate ($\dot{E}_v$ −), see the x-log scale in the upper box.

The non-physical decay of the transverse kinetic energy that is observed reduces with grid refinement but is still non-negligible for the finest grid. In agreement with existing experience [46, 64], this spurious phenomenon is attributed to numerical dissipation and sets the requirement of having the downstream plane as close as possible to the body.

2) Direct and Indirect Thermal Exergy Methods. The direct and indirect methods for each flow regime can are compared in Fig. B-6.

---

[2]Note that, in the worst case of the high-subsonic flow (M_∞ = 0.50) with the coarse mesh, the spurious drag can be nearly as
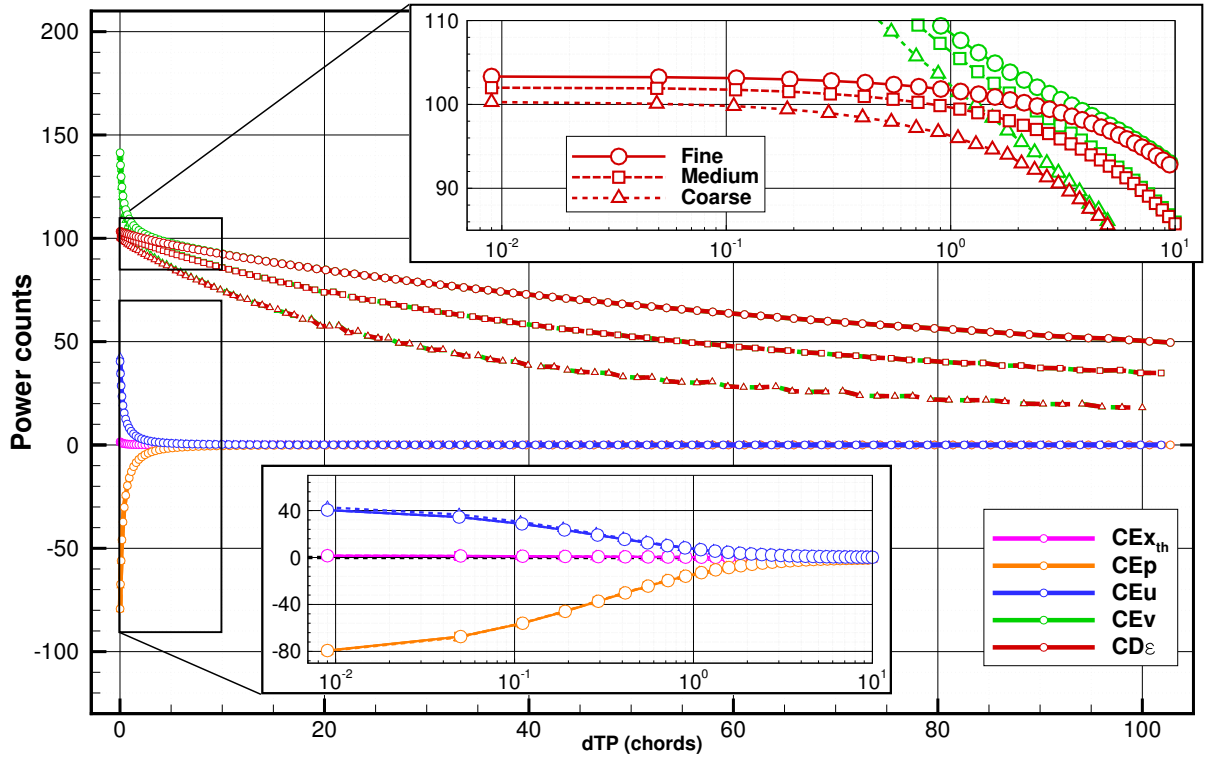
Figure B-5: 3D elliptical Wing in inviscid at $M_\infty = 0.20$ and $6\deg$ incidence: wake analysis up to a 100 root chord-distance. Grid refinement: coarse (triangles), medium (squares) and fine (circles).

(a) $M_\infty = 0.20$.

(b) $M_\infty = 0.50$.
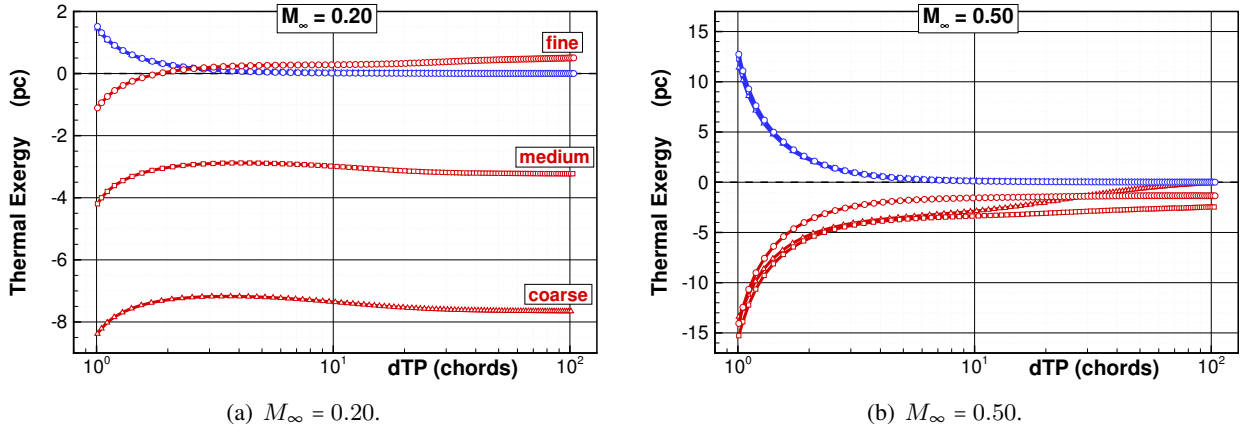
Figure B-6: 3D elliptical Wing in inviscid and subsonic flows at $6\deg$ incidence: direct (—) and indirect (—) methods for thermal exergy calculation.

At $M_\infty = 0.20$, see Fig. B-6a, the indirect method (—) is completely absurd. It gets slightly better with mesh refinement bu never tends towards zero far from the wing. The behavior of this term is somewhat better at a higher *Mach* number, see Fig. B-6b, there is little improvement: the values are still negative and not converging towards zero.

Because it provides a coefficient that behaves better in terms of physics, the direct method should be preferred for drag prediction.

---

high as the reference drag value!

3) Control Volume Definition. Because the fluid is inviscid and calorically perfect, all terms neglected in the formulation are in fact zero in this case. As a consequence, there is no minimal distance for the chordwise position of the downstream plane. Following the above wake analysis, the transverse plane is therefore located 0.02 root chord length downstream of the wing in order to avoid numerical dissipation. The corresponding control volume is depicted as the blue region in Fig. B-7.
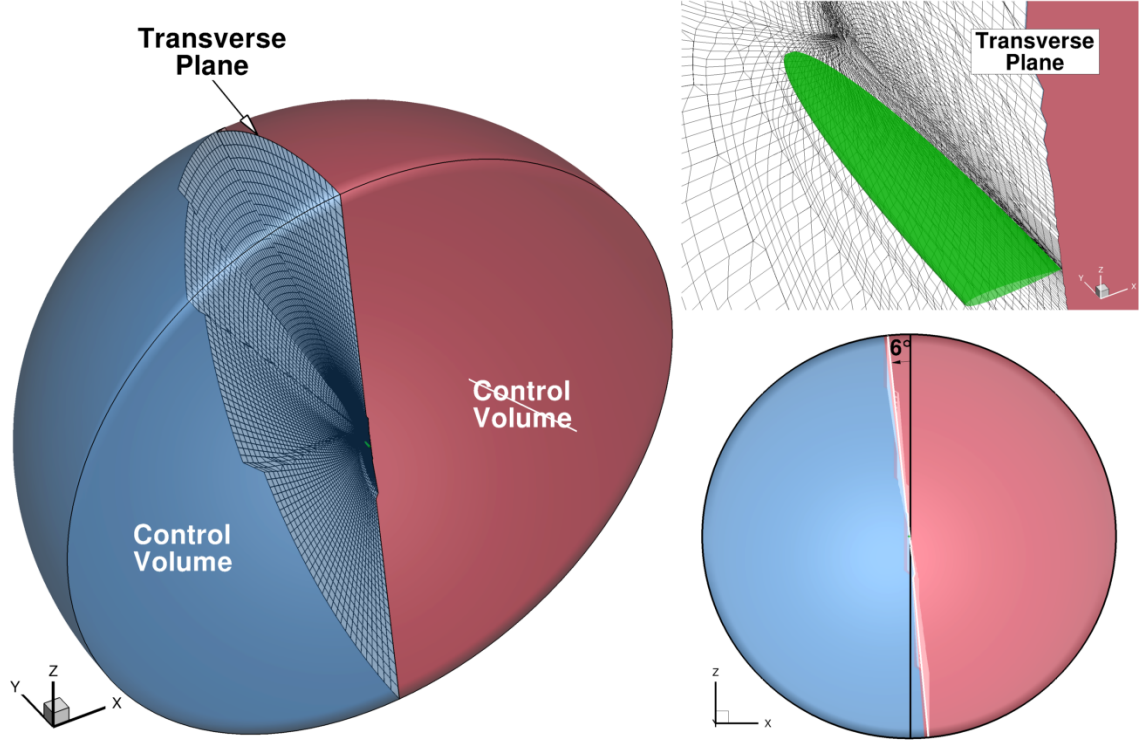
Figure B-7: 3D elliptical Wing in inviscid and subsonic flows at $6\,\mathrm{deg}$ incidence: control volume definition. Medium mesh.

Note that the transverse plane is perpendicular to the freestream at an incidence of 6 degrees as highlighted by the bottom-right planar view. For the left-hand side overall view, one can see that the transverse plane is not strictly speaking a *plane* because the spatial discretization yields finite-volume cells. Top-right view highlights the proximity of the downstream plane to the trailing edge of the wing.

4) Drag Prediction. The drag decomposition from the exergy standpoint is given in Table B.3 where the theoretical reference value is reminded.

| M_∞ | Mesh | CL | CD_{ref} | far-field exergy *via ffx* | | | | | CD_{nf} |
				$C\dot{\mathcal{E}}_m$	$C\dot{\mathcal{E}}^d_{th}$	CD^d_ε	$C\dot{\mathcal{E}}^i_{th}$	CD^i_ε	
	Coarse	0.554	**101.64**	98.86	1.41	**100.27**	-16.88	**81.98**	157.01
0.20	Medium	0.560	**103.59**	100.54	1.44	**101.98**	-2.30	**98.24**	119.54
	Fine	0.562	**104.14**	101.84	1.46	**103.31**	1.07	**102.92**	108.27
	Coarse	0.596	**117.33**	109.51	11.12	**120.63**	13.30	**122.81**	219.50
0.50	Medium	0.615	**125.05**	112.28	11.84	**124.12**	14.93	**127.21**	156.98
	Fine	0.624	**128.62**	115.54	12.29	**127.82**	13.64	**129.17**	137.07

Table B.3: 3D elliptical Wing in inviscid and subsonic flows at $6\,\mathrm{deg}$ incidence: exergy-based coefficients expressed in power counts (10^{-4}) for a plane 0.02 root chord downstream the body.

The mechanical exergy outflow is the largest contributor, as expected, and the thermal exergy is effec-

tively much lower at M_∞ = 0.20 than at M_∞ = 0.50. Both terms are only weakly dependent on mesh density.

For both flow regimes, very satisfactory results are provided by the exergy-based formulation whose accuracy always outperforms (by far) the near-field approach. Always close to the theoretical reference value, an accuracy similar to the far-field drag approach is exhibited.

5) Outflows Decomposition. Table B.4 gives additional information about the outflows and especially on the (rather *surprisingly*) relative independence of the direct method of thermal exergy calculation to grid density.

M_∞	Mesh	$C\dot{E}_u$	$C\dot{E}_v$	$C\dot{E}_p$	$C\dot{\mathcal{E}}_m$	$C\dot{E}_{th}$	$C\dot{E}_W$	$C\dot{A}$	$C\dot{\mathcal{E}}_{th}^d$
						Outflows decomposition from *ffx*			
	Coarse	41.25	134.07	-76.46	98.86	-221.32	249.45	26.71	1.41
0.20	Medium	38.61	137.72	-75.79	100.54	-182.27	195.45	11.74	1.44
	Fine	37.98	139.57	-75.71	101.85	-182.96	186.45	2.03	1.46
	Coarse	59.03	149.97	-99.49	109.51	-270.90	380.58	98.56	11.12
0.50	Medium	52.84	160.83	-101.39	112.28	-253.78	296.80	31.18	11.84
	Fine	51.82	166.51	-102.79	115.54	-258.16	279.52	9.07	12.29

Table B.4: 3D elliptical Wing in inviscid and subsonic flows at $6\deg$ incidence: exergy outflows coefficients expressed in power counts (10^{-4}) for a plane 0.02 root chord downstream the body.

The thermal exergy coefficient has the particularity of being the sum of three equally imprecise terms, their sum however appears to be relatively constant with grid refinement.

In the last column, large discrepancies are observable for the outflow of anergy which is theoretically zero in this isentropic flow. This spurious entropy generation is a known indicator of the inaccuracy of the numerical flow solution [73]. Note that as the mesh is refined, the level of numerical anergy reduces accordingly and that it has the same order of magnitude as the spurious drag identified by the far-field drag method implemented in $ffd72$.

B.2.3   Summary of the Key Findings

At the low *Mach* number, the indirect method for thermal exergy calculation did not provide a thermal exergy that vanishes in the far-field of the wing, which is in contradiction with Second Law considerations. As, in this case, the indirect thermal exergy expression reduces to $\dot{E}_{PV}$, the suspicions of this term, that have arisen from the study of the transonic flow over the NACA 0012 Airfoil, are reinforced.

As regards drag prediction, excellent results can be obtained with the direct method and with the code ffx upon a careful choice of the transverse plane position.

B.3 Wake-ingesting Configuration Grids
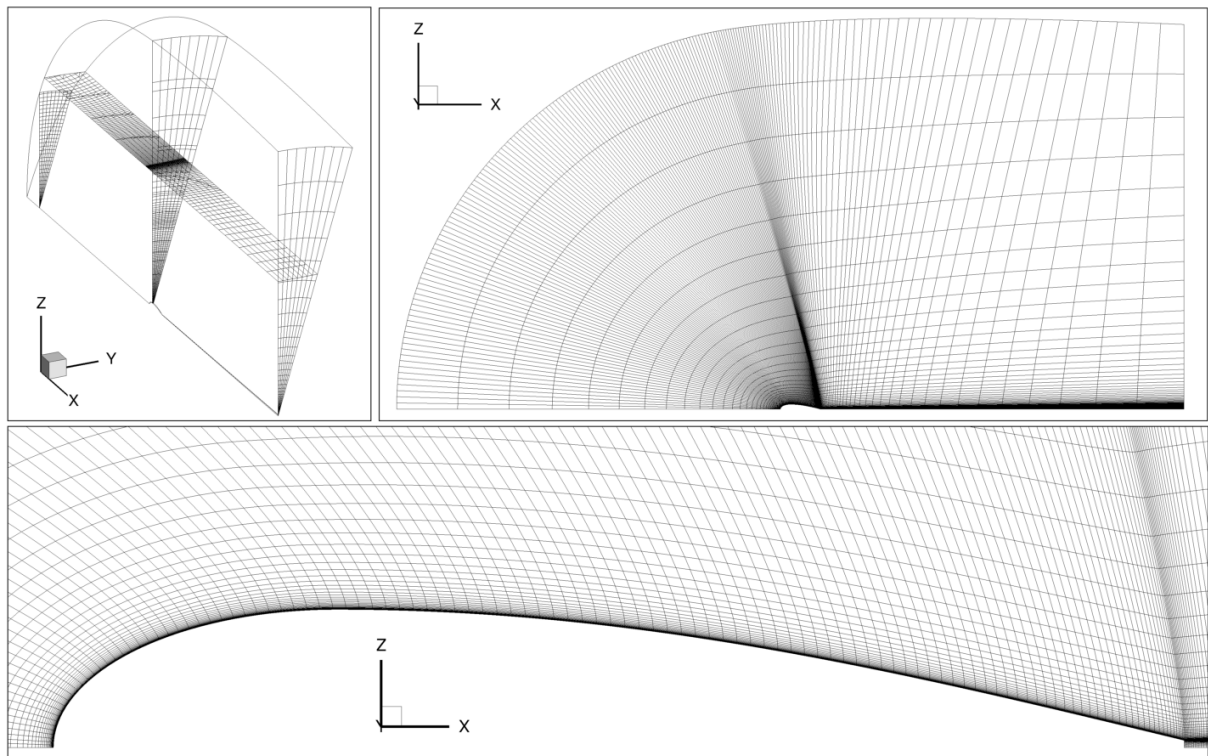
Figure B-8: Isolated Fuselage Grid examined in section 4.3 (p. 133).
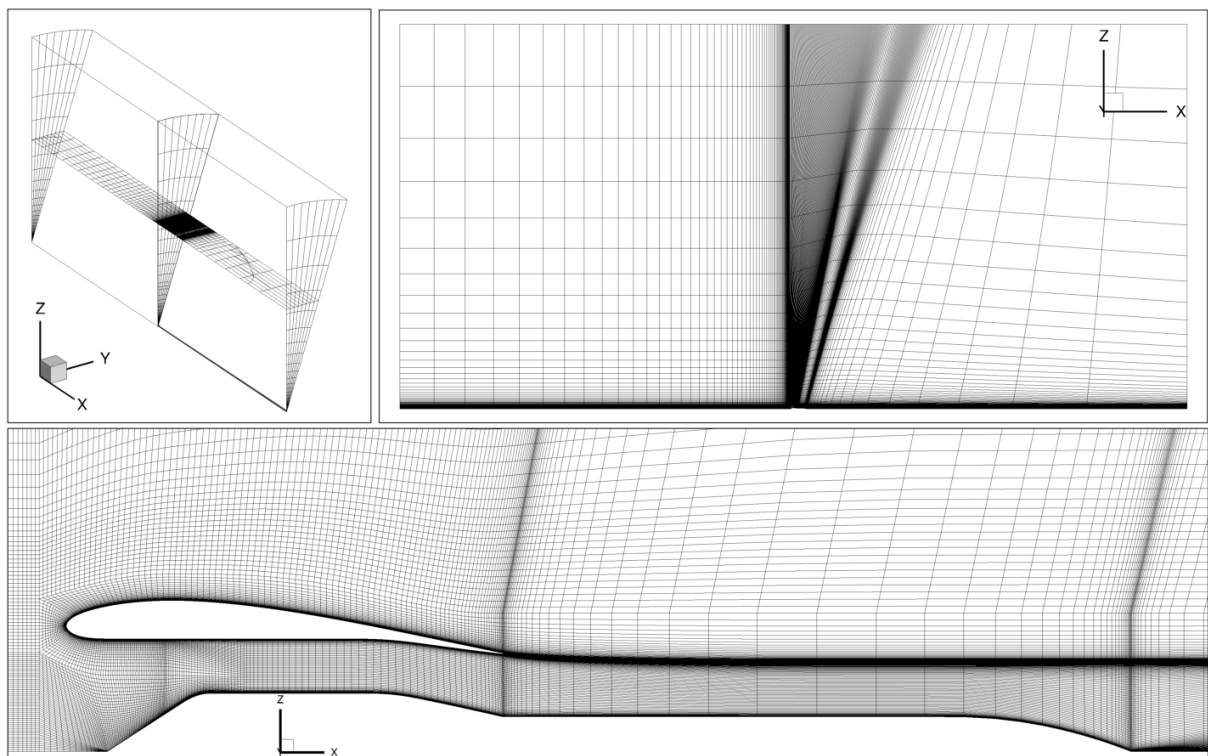
Figure B-9: Isolated Nacelle Grid examined in section 4.3 (p. 133).

195

Figure B-10: Fuselage + Nacelle Grid examined in section 4.3 (p. 133).

List of Figures

List of Tables

Bibliography

[1] ABE, K., KONDOH, T., AND NAGANO, Y., "A New Turbulence Model for Predicting Fluid Flow and Heat Transfer in Separating and Reattaching Flows - I. Flow Field Calculations," *International Journal of Heat and Mass Transfer*, Vol. 37, 1994, pp. 139–151. (Cited on page 23.)

[2] ABEYOUNIS, W. K., PATTERSON, JR., J. C., STOUGH, III, H. P., WUNSCHEL, LT. COL., A. J., AND CURRAN, P. D., "Wingtip Vortex Turbine Investigation for Vortex Energy Recovery," SAE Aerotech '90, 1990 SAE Aerospace Technology Conference & Exposition, 1–4 October 1990. (Cited on page 43.)

[3] ADEYINKA, O. B., AND NATERER, G. F., "Modeling of Entropy Production in Turbulent Flows," *Journal of Fluids Engineering*, Vol. 126, 2004, pp. 893–899. (Cited on page 24.)

[4] ADEYINKA, O. B., "Numerical and Experimental Studies of Available Energy Losses in Laminar and Turbulent Flows," Ph.D. Dissertation, Dept. of Mechanical and Manufacturing Engineering, University of Manitoba, Winnipeg, Canada, 2005. (Cited on page 24.)

[5] ADVISORY COUNCIL FOR AERONAUTICS RESEARCH IN EUROPE, "Strategic Research Agenda," October 2004. (Cited on page 1.)

[6] ALABI, K., LADEINDE, F., VON SPAKOVSKY, M., MOORHOUSE, D., AND CAMBEROS, J. A., "The Use of the 2nd Law as a Potential Design Tool for Aircraft Air Frame Subsystems," *Int. J. of Thermodynamics*, Vol. 9, No. 4, 2006, pp. 1–14. (Cited on pages 23, 24, 108, and 176.)

[7] AMANT, S., "Drag Prediction and Decomposition, from Wake Surveys and Calculations, in Subsonic Flows," 19th AIAA Applied Aerodynamics Conference, Anaheim, CA, 11-14 June 2001. (Cited on page 58.)

[8] AMANT, S., "Calcul et décomposition de la trainée aérodynamique des avions de transport a partir de calculs numériques et d'éssais en soufflerie," Ph.D. Dissertation, Ecole Nationale Supérieure de l'Aéronautique et de l'Espace, 2002. (Cited on page 178.)

[9] ANDERSON, JR., J. D., *Aircraft Performance and Design*, McGraw-Hill, 1st ed., 1999, Chaps. 7, 8. (Cited on pages 2 and 178.)

[10] ARNTZ, A., ATINAULT, O., AND DESTARAC, D., "Numerical Airframe Aerodynamic Performance Prediction: An Exergy Point of View," 49th International Symposium of Applied Aerodynamics, AAAF, Lille, France, 24–26 March 2014. (Cited on pages 5, 67, and 79.)

[11] ARNTZ, A., ATINAULT, O., DESTARAC, D. AND MERLEN, A., "Exergy-based Aircraft Aeropropulsive Performance Assessment: CFD Application to Boundary Layer Ingestion," 32nd AIAA Applied Aerodynamics Conference, AIAA Aviation 2014, Atlanta, GA, 16–20 June 2014. (Cited on pages 5 and 133.)

[12] ARNTZ, A., ATINAULT, O., AND MERLEN, A., "Exergy-based Formulation for Aircraft Aeropropulsive Performance Assessment: Theoretical Development," *AIAA Journal*, Accepted for publication on August 18th, 2014. (Cited on pages 5 and 27.)

[13] ARNTZ, A., AND ATINAULT, O., "Exergy-based Performance Assessment of a Blended Wing-Body with Boundary-Layer Ingestion," *AIAA Journal*, **In review**. (Cited on pages 5 and 143.)

[14] ARNTZ, A., AND HUE, D., "Exergy-based Performance Assessment of the NASA Common Research Model," *AIAA Journal*, **In review**. (Cited on pages 5 and 101.)

[15] ASHCRAFT, S. W., PADRON, A. S., PASCIONI, K. A., STOUT, G. W., JR., AND HUFF, D. L., "Review of Propulsion Technologies for N+3 Subsonic Vehicle Concepts," NASA TM-2011-217239, 2011. (Cited on pages 2 and 143.)

[16] ATINAULT, O., CARRIER, G., GRENON, R., VERBECKE, C., AND VISCAT, P., "Numerical and Experimental Aerodynamic Investigations of Boundary Layer Ingestion for Improving Propulsion Efficiency of Future Air Transport," 31st AIAA Applied Aerodynamics Conference, San Diego, CA, 24-27 June 2013. (Cited on page 133.)

[17] BANKE, J., "Beauty of Future Airplanes is More than Skin Deep," NASA Press Release, May 17, 2010. (Cited on page 2.)

[18] BEJAN, A., *Entropy Generation through Heat and Fluid Flow*, Wiley, New-York, 1982. (Cited on pages 14 and 160.)

[19] BEJAN, A., TSATSARONIS, G., AND MORAN, M., *Thermal Design and Optimization*, John Wiley & Sons, Inc., New York, 1996, Chap. 8, pp. 405–462. (Cited on pages 14, 20, and 53.)

[20] BEJAN, A., "Entropy Generation Minimization: The New Thermodynamics of Finite-size Devices and Finite-time Processes," *Journal of Applied Physics*, Vol. 79, No. 3, 1996, pp. 1191–1218. (Cited on pages 14, 15, 17, 18, and 19.)

[21] BEJAN, A., *Entropy Generation Minimization: The Method of Thermodynamic Optimization of Finite-Size Systems and Finite-Time Processes*, Mechanical and Aerospace Engineering Series, CRC Press, Inc., 1996, Chaps. 4, 5. (Cited on pages 14, 160, and 168.)

[22] BEJAN, A., AND SIEMS, D. L., "The Need for Exergy Analysis and Thermodynamic Optimization in Aircraft Development," *Exergy, an International Journal*, Vol. 1, No. 1, 2001, pp. 14–24. (Cited on page 22.)

[23] BEJAN, A., "Fundamentals of exergy analysis, entropy generation minimization, and the generation of flow architecture," *Int. J. Energy Res.*, Vol. 26, 2002, pp. 545–565. (Cited on pages 17, 18, and 20.)

[24] BEJAN, A., *Advanced Engineering Thermodynamics*, 3rd ed., John Wiley & Sons, Inc., 2006, Chaps. 3, 8, 9, 10. (Cited on pages 14, 17, 19, 50, and 160.)

[25] BEJAN, A., CHARLES, J. D., AND LORENTE, S., "The Evolution of Airplanes," *Journal of Applied Physics*, Vol. 116, No. 4, 2014, 6 p. (Cited on page 18.)

[26] BERG, F. T. N., BALCHIN, M. J., AND KEOGH, P. S., "New Principles for Dynamic Aircraft Exergy Mapping," *Journal of Aircraft*, Vol. 50, No. 4, 2013, pp. 1088–1098. doi: 10.2514/1.C032040. (Cited on pages 22 and 174.)

[27] BERGHOF, R., SCHMITT, A., EYERS, C., HAAG, K., MIDDEL, J., HEPTING, H., GRÜBLER, A., AND HANCOX, R., "CONSAVE 250," Final Technical Report, G4MA-CT-2002-04013, July 2005. (Cited on page 1.)

[28] BETZ, A., "Ein verfahren zur direkten ermittlung des profilwiderstandes," *Zeitschrift für Flugtechnik un Motorluftschiffahrt*, Vol. 16, 1925, pp. 42–44. (Cited on page 49.)

[29] BLAZEK, J., *Computational Fluid Dynamics: Principles and Applications*, Elsevier Sciences Ltd., Oxford, 2001, Chap. 7, pp. 225–265. (Cited on page 29.)

[30] BOEING COMMERCIAL AIRPLANES, *777-200/300 Airplane Characteristics for Airport Planning*, D6-58329, 1998, p. 15. (Cited on page 101.)

[31] BOREL, L., *Thermodynamique et Énergétique*, 3rd ed., Vol. 1, Presses Polytechniques et Universitaires Romandes, 1991, Chaps. 1, 10. (Cited on pages v, 14, 15, 19, 36, 45, and 130.)

[32] BRODERSEN, O., AND STÜRMER, A., "Drag Prediction of Engine-Airframe Interference Effects using Unstructured Navier-Stokes Calculations," 19th AIAA Applied Aerodynamics Conference, 11–14 June 2001, Anaheim, CA. (Cited on page 122.)

[33] CAMBEROS, J. A., AND MOORHOUSE, D. J., "Systems Engineering in Terms of Exergy," *International Journal of Aerospace Engineering*, Vol. 2009, Article ID 735680, 7 p. (Cited on pages 17 and 20.)

[34] CAMBEROS, J. A., AND DOTY, J. H., "Fundamentals of Exergy Analysis," in *Exergy Analysis and Design Optimization for Aerospace Vehicles and Systems*, edited by Moorhouse, D. J. and Camberos, J. A., Progress in Astronautics and Aeronautics, AIAA, 2011, Chap. 2, pp. 9–76. (Cited on pages 15 and 37.)

[35] CAMBIER, L., HEIB, S., AND PLOT, S., "The Onera *elsA* CFD Software: Input from Research and Feedback from Industry," *Mechanics & Industry*, Vol. 14, No. 3, 2013, pp. 159–174. (Cited on pages 58, 65, 91, 102, 120, and 135.)

[36] CANDEL, S., *Mécanique des fluides*, Dunod, 1990, Chap. 11. (Cited on pages 31 and 34.)

[37] CARNOT, S., *Réflexions sur la puissance motrice du feu et sur les machines propres à développer cette puissance* (French), Bachelier Libraire, 1824. (Cited on page 17.)

[38] CENGEL, Y. A., AND BOLES, M. A., *Thermodynamics: An Engineering Approach*, 5th ed., McGraw-Hill Higher Education, Boston, MA, 2005, Chap. 8, pp. 423–485. (Cited on pages v, 14, 15, 16, 17, 37, and 197.)

[39] CHAO, D. D., AND VAN DAM, C, P., "Wing Drag Prediction and Decomposition," *Journal of Aircraft*, Vol. 43, No. 1, 2006, pp. 82–90. doi: 10.2514/1.C031766 (Cited on pages 49 and 53.)

[40] CLARKE, J. M., AND HORLOCK, J. H., "Availability and Propulsion," *Journal Mechanical Engineering Science*, Vol. 17, No. 4, 1975, pp. 223–232. (Cited on pages 21, 39, 41, 45, 129, and 132.)

[41] CLUMPSTY, N. A., *Jet Propulsion*, Cambridge University Press, Cambridge, UK. (Cited on pages 39 and 129.)

[42] COVERT, E. E. (ED.), JAMES, C. R., KIMZEY, W. F., RICHEY, G. K. AND ROONEY, E. C., *Thrust and Drag: Its Prediction and Verification*, Progress in Astronautics and Aeronautics, AIAA, 1985. (Cited on pages 3, 40, 53, 122, 132, and 146.)

[43] DAHM, W. J. A., ALLEN, N., RAZOUK, R. R. AND SHYY, W., "Challenges and Opportunities in the Next Two Decades of Aerospace Engineering," *Encyclopedia of Aerospace Engineering* [online journal], Wiley Online Library, Chap. 2, 2010, pp. 27–37. (Cited on page 2.)

[44] DENTON, J. D., "The 1993 IGTI Scholar Lecture: Loss Mechanisms in Turbomachines," *Journal of Turbomachinery*, Vol. 115, 1993, pp. 621–656. (Cited on pages 12, 15, 21, 39, 62, 132, 174, and 176.)

[45] DE OLIVEIRA, JR., S., *Exergy: Production, Cost and Renewability*, 1st ed., Springer-Verlag, London, 2013, Chaps. 1, 8. (Cited on pages v, 14, 19, 37, and 174.)

[46] DESTARAC, D., "Far-field / Near-field Drag Balance and Applications of Drag Extraction in CFD," CFD-based Aircraft Drag Prediction and Reduction Lecture Series, Von Karman Institute for Fluid Dynamics, Hampton, VA, 2003. (Cited on pages 23, 49, 57, 66, 72, 83, 90, 100, 116, 118, 174, and 191.)

[47] DINCER, I., AND ROSEN, M. A., *Exergy, Energy, Environment and Sustainable Development*, Elsevier Science Ltd., 2007, Chaps. 1, 2, 18. (Cited on pages 14, 16, 19, 39, 122, 129, and 203.)

[48] DRELA, M., "Aerodynamics of Heat Exchangers for High-Altitude Aircraft," *Journal of Aircraft*, Vol. 33, No. 2, 1996, pp. 176–184. (Cited on page 164.)

[49] DRELA, M., "Power Balance in Aerodynamics Flows," *AIAA Journal*, Vol. 47, No. 7, 2009, pp. 1761–1771. doi: 10.2514/1.42409 (Cited on pages 4, 8, 10, 11, 12, 25, 37, 46, 47, 48, 53, 62, 73, 174, 183, 189, and 197.)

[50] DRELA, M., "Development of the D8 Transport Configuration," 29th AIAA Applied Aerodynamics Conference, 27–30 June 2011, Honolulu, HI. (Cited on pages 2 and 13.)

[51] ENSIGN, T. R., "Performance and Weight Impact of Electric Environmental Control System and More Electric Engine on Citation CJ2," 45th AIAA Aerospace Sciences Meeting & Exhibit, Reno, NV, 08–11 January 2007. (Cited on page 2.)

[52] ETELE, J., AND ROSEN, M. A., "Exergy Losses for Aerospace Engines: Effect of Reference-Environments on Assessment Accuracy," 39th AIAA Aerospace Sciences Meeting & Exhibit, Reno, NV, 10–13 January 2000. (Cited on pages 22, 122, and 129.)

[53] FAROKHI, S., *Aircraft Propulsion*, John Wiley & Sons, Inc., 2009, Chap. 3, pp. 97–126. (Cited on pages 40, 53, 122, 132, and 146.)

[54] FELDER, J., KIM, H. D., AND BROWN, G., "Turboelectric Distributed Propulsion Engine Cycle Analysis for Hybrid-Wing-Body Aircraft," 47th AIAA Aerospace Sciences Meeting Including The New Horizons Forum and Aerospace Exposition, Orlando, FL, 5–8 January 2009, AIAA 2009-1132. (Cited on pages 2, 3, and 143.)

[55] FELDER, J. J., BROWN, G. V., KIM, H. D. AND CHU, J., "Turboelectric Distributed Propulsion in a Hybrid Wing Body Aircraft," 20th ISABE Conference, Gothenburg, Sweden, 12–16 September 2011. (Cited on pages 2 and 143.)

[56] FELDER, J. J., KIM, H. D., BROWN, G. V., AND CHU, J., "An Examination of the Effect of Boundary Layer Ingestion on Turboelectric Distributed Propulsion Systems," 49th AIAA Aerospace Sciences Meeting, Orlando, FL, 4–7 January 2011, AIAA 2011-300. (Cited on page 3.)

[57] FERNÁNDEZ-VILLACÉ, V., AND PANIAGUA, G., "On the exergetic effectiveness of a combined-cycle engines for high speed propulsion," *Energy*, Vol. 51, 2013, pp. 382–394. doi: (Cited on page 22.)

[58] FERRAR, A. M. AND O'BRIEN, W. F., "Progress in Boundary Layer Ingesting Embedded Engine Research," 48th AIAA/ASME/SAE/ASEE Joint Propulsion Conference & Exhibit, Atlanta, GA, 30 July – 01 August, 2012, AIAA 2012-4283. (Cited on page 52.)

[59] FIGLIOLA, R. S., TIPTON, R., AND LI, H., "Exergy Approach to Decision-Based Design of Integrated Aircraft Thermal Systems," *Journal of Aircraft*, Vol. 40, 2003, pp. 49–55. (Cited on pages 22 and 25.)

[60] FLOREA, R. V., VOYTOVYCH, D., TILLMAN, F., STUCKY, M., SHABBIR, A., SHARMA, O. AND HANNON, J., "Aerodynamic Analysis of a Boundary-Layer-Ingesting Distortion-Tolerant Fan," ASME Turbo Expo 2013, San Antonio, TX, 2013, Paper GT2013-94656. (Cited on page 144.)

[61] GAMBILL, J., WIESE, D., CLAEYS, H. MATULICH, D., AND WEISS, C., "Integrated Aircraft Thermal Management and Power Generation," SAE Technical Paper 932055, 1993. doi:10.4271/932055 (Cited on page 2.)

[62] GANDOLFI, R., PELLEGRINI, L. F., DA SILVA, G. A. L. AND DE OLIVEIRA JR., S., "Exergy Analysis Applied to a Complete Flight Mission of a Commercial Aircraft," 46th AIAA Aerospace Sciences Meeting and Exhibit, Reno, NV, 7–10 January, 2008. (Cited on pages 2, 22, and 25.)

[63] GANDOLFI, R., PELLEGRINI, AND DE OLIVEIRA, JR., S., "More Electric Aircraft Analysis Using Exergy as a Design Comparison Tool," 48th AIAA Aerospace Sciences Meeting, Orlando, FL, 4–7 January 2010, AIAA 2009-1132. (Cited on pages 2, 22, and 25.)

[64] GILES, M. B., AND CUMMINGS, R. M., "Wake Integration for Three-Dimensional Flowfield Computations: Theoretical Development," *Journal of Aircraft*, Vol. 36, No. 2, 1999, pp. 357–365. (Cited on pages 36, 39, 48, 49, 53, 100, 186, and 191.)

[65] GOHARDANI, A. S., DOULGERIS, G., AND SINGH, R., "Challenges of future aircraft propulsion: A review of distributed propulsion technology and its potential application for the all electric commercial aircraft," *Progress In Aerospace Sciences*, Vol. 47, 2011, pp. 369–391. (Cited on page 2.)

[66] GREITZER, E. M., BONNEFOY, P. A., DE LA ROSA BLANCO, E., *et al.* , "N+3 Aircraft Concept Designs and Trade Studies Final Report," Volume 1, NASA/CR–2010-216794/VOL1, 2010. (Cited on page 2.)

[67] GREITZER, E. M., BONNEFOY, P. A., DE LA ROSA BLANCO, E., *et al.* , "N+3 Aircraft Concept Designs and Trade Studies Final Report," Volume 2: Appendices–Design Methodologies for Aerodynamics, Structures, Weight, and Thermodynamic Cycles, NASA/CR–2010-216794/VOL2, 2010. (Cited on pages 52, 174, and 181.)

[68] HARDIN, L. W., TILLMAN, G., SHARMA, O. P., BERTON, J. AND AREND, D. J., "Aircraft System Study of Boundary Layer Ingesting Propulsion," 48th AIAA/ASME/SAE/ASEE Joint Propulsion Conference & Exhibit, Atlanta, GA, 30 July – 01 August 2012. (Cited on page 3.)

[69] HARRIS, C. D., "Two-Dimensional Aerodynamic Characteristics of the NACA 0012 Airfoil in the Langley 8-Foot Transonic Pressure Tunnel," NASA TM-81927, 1981. (Cited on pages 4 and 73.)

[70] HEIB, S., PLOT, S., AND LANTOS, N., "*elsA* Theoretical Manuel," Ref. STB-97020, version 2.2, January 20, 2014. (Cited on page 91.)

[71] HERWIG, H. AND SCHMANDT, B., "How to Determine Losses in a Flow Field: A Paradigm Shift towards the Second Law Analysis," *Entropy*, No. 16, 2014, pp. 2956–2989. doi:10.3390/e16062959. (Cited on page 23.)

[72] HILEMAN, J. I., SPAKOVSKY, Z. S., DRELA, M., SARGEANT, M. A., AND JONES, A., "Airframe Design for Silent Fuel-Efficient Aircraft," *Journal of Aircraft*, Vol. 47, No. 3, 2010, pp. 956-969. (Cited on pages 8 and 143.)

[73] HIRSCH, C., *Numerical Computation of Internal & External Flows*, Volume 1: Fundamentals of Computational Fluid Dynamics, 2nd ed., Butterworth-Heinemann, Elsevier, Oxford, 2007, Chap. 11. (Cited on page 194.)

[74] HOERNER, S. F., *Fluid-Dynamic Drag*, Hoerner Fluid Dynamics, Bakersfield, CA, 1965, Chaps. 8 and 9. (Cited on pages 13, 160, and 164.)

[75] HUE, D., "Fifth Drag Prediction Workshop: Computational Fluid Dynamics Studies Carried Out at ONERA," *Journal of Aircraft*, Vol. 51, No. 4, 2014, pp. 1295-1310. (Cited on pages 58, 102, 104, and 117.)

[76] ISIKVEREN, A. T., SEITZ, A., BIJEWITZ, J., HORNUNG, M., MIRZOYAN, A., ISYANOV, A., GODARD, J.-L., STÜCKL, S., AND VAN TOOR, J., "Recent Advances in Airframe-Propulsion Concepts with Distributed Propulsion," 29th Congress of the International Council of the Aeronautical Sciences (ICAS), St. Petersburg, Russia, 7–12 January 2014. (Cited on page 143.)

[77] JENKINSON, L. R., SIMPKIN, P., AND RHODES, D., *Civil Jet Aircraft Design*, Arnold co-published by AIAA, 1st ed., 1999. (Cited on page 178.)

[78] KAWAI, R. T., FRIEDMAN, D., AND SERRANO, L., "Blended Wing Body (BWB) Boundary Layer Ingestion (BLI) Inlet Configuration and System Studies," NASA CR-2006-214534, 2006. (Cited on pages 3, 146, and 197.)

[79] KEENAN, J. H., "Availability and irreversibility in thermodynamics," *British Journal of Applied Physics*, Vol. 2, No. 7, 1951, pp. 183–192. (Cited on page 17.)

[80] KIM, H., AND LIOU, M.-S., "Flow Simulation of N3-X Hybrid Wing-Body Configuration," 51st AIAA Aerospace Sciences Meeting, 07–10 January 2013, Grapevine, TX. (Cited on pages 134 and 144.)

[81] KOCK, F., AND HERWIG, H., "Local entropy production in turbulent shear flows: a high-Reynolgs number model with wall functions," *International Journal of Heat and Mass Transfer*, Vol. 47, 2004, pp. 2205–2215. (Cited on pages 24 and 174.)

[82] KOCK, F., AND HERWIG, H., "Entropy production calculation for turbulent shear flows and their implementation in cfd codes," *International Journal of Heat and Mass Transfer*, Vol. 26, 2005, pp. 672–680. (Cited on pages 24 and 174.)

[83] KOK, J., "Improvements of Two-Equation Turbulence Models in Multi-Block Flow Solvers: Free-Stream Dependency and Transition," Technical Report, AVTAC/TR/NLR/JCK990520, 1999. (Cited on page 91.)

[84] KRAMER-BEVAN, J. S., "A Tool for Analysis Fluid Flow Losses", MSc Thesis, University of Waterloo, 1992. (Cited on page 24.)

[85] KUNDU, A. K., *Aircraft Design*, Cambridge Aerospace Series, Cambridge University Press, New York, 2010, Chap. 13, pp. 417–463. (Cited on pages 30 and 180.)

[86] LAMISCARRE, B., HERMETZ, J., LE TALLEC, C., BRUNET, M, JOULIA, A., AND CHABOUD, T., "Transport aérien 2050 - Des recherches pour préparer l'avenir," ONERA - The French Aerospace Lab, October 2004. (Cited on page 1.)

[87] LANCHESTER, F. W., *Aerodynamics*, Constable and Co., Ltd., London, 1907. (Cited on page 42.)

[88] LANDRUM, D. B., AND MACHA, J. M., "Influence of a Heated Leading Edge on Boundary Layer Growth, Stability, and Transition," AIAA Paper 87-1259, 1987. (Cited on page 154.)

[89] LOZANO, M. A., AND VALERO, A., "Theory of Exergetic Cost," *Energy*, Vol. 18, No. 9, 1993, pp. 939–960. (Cited on pages 20 and 174.)

[90] LEAHY, J., "Airbus Global Market Forecast, Future Journeys 2013–2032," October 2013. (Cited on page 1.)

[91] LEE, J. D., "The Influence of Heat Transfer the Drag of Airfoils," Air Force Wright Aeronautical Laboratories, TR-81-3030, 1981. (Cited on page 154.)

[92] LEVY, D. W., LAFLIN, K. R., TINOCO, E. N., VASSBERG, J. C., MANI, M., RIDER, B., RUM-SEY, C. L., WAHLS, R. A., MORRISON, J. H., BRODERSEN, O. P., CRIPPA, S., MAVRIPLIS, D. J., MURAYAMA, M., "Summary of Data from the Fifth Computational Fluid Dynamics Drag Prediction Workshop," *Journal of Aircraft*, Vol. 51, No. 4, 2014, pp. 1194-1213. (Cited on pages 4 and 116.)

[93] LEWIS, J. H., "Propulsive Efficiency from an Energy Utilization Standpoint," *Journal of Aircraft*, Vol. 13, No. 4, 1976, pp. 299–302. (Cited on pages 21 and 39.)

[94] LI, H., STEWART, J., AND FIGLIOLA, R., "Exergy Based Design Methodology for Airfoil Shape Optimization and Wing Analysis," 25th International Congress of the Aeronautical Sciences, ICAS 2006, Hamburg, Germany, 3–8 September 2006. (Cited on pages 23, 24, 48, and 53.)

[95] LIEBECK, R. H., "Design of the Blended Wing Body Subsonic Transport," *Journal of Aircraft*, Vol. 41, No. 1, 2004, pp. 10–25. (Cited on page 143.)

[96] LIU, C., DOULGERIS, G., LASKARIDIS, P. AND SINGH, R., "Thermal cycle analysis of tur-boelectric distributed propulsion system with boundary layer ingestion," *Aerospace Science and Technology*, Vol. 27, 2013, pp. 163–170. (Cited on page 3.)

[97] LOVELY, D., AND HAIMES, R., "Shock Detection from Computational Fluid Dynamics Results," AIAA Paper 99-33493, 1999. (Cited on page 60.)

[98] MANI, M., RIDER, B. J., SCLAFANI, A. J., WINKLER, C., VASSBERG, J., DORGAN, A. J., CARY, A., AND TINOCO, E. N., "Reynolds-Averaged Navier-Stokes Technology for Transonic Drag Prediction: A Boeing Perspective," *Journal of Aircraft*, Vol. 51, No. 4, 2014, pp. 1118-1134. (Cited on page 3.)

[99] MARLEY, C. D., AND RIGGINS, D. W., "The Thermodynamics of Exergy Losses and Thrust Production in Gas Turbine Engines," 47th AIAA/ASME/SAE/ASEE Joint Propulsion Conference & Exhibit, San Diego, CA, 31 July – 03 August 2011. (Cited on page 22.)

[100] MARONGIU, C., TOGNACCINI, R., AND UENO, M., "Lift and Lift-Induced Drag Computation by Lamb Vector Integration," *AIAA Journal*, Vol. 51, No. 6, 2013, pp. 1420–1430. (Cited on page 11.)

[101] MASER, A. C., GARCIA, E., AND MAVRIS, D. N., "Characterization of Thermodynamic Ir-reversibility for Integrated Propulsion and Thermal Management Systems Design," 50th AIAA Aerospace Sciences Meeting including the New Horizons Forum and Aerospace Exposition, Nashville, TN, 9–12 January 2012. (Cited on page 22.)

[102] MCELIGOT, D. M., WALSH, E. J., LAURIEN, E., AND SPALART, P. R., "Entropy Generation in the Viscous Parts of Turbulent Boundary Layers," *Journal of Fluids Engineering*, Vol. 130, 2008, 12 p. (Cited on pages 25 and 174.)

[103] MC LEAN, D., "Wingtip Devices: What They Do and How They Do It," Boeing Performance and Flight Operations Engineering Conference, 2005. (Cited on pages 3 and 118.)

[104] MÉHEUT, M., ARNTZ, A., AND CARRIER, G., "Aerodynamic Shape Optimizations of a Blended Wing Body Configuration for Several Wing Planforms," 30th AIAA Applied Aerodynamics Con-ference, New Orleans, LA, 25–28 June 2012. (Cited on page 58.)

[105] MEMON, M. O., WABICK, K., ALTMAN, A., AND BUFFO, R. M., "Wingtip Vortices from an Exergy-Based Perspective," 52th AIAA Aerospace Sciences Meeting, National Harbor, MD, 13–17 January 2014. (Cited on page 174.)

[106] MENTER, F. R., "Zonal Two Equation ($k-\omega$) Turbulence Models for Aerodynamics Flows," 24th Fluid Dynamics Conference, Orlando, FL, 06–09 July 1992, AIAA Paper 93-2906. (Cited on page 92.)

[107] MONSCH, S., LI, H., HARRIS, R., STEWART, J., FIGLIOLA, R., AND CAMBEROS, J., "Exergy Based Design Methodology for Wing Shape Optimization and Analysis," 39$^{\text{th}}$ AIAA Thermophysics Conference, Miami, FL, 25–28 June 2007. doi: 10.2514/6.2007-4053. (Cited on pages 23, 24, 48, and 53.)

[108] MOORE, J., AND MOORE, J. G., "Entropy Production Rates from Viscous Flow Calculations, Part I. A Turbulent Boundary Layer Flow," ASME Paper 83-GT-70, ASME Gas Turbine Conference, Phoenix, AZ, 1983. (Cited on pages 24, 25, 32, 34, 69, 77, 78, 82, 118, and 173.)

[109] MOORE, J., AND MOORE, J. G., "Entropy Production Rates from Viscous Flow Calculations, Part II – Flow in a Rectangular Elbow," ASME Paper 83-GT-70, ASME Gas Turbine Conference, Phoenix, AZ, 1983. (Cited on page 24.)

[110] MOORHOUSE, D. J., "Proposed System-Level Multidisciplinary Analysis Technique Based on Exergy Methods," *Journal of Aircraft*, Vol. 40, No. 1, 2003, pp. 11–15. (Cited on pages 20 and 53.)

[111] MOORHOUSE, D. J., AND CAMBEROS, J. A., *Exergy Analysis and Design Optimization for Aerospace Vehicles and Systems*, Progress in Astronautics and Aeronautics, American Institute of Aeronautics and Astronautics, 2011. doi: 10.2514/4.868405 (Cited on page 19.)

[112] MORDEN, D. B., "Engine/Airframe Performance Matching," *Aircraft Propulsion Systems Technology and Design*, edited by G. C. Oates, AIAA Education Series, AIAA, Washington, DC, 1989, Chap. 3, pp. 169–237. (Cited on pages 132 and 180.)

[113] MOUTON, S., "Conditions d'équilibre méécanique et énergétique d'un aéronef en mouvement horizontal permanent dans l'atmosphère," ONERA internal document, November 2011, 14 p. (Cited on pages 21 and 47.)

[114] MORAN, M. J., AND SCIUBBA, E., "Exergy Analysis: Principles and Practice," *Journal of Engineering for Gas Turbines and Power*, Vol. 116, 1994, pp. 285–290. (Cited on pages 16, 17, 39, and 129.)

[115] NATALINI, G., AND SCIUBBA, E., "Minimization of the Local Rates of Entropy Production in the Design of Air-cooled Gas Turbine Blades," *Journal of Engineering for Gas Turbines and Power*, Vol. 121, 1999, pp. 466–475. (Cited on page 21.)

[116] OBERKAMPF, W. L., AND TRUCANO, T. G., "Validation Methodology in Computational Fluid Dynamics," AIAA Fluids 2000, Denver, CO, 19–22 June 2000. (Cited on pages 65 and 66.)

[117] OHTA, T., *Energy Technology: Sources, Systems and Frontier Conversion*, 1$^{\text{st}}$ ed., Pergamon Press, 1994, Chap. 3, pp. 89–116. (Cited on pages 14 and 43.)

[118] OSWATITSCH, K., *Gas Dynamics*, Academic Press Inc., New-York, 1956, Chap. 4 and 11. (Cited on pages 28, 31, 34, 50, 57, 86, 185, and 186.)

[119] PANDYA, S., "External Aerodynamics Simulations for the MIT D8 "Double-Bubble" Aircraft Design," 7$^{\text{th}}$ International Conference on Computation Fluid Dynamics (ICCFD7), Big Island, Hawaii, 9–13 July 2012, ICCFD7-4304. (Cited on page 13.)

[120] PANDYA, S. A., HUAND, A., ESPITIA, A. AND URANGA, A., "Computational Assessment of the Boundary Layer Ingesting Nacelle Design of the D8 Aircraft," 52$^{\text{th}}$ AIAA Aerospace Sciences Meeting, National Harbor, MD, 13–17 January 2014. (Cited on pages 13, 14, 139, and 142.)

[121] PAPARONE, L., AND TOGNACCINI, R., "Computational Fluid Dynamics-Based Drag Prediction and Decomposition," *AIAA Journal*, Vol. 41, No. 9, 2003, pp. 1647–1657. (Cited on pages 49 and 53.)

[122] PATTERSON, JR., J. C., AND FLECHNER, S. G., "Exploratory Wind-Tunnel Investigation of a Wingtip-Mounted Vortex Turbine for Vortex Energy Recovery," NASA Technical Paper 2468, 1985. (Cited on page 43.)

[123] PATTERSON, JR., J. C., "Wingtip Vortex Turbine," US Patent Number: 4,917,332, Newport News, VA, Apr. 17, 1990. (Cited on page 43.)

[124] PELLEGRINI, L. F., GANDOLFI, R., DA SILVA, G. A. L., AND DE OLIVEIRA, JR., S., "Exergy Analysis as a Tool for Decision Making in Aircraft Systems Design," 45th AIAA Aerospace Sciences Meeting, Reno, NV, 8–11 January 2007, AIAA 2009-1132. (Cited on pages 22 and 25.)

[125] PERIANNAN, V., "Investigation of the Effects of Various Energy and Exergy-Based Objectives/Figures of Merit on the Optimal Design of High Performance Aircraft System," MSc Dissertation, Virginia Polytechnic Institute and State University, Blacksburg, VA, 2005. (Cited on page 23.)

[126] PERIANNAN, V., VON SPAKOVSKY, M. R., AND MOORHOUSE, D. J., "Investigation of the effects of various energy and exergy-based figures of merit on the optimal design of a high performance aircraft system," ASME 2006 International Mechanical Engineering Congress and Exposition, Paper No. IMECE2006-14186, pp. 337-347, Chicago, IL, 5–10 November 2006. (Cited on page 23.)

[127] PLAS, A., "Performance of Boundary Layer Ingesting Propulsion System", MSc Thesis, Massachusetts Institute of Technology, 2006. (Cited on page 134.)

[128] RANSICK, T. F., "Wingtip Turbine," US Patent Number: 5,150,859, Sundstrand Corporation, Rockford, Ill, Sep. 29, 1992. (Cited on pages 42 and 43.)

[129] RANT, Z., "Exergie, ein neues Wort für technische Arbeitsfähigkeit," *Forsch. Ing. Wes.*, Vol. 22, No. 1, 1956, pp. 36–37. (Cited on pages v, 15, and 16.)

[130] RIGGINS, D. W., "Evaluation of Performance Loss Methods for High-Speed Engines and Engine Components," *Journal of Propulsion and Power*, Vol. 13, No. 2, 1997, pp. 296–304. (Cited on page 21.)

[131] RIGGINS, D. W., MCCLINTON, C. R., AND VITT, P. H., "Thrust Losses in Hypersonic Engines Part 1: Methodology," *Journal of Propulsion and Power*, Vol. 13, No. 2, 1997, pp. 281–287. (Cited on pages 21, 53, and 129.)

[132] RIGGINS, D. W., "The Thermodynamic Continuum of Jet Engine Performance: The Principle of Lost Work due to Irreversibility in Aerospace Systems," *Int. J. Thermodynamics*, ISSN 1301-9724, Vol. 6, No. 3, 2003, pp. 107–120. (Cited on pages 122 and 129.)

[133] RIGGINS, D. W., TAYLOR, T., AND MOORHOUSE, D. J., "Methodology for Performance Analysis of Aerospace Vehicles Using the Laws of Thermodynamics," *Journal of Aircraft*, Vol. 43, No. 4, 2006, pp. 953–963. (Cited on pages 20, 47, 50, and 53.)

[134] RIGGINS, D. W., MOORHOUSE, D. J., AND CAMBEROS, J. A., "Characterization of Aerospace Vehicle Performance and Mission Analysis Using Thermodynamic Availability," *Journal of Aircraft*, Vol. 47, No. 3, 2010, pp. 904–916. (Cited on pages 20, 50, and 53.)

[135] RIGGINS, D. W., CAMBEROS, J., WOLFF, M. AND BOWCUTT, K., "Mission-Integrated Exergy Analysis for Hypersonic Vehicles: Methodology and Application," *Journal of Propulsion and Power*, Vol. 29, No. 3, 2013, pp. 610–620. (Cited on pages 20, 21, 25, 50, and 53.)

[136] RIVERS, M. B., AND DITTBERNER, A., "Experimental Investigation of the NASA Common Research Model," 28th AIAA Applied Aerodynamics Conference, Chicago, IL, 28 June – 01 July 2010, AIAA 2010-4218. (Cited on pages 4, 101, 116, and 117.)

[137] RIVERS, M. B., AND DITTBERNER, A., "Experimental Investigation of the NASA Common Research Model in the NASA Langley National Transonic Facility and NASA Ames 11-Ft Transonic Wind Tunnel," 49th AIAA Aerospace Sciences Meeting, Orlando, FL, 4–7 January 2011, AIAA 2011-1126. (Cited on pages 4, 101, 116, and 117.)

[138] ROSKAM, J., AND LAN, C-T. E., *Airplane Aerodynamics and Performance*, Design, Analysis and Research Corporation, 1st ed., 1997. (Cited on page 178.)

[139] ROTH, B. A., "A Theoretical Treatment of Technical Risk in Modern Propulsion System Design," Ph.D. Dissertation, Dept. of Aerospace Engineering, Georgia Institute of Technology, Atlanta, GA, 2000. (Cited on pages 20 and 129.)

[140] ROTH B., AND MAVRIS, D., "Minimizing Vehicle Environmental and Economic Cost Via Thermodynamic Work Potential," NSF DMII Grantees Conference, Tampa, FL, 2001. (Cited on pages 7, 20, 41, and 53.)

[141] ROTH, B. A., AND MAVRIS, D. N., "Comparison of Thermodynamic Loss Models Suitable for Gas Turbine Propulsion," *Journal of Propulsion and Power*, Vol. 17, No. 2, 2001, pp. 324–332. (Cited on pages 20, 21, 53, 122, and 129.)

[142] ROTH B., "Aerodynamic Drag Loss Chargeability and Its Implications in the Vehicle Design Process," 1st AIAA Aircraft, Technology, Integration, and Operations Forum, Los Angeles, CA, 2001. (Cited on pages 20, 23, and 53.)

[143] ROTH, B., "Work Potential Perspective of Engine Component Performance," *Journal of Propulsion and Power*, Vol. 18, No. 6, 2002, pp. 1183–1190. (Cited on pages 20 and 21.)

[144] ROTH, B. A., AND MAVRIS, D. N., "A Generalized Model for Vehicle Thermodynamic Loss Management and Technology Concept Evaluation," *Journal of Aircraft*, Vol. 40, No. 1, 2003, pp. 62–69. (Cited on pages 20, 23, 47, and 53.)

[145] SATO, S., "Assessment of Propulsion System Configuration and Fuel Consumption on Hybrid Wing Body Fuel Efficiency," 49st AIAA Aerospace Sciences Meeting, 4–7 January 2011, Orlando, FL, 2011. (Cited on page 13.)

[146] SATO, S., "The Power Balance Method For Aerodynamic Performance Assessment," Ph.D. Dissertation, Aeronautics and Astronautics Dept., Massachusetts Institute of Technology, Cambridge, MA, 2012. (Cited on pages 8, 13, 146, and 176.)

[147] SCHLICHTING, H., *Boundary-Layer Theory*, 7th ed., McGraw-Hill Series in Mechanical Engineering, 1978, Chap. XXII. (Cited on pages 12, 154, 155, and 185.)

[148] SCHWAMBORN, D., GERHOLD, T., AND HEINRICH, R., "The DLR TAU-Code: Recent Applications in Research and Industry," Invited Lecture in Proceedings on CD of the European Conference on Computational Fluid Dynamics ECCOMAS CFD 2006, P. Wesseling, E. Onate, J. Périaux (Eds), The Netherlands, 2006. (Cited on page 58.)

[149] SCIUBBA, E., AND WALL, G., "A brief Commented History of Exergy From the Beginnings to 2004," *Int. J. of Thermodynamics*, Vol. 10, No. 1, 2007, pp. 1–26. (Cited on pages v, 17, 18, and 19.)

[150] SEROVY, G. K., "Axial Flow Compressor Aerodynamics," *Aerothermodynamics of Aircraft Engine Components*, edited by G. C. Oates, AIAA Education Series, AIAA, Washington, DC, 1985, Chap. 4, pp. 148–220. (Cited on page 132.)

[151] SIU, N., TITCHENER, N., CASSES, C., HUANG, A., URANGA, A., DRELA, M. AND GREITZER, E., "Evaluating Propulsor Mechanical Flow Power in Powered Aircraft Wind Tunnel Experiments," 32nd AIAA Applied Aerodynamics Conference, AIAA Aviation 2014, Atlanta, GA, 16–20 June 2014. (Cited on pages 13, 14, and 144.)

[152] SMITH, L. H., JR., "Wake Ingestion Propulsion Benefit," *Journal of Propulsion and Power*, Vol. 9, No. 1, 1993, pp. 73–82. doi:10.2514/3.11487 (Cited on pages 41 and 52.)

[153] SMITH, B. R., "A Near Wall Model for the $k-l$ Two Equation Turbulence Model," 25th Fluid Dynamics Conference, Colorado Springs, CO, 20–23 June 1994, AIAA Paper 94-2386. (Cited on page 92.)

[154] SMITH, S. C., "A Computational and Experimental Study of Non-Linear Aspects of Induced Drag," NASA Technical Paper 3598, 1996. (Cited on page 11.)

[155] SPALART, P. R., "On the far wake and induced drag of aircraft," *J. Fluid Mech.*, Vol. 603, 2008, pp. 413–430. (Cited on page 11.)

[156] SPALART, P. R., AND ALLMARAS, S. R., "A One-Equation Turbulence Model for Aerodynamic Flows," *Recherche Aerospatiale*, No. 1, 1994, pp. 5-21. (Cited on pages 4, 24, 65, 67, 71, 92, 102, 118, and 135.)

[157] STOLIKER, F. N., "Guide to In-Flight Thrust Measurement of Turbojets and Fan Engines," Advisory Group for Aerospace Research and Development, MIDAP Study Group, AG-237, 1979. (Cited on pages 3, 146, 147, 178, and 179.)

[158] THIBERT, J. J., RENEAUX, J., AND SCHMITT, V., "ONERA Activities on Drag Reduction," 17th ICAS Congress, Stockholm, Sweden, 9–14 September 1990. (Cited on page 43.)

[159] TILLMAN, T. G., "System Study and Distortion-Tolerant Fan Design for a Boundary Layer Ingesting Propulsion System," NASA NRA NNC07CB59C Phase 2 Final Report, 2010. (Cited on page 144.)

[160] TINSETH, R., "Boeing Current Market Outlook, 2013–2032," 2013. (Cited on page 1.)

[161] TOGNACCINI, R., "Methods for drag decomposition, Thrust-drag bookkeeping from CFD calculations," CFD-based Aircraft Drag Prediction and Reduction Lecture Series, Von Karman Institute for Fluid Dynamics, Hampton, VA, 2003. (Cited on page 146.)

[162] TONA, C., RAVIOLO, P. A., PELLEGRINI, L. F., AND DE OLIVEIRA JR, S., "Exergy and thermoeconomic analysis of a turbofan engine during a typical commercial flight," *Energy*, Vol. 35, 2010, pp. 952–959. (Cited on page 22.)

[163] TOUBIN, H., SALAH EL DIN, I., MÉHEUT, M., "Multipoint Aerodynamic High Fidelity Shape Optimization of an Isolated Engine Nacelle," 52nd AIAA Aerospace Sciences Meeting and Exhibit, National Harbor, MD, 13–17 January 2014. (Cited on page 123.)

[164] TOUBIN, H., AND BAILLY, D., "Far-Field Drag Decomposition for Unsteady Flows," 49th International Symposium of Applied Aerodynamics, AAAF, Lille, France, 24–26 March 2014. (Cited on pages 58 and 174.)

[165] TOUBIN, H., AND BAILLY, D., "Development and Application of a New Unsteady Far-Field Drag Decomposition Method," 32nd AIAA Applied Aerodynamics Conference, Atlanta, GA, 16–20 June 2014. (Cited on page 58.)

[166] TSATSARONI, G., "Thermoeconomic Analysis and Optimization of Energy Systems," *Prog. Energy Comb. Sci.*, Vol. 19, 1193, pp. 227–257. (Cited on pages 20 and 174.)

[167] TSATSARONI, G., "Definitions and Nomenclature in Exergy Analysis and Exergoeconomics," *Energy*, Vol. 32, 2007, pp. 249–253. (Cited on page v.)

[168] TSATSARONI, G., "Comments on the Paper «A Brief Commented History of Exergy from the Beginnings to 2004»," *Int. J. of Thermodynamics*, Vol. 10, 2007, pp. 187–192. (Cited on page v.)

[169] TURAN, O., "Effect of reference altitudes for a turbofan engine with the aid of specific-exergy based method," *In. J. Exergy*, Vol. 11, No. 2, 2012, pp. 252–270. (Cited on page 22.)

[170] UENO, M., YAMAMOTO, K., TANAKA, K., MURAYAMA, M., AND TOGNACCINI, R., "Far-Field Drag Analysis of NASA Common Research Model Simulation," *Journal of Aircraft*, Vol. 50, No. 2, 2013, pp. 388–397. (Cited on pages 49, 53, 111, and 117.)

[171] URANGA, A., DRELA, M., GREITZER, E. M., TITCHENER, N. A., LIEU, M. K., SIU, N. M., HUANG, A. C., GATLIN, G. M., AND HANNON, J. A., "Preliminary Experimental Assessment of the Boundary Layer Ingestion Benefit for the D8 Aircraft," 52th AIAA Aerospace Sciences Meeting, National Harbor, MD, 13–17 January 2014. (Cited on pages 13, 14, 174, and 197.)

[172] VACHON, M. J., RAY, R. J., WALSH, K. R., AND ENNIX, K., "F/A-18 Performance Benefits Measured During the Autonomous Formation Flight Project," NASA/TM-2003-210734, 2003. (Cited on page 42.)

[173] VAN DAM, C. P., "Recent experience with different methods of drag prediction," *Progress In Aerospace Sciences*, Vol. 35, 1999, pp. 751–798. (Cited on pages 23, 49, 53, 57, and 178.)

[174] VAN DER VOOREN, J., AND DESTARAC, D., "Drag/thrust analysis of jet-propelled transonic transport aircraft; Definition of physical drag components", *Aerospace Science and Technology*, Vol. 8, 2004, pp. 545–556. (Cited on pages 57, 66, 116, 118, and 174.)

[175] VAN DER VOOREN, J., AND SLOOFF, J. W., "CFD-Based Drag Prediction: State-of-the-Art, Theory, and Prospects," Lectures Notes, AIAA Professional Studies Series, Course on Drag-Prediction and Measurement, Dutch Aerospace Lab, NLR TP 90247, 1990. (Cited on page 49.)

[176] VASSBERG, J. C., AND JAMESON, A., "In Pursuit of Grid Convergence for Two-Dimensional Euler Solutions," *Journal of Aircraft*, Vol. 47, No. 4, 2010, pp. 1152–1166. (Cited on page 189.)

[177] WANG, T., MARTIN, P. B., AND BRITCHER, C. P., "Surface Heat Exchangers For Aircraft Applications: A Technical Review and Historical Survey," 37th AIAA Aerospace Sciences Meeting & Exhibit, Reno, NV, 11–14 January 1999. (Cited on page 154.)

[178] WEEKS, T. M. (ed.), *Journal of Aircraft*, Vol. 40, No. 1, 2003, 223 p. (Cited on page 19.)

[179] WHITE, F. M., *Viscous Fluid Flow*, 2nd ed., McGraw-Hill, Inc., 1991, p. 72. (Cited on page 184.)

ABSTRACT

A new exergy-based formulation is derived for the assessment of the aerothermopropulsive performance of civil aircraft. The choice of exergy is motivated by its ability to provide a well-established and consistent framework for the design of aerospace vehicles. The output of the derivation process is an exergy balance between the exergy supplied by a propulsion system or by heat transfer, the mechanical equilibrium of the aircraft, and the exergy outflow and destruction within the control volume. The theoretical formulation is subsequently numerically implemented in a Fortran code named *ffx* for the post-processing of CFD-RANS flow solutions. Unpowered airframe configurations are examined with grid refinement studies and a turbulence model sensitivity analysis is preformed. A numerical correction is introduced and calibrated to obtain an accuracy similar to the near-field drag method. The code is thereby validated against well-tried methods of drag prediction and wind-tunnel tests, when available.

The investigation of powered configurations demonstrates the ability of the approach for assessing the performance of configurations with aerothermopropulsive interactions. First, the formulation is validated for the simple case of a turbojet engine for which consistent figures of merit are exhibited. The method is also proved robust for assessing the overall performance of a boundary layer ingesting propulsion system placed on the upper surface of a simplified blended wing-body architecture. Moreover, this configuration enables the investigation of thermopropulsive interactions by the transfer of heat upstream of the propulsion system. Subsequently, the integration of a heat exchanger on a commercial aircraft is examined for which the exergy point of view provides guidelines for an efficient design. The ability of the formulation to consistently assess all these types of subsystems is a clear benefit of this method.

Keywords: exergy, energy, performance, CFD, aerodynamics, propulsion, boundary-layer ingestion

Résumé

Une nouvelle formulation basée sur la notion d'exergie est introduite pour la détermination des performances aéro-thermo-propulsives des avions civils. Le choix du concept d'exergie est motivé par sa capacité à fournir un cadre de travail bien établi pour la conception de véhicules aérospatiaux. Les performances avions sont établies à partir d'une équation bilan qui met en relation l'exergie fournie, par un système propulsif ou par transfert de chaleur, l'équilibre mécanique de l'appareil, et sa destruction partielle dans le volume de contrôle. Cette formulation théorique est ensuite implémentée numériquement dans un code Fortran, appelé *ffx*, pour le post-traitement de solutions CFD-RANS. Des configurations non propulsées sont étudiées avec raffinement de maillage et une analyse de la sensibilité du code au modèle de turbulence employé pour obtenir la solution CFD est réalisée. Le code est ainsi validé par rapport à des méthodes éprouvées de détermination de la traînée et à des essais en soufflerie, si disponibles.

L'approche est ensuite appliquée pour la détermination des performances de configurations propulsées présentant de fortes interactions aéro-thermo-propulsives. Dans un premier temps, la cohérence de la formulation est validée pour un turbojet pour lequel des indicateurs de performances cohérents sont obtenus. La méthode est également prouvée robuste pour l'analyse des performances globales de l'ingestion de couches limites par un moteur placé à l'arrière d'une aile volante simplifiée. Cette architecture permet également l'étude des interactions thermopropulsives lors d'un transfert de chaleur imposé en amont du système propulsif. Enfin, l'intégration d'un échangeur de chaleur sur un avion commercial est examinée pour en déduire des recommandations pour une conception efficace d'un point de vue exergétique. La capacité de la formulation à pouvoir traiter de façon cohérente ces différents types de sous-systèmes est le principal avantage de cette méthode.

Keywords: exergie, énergie, performances, CFD, aérodynamique, propulsion, ingestion couches limites